

© 2017 Ashley Armstrong

MODELING AND CONTROL OF AN EASY-TO-USE DIRECT WRITE PRINTING
SYSTEM FOR FABRICATION OF BONE SCAFFOLDS

BY

ASHLEY ALLISON ARMSTRONG

THESIS

Submitted in partial fulfillment of the requirements
for the degree of Master of Science in Mechanical Engineering
in the Graduate College of the
University of Illinois at Urbana-Champaign, 2017

Urbana, Illinois

Advisers:

Professor Andrew G. Alleyne
Professor Amy Wagoner Johnson

Abstract

3D printing is a diverse field, in particular for biological or bioengineering applications. As a result, research teams working in this area are often multidisciplinary. A (bio) 3D printer in this research environment should balance performance with ease of use to enable system adjustments and operation for all machine users from a wide range of disciplines. This work presented results in the development of an easy-to-use direct-write (DW) printing system for fabrication of rectilinear bone scaffolds. Common motion control problems, which are barriers to ease of use, were addressed and implemented in a way that researchers outside of the controls field could easily understand. The main goal of this work was to ensure that this system could be easily operated and adjusted by future users to enable a wide range of projects. In addition, we hope the design and development steps presented can be extended to other systems to lower the technical hurdle of motion control for any laboratory or researcher with an interest in using DW printing in his or her field.

The design aspects and control parameters included a dynamic model of a 3-stage positioning system for bone scaffold fabrication, a feedforward plus feedback controller design, active pressure regulation, and a user-friendly iterative learning control (ILC) compensator. The ability of the (bio) 3D printer to print rectilinear bone scaffolds is presented. Further, preliminary work in precise start/stop of ink flow and curved scaffold rods was presented to enable printing of multi-material and curvilinear bone scaffolds in future projects.

To my family, friends, dogs and teachers.

Acknowledgements

I would like to begin by thanking my advisers, Dr. Andrew Alleyne and Dr. Wagoner Johnson. Without their guidance and commitment to my development as a researcher, none of my experiences at the University of Illinois would have been possible. Both Dr. Alleyne and Dr. Wagoner Johnson demonstrate a unique commitment to each students' experience in graduate school. They've helped me develop as a well-rounded individual, which has positively impacted all facets of my life. Working with the both of them has been extremely rewarding and an enjoyable experience, and is something I'll always be thankful for.

I would also like to thank my parents and my younger sister for their unwavering support over the last few years. I attribute my strong work ethic to both my mother and father, who not only instilled in me from a young age to believe in myself and to never give up, but lead by example. My sister, Sarah, has willingly helped cover my basic human needs during busy times, which included taking care of my dog, Marshmallow. I am forever grateful for the three of them.

To my fellow labmates in the Alleyne Research Group and the Wagoner Johnson Group, thank you for both improving my research skills and making my time enjoyable. To the senior lab members, Justin, Matt, Herschel, Bryan, Laurie, and Jie, thank you for being outstanding examples of great researchers. Your accomplishments have and always will motivate and inspire me, and I truly appreciate your willingness to help me with my own work. To Zack, Pamela, Nate, Spencer, Malia, and Oyuna, thank you for being the best classmates and even better friends. To the original S³ (Sarah, Sunny, and Spencer), thank you for bringing such a positive and fun attitude to the lab. All of my labmates have made my time in graduate school so memorable, and I feel very fortunate to have been a part of these outstanding groups.

Finally, I would like to acknowledge the financial support provided by the National Science Foundation (NSF), and the Graduate Research Fellowship Program (GRFP). This support has given me the flexibility to work with two advisers and conduct research, which interests me and has societal value.

Tables of Contents

LIST OF FIGURES	IX
LIST OF TABLES	XVII
CHAPTER 1 INTRODUCTION	1
1.1 Goal/Motivation	2
1.2 User-centered design	6
1.3 Direct-Write Printing.....	7
1.4 Manufacturing space of current AM technology	9
1.4.1 State of the art extrusion printers	10
1.4.2 Direct write printing with ceramic-based colloidal inks	12
1.5 Thesis outline	13
CHAPTER 2 SYSTEM DESCRIPTION.....	14
2.1 Introduction	14
2.2 End-user Description.....	15
2.3 Extrusion System.....	15
2.3.1 Extrusion system in this work	16
2.4 Positioning System.....	17
2.4.1 Positioning system in this work	17
2.5 Motion control system.....	19
2.5.1 Encoders.....	21
2.5.2 Servo Drives.....	22
2.5.3 Limit Switches	22
2.5.4 Pressure Regulator	23
2.5.5 Controller	26
2.5.6 Power Supplies.....	28
2.6 Program Selection	29

2.6.1 LabVIEW user interface.....	29
2.6.2 SoftMotion	30
2.6.3 SoftMotion program examples.....	31
2.6.4 Fabrication of the lattice structure within SoftMotion	33
2.6.5 Software Limitations.....	35
2.7 Program description for bone scaffold fabrication.....	36
2.7.1 Initialization	36
2.7.2 Main Program.....	37
2.7.3 Shutdown.....	46
2.8 Conclusion.....	47
CHAPTER 3 MATERIAL PREPARATION.....	48
3.1 Introduction	48
3.2 Colloidal Science.....	49
3.2.1 Powder Preparation	50
3.2.2 Colloid Stability	53
3.2.3 Suspension Rheology	56
3.2.4 Fluid to Gel Transition	60
3.2.5 Ink Behavior during Printing.....	60
3.3 CaP Based Ink Preparation.....	61
3.3.1 Powder Preparation	61
3.3.2 Stabilization of Colloidal HA Ink	68
3.3.3 Rheological Adjustments	68
3.3.4 Fluid to Gel Transition of HA Colloidal Ink.....	69
3.4 Post Processing Scaffolds.....	69
CHAPTER 4 SYSTEM MODEL AND CONTROL STRATEGIES.....	70
4.1 System Identification.....	70
4.1.1 Plant Dynamics	71
4.1.2 System Disturbances	72
4.1.3 Plant Models.....	78
4.1.4 System Identification Techniques	79

4.2 Control Architecture.....	86
4.2.1 Feedback Controllers	87
4.2.2 User friendly iterative learning control	95
4.2.3 Pressure regulation	97
CHAPTER 5 BONE TISSUE ENGINEERING.....	101
5.1 Tissue Engineering.....	101
5.2 Review of Bone Anatomy	102
5.2.1 Composition of Bone	102
5.2.2 Bone Structure.....	103
5.2.3 Bone Cells	105
5.2.4 Cell Differentiation	107
5.2.5 Bone Functions.....	110
5.2.6 Bone Remodeling.....	110
5.3 Artificial Bone Scaffolds.....	112
5.3.1 Biological Considerations	113
5.3.2 Mechanical Requirements	115
5.3.3 Material Requirements	115
5.4 Scaffold system of interest in this work	118
CHAPTER 6 MACHINE CAPABILITIES AND FUTURE DIRECTIONS.....	120
6.1 Goal assessment	120
6.1.1 Machine Performance	120
6.1.2 Usability	121
6.2 Machine Capabilities and Limitations.....	122
6.2.1 Capabilities.....	122
6.2.2 Limitations	133
6.2.3 Placement in current manufacturing space.....	133
6.3 Future Directions	134
6.3.1 Future work for this DW printer	134
6.3.2 Bone Tissue Engineering (BTE)	136
6.3.3 Additive Manufacturing (AM)	137

6.4 Thesis Summary	139
REFERENCES	141
APPENDIX A POWDER PREP AND XRD TIPS	155
A.1 Powder Preparation	155
A.2 Ink Formulation	158
A.3 Furnace Operation and Thermal Processing Tips	158
A.4 XRD SOP	159
A.4.1 Sample preparation in the lab	159
A.4.1 Sample loading in XRD machine	159
A.5 XRD Software	160
A.5.1 Jade Software	161
A.5.2 Profex Software	161
APPENDIX B ROBERTA OPERATING INSTRUCTIONS	162
B.1 Instructions for Scaffold Fabrication	162
APPENDIX C ADJUSTMENT INSTRUCTIONS FOR FUTURE WORK	167
C.1 Modify Axis Properties	167
C.1.1 Modify Control gains	168
C.1.2 Encoder Units	168
C.1.3 Limit Switch Information	168
APPENDIX D PROGRAM DESCRIPTIONS	170
D.1 Zero Axes	172
D.2 Lead in Lines	173
D.3 Calibration Layers and Updating Reference Command	173
D.4 Layers 1 and 2	175
APPENDIX E ELECTRICAL WIRING	176
E.1 Breadboards	177
E.2 Electrical and Power Connections	179

List of Figures

Figure 1.1 Histology sections of implanted (A) single-domain and (B) multi-domain scaffolds with manufacturing defects. Bone is shown in pink/red, and macropores without bone appear bright white. The red-dashed line indicates the bone growth front. Manufacturing defects in multi-domain scaffolds cause full blocking (*) or partial obstruction (~) of macropores. Image from [22].	4
Figure 1.2 Previously used micro-robotic deposition system. (a) Robotic positioning system and gantry set up. (b) Zoomed in view of the vision system. Image from [24].	5
Figure 1.3 Direct-write printing of a 3D periodic structure. (a) Computer-controlled cartesian XYZ robot, (b) filament deposition of a single 2D layer, (c) close-up view of a periodic microstructure. Image from [42].	8
Figure 1.4 Rectilinear, porous lattice structure used as a bone scaffold fabricated using direct-write printing. Image from [45].	9
Figure 2.1 Direct-write printer designed to print artificial bone scaffolds. (1) Dispensing material (ink) inside the syringe barrel. (2) Substrate (black metal plate) onto which the ink was deposited. (3) Pneumatic-based extrusion system (shown in more detail in Figure 2.3). (4) Positioning system, which includes the XYZ axes (labeled in red).	14
Figure 2.2 Types of dispensing mechanisms for DW printing: (A) pneumatic extrusion and (B) mechanical extrusion. Image adapted from [1].	16
Figure 2.3 Pneumatic extrusion for DW printing. (A) Extrusion system used in this research. The black cylinder is part of the ball screw mechanism. (B) Schematic of the extrusion process, adapted from [24].	17
Figure 2.4 Illustration (left) and schematic (right) of the Z axis set up of the DW printer.	19
Figure 2.5 Components of a motion control platform illustrated as a feedback loop.	20

Figure 2.6 Electrical connection diagram for the DW printer. Details of each individual connection (A.1, A.2, etc.) can be found in Appendix E.....	21
Figure 2.7 Zeroing circuit, which also serves as the Z axis reverse limit switch.	23
Figure 2.8 Pressure regulator (Marsh Bellofram), and the DIP switch settings.	24
Figure 2.9 Calibration plot of the pressure regulator. The regulator performance was slightly different than the factory calibration. The “FINE” and “SPAN” potentiometers were slightly adjusted to ensure full pressure range. The equation of the calibration line is pressure (psi) = 2.93*voltage + 0.77, where pressure is the output pressure of the regulator, and voltage is the 0-10 V analog input signal.	25
Figure 2.10 cRIO system, including the controller and chassis with 5 I/O modules.....	26
Figure 2.11 PID plus Feedforward control loop embedded in the NI 9514 modules.	27
Figure 2.12 Power supply connections for each piece of hardware in the DW printer.	28
Figure 2.13 Graphical user interface of the DW printer for bone scaffold fabrication.	30
Figure 2.14 “Express” program examples within LabVIEW that are useful for motion control.	32
Figure 2.15 Data-flow programming example within LabVIEW using “express” programs. The error bars can be used to induce a specific order. In this frame, the X axis is first commanded to move 10 mm at 2mm/s, and is then commanded to stop.....	32
Figure 2.16 Scaffold architecture broken down into two layers, which were repeated to form the three-dimensional structure. In this diagram, each layer was repeated twice to form a 4 layer scaffold.	33
Figure 2.17 Program code for the fabrication of a lattice structure, which was organized into two tabs for Layer 1 and Layer 2. Each array element was associated with a “Position” input on an Express VI. X Position 1 was $\Delta X1$, and Y Position 1 was $\Delta Y1$. X Position 2 was $\Delta X2$, and Y Position 2 was $\Delta Y2$	35
Figure 2.18 Initialization code in a flat sequence structure, which includes 8 steps (a-h). Each step occurs before moving onto the main program.	37
Figure 2.19 Bone scaffold with lead-in lines, which are outlined in a red dashed box.	38

Figure 2.20 Main program of the bone scaffold fabrication code, which includes 4 loops: producer loop, consumer loop 1 (CL1), consumer loop 2 (CL2), and a printing loop.....	39
Figure 2.21 Zoomed in view of the communication between the producer loop and CL1 using a queue. The communication involved three steps: (1) queue was created in the Initialization Step (Figure 2.18), (2) the producer loop enqueued data, and (3) CL1 dequeued and used this data.....	41
Figure 2.22 Zoomed in view of the communication between the producer loop and CL2 using a notifier. Similar to the queue, the communication involved three steps: (1) notifier was created in the Initialization Step (Figure 2.18), (2) the producer loop sent a message to the notifier, and (3) CL2 waited for this data.	42
Figure 2.23 Producer loop for the bone scaffold fabrication code. The queue is highlighted by a red arrow.	43
Figure 2.24 Consumer loop 1 for the bone scaffold fabrication code. The outer structure was a while loop running at 1 kHz, with a queue handler and case structure inside. The three elements of a case structure include: (1) selector terminal, (2) case selector label, and (3) subdiagram (case).	44
Figure 2.25 Consumer loop 2 for the bone scaffold fabrication code. The outer structure was a while loop running at 10 Hz, with a notifier and case structure inside, which contained the same 3 elements as Figure 2.24.....	45
Figure 2.26 Printing loop for the fabrication of a lattice structure, which was a while loop containing three Read Express VIs to read the position of each axis and output this to the graph on the GUI.	46
Figure 2.27 Shutdown code in a flat sequence structure, which included 6 steps (a-f). Each step occurred before exiting the bone scaffold fabrication code.	47
Figure 3.1 Scaffolds printed with poorly-tuned ink in which the ink viscosity decreased mid print due to phase separation, or “filter-pressing”.	49
Figure 3.2 Illustration of speed dependent milling media motion in a ball mill. Tumbling (left) and falling (right). Typically, $\omega_1 < \omega_2$	52

Figure 3.3 Diagram illustrating (A) electrostatic and (B) steric stabilization. Image from [93].	54
Figure 3.4 Adsorbed polyelectrolyte species on a ceramic surface (blue) as a function of pH and ionic strength. δ is the steric interaction length. Image from [80].	55
Figure 3.5 Types of rheological behavior for shear rate vs. yield stress (A) and shear rate vs. viscosity (B). (a) Newtonian flow; (b) shear thinning; (c) shear thickening; (d) Bingham plastic; and (e) pseudoplastic with a yield stress. Image from [80].	57
Figure 3.6 Potential energy as a function of h , the separation distance between particles for hard sphere and soft sphere systems. Image adapted from [80].	58
Figure 3.7 Krieger-Dougherty relationship, with the region of typical solids loading values for colloidal ink shaded in green. Image from [24].	59
Figure 3.8 Behavior of cellulose binder fibers under shear. Image from [24].	59
Figure 3.9 Fluid to gel transition for colloidal inks. Image from [78].	60
Figure 3.10 SEM images of the raw precursor powders: a) CaHPO_4 and b) CaCO_3 .	62
Figure 3.11 Unpublished CaP phase diagram at PH₂O = 550 mm Hg developed by colleagues at RMS. The data for 1700-1200 °C was obtained from [96], 1200-1000 °C data was obtained from [97], and the 0-1000 °C data was obtained from data at RMS. $\text{CaO (wt-\%)} = \text{CaO}/(\text{CaO} + \text{P}_2\text{O}_5)$. The biphasic region of interest in this work is outlined in red dashed lines.	64
Figure 3.12 SEM image of the final powder blend after heat treatment and ball milling. The particles are sufficiently small (~1-2 μm) and have a tight PS distribution.	68
Figure 4.1 Control effort plotted as a function of velocity for sliding friction compensation. The black dots represent an example of data points collected by commanding a range of control inputs and recording the corresponding axis velocity.	73
Figure 4.2 Friction compensation results for the X and Y-axes.	74
Figure 4.3 Friction compensation results for the Z-axis.	75

Figure 4.4 The Z-Axis positioned horizontally to remove the effects of gravity during friction compensation.....	75
Figure 4.5 PID plus Feedforward control loop embedded in the NI 9514 modules.	76
Figure 4.6 Gravity offset determination.....	78
Figure 4.7 Logarithmic decrement system identification method implemented on the X-Axis.....	81
Figure 4.8 Step response for X-axis model validation.....	84
Figure 4.9 Step response for Y-axis model validation.....	85
Figure 4.10 Step response for Z-axis model validation.	86
Figure 4.11 Illustration of a feedback diagram used for reference tracking.	87
Figure 4.12 Performance of the X axis to a 2 mm step input with the designed PI controller implemented.	90
Figure 4.13 Performance of the Y axis to a 2 mm step input with the designed PI controller implemented.	91
Figure 4.14 Performance of the Z axis to a 1 rev step input with the designed PI controller implemented.	92
Figure 4.15 Region for stable operating PI gains for the X axis. The PI gains chosen for operation are indicated by an asterisk.	93
Figure 4.16 Region for stable operating PI gains for the Y axis. The PI gains chosen for operation are indicated by an asterisk.	94
Figure 4.17 Region for stable operating PI gains for the Z axis. The PI gains chosen for operation are indicated by an asterisk.	95
Figure 4.18 Position arrays before (left) and after (right) the ILC test run.	97
Figure 4.19 Single layer scaffolds printed before (left) and after (right) active pressure control.	98
Figure 4.20 Pressure reduction and subsequent increase subVIs implemented in the main code structure (A). Code layout of the pressure reduction (B) and pressure increase (C) subVIs.	98
Figure 4.21 Main program GUI where the user was able to modify the two parameters for both pressure reduction and pressure increase.	99

Figure 5.1 Hierarchical organization of bone. Image from [118]..... 103

Figure 5.2 Bone anatomy, which is made up of compact bone (cortical bone), spongy bone (trabecular bone), and bone marrow. Cortical bone makes up the outer layer, while trabecular bone, which contains red marrow, is mostly found at the ends of long bones (A), or between plates of compact bone for flat bones (B). Red marrow contains blood stem cells which differentiate into red blood cells, white blood cells, or platelets. Yellow marrow is largely composed of adipocytes and is found in the medullary cavity. Images from [120]..... 105

Figure 5.3 Physical factors regulating lineage commitment of MSCs. The physical factors involved in stem cell fate decision include cell shape, external mechanical forces, extracellular matrix, and geometric structures. A) Spread cells tend to differentiate into osteoblasts while round cells tend to become adipocytes. B) Physical forces can direct MSC differentiation by controlling motor proteins such as myosin II. C) ECM components can regulate differentiation by binding to cell adhesion molecules like integrins. D) Geometric changes can also dictate cell differentiation. Image from [126]. 109

Figure 5.4 Bone scaffold with an inter-rod microporosity and macroporosity between rods. Lattice structures can be prepared with or without microporosity, which is created by pore forming agents during ink fabrication. Image from [24]..... 114

Figure 5.5 Structural length scales considered in the design of bone scaffolds. The defect site is highlighted in blue. Here, the envelope involves multiple domains with different macro and microscale properties. Scaffolds made of orthogonal layers of rods can incorporate single or multiple domains, which have different macropore spacing. Further, rods can either be microporous (MP) or nonmicroporous (NMP). Image from [22]..... 119

Figure 6.1 Bone scaffold deposition to test controller effectiveness. 121

Figure 6.2 Multiple bone scaffolds printed in the same printing session. Here, the user chose $n=2$ and $m=4$ 123

Figure 6.3 Ink dynamics during ink start-up and material termination. The response included a time delay and a slow time constant, which made precise start/stop of the ink flow challenging. Image from [24]. 124

Figure 6.4 Timing diagram for start/stop flow of the polymer material in a Stratasys FDM printer [153]..... 125

Figure 6.5 GUI in the start/stop ink flow LabVIEW code. The user-adjustable parameters are shown on the left, and the colors correspond to the parameters labeled in the time vs. pressure plot. Points A-D refer to specific locations in a scaffold print, shown in the black and white scaffold image..... 127

Figure 6.6 Preliminary results of start/stop flow of the ink in a single scaffold layer..... 128

Figure 6.7 Cross section of a femur bone illustrating curved and non-uniform trabeculae (left), and a schematic highlighting how trabeculae follow principle stress-directions (middle). An example of a material deposition pattern for a curvilinear scaffold (right). Left two images adapted from [154], [155]..... 128

Figure 6.8 Initial Solidworks sketch of a scaffold with curvilinear rods in a single layer. The ideal end-effector path is outlined in blue. Each arc is labeled with a number. 130

Figure 6.9 GUI of the curvilinear scaffold code implemented in LabVIEW. For each of the arc segments, the user must define the radius, SA, TA, and axis velocity. The parameters for each arc segment are organized as tabs. 131

Figure 6.10 Implementation of the curvilinear architecture on the DW printer with colloidal ink. The vertical rod at the top of the image is part of the lead-in-line, which was incorporated to ensure fully developed ink flow before starting scaffold fabrication. 132

Figure 6.11 Modified pressure reference signal, where a pressure spike (PS) was incorporated to attempt to reduce the time delay in the development of full ink flow. 135

Figure A.1 Image looking down into tall cylindrical crucibles to illustrate the blue and white patches present in a powder mixture. The top of the powder mixture (left)

and the mixture with the first layer pierced into (right) to highlight the blue and white regions.	159
Figure B.1 Substrate holder placed in the region outlined by the blue tape, and a substrate with the location of the four screws to secure the substrate into the substrate holder.	163
Figure B.2 Layer 1 and Layer 2 tabs in the front panel GUI of the main scaffold code. The values outlined in a red dashed box correspond to the desired scaffold width, and the values outlined in a blue dashed box correspond to the desired distance between rods.	165
Figure C.1 Axis Configuration window in SoftMotion.	167
Figure C.2 Position Loop information in the Axis Configuration Window.	168
Figure C.3 Encoder units and counts per unit configuration window.	168
Figure C.4 Limit switch information in the Axis Configuration Window.	169
Figure D.1 Project window for the Roberta LabVIEW project. The code that will be used most often is highlighted.	170
Figure D.2 Code structure of the Zero X case structure implemented in LabVIEW. A similar format was followed for the Y and Z axes.	173
Figure D.3 Code structure for the Lead in Lines case.	173
Figure D.4 Code structure for Calibration Layer 1. Calibration Layer 2 follows a similar structure.	174
Figure D.5 Code structure for the Update Case.	175
Figure D.6 Code structure for Layers 1 and 2.	175
Figure E.1 Organization of all electrical components used for the DW printer.	176
Figure E.2 Breadboard 1 enclosure on top of the X axis.	177
Figure E.3 The three breadboards used for electrical wiring.	177
Figure E.4 Electrical connection diagrams for the DW printer. Details of each individual connection (A.1, A.2, etc.) are listed in the tables below.	180

List of Tables

Table 3.1 Physical and chemical characteristics of the starting powders and the ideal final blend.	61
Table 3.2 Optimal ball mill conditions determined empirically.	63
Table 3.3 Example calculation of the number of moles of Ca and P in a 100 g sample which is 90 wt-% HA and 10 wt-% β -TCP.....	65
Table 3.4 Example of the theoretical calculation of the final phase composition. For a 0.5 g increase in CaHPO ₄ in the starting powder, the final phase composition shifts by ~ 5%.	66
Table 4.1 Identified coulombic friction parameters for each axis.	77
Table 4.2 Model parameters from system identification tests for the X axis.	78
Table 4.3 Model parameters from system identification tests for the Y axis.	78
Table 4.4 Model parameters from system identification tests for the Z axis.....	78
Table 4.5 System identification results, which match between experiment and simulation, for each axis.	78
Table 4.6 PI controllers designed in simulation using the system models for each axis.....	78
Table 4.7 PI controllers designed for printing operation for each axis.....	78
Table 6.1 Machine characteristics which address common motion control problems.	78
Table 6.2 Arc segment parameters defined in Figure 6.9 used to fabricate the curvilinear scaffold shown in Figure 6.10.	78
Table A.1 Amount of precursor powder to achieve the desired final phase composition. The amounts listed are for a half batch of ink.....	78
Table D.1 Names and uses of each program listed in the Roberta project window.	78
Table E.1 Electrical connection information for each breadboard.	78
Table E.2 Details of electrical connection A.1 in Figure 3.4.....	78
Table E.3 Details of electrical connection A.2 in Figure 3.4.....	78
Table E.4 Details of electrical connection A.3 in Figure 3.4.....	78

Table E.5 Details of electrical connection A.4 in Figure 3.4.....	78
Table E.6 Details of electrical connection A.5 in Figure 3.4.....	78
Table E.7 Details of electrical connection A.6 in Figure 3.4.....	78
Table E.8 Details of electrical connection A.7 in Figure 3.4.....	78
Table E.9 Details of electrical connection A.8.1 in Figure 3.4.....	78
Table E.10 Details of electrical connection A.8.2 in Figure 3.4.....	78
Table E.11 Details of electrical connection A.9 in Figure 3.4.....	78
Table E.12 Details of electrical connection A.10.1 in Figure 3.4.....	78
Table E.13 Details of electrical connection A.10.2 in Figure 3.4.....	78
Table E.14 Details of electrical connection A.11 in Figure 3.4.....	78
Table E.15 Details of electrical connection A.12.1 in Figure 3.4.....	78
Table E.16 Details of electrical connection A.12.2 in Figure 3.4.....	78
Table E.17 Details of electrical connection A.13 in Figure 3.4.....	78
Table E.18 Details of electrical connection A.14 in Figure 3.4.....	78
Table E.19 Details of electrical connection A.15 in Figure 3.4.....	78
Table E.20 Details of electrical connection A.16 in Figure 3.4.....	78
Table E.21 Details of electrical connection A.17 in Figure 3.4.....	78
Table E.22 Details of electrical connection A.18 in Figure 3.4.....	78
Table E.23 Details of electrical connection A.19 in Figure 3.4.....	78
Table E.24 Details of electrical connection A.20 in Figure 3.4.....	78
Table E.25 Details of electrical connection A.21 in Figure 3.4.....	78
Table E.26 Details of electrical connection A.22 in Figure 3.4.....	78

Chapter 1

Introduction

3D printing for biological applications is a diverse field, requiring expertise in the areas of biology, materials science, electrical engineering, and controls. Consequently, it would be optimal if the 3D printing systems used in this multidisciplinary research were more user-friendly for the diverse range of expertise of the investigators. Fine motion control for 3D printing is critical for biological applications since the design space is often at the micrometer or nanometer scale [1]. For example, current 3D printing challenges in biology include reproducing complex biological architecture with sufficient resolution and smooth material transition for multi-material printing of organs and other biological tissues [1]–[6]. Accordingly, it is important to have a robust, stable and accurate 3D printer for biological applications. In practice, however, common motion control problems in 3D printers and robotics are not trivial and often serve as barriers to ease of use.

This thesis presents the development of an easy-to-use fabrication system that sufficiently balances performance with ease of use. Common motion control problems in positioning systems include closed-loop control, system modeling, and disturbance rejection. In this work, these elements are addressed and implemented in a way that researchers outside of the controls field can more easily understand, which will allow a greater number of machine users to not just use, but to adapt the system as projects and goals change. The specific system is a 3D printer, and we focus on layer-by-layer extrusion techniques, specifically direct-write (DW) printing. Further, we implement the approach for a specific target application: additive manufacturing (AM) for rectilinear bone scaffold fabrication.

The design aspects and control parameters, which were chosen based on previous projects that included researchers outside of the controls field [7]–[12], include a dynamic model of a 3-stage position system for bone scaffold fabrication, a control design for a feedforward plus feedback controller, and a user-friendly iterative learning control (ILC) feedforward compensator. In addition, we demonstrate the ability of the (bio) 3D printer to print bone scaffolds and the effectiveness of the control architecture.

The remainder of this chapter is organized as follows. The main goal of this research project and an overview of the application is presented. Further, the 3D printing technology employed in this work is defined, followed by a brief review of the current manufacturing space. This chapter concludes with a thesis outline.

1.1 Goal/Motivation

With nearly two million bone graft procedures annually in the United States alone [13], [14], the treatment of large, load-bearing defects remains a challenge. By the year 2020, the number of bone defect repairs in the US is expected to double due to increased life expectancy and aging of the baby-boomer population [15]. Further, bone defect repairs have a significant economic impact, with US annual healthcare costs exceeding \$2.5 billion [15]. Bone tissue can fail due to mechanical loads above the stress limits of healthy bone, or reduced mechanical properties of the bone matrix caused by various diseases, which make bones weak and prone to damage [16]. Some bone tissue diseases that can cause large bone defects include [16]:

- Traumatic injury: partial or total loss of bone continuity caused by mechanical loads which exceed the allowable stresses of bone.
- Osteogenesis imperfecta: bone embrittlement due to collagen deficiencies.
- Osteoporosis: loss of bone minerals due to hormonal deficiencies.
- Osteomalacia: loss of bone mineral due to nutritional deficiencies.
- Osteomyelitis: bone infection from bacteria.
- Cancer: primary or metastatic tumors cause progressive bone tissue damage.

Despite the development of commercial bone scaffolds, autografts remain as the “gold standard” for healing large bone defects [17]. In autograft procedures, donor bone from a non-load bearing site in the patient is implanted to the defect site. While this surgery typically has

a high success rate for simple and non-load bearing defects [18], there are drawbacks, including limited bone supply, nerve injury, infection, pain and morbidity at the donor site, and increased bone resorption during healing [19].

An alternative to autografts is synthetic bone scaffolds, which theoretically have an unlimited supply and do not transmit diseases [15]. Creating large, vascularized bone scaffolds with proper biomechanical function, however, remains a challenge, and has limited the use of scaffolds to the repair of small defects [20]. In general, large tissue replacements have failed due to necrosis at the center of the scaffold, which is the result of slow penetration of host vasculature [20]. There is currently no consensus on the optimal scaffold design for bone regeneration.

The multidisciplinary project relevant to this work is the fabrication of artificial bone scaffolds that fill bone defects that are several mm to several cm in size, and have controlled porosity that enables bone regeneration and encourages vascular networks. There are two areas of work contributing to the slow transition of bone scaffolds from the research environment to the clinic. First, fundamental biological principles are not fully understood, which is discussed more in Chapter 5. And second, limitations in manufacturing resolution negatively effect the functional outcomes of 3D printed biological materials.

High print resolution is a challenge for many researchers using direct write printing for biological applications [21]. Further, the functional outcomes of bone scaffolds, measured by the amount of bone regeneration, is negatively effected by a variety of manufacturing defects. Rustom et al. conducted *in vivo* studies with bone scaffolds, and the bone regeneration was inferior in scaffolds with manufacturing defects [22]. The scaffold material blocking or partially obstructing macropores acted as a physical barrier and hindered the level of bone growth (Figure 1.1). [21] demonstrates the need for precision motion and material control in (bio) 3D printing.

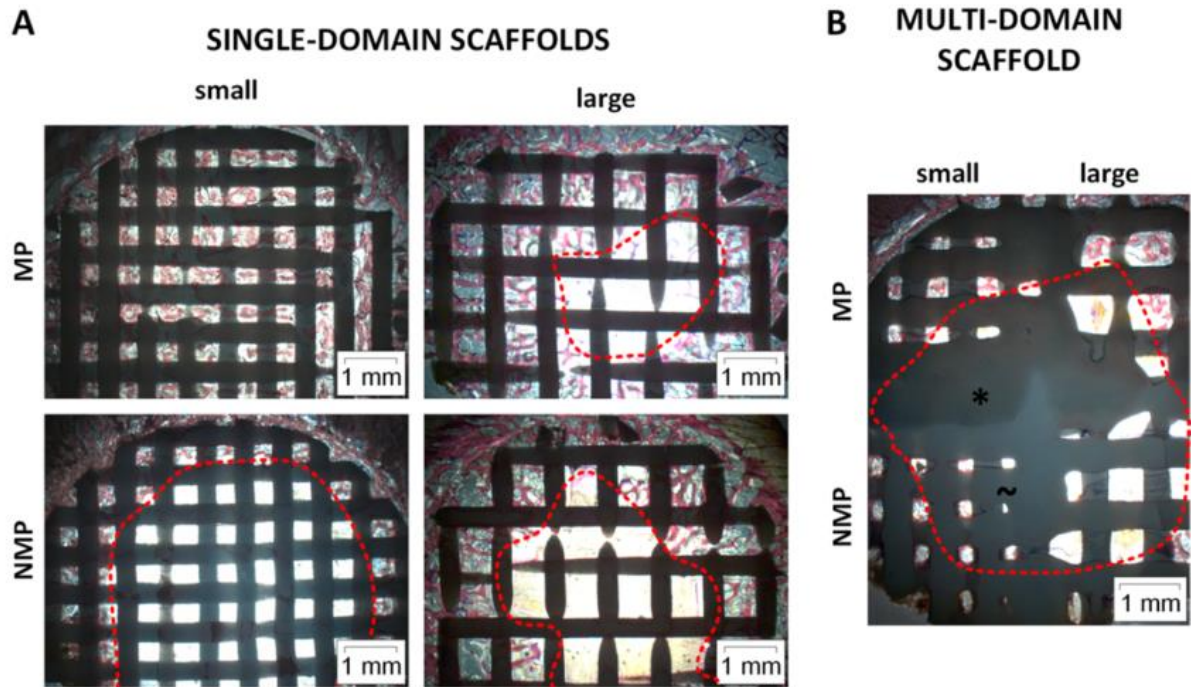


Figure 1.1 Histology sections of implanted (A) single-domain and (B) multi-domain scaffolds with manufacturing defects. Bone is shown in pink/red, and macropores without bone appear bright white. The red-dashed line indicates the bone growth front. Manufacturing defects in multi-domain scaffolds cause full blocking (*) or partial obstruction (~) of macropores. Image from [22].

The previously used micro-robotic deposition system (Figure 1.2a) for bone scaffold fabrication in this lab [9], [23] failed in 2015 after over 10 years of use. The printer was a linear motor gantry system controlled using a PC running Matlab, Simulink with WinCon, and RTZ real-time software. Ink extrusion through a single nozzle was driven by a motor and lead screw assembly. Further, a video camera and lighting system (Figure 1.2b) focused on the nozzle tip for zeroing and implementation of an advanced control algorithm, iterative learning control (ILC). Difficulties encountered in the use of this machine to print scaffolds included:

- The camera used for zeroing the Z axis frequently broke down and, due to the software complexity, the user did not know how to take corrective measures. As a consequence, the system resolution was decreased since the user had to manually zero the Z axis. Manual zeroing can introduce errors in the first layer

as the nozzle may be too close or too far from the substrate, which would compound to other layers and result in a defective part.

- An advanced control algorithm, ILC, was not being used to improve reference tracking, and the user was not able to incorporate that algorithm.
- Precise start/stop flow of the ink was exceedingly difficult, which caused undesirable and uncontrolled material flow (“drool”) and inconsistent printed parts.
- The motor used for mechanical extrusion added undue complexity, and the user was not able to readily fix the motor when problems arose. This would cause delays in research progress when extrusion was not possible.
- The motor used for mechanical extrusion was overworking in order to overcome friction along the syringe walls, which resulted in frequent ink blobs as the motor overcame the static friction.

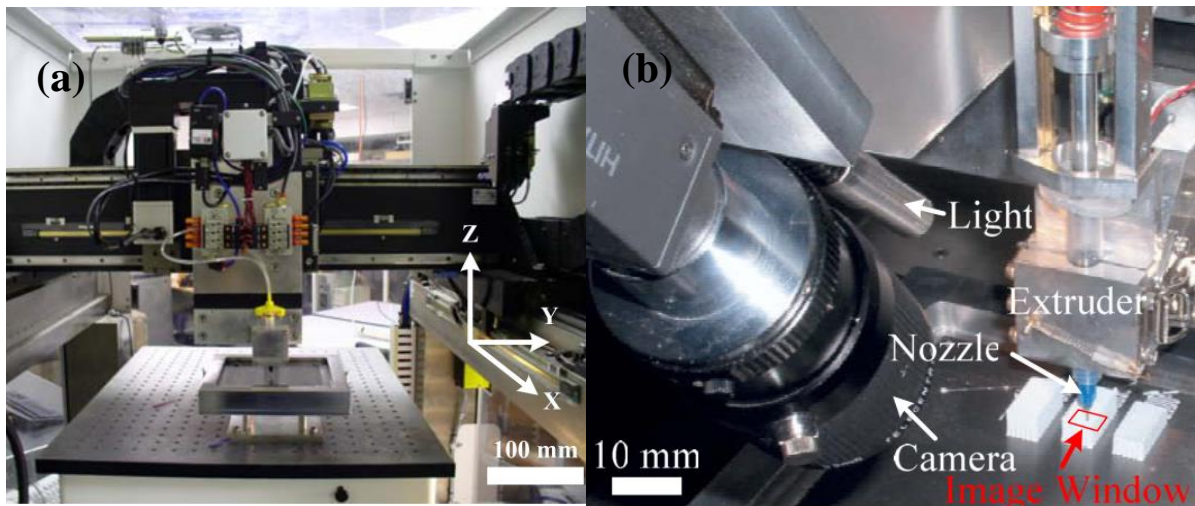


Figure 1.2 Previously used micro-robotic deposition system. (a) Robotic positioning system and gantry set up. (b) Zoomed in view of the vision system. Image from [24].

Issues that previously arose required a dedicated motion controls and robotics expert. For a new 3D printing system to be accessible to a wider field of users, a more intuitive programming environment that was easier to fix and fine tune over time as project goals evolved was required. The goal of this thesis is to design a deposition system with these end-

user requirements in mind, so as to enable continued research of scaffold design features that encourage osteogenesis.

1.2 User-centered design

The academic environment for research is dynamic: graduate students come and go; project goals evolve; and interest in specific fields increase or even die out with changes in public policies or goals of funding agencies. Furthermore, research fields and projects are becoming increasingly interdisciplinary, requiring diverse knowledge and expertise. In research labs, empowerment of all potential end-users across disciplines can translate into productive collaboration and time-efficient equipment modifications. Therefore, it would be beneficial if 3D printing lab equipment was 1) flexible to adapt with these changes, and 2) user-friendly to be accessible to researchers across multiple fields. In this context, flexibility means the user can continuously adapt the system as goals and projects change.

End-user development (EUD) can be defined as a set of methods, techniques, and tools which allow end users, who are acting as non-professional software or program developers, to create, modify, or extend a software artifact [25]. Further, user-centered design (UCD) focuses on understanding the user and involving the user in the creation of the product [26]. EUD and UCD are common topics in fields such as robot-human interaction [27], human machine interface (HMI) [26], [28], human-computer interface (HCI) [25], and brain-computer interface (BCI) [29], [30]. In HCI goals have evolved from making systems easy-to-use, to making systems that are easy to modify and develop by end-users [31]. A fundamental challenge in these fields is to develop systems that allow users who do not have a programming background to develop or modify the application [31].

UCD and EUD have also been considered in additive manufacturing (AM) [32], [33]; however, most current printers in the market are typically closed source and non-customizable [33], which is not optimal for a research environment. The successful application of UCD and EUD to DW printing would involve the development of a system that has an easy-to-use interface and a programming environment that is readily adjustable as project goals change and develop. Toward this end, Ferreira et. al retrofitted a decommissioned Stratasys FDM printer to allow open selection of filament materials [33]. Their focus was to convert a Stratasys

system into an open-source 3D printer in order to expand the printing material base. This approach, however, lacked consideration of simple end-user development; in fact, the control architecture, hardware and programming were not easily adjustable by the end-user.

As a controls community, the researchers need to be able to package and present some of the problems we see in motion control to an audience that does not have a controls background. UCD and EUD considerations from computer science and robotics should be implemented in controls, in particular for multidisciplinary projects, such as DW printing of artificial bone scaffolds.

1.3 Direct-Write Printing

Material extrusion encompasses any process in which materials are deposited as a continuous strand through a nozzle in a layer-by-layer fashion which will yield a 3D product upon material solidification [34]. The material extrusion technique employed in this work was direct-write (DW) printing (Figure 1.3) with CaP-based ceramic materials. Briefly, DW printing, also known as robocasting or direct ink writing, is a solid freeform fabrication method in which an ink is extruded through a nozzle in a defined trajectory [24]. The position of the nozzle is controlled through a cartesian robot. A dispensing apparatus is mounted on the Z axis, and carries the ink material which is extruded by mechanical extrusion or pneumatic pressure. The rheologic properties of the ink are carefully tuned to ensure that the ink exits the nozzle in a liquid state, but retains its shape immediately after deposition. The resolution of the printing process depends on the size of the nozzle, the stability of the ink, and the precision of the cartesian robot moving the deposition head.

DW printing has been employed in a variety of contexts, including the fabrication of cell-laden hydrogels [35], conductive traces on thin and flexible substrates for scientific instruments used in space [36], resistor strain sensors [37], radio frequency microelectromechanical systems (RFMEMS) [38], human-scale tissue constructs [39], [40], and, more recently, lattices made of metallic alloys [41].

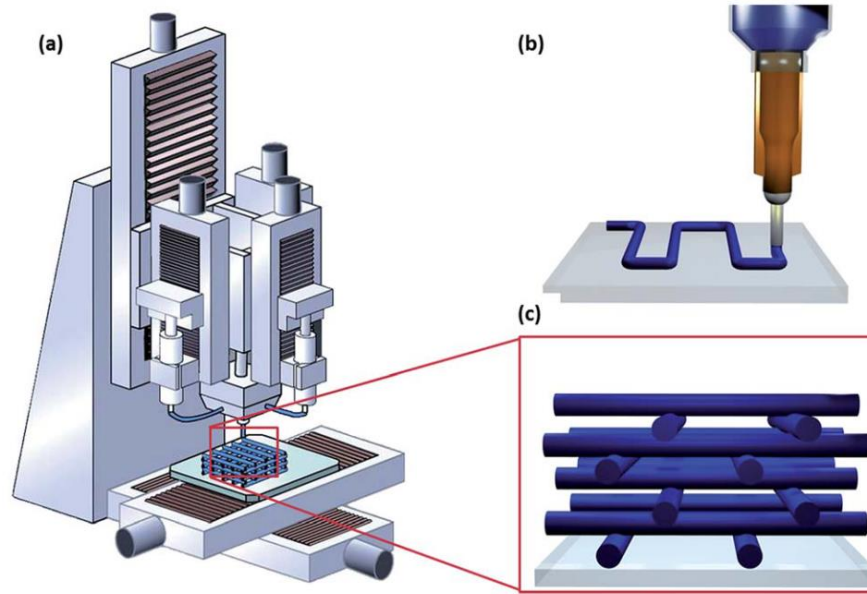


Figure 1.3 Direct-write printing of a 3D periodic structure. (a) Computer-controlled cartesian XYZ robot, (b) filament deposition of a single 2D layer, (c) close-up view of a periodic microstructure. Image from [42].

DW printing has many advantages relative to other material extrusion techniques. DW printing enables the printing of a wide array of bioinks including colloidal inks, cell aggregates, cell-laden hydrogels, and micro-carriers [1]. In addition, DW printing enables bioprinting of porous constructs [43], which is challenging when using other 3D printing techniques [1].

One disadvantage of DW printing, however, is limited print resolution, which is largely dependent on the size of the nozzle. The smallest feature size of DW printed constructs is 100 μm , which means that cells cannot be precisely organized and patterned [1]. An additional disadvantage is that the bioink must possess shear thinning capabilities to overcome the surface tension within the nozzle to be extruded as smooth, cylindrical rods. Further, the writing speed of DW printing is slower than comparable extrusion methods [44], which limits its application. As a consequence, DW printing techniques are rarely used for industrial mass production due to the slow linear deposition process [44].

Despite these limitations for other applications, DW printing can be a useful and cost-effective way to fabricate patient-specific designs and prototypes, and, as a result, the

technology is extensively used in the biomedical field. Further, DW printing is effective for the fabrication of rectilinear, porous ceramic bone scaffolds (Figure 1.4). The colloidal ink has specially tuned rheological properties, which enable smooth flow out of the nozzle during deposition, and maintenance of sufficient stiffness for the ink to span gaps, permitting the fabrication of porous structures. The deposition of cylindrical rods in a layer-by-layer fashion with each layer oriented orthogonal to the prior layer results in a three-dimensional lattice structure. Even with the slower deposition speed relative to other printing technologies, the colloidal ink is deposited in a pool of lamp oil, so the ink does not dry out and maintains structural integrity throughout the duration of the print. Moreover, cells are not used in ceramic bone scaffold ink, so potential dehydration exposure to dehydration or a lack of nutrients are not of paramount concern.



Figure 1.4 Rectilinear, porous lattice structure used as a bone scaffold fabricated using direct-write printing. Image from [45].

1.4 Manufacturing space of current AM technology

While there are numerous reviews outlining the specific types of 3D printing techniques and their applications [46], [47], this brief review will first focus on layer-by-layer extrusion techniques to present the current manufacturing space of the AM technology exploited in this thesis: DW printing. After a brief overview of some of the state of the art extrusion printers, the scope is narrowed to DW printing of ceramic-based colloidal inks since this type of material was used in this work for fabrication of bone scaffolds.

1.4.1 State of the art extrusion printers

The market for low-cost extrusion 3D printers, defined as an AM machine that costs under \$5,000, has had an average growth rate of 170% from 2008 [48]. Most of these low-cost printers exploit the fused deposition modeling (FDM) technology, another extrusion-based 3D printing technique, and are fabricated by companies such as MakerBots, M3D, and XYZprinting. The accuracy of standard desktop FDM machines, however, are on the mm scale [49]. Further, these low-cost, desktop printers have limited build volume and are restricted to a few types of materials, largely polymers. For applications requiring different materials and tighter resolution requirements, industrial printers and other type of printing technologies are required [49].

There have been significant technological advancements in industrial printers, which have led to tighter resolutions and more advanced constructs. SI2 Technologies, for example, has developed a micropen printing process that prints electronic circuits on curved or flexible surfaces, enabling manufacture of flexible electronics [50]. Within the bio field, Organovo's exVive3D printer has fabricated a human-scale liver currently used as a diagnostic tool for cell-based assays for drug testing and other therapies to supplement in vitro and preclinical animal testing [51]. Additional companies that make bioprinters that employ the extrusion printing technique include envisionTEC, RegenHU, Cyfuse Biomedical, CELLINK, and Ourobotics.

Access to AM technologies with smaller resolutions, however, is limited due to the cost of current industrial printers. A multi-material extrusion system with micron resolution from Stratasys, for example, costs \$250k with material costing \$500 per kilogram [52]. In addition to cost, the material library, hardware, and software are limited, proprietary and inextensible [53]. These expensive machines with limited flexibility are not suitable for a research environment, so many custom-built systems are used in academia. A few of the state of the art printers, some of which enable multi-material printing, are reviewed below.

Raza et al. presented the development of a custom-built multi-material AM system capable of depositing three different materials during one print using both extrusion and droplet-based extrusion methods [54]. This multi-material printer successfully fabricated a composite object out of metal, rubber and plastic [54]. There was no discussion, however, of

system resolution or any errors in the fabricated part. While there are similar printers that incorporate multiple nozzles for fabrication of multi-material architectures, precise start-stop-flow of the ink and movement coordination between nozzles remains a challenge [55]. Further, building multi-material structures is not as simple as turning one material off and another one on; there is a time delay before ink flows out of the nozzle, and an additional time delay before a fully developed ink flow is achieved [56]. In attempt to avoid these challenging requirements with multi-nozzle setups, Hardin et al. have demonstrated multi-material printing using a microfluidic printhead designed for seamlessly switching between two viscoelastic materials during fabrication [55]. The two materials flowed through the same nozzle and two actuated syringe pumps were used to control the flow of each material independently. Despite initial success, there were three main sources of error in the set up: mechanical backlash in the syringe pump, syringe, and nozzle; air bubbles strongly affected system compressibility; and their remained synchronization error between the two pumps [55]. Moreover, this technique would be challenging for printing two materials with vastly different viscosities.

In the field of bio extrusion printing, Kang et al. developed an integrated tissue-organ printer (ITOP) that can fabricate stable, human-scale tissue constructs of any shape [39]. The ITOP consists of a three-axis motorized stage system and a dispensing module with multiple cartridges, enabling the delivery of cells and polymers in a single construct. Using cell-laden composite hydrogels, Kang et al. have successfully printed near-net shape tissue constructs such as a scaffold for a mandible bone defect, for ear cartilage reconstruction, and for a skeletal muscle construct [39]. The shape of the tissue construct was achieved by representing clinical imaging data as a computer model, and translating the model into text-based motion program to move each of the three axes.

Reid et al. designed and 3D printed components for an extrusion platform that can fit onto the positioning stages of many commercially available 3D printers [57]. Using this microextrusion bioprinting system, consisting of a pulled-glass capillary pipette to minimize shear stress and optimize position control, the authors successfully printed human induced pluripotent stem cells (hiPSCs) while maintaining pluripotency [57]. This set up is the first bioprinting system to reliably achieve single cell print resolutions while also exerting minimal stress on the cells to ensure full functionality post-print [57].

While these machines and technologies both in academia and industry highlight the recent advancement of extrusion printing technology, these printing advancements are not currently possible with DW printing of ceramic-based inks since CaP constructs are considerably more difficult to manufacture than their polymeric counterparts [12]. There is a need for technological advancement in both process control and material development in the field of DW printing with colloidal inks to fabricate more advanced constructs, particularly in the field of (bio) 3D printing.

1.4.2 Direct write printing with ceramic-based colloidal inks

Although current DW printing technology can achieve a high degree of positional accuracy in plane, there is a substantial limitation in the ability to print overhanging or unsupported parts since the technique lacks support material from previous layers [51]. In addition, direct process control and more advanced control architectures to detect curvature errors are required for curvilinear printing. These limitations often confine the fabricated parts to simple, rectilinear structures. In fact, numerous DW printers used in academia are capable of printing single-material rectilinear structures with ceramic-based colloidal inks [58]–[62].

There are, however, a few exceptions to simple, rectilinear DW printing with ceramic-based colloidal inks. A few researchers have printed complex shapes incorporating multiple geometric features, such as short and large radii of curvature with ceramic-based colloidal inks [12], [63], [64]. Ricci et al. have developed a DW printer capable of printing more complex scaffold architectures, including scaffolds with multiple materials and alternating radial and circumferential layers [65]. Further, Xie et al. presented the development of a DW printer capable of printing scaffolds with structures more closely resembling a defect site. Two main features of this system have advanced the current state of the art in DW printing. First, net shape scaffolds were fabricated using both the self-supporting nature of layer-by-layer AM fabrication for steep draft angles and polymer molds for shallow draft angles [12]. Second, the set up included multiple print heads to integrate different material domains within a single scaffold without retooling [12]. This system is the current state of the art DW printer in academia, and has enabled fabrication of net shaped bone scaffolds with complex 3D envelopes and multiple material domains [12]. As discussed earlier, these capabilities are

readily available for polymer composites using commercial AM technology, but Xie et al. was the first to demonstrate these capabilities with fully dense, pure CaP materials.

This brief review will be revisited in Chapter 6, where the placement of the DW printer developed in this work within the DW printing manufacturing space will be discussed.

1.5 Thesis outline

This thesis is organized as follows: Chapter 2 presents the system description, which discusses the machine set up, hardware, software selection, and end-user description. Chapter 3 reviews background information in colloidal science. The powder and ink preparation are then discussed in detail. Chapter 4 presents system modeling and the control strategies employed, which include a feedback plus feedforward controller. Chapter 5 briefly reviews tissue engineering and bone anatomy. In chapter 6, the manufacturing space of an easy-to-use DW printer is presented, with the capabilities and limitations of this machine discussed. Finally, this thesis concludes with a summary of research developments and directions for future work. The appendix includes extensive documentation of the machine wiring, a machine user manual, and tips (learned through trial and error) for powder and ink characterization techniques.

Chapter 2

System Description

2.1 Introduction

The four main components of a direct-write (DW) printing system include the dispensing material, substrate, extrusion system, and positioning system. The dispensing material forms the three-dimensional structure, and in this application, the dispensing material was an ink with a base of ceramic powder (Chapter 3) housed in a syringe barrel during deposition. The substrate refers to the material onto which ink is deposited, and can be any material that does not react with the ink. In this work, the substrate was an aluminum plate spray-painted with black paint in order to provide contrast to the white ink. The extrusion system dispenses the colloidal ink, and the positioning system positions the extrusion system to enable the fabrication of three-dimensional structures. The four components of the DW printer used for bone scaffold fabrication are highlighted in Figure 2.1. This chapter will discuss both the extrusion and positioning systems of this printer in depth.

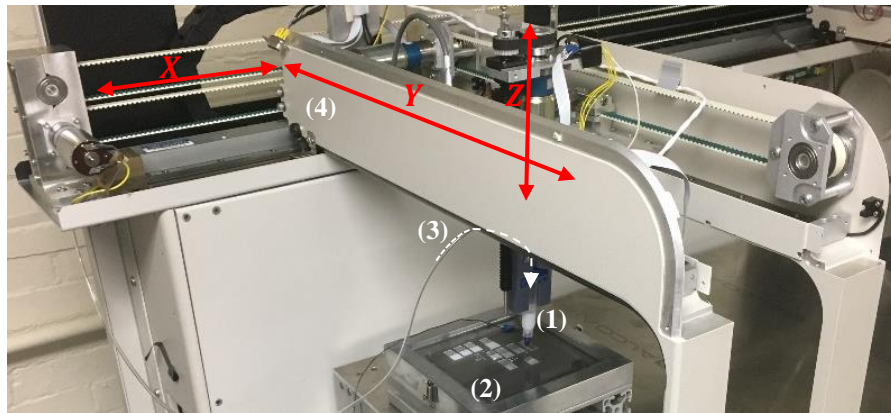


Figure 2.1 Direct-write printer designed to print artificial bone scaffolds. (1) Dispensing material (ink) inside the syringe barrel. (2) Substrate (black metal plate) onto which the ink was deposited. (3) Pneumatic-based extrusion system (shown in more detail in Figure 2.3). (4) Positioning system, which includes the XYZ axes (labeled in red).

2.2 End-user Description

Before describing the system attributes, a description of the end-user will first be described. The main constraint that dictated the design of the DW printer is the end-user, who is assumed to have minimal knowledge of motion control. In this application, the end-user was typically a graduate student in bioengineering or materials science who used the machine to print bone scaffolds. The user should be able to easily modify the lattice geometry and adjust the supplied pressure since multiple materials with varying viscoelastic properties will be utilized across projects. Further, adjustment of programming architecture and control parameters (Chapter 4) should be accomplished with a minimal amount of user programming.

2.3 Extrusion System

The extrusion system can be driven by pneumatic- or mechanical-based configurations (Figure 2.2) to extrude continuous filaments of material [1]. In pneumatic extrusion (Figure 2.2A), a controlled pressure is applied to the ink reservoir for deposition. In mechanical extrusion (also called positive displacement, Figure 2.2B), a piston is driven by a motor and lead screw assembly. The piston is driven by a distance either in the positive direction to deposit ink or negative direction to retract ink.

The most common extrusion methods for 3D bioprinting applications include mechanical ([7], [12], [55], [66], [67]) and pneumatic ([39], [44], [68]–[70]) systems. Mechanically driven mechanisms provide greater spatial control, but have reduced maximum force capabilities and more complex components [2]. Pneumatically driven systems have a simpler drive mechanism, are easier to set up and maintain, and a force output equal to the available air supply [2]. Further, pneumatic extrusion provides greater control of the supplied pressure, whereas it is difficult to de-pressurize a mechanically driven system in order to stop flow. Relative to mechanical extrusion, however, pneumatic extrusion is less effective in steady state since the flowrate is more sensitive to ink rheology.

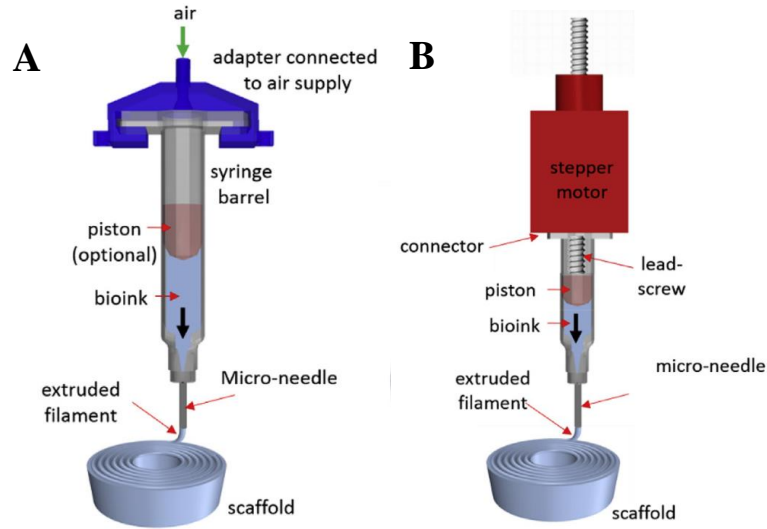


Figure 2.2 Types of dispensing mechanisms for DW printing: (A) pneumatic extrusion and (B) mechanical extrusion. Image adapted from [1].

2.3.1 Extrusion system in this work

A single nozzle pneumatic extrusion system (Figure 2.3) was employed since the bone scaffold fabrication under consideration required only one material. Moreover, a pneumatic based configuration is easier to set up and maintain by the end user relative to a mechanical extrusion system, which would require an additional motor and control design. The setup of this pneumatically-based configuration, which is attached to the vertical Z axis, will now be briefly described.

Control of supplied pressure was accomplished internally through an off-the shelf pressure regulator, which reduced the input pressure from the lab air supply (100 psi) to the desired working range for ink deposition (0-30 psi). An Adapter Assembly (Nordson EFD) transferred pressure from the output of the pressure regulator to the syringe barrel (Nordson EFD), where the ink was housed. A piston (Nordson EFD) was inserted into the syringe, which sat flush with the ink and was used to ensure uniform dispensing force for more accurate depositions. Cylindrical nozzles (Nordson EFD) screwed into the syringe barrel and extruded ink as cylindrical rods onto the substrate.

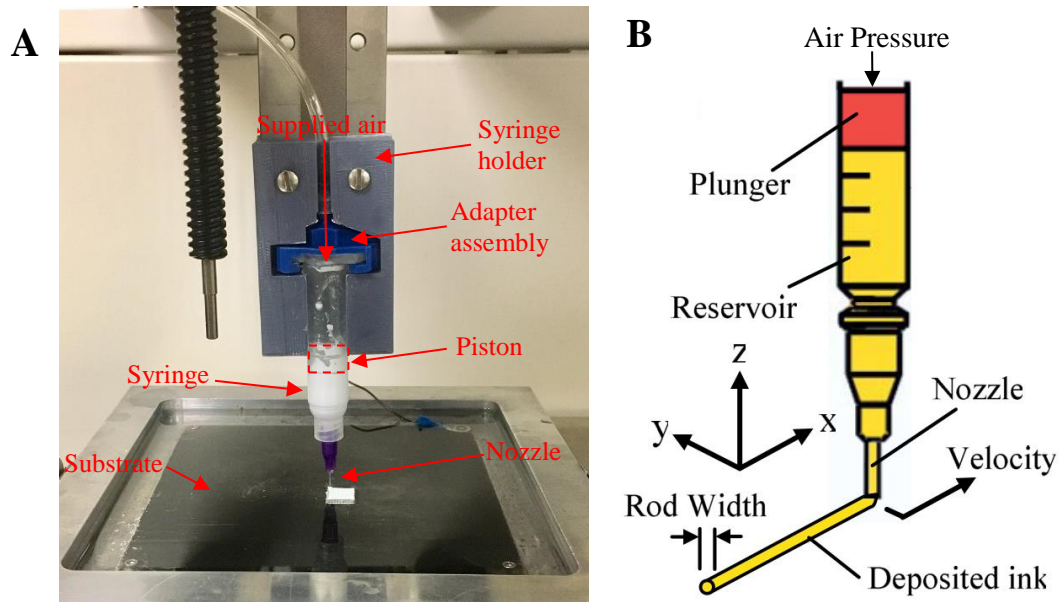


Figure 2.3 Pneumatic extrusion for DW printing. (A) Extrusion system used in this research. The black cylinder is part of the ball screw mechanism. (B) Schematic of the extrusion process, adapted from [24].

2.4 Positioning System

Positioning systems in DW biomedical printing applications are primarily three-axis cartesian robots ([39], [44], [66], [68], [71]), which move the extrusion system in a defined trajectory. Further, the three principal axes in a cartesian robot are linear and are at right angles to each other. The requirements on the positioning system in this application are not strict relative to high speed and nano-positioning systems [24]. A resolution of 10 μm is sufficient to achieve repeatable macropore space (gaps within a layer) in the lattice structure [24].

2.4.1 Positioning system in this work

The DW printer in this work was developed by the transformation of an existing liquid dispensing machine (Biomek FX^P, Beckman Coulter) into an additive manufacturing platform. The original machine base, motors, and encoders were used, while the hardware and electrical components were stripped. Further, the Z axis and substrate were modified for ink deposition.

The positioning system of the DW printer consisted of three, independently controlled axes, with the X and Y-axes oriented in plane and the Z-axis oriented out of plane (Figure 2.1)

to establish standard Cartesian coordinates. The X and Y-axes were belt driven, while the Z-axis was driven through a ball screw. Belt drives translate rotary motion of the motor to linear motion through a grooved timing belt connected between two geared pulleys. The carriage, which holds the axis components, rides on top of the belt drive. Belt drives are low-cost, low-maintenance, and have a relatively long travel range, allowing for a larger design space. A ball screw drive translates rotational motion to linear motion with little friction, and consists of a ball screw and a ball nut with recirculating ball bearings. The vertical Z axis used a ball-screw drive (Thomson, XCT15-12X3M) since this type of actuator can hold a load stationary without motor power consumption. Alternatively, the X and Y axes used belt-driven systems since this set up is more cost effective for long travel distances compared to ball screw actuators. The travel range of each axis is listed below:

- X axis: 1000 mm
- Y axis: 400 mm
- Z axis: 140 mm

The actuation system for the X and Y axes was comprised of a brushed DC motor (Faulhaber) and a planetary gearhead with a 14:1 reduction ratio. The gear head was attached to the geared pulley, which translated the geared belt and axis carriage. The Z axis actuation system (Figure 2.4) contained a brushed DC motor (Faulhaber) and a planetary gearhead with a 3.71:1 reduction ratio. The rotating motor shaft turned a timing belt, which turned a ball-screw, which moved a translational slide in the vertical direction.

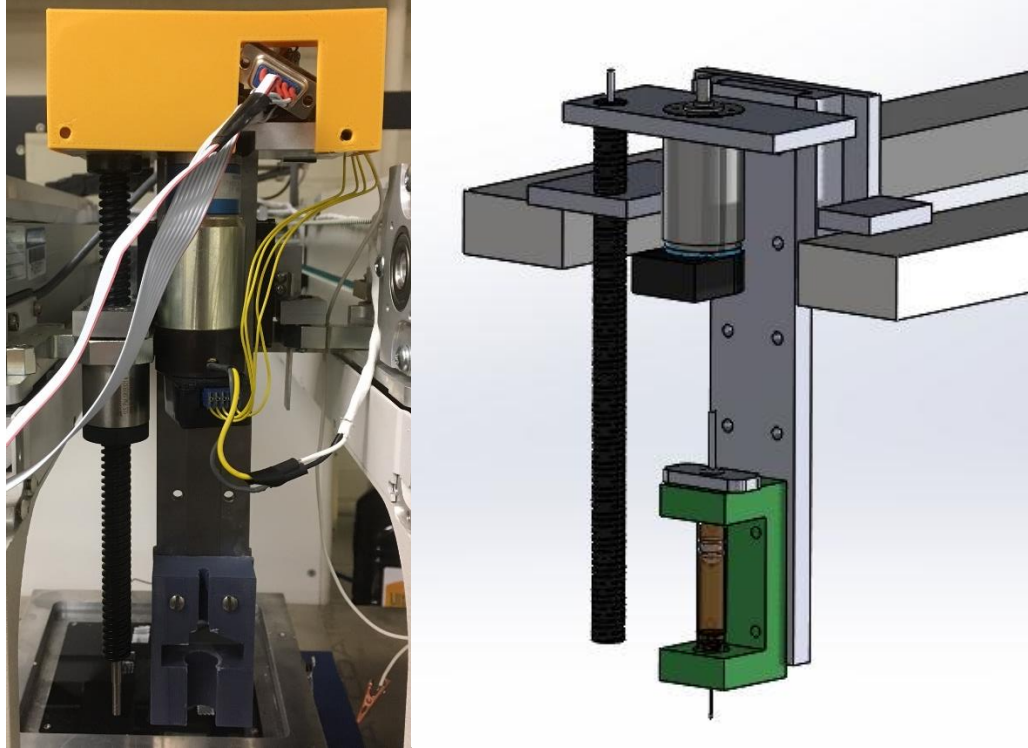


Figure 2.4 Illustration (left) and schematic (right) of the Z axis set up of the DW printer.

2.5 Motion control system

The components of a motion control system are illustrated in a feedback diagram (Figure 2.5). An application software is used for the user to input target positions. The motion controller acts as the brain of the system, which outputs command signals ($u \in [-10V, +10V]$) for the servo motors based on the desired positions. The motor drivers take the low current controller output and amplify it to generate the current level necessary to drive the motor. The motor produces the torque required to move the axis to the desired position. Feedback senses the motor position and closes the loop by reporting this information back to the controller.

In Figure 2.5, the signal type between two components are listed in red. The motion control platform in this application included a NI 9514 Motion Controller [72], an AMC AZB12A8 Motor Driver [73], a Faulhaber Series 3557 Brushed DC motor [74], and two types of encoders for position feedback: a HEDS 5500 rotary encoder [75] for the Z axis, and a Gurley Precision Instruments Linear Encoder [76] for the X and Y axes.

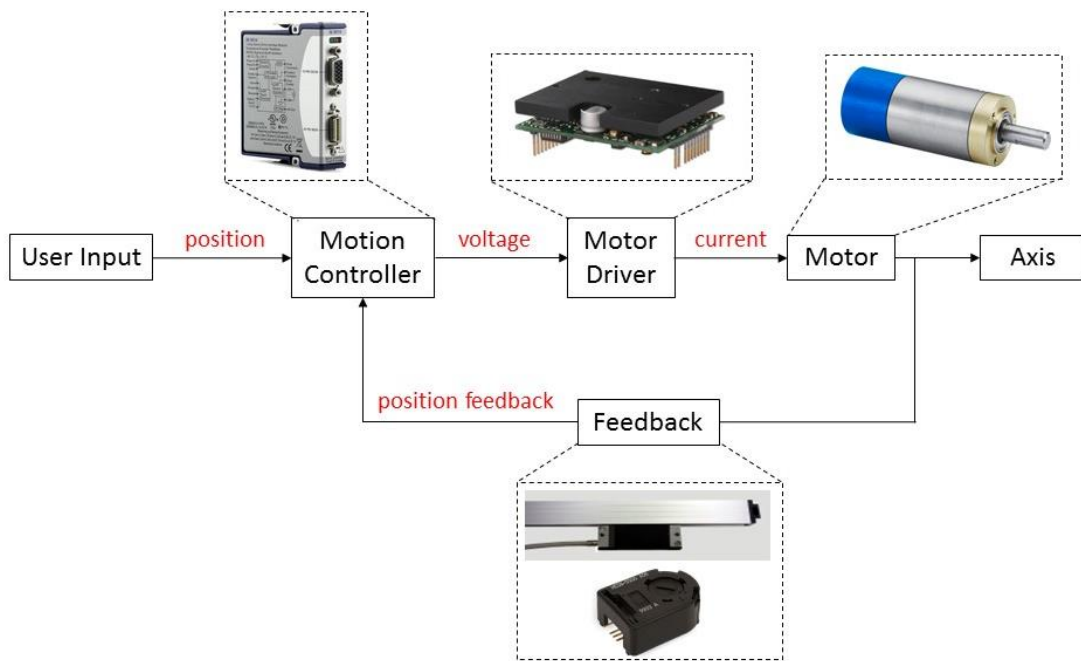


Figure 2.5 Components of a motion control platform illustrated as a feedback loop.

The electrical instrumentation connects each component to enable communication within the motion control platform. Three breadboards were used to interface each of the electrical components (Appendix E.1). Figure 2.6 illustrates the complete electrical connection diagram for the DW printer. Additional details of individual electrical connections (A.1, A.2, etc.) can be found in Appendix E. Further, data sheets for each piece of equipment can be found in the “Spec Sheet” folder within the “Roberta” folder on the Desktop.

This chapter discusses each component of the motion control system used in the DW printer for the fabrication of bone scaffolds, and will highlight some of the electrical requirements between the two components.

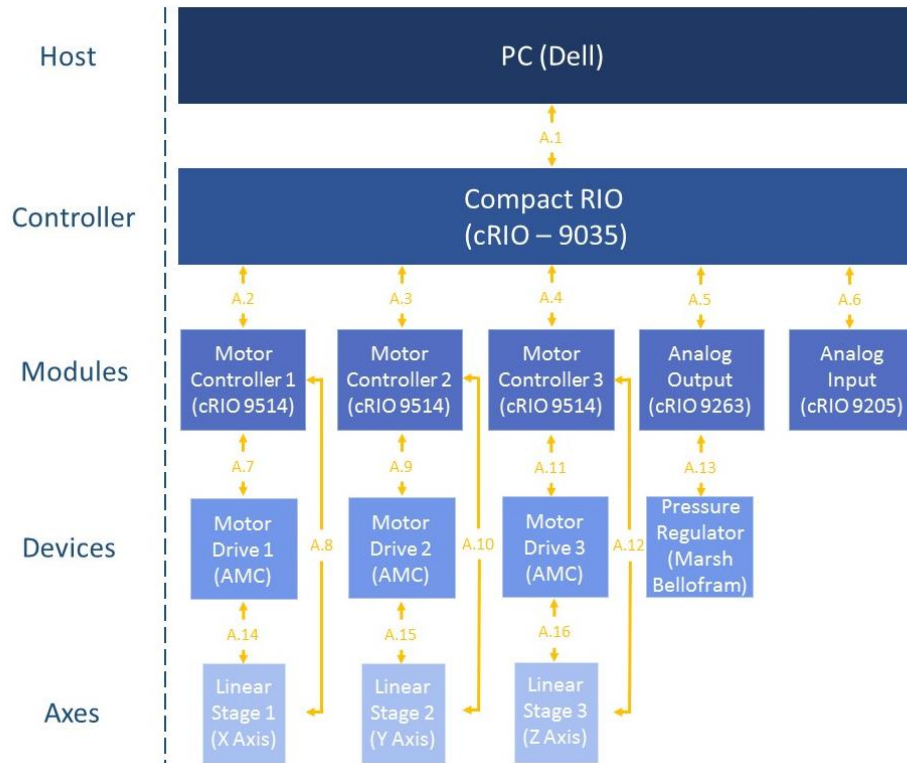


Figure 2.6 Electrical connection diagram for the DW printer. Details of each individual connection (A.1, A.2, etc.) can be found in Appendix E.

2.5.1 Encoders

An encoder is an electro-mechanical device that generates digital signals in response to motion. The digital signal is a series of pulses which are used to determine position and speed. There are two main types of encoders: linear and rotary encoders. Linear encoders respond to motion along a path, while rotary encoders are connected to the motor shaft and respond to rotational motion. Linear encoders help minimize errors in motion transmission since they measure the distance directly. For the same actuation system, a linear motor would provide a more accurate measurement of the axis position since it moves directly with the carriage.

Gurley Precision Instrument linear encoders were used for the X (LE25) and Y (LE18) axes, which have a 5 μm resolution and 200 counts per mm. An optical, incremental rotary encoder was used for the Z axis (HEDS-5500), which has 500 counts per revolution. Since

each encoder has two output channels (Channels A and B), the number of pulses per revolution is quadrupled due to the leading and trailing edges of both channels. With quadrature and a 3.71:1 gear head, this encoder provided 7420 counts ($500 \times 4 \times 3.71$) per 1 revolution of the motor. The linear encoders required a +5 V supply voltage at 100 mA max. The rotary encoder required a +5 V supply voltage at 40 mA max.

2.5.2 Servo Drives

Motor drivers take low current control signals from the controller and amplify them to drive a motor. Three servo drives (Advanced Motion Control (AMC), AZB12A8) interfaced with each axis of motion. Each drive received a command from the motion controller ($u \in [-10V, +10V]$), and communicated with the axis motor to achieve the desired amount of motion. The driver interfaced with the NI 9514 Servo Drive Modules (Section 2.5.4.1). The driver required a 20-80 VDC Power Supply and sat in a mounting card (AMC, MC1XAZ01) to enable pin access through screw terminals.

2.5.3 Limit Switches

In addition to mechanical stops on both sides of each axis carriage, limit switches (Panasonic, PM24) were added to disable axis motion before reaching these mechanical stops. Limit switches provide information about the end of travel to avoid damage; when the limit switch sensor is triggered, the motion system stops moving. The LED inside the sensor will turn on when an axis comes within a certain range of the sensor. The limit switches require a 5-24 VDC with 50 mA max supply current. The power supplies used to power the limit switches outputted 24 VDC and 2.5 A. Thus, a resistor was implemented in the circuit to limit the current flowing through each limit switch. Without a current-limiting sensor, too much current would flow through the resistor and destroy it. Ohm's law was used to determine the required resistor size; with a 24V supply and a 50 mA supply current, the minimum resistor size was 480Ω . A $1 \text{ k}\Omega$ resistor was connected between the power supply output and the +V line of each limit switch to ensure the supply current remained below 50 mA.

Each axis employed two of these sensors: forward limit and home for the X axis, forward and reverse limits for the Y and Z axes. For the Z axis reverse limit, a self-made

zeroing circuit commonly used in CNC machining was made (Figure 2.7). The white wire was attached to the nozzle and was tied to the forward limit line on the motion controller, and the black wire was attached to the substrate and was tied to the COM line on the motion controller. When the nozzle touched the substrate, the circuit closed, which activated the reverse limit. The limit switch connections are highlighted in Figure 2.6 (A.14-A.16) and additional details on the connections are listed in Appendix E.

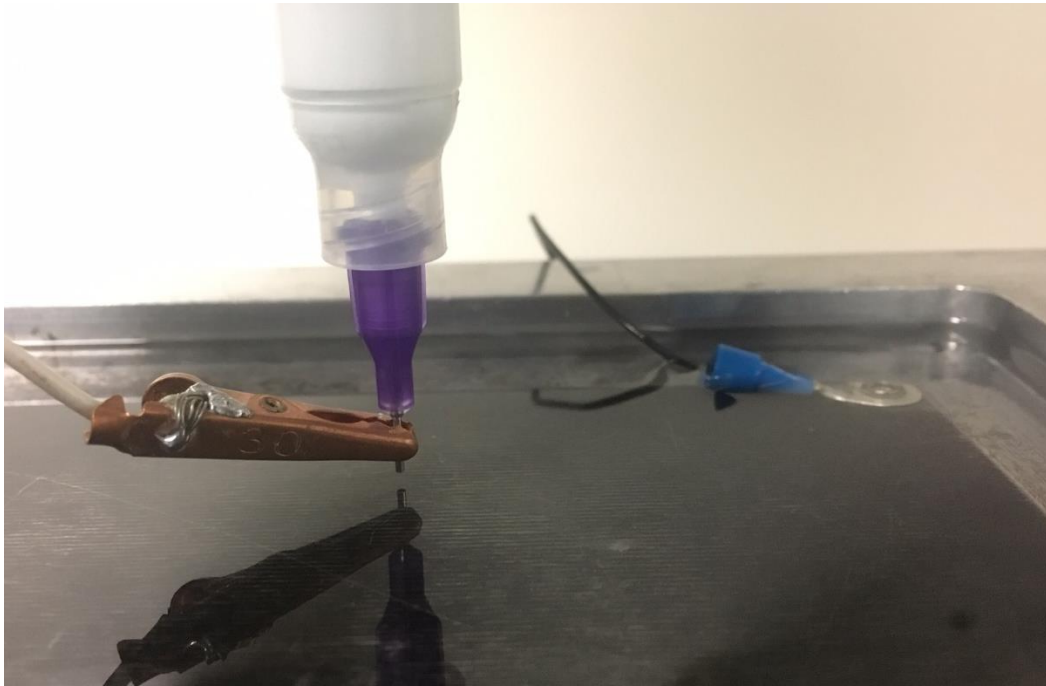


Figure 2.7 Zeroing circuit, which also serves as the Z axis reverse limit switch.

2.5.4 Pressure Regulator

The pressure regulator (Marsh Bellofram, 2KSNNF01DF03000) was an electro-pneumatic device, which regulates a supply pressure (supply pressure line in the lab) to an electronically-controlled output pressure. The regulator output 0-30 psi and required a 5-28 V power supply and a 35-100 psi input pressure. The output pressure was controlled with an analog voltage signal, and input power was taken from the +6 V channel of the Z axis motor driver.

A mapping from output pressure to input voltage was generated by recording several data points and using a linear equation to fit the data (Figure 2.9). This equation was used in

the deposition code to determine the voltage signal required to achieve the desired output pressure.



Switch No.	1	2	3	4	5	6	7	8	9
State	ON	OFF	OFF	ON	ON	ON	OFF	ON	OFF

Figure 2.8 Pressure regulator (Marsh Bellofram), and the DIP switch settings.

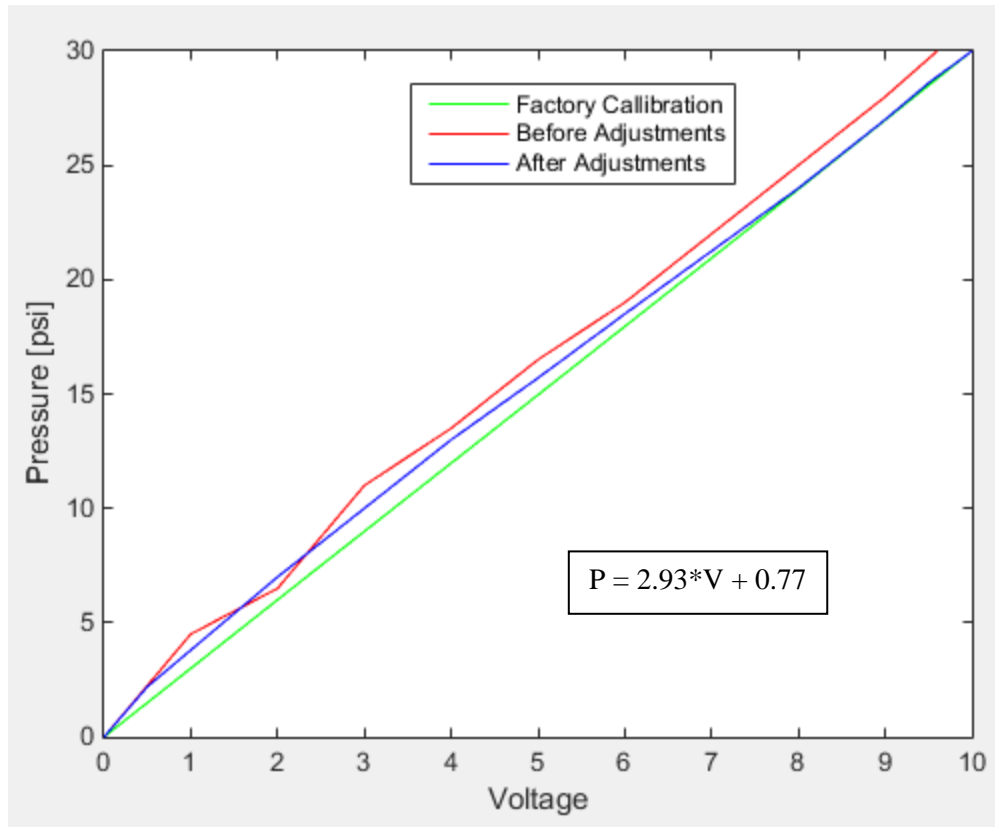


Figure 2.9 Calibration plot of the pressure regulator. The regulator performance was slightly different than the factory calibration. The “FINE” and “SPAN” potentiometers were slightly adjusted to ensure full pressure range. The equation of the calibration line is pressure (psi) = 2.93*voltage + 0.77, where pressure is the output pressure of the regulator, and voltage is the 0-10 V analog input signal.

2.5.4.1 Pressure Regulator Calibration

Inside the pressure regulator, there are 9 DIP switches which need to be configured properly (Figure 2.8). There are also 4 potentiometers for calibration adjustments. Remove the top cover to gain access to the supply power terminals, DIP switches, and potentiometers.

To calibrate the regulator, start by ensuring the output pressure is 0 psi under a 0 V input signal. If this is not the case, use the “FINE” (fine zero) potentiometer to adjust the output pressure to 0 psi. To maximize the full range of the output pressure, send a 10 V signal and use the “SPAN” potentiometer to tune the output pressure to 30 psi.

2.5.5 Controller

All motion control and measurement signals (from the equipment described in Sections 2.5.1-2.5.3) were transmitted to a host PC via a NI Real Time (RT) target: Compact RIO (cRIO-9035, National Instruments). A cRIO is a RT embedded controller, which includes a processor for implementing control algorithms. The cRIO system (Figure 2.10) is an integrated RT controller and chassis. Reconfigurable input-output (I/O) modules plug into the chassis and serve as the DAQ tools. The chassis consists of a frame that houses and connects the modules to the controller. It also controls the timing, synchronization, and data transfer between the cRIO controller and the I/O modules.

The cRIO has two programming modes: LabVIEW field-programmable gate array (FPGA) Interface mode and Scan Interface mode. With FPGA, the user writes the LabVIEW code and designs the circuit, which enables more flexibility and customization, but adds an additional, complex step. In Scan Interface mode, the modules can be used in LabVIEW in RT, meaning the FPGA does not have to be developed. The cRIO programs the FPGA to fit the user’s needs behind the scenes.

In this work, Scan Interface mode was used, which reduced development time and complexity. The cRIO System was primarily used to coordinate the motion of the three axes. The cRIO system communicated with the host PC over the UIUC network, and the cRIO connected to the UIUC network via Ethernet. Further, the cRIO controller required a 9-30 V power supply.



Figure 2.10 cRIO system, including the controller and chassis with 5 I/O modules.

2.5.5.1 C Series Modules

The reconfigurable I/O modules provide high-accuracy I/O with measurement-specific signal conditioning for connection to any sensor or piece of hardware. In this work, three C Series Motor Drive Interface Modules (NI 9514) were used to interface with each axis. The NI 9514 modules communicated with the encoders to obtain feedback signals, sent control inputs to the motor drivers, and provided I/O for home and limit switches. Further, each 9514 contains a processor running a PID and feedforward control loop (Figure 2.11), which will be discussed further in Chapter 4. The NI 9514 module has two connectors: a 15-pin DSUB drive interface connector and a 20-pin MDR feedback connector. The DSUB connector interfaced with the motor driver while the MDR connector received signals from the encoders and limit switches.

Two additional modules housed in the cRIO chassis include an analog output (AO) module (NI 9263) and an analog input (AI) module (NI 9205). The AO module controlled the output pressure from the pressure regulator with a 0-10 V signal, and the AI module was used to measure any analog signals from sensors or other hardware in the system.

The 9514 modules required an external power supply outside of the cRIO power supply. The AI and AO modules did not require external power since these modules simply sent or received analog signals to the cRIO.

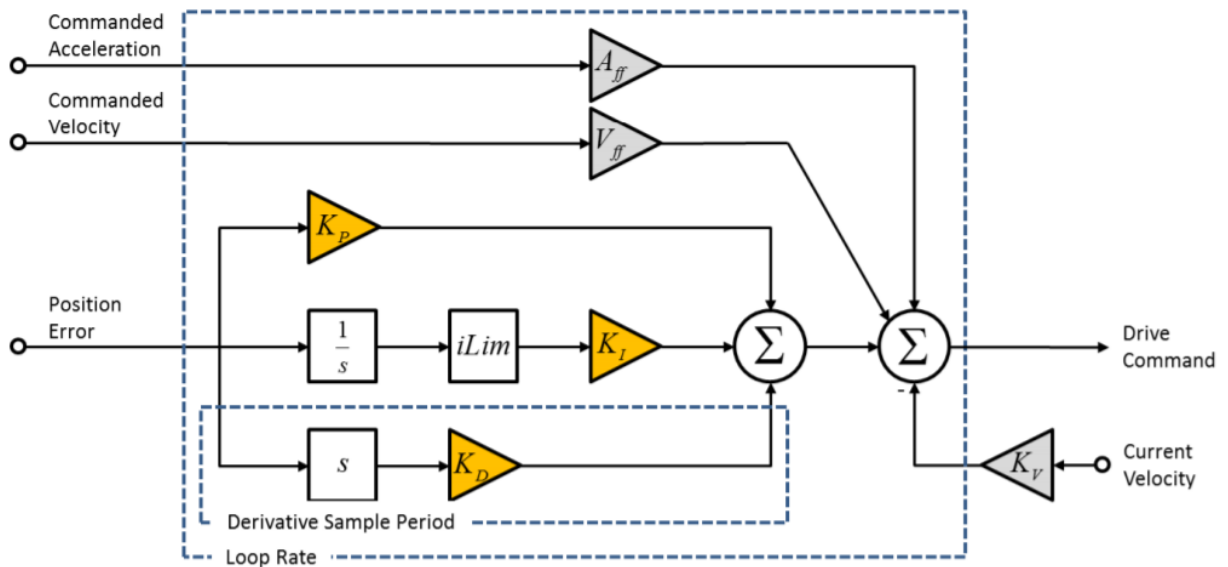


Figure 2.11 PID plus Feedforward control loop embedded in the NI 9514 modules.

2.5.6 Power Supplies

The power supply connections for the DW printer are illustrated in Figure 2.12. Three Eaton DC power supplies were used to power the cRIO, the NI 9514 modules, and the LEDs on the limit switches for each axis. Each Eaton power supply required a 100-240 VAC input and outputted 24 VDC and 2.5 A. All three servo drives were powered by a single AMC (PS4X3W24) power supply, which outputted 24 VDC and 12A. Finally, each encoder was powered by a variable power supply (Yescom), which required a 110V Input and have a 0-30V output. The output voltage and current was controlled manually on variable the power supply, to ensure the encoders did not receive a supply current outside the acceptable range.

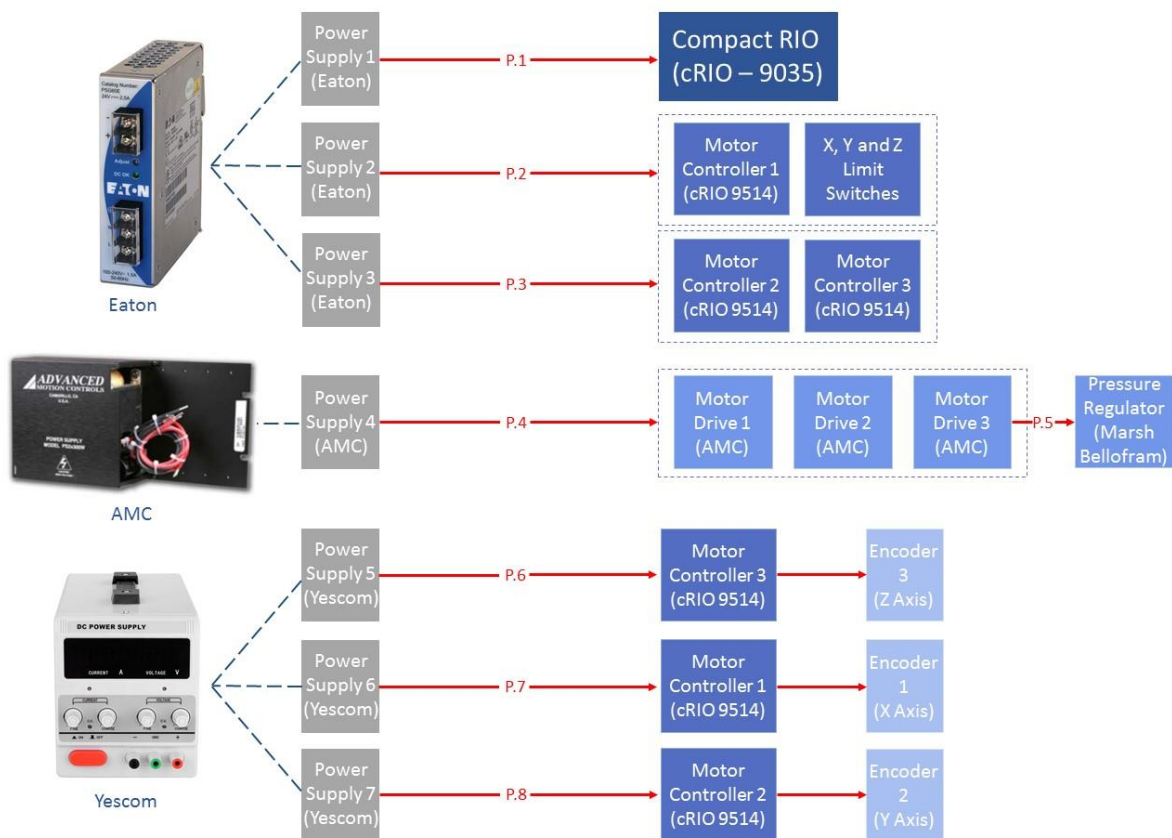


Figure 2.12 Power supply connections for each piece of hardware in the DW printer.

2.6 Program Selection

The programming environment was selected before the hardware purchases (discussed above), since certain equipment often interfaces with only a few types of programs. Out of the common programming environments (MATLAB, cRIO, ControlDesk, etc), the LabVIEW programming environment was chosen since it was determined to be simpler for the end-user to understand, learn, and modify on his or her own relative to competing programs for motion control applications. Further, since LabVIEW uses data-flow programming, it is easy to control the execution order of specific actions within a program. The cRIO equipment (discussed in Section 2.5) is compatible with the LabVIEW programming environment.

2.6.1 LabVIEW user interface

Within the LabVIEW programming environment, each program is called a virtual instrument (VI). When a new VI is created, two windows appear: the front panel window and the block diagram. The front panel is associated with the user interface and the block diagram contains the graphical source code which controls the front panel objects and moves the axes. The block diagram will be discussed in detail in Section 2.7.

2.6.1.1 Front Panel

The Graphical User Interface (GUI) for bone scaffold fabrication on the DW printer was developed in LabVIEW in the front panel window (Figure 2.13). The GUI enabled users to start/stop the program, set scaffold parameters (layer number, space between rods, and width), modify axis parameters (velocity), view axis positions, and change control parameters. Each function was grouped into a cluster (illustrated as tabs) to better organize the GUI. Detailed descriptions of each adjustable parameter and each tab within the GUI are included in Appendix C.

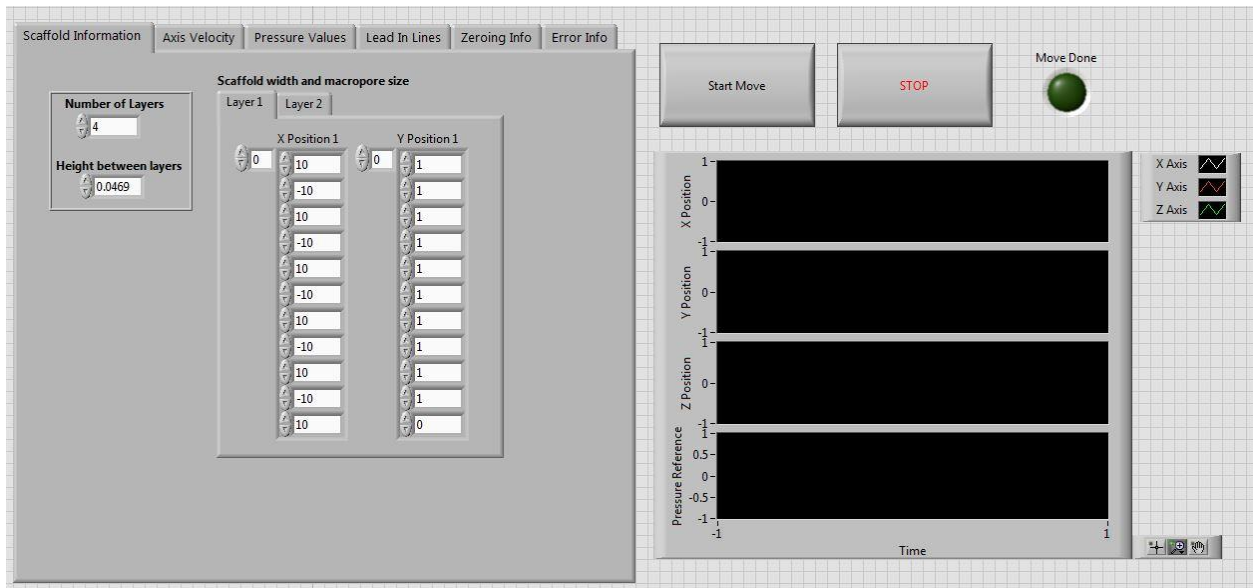


Figure 2.13 Graphical user interface of the DW printer for bone scaffold fabrication.

2.6.2 SoftMotion

Within LabVIEW, the SoftMotion Module was utilized, which enables graphical development of custom motion control applications and is an external package outside of the LabVIEW base code. This program module interfaced with the NI 9514 modules to perform motion control through the control loop shown in Figure 2.11.

SoftMotion simplifies motion control for many reasons, including:

- Motion control and axis measurements are implemented on the same controller.
- Control gains, I/O and feedback settings are configured in an intuitive user interface.
- Motion, I/O and user-defined control algorithms are tightly synchronized.
- “Express” programs allow for simple axis communication.
- Translation of encoder pulses to axis position is done within the software.

To operate within the Softmotion module, the cRIO chassis must be in the “Scan Engine Mode”. In addition, there are several axis settings that must be configured in the SoftMotion program, such as the control gains (discussed more in Chapter 4), motion profile,

limit switch directions, and encoder counts. The axis settings configured on this DW printer can be found in Appendix C.

2.6.3 SoftMotion program examples

Examples of useful “Express VI” programs for motion-control applications are illustrated in Figure 2.14. These programs illustrate the intuitive graphical nature of SoftMotion. Express VIs are loaded into the block diagram and the commands or targets are wired to the inputs, as opposed to writing a line of complicated code connecting to specific microprocessor pins in other programming environments. The Express VI’s listed in Figure 2.14 will be reviewed from left to right. The Power program easily enables/disables a motor drive by connecting the target resource (X, Y or Z axis), and sending a true/false constant for enable/disable. The Read program outputs the axis position directly, bypassing the translation of encoder pulses. The position, velocity and applied torque can be read from each axis. The Straight-Line Move program allows the user to easily specify the desired axis displacement by wiring a constant into the position input. The Stop Move Program stops the specified axis. Finally, the Find Reference Move program allows the user to set up a simple zeroing or homing protocol.

Using a combination of Express VIs, like the ones illustrated in Figure 2.14, will enable the user to develop a simple motion-control program. Moreover, if the user wants to make changes to pre-existing code to enable a new project, these features can be easily adapted by the end-user.

Further, the order in which these actions take place can be controlled via data flow programming through the use of error bars (Figure 2.15). In LabVIEW, a block (or in this case, and “express” program) will not execute unless all data is received at each input. Thus, the error bars can be used to induce a specific program order.

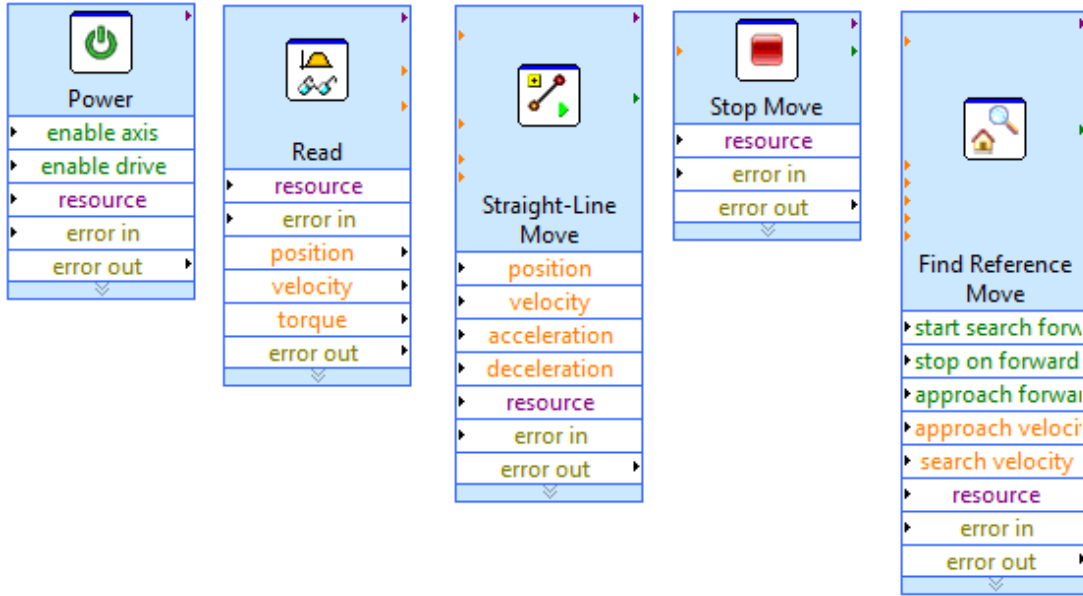


Figure 2.14 “Express” program examples within LabVIEW that are useful for motion control.

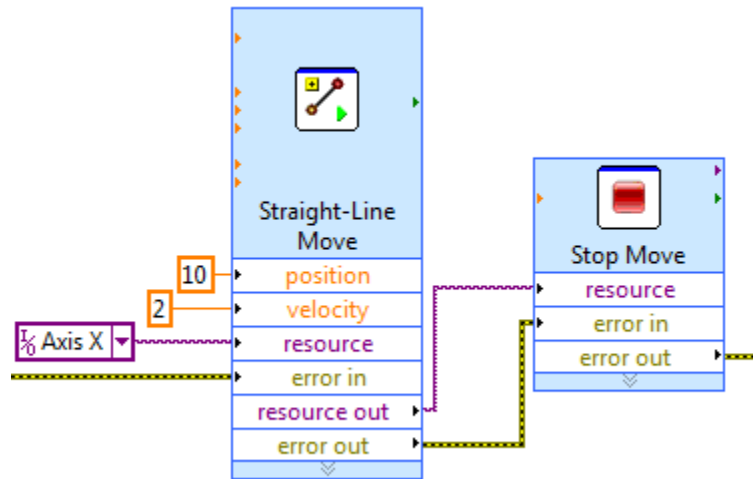


Figure 2.15 Data-flow programming example within LabVIEW using “express” programs. The error bars can be used to induce a specific order. In this frame, the X axis is first commanded to move 10 mm at 2mm/s, and is then commanded to stop.

2.6.4 Fabrication of the lattice structure within SoftMotion

Since bone scaffolds are typically lattice structures, and therefore have repeated features, the scaffold architecture was easily programmed within the SoftMotion programming environment. The motion profile was a single-axis, point-to-point motion where each axis was completely decoupled from the others. To simplify fabrication, the rectilinear bone scaffold architecture was broken down into two move profiles (Layer 1 and Layer 2), which are defined in Figure 2.19. Layer 1 and Layer 2 were orthogonal, and were repeated to form a three-dimensional scaffold. The scaffold layers were implemented as relative position commands using Straight Line Move Express VIs (Figure 2.14), which, at the minimum, required the reference axis and the target final position as inputs. If velocity and acceleration information are not provided, the motion controller chose these parameters automatically.

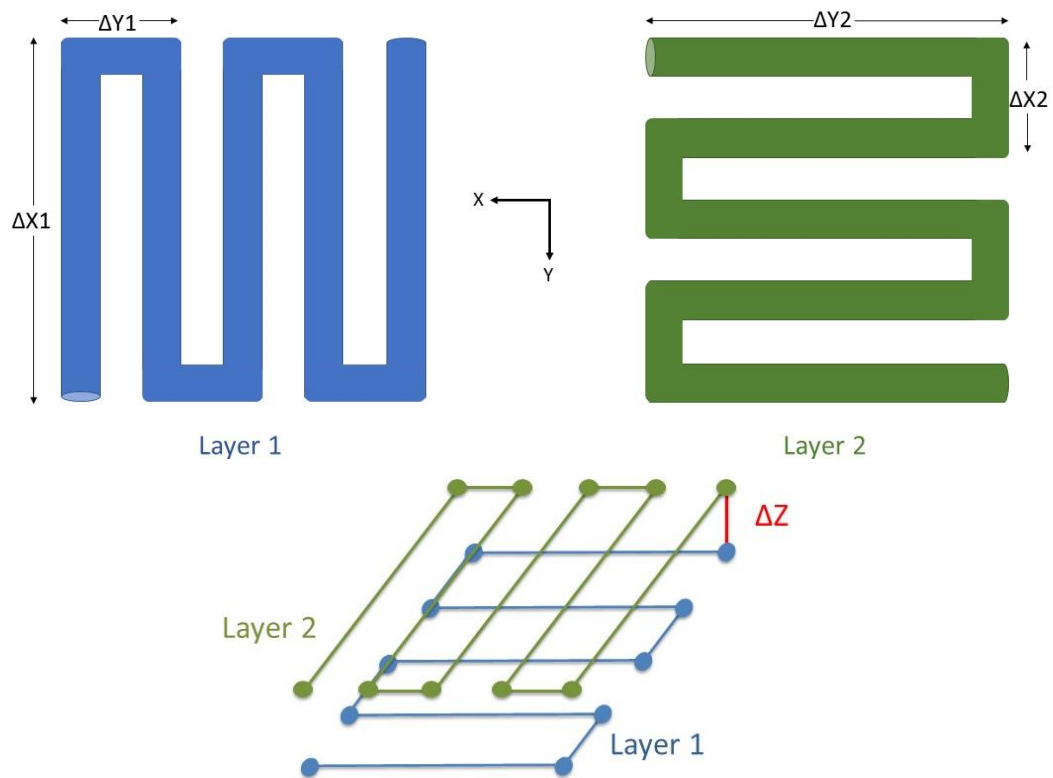


Figure 2.16 Scaffold architecture broken down into two layers, which were repeated to form the three-dimensional structure. In this diagram, each layer was repeated twice to form a 4 layer scaffold.

A bone scaffold was completely described by 4 parameters which were modified on the GUI (Figure 2.13):

1. Number of Layers
2. Height between layers (ΔZ)
3. Scaffold width (which set $\Delta X1$ and $\Delta Y2$)
4. Gap width (which set $\Delta Y1$ and $\Delta X2$).

As an example, for a rectilinear bone scaffold with a width of 10 mm with 1 mm rod spacing, the X-axis was commanded to move 10 mm ($\Delta X1$), then the Y-axis ($\Delta Y1$) was commanded to move 1 mm. The execution order was enforced using error bars (Figure 2.15). This X-Y movement pattern was repeated to complete Layer 1. The Z-axis was then commanded to move up a distance equal to the nozzle diameter (ΔZ). For the next layer, the Y-axis moved 10 mm ($\Delta Y2$), and the X-axis moved 1 mm ($\Delta X2$), forming Layer 2. Since this was a repetitive process, the move profile for Layer 1 and 2 were implemented as position arrays (Figure 2.17) and were repeated for the user-specified number of layers.

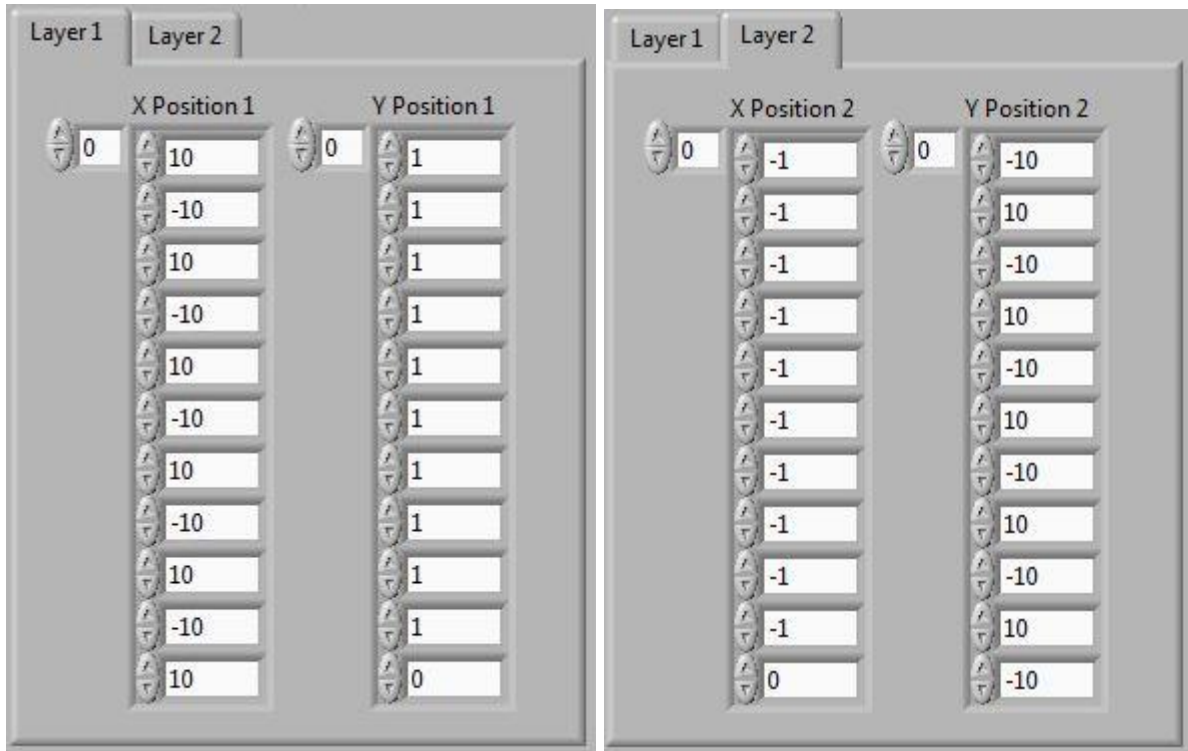


Figure 2.17 Program code for the fabrication of a lattice structure, which was organized into two tabs for Layer 1 and Layer 2. Each array element was associated with a “Position” input on an Express VI. X Position 1 was $\Delta X1$, and Y Position 1 was $\Delta Y1$. X Position 2 was $\Delta X2$, and Y Position 2 was $\Delta Y2$.

2.6.5 Software Limitations

While ease of use was critical, a consequence of SoftMotion was an inflexible and constrained control development environment. For example, the closed-loop control loop shown in Figure 2.11 was embedded in the NI modules and could not be adjusted without using FPGA. All triangle blocks were control gains, and the output of the control loop was sent directly to the drive and could not be further adjusted. While the easy-to-use software may have limited the complexity of the control strategies implemented on the system, it helped achieve the final end goal: a user-friendly motion control platform.

The limit on control development can be viewed as another constraint in this DW printer design: it was challenging to achieve a high level of precision within such a constrained controller environment. This challenge will be discussed further in Chapter 4.

2.7 Program description for bone scaffold fabrication

The scaffold fabrication VI was broken down into three sections: initialization, main program, and shutdown. This section will describe the code structure for each of these sections, which were designed to print a single, rectilinear bone scaffold (“Bone Scaffold Fabrication.vi”). There are other programs within the LabVIEW project that enable printing of multiple bone scaffolds (Chapter 6), but the base program structures are very similar to the code discussed here. Further, the deposition procedure and the steps to turn on all hardware and locate each program are discussed in Appendix C.

2.7.1 Initialization

The functions involved in the initialization step were confined in a flat sequence structure (Figure 2.18). A flat sequence structure consists of one or more frames, which execute from left to right, and all functions within a frame execute before moving to the next frame. In this application, the initialization step was a single frame containing 8 processes (a-h), which are all executed before moving onto the Main Program. These 8 processes included: (a) each axis was enabled to prepare the machine for printing, (b) the error constant was initialized, (c) the Move Position graph on the GUI was cleared, (d) Boolean variables used in the code logic were set to false, (e) scaffold parameters were bundled, (f) code parameters were set to their default values, (g) the queue and notifier structures were created and initialized, and (g) the layer count and scaffold number were initialized to one. After all parameters and axes were configured, the program waited for the user to click “Start Move” to enter the main program.

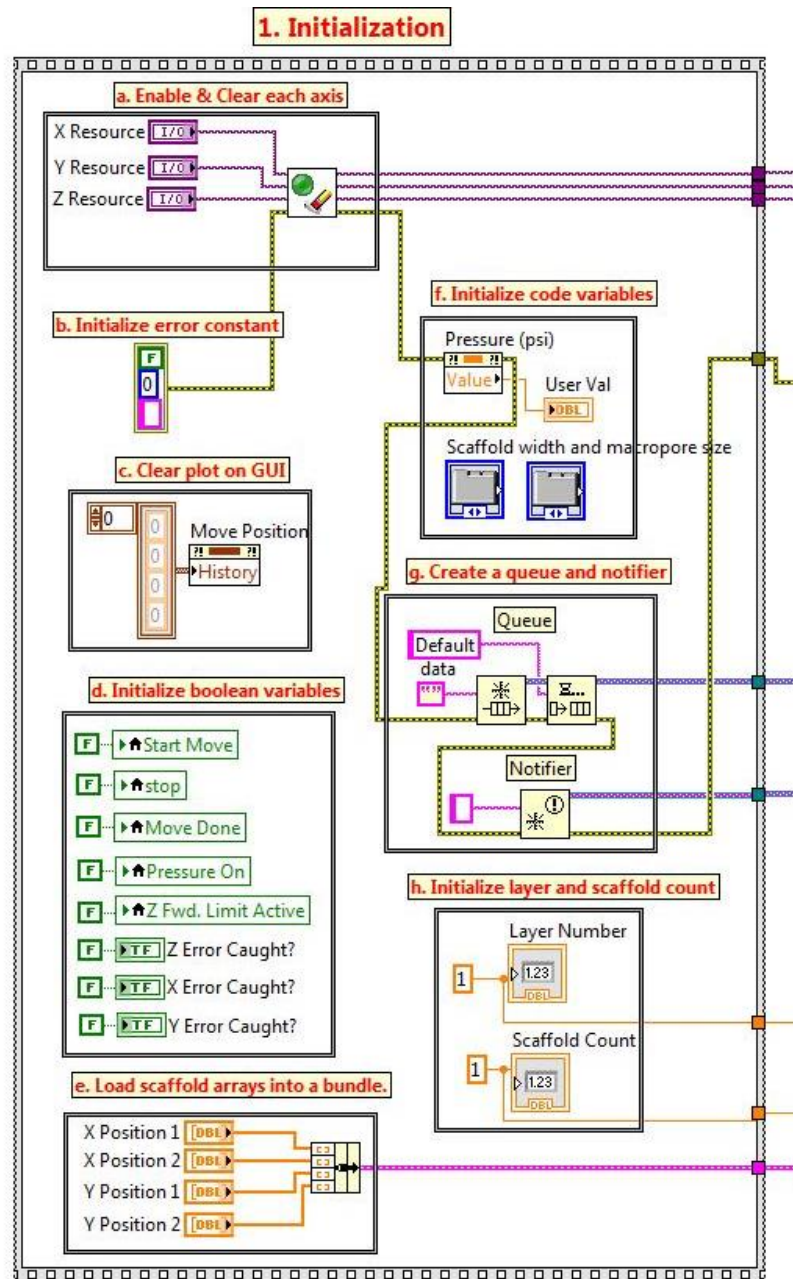


Figure 2.18 Initialization code in a flat sequence structure, which includes 8 steps (a-h). Each step occurs before moving onto the main program.

2.7.2 Main Program

The main program consisted of axis zeroing, lead-in lines, and scaffold fabrication. During axis zeroing, each axis moved toward one of the limit switches using the Find

Reference Move Express VI (Figure 2.14), and then moved a specified distance to locate the starting position. Lead in lines (Figure 2.19) are single-layer scaffold layers that were used to test the ink flow before fabricating a scaffold. During the deposition of lead-in lines, the user can monitor ink flow and modify the input pressure to ensure a smooth and continuous ink flow.

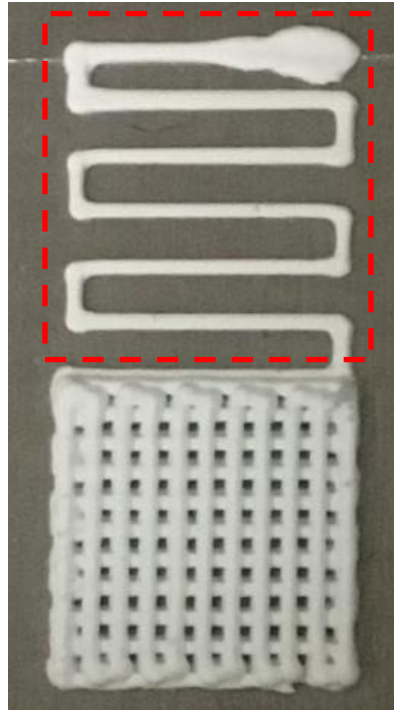


Figure 2.19 Bone scaffold with lead-in lines, which are outlined in a red dashed box.

The code structure of the main program contained four loops: a producer loop, two consumer loops (CL1 and CL2), and a printing loop (Figure 2.20). The producer loop controlled the actions of both consumer loops through a LabVIEW producer/consumer design pattern, while the printing loop ran continuously at its own execution rate.

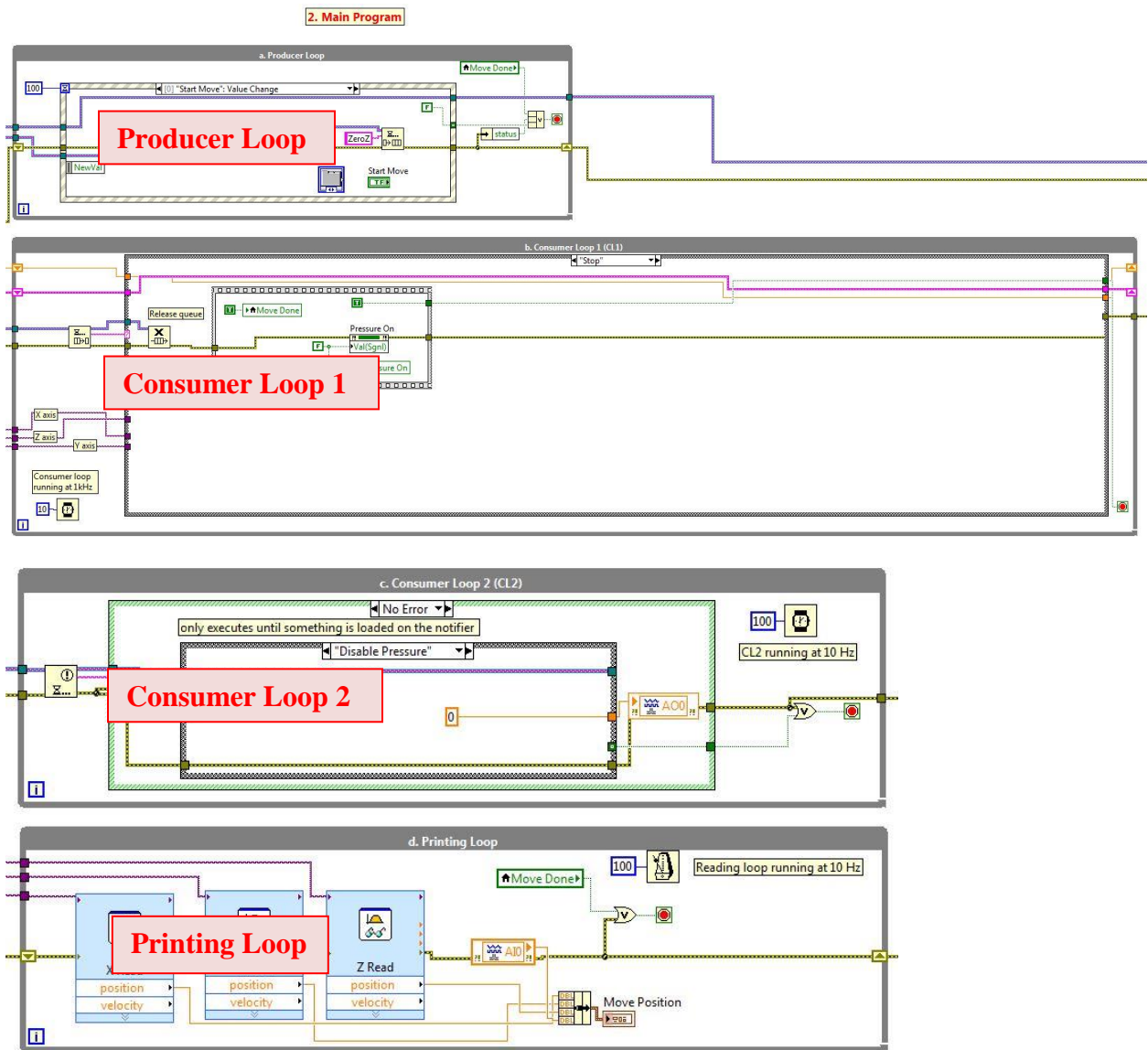


Figure 2.20 Main program of the bone scaffold fabrication code, which includes 4 loops: producer loop, consumer loop 1 (CL1), consumer loop 2 (CL2), and a printing loop.

Producer/consumer design patterns are based on the master/slave pattern and enable the execution of multiple processes which run at different rates. Motor control, for example, should execute at a much faster rate than a loop that plots position data. In addition, this design pattern is used to execute the sequence of events in the proper order and enables communication between the producer and consumer loops through data queues, which use a first-in/first-out protocol. The producer loop produces data for the consumer loop and adds

data to the queue. The consumer loop, on the other hand, removes data from the queue. Since queues are first-in/first-out, the data will be processed by the consumer in the order it was added by the producer.

In this bone scaffold fabrication code, the GUI was the producer since the GUI collected data from the user. The loop that moved the axes or adjusted the output pressure based on the user instructions was the consumer. The two consumer loops included a loop to control axis movement (CL1) and another to instantaneously respond to a change in the applied pressure (CL2), which could be changed at any time by the end user. The former contained a case structure, and the latter utilized a notifier. A more detailed description of the communication between these loops are illustrated in Figures 2.21 and 2.22. The data for both a queue and a notifier were passed between loops along the thick purple lines, which are highlighted in red dashed lines in both figures. Communication for both a queue and a notifier involved three steps: (1) the queue or notifier structure was created in the Initialization step, (2) the producer loop added or sent data to the structure, and (3) the consumer loop received and used the data from the producer loop. Both loops were necessary to enable both processes to occur at the same time. In fact, if user-modified pressure values were incorporated into CL1, axis movement would have temporarily paused to change the pressure, which would have disrupted deposition. The coding logic behind each of the four loops will now be discussed in detail.

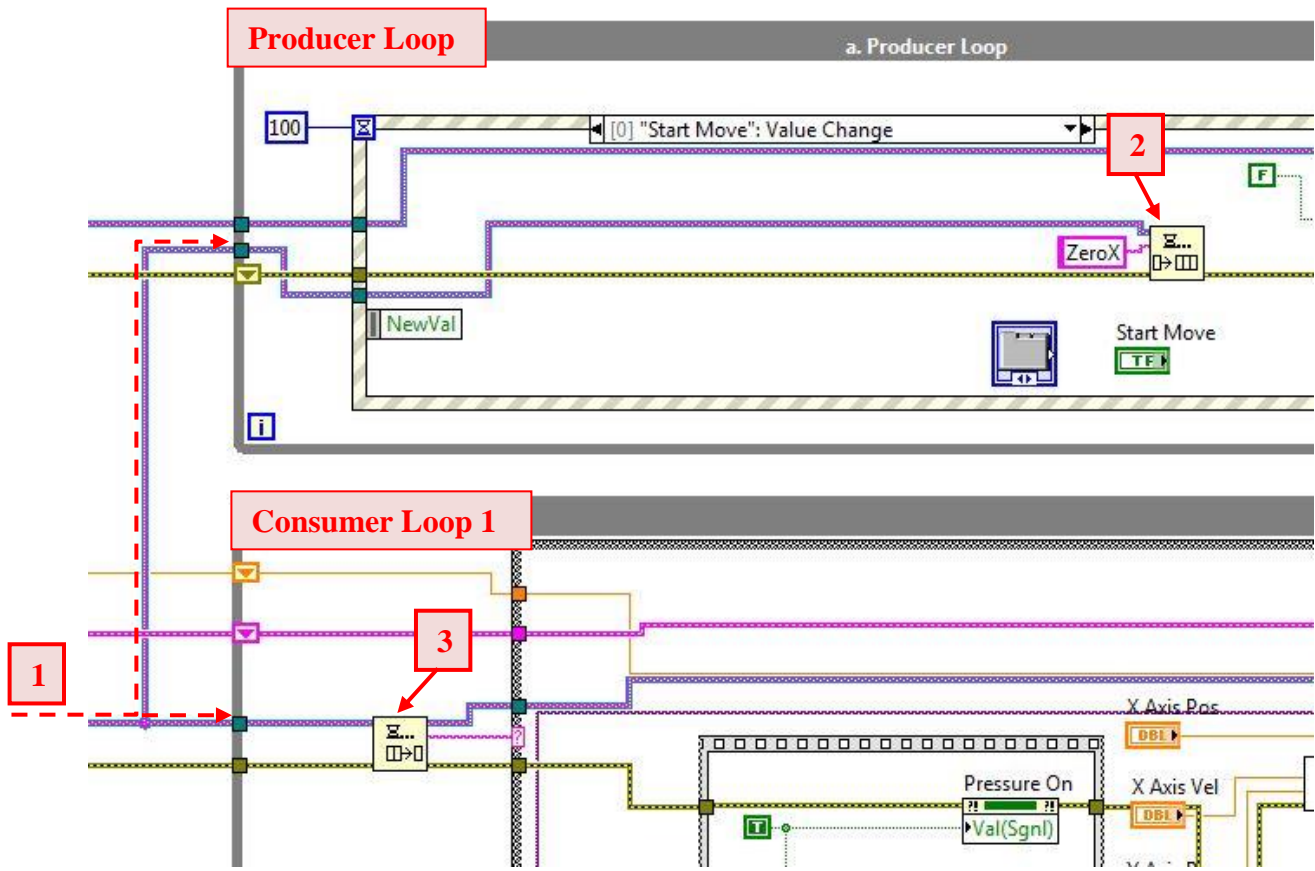


Figure 2.21 Zoomed in view of the communication between the producer loop and CL1 using a queue. The communication involved three steps: (1) queue was created in the Initialization Step (Figure 2.18), (2) the producer loop enqueued data, and (3) CL1 dequeued and used this data.

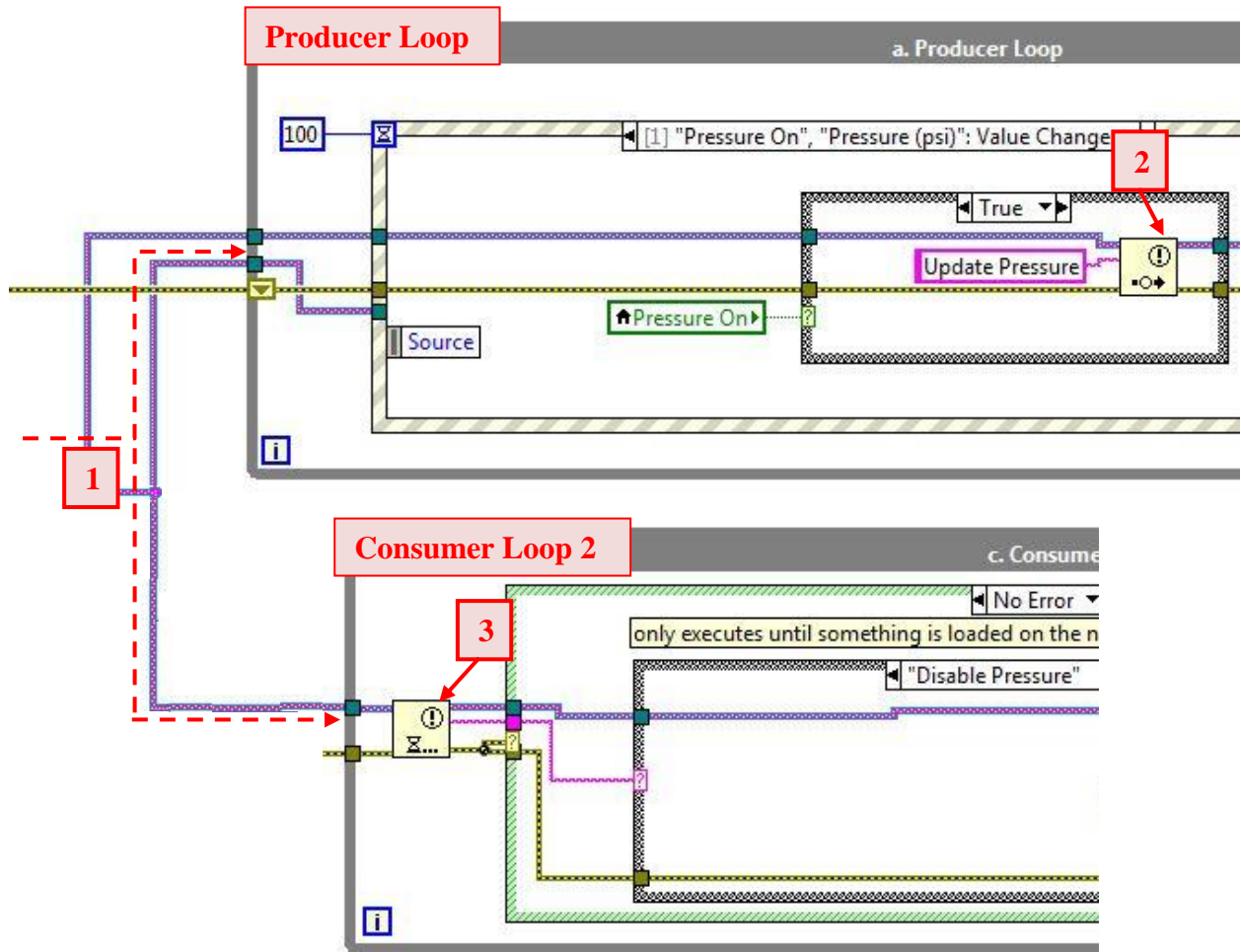


Figure 2.22 Zoomed in view of the communication between the producer loop and CL2 using a notifier. Similar to the queue, the communication involved three steps: (1) notifier was created in the Initialization Step (Figure 2.18), (2) the producer loop sent a message to the notifier, and (3) CL2 waited for this data.

2.7.2.1 Producer loop

The producer loop (Figure 2.23) was a while loop containing an event structure, which waited until an event occurred and executed the appropriate case to handle that event; the event structure waited for the buttons on the GUI to be modified by the end user and responded appropriately. If the “Start Move” button was pressed, the producer loop enqueued data (a string of characters defining a case) to be processed by the queue handler within CL1. An example is illustrated in Figure 2.23, where the user had clicked the “Start Move” button. The

event case associated with this button enqueued a string of characters (“ZeroX”), which was processed by the queue handler in CL1.

Once CL1 received the start command, this loop ran the bone scaffold code independently from the producer loop. The producer loop was, however, able to stop this code at any moment. When the user clicked the “Stop” button, or when printing was finished, the producer loop added the “Stop” case to the front of the queue, enforcing its immediate execution. Further, when the user changed the pressure value during printing, the producer added an element to the notifier to be processed by CL2.

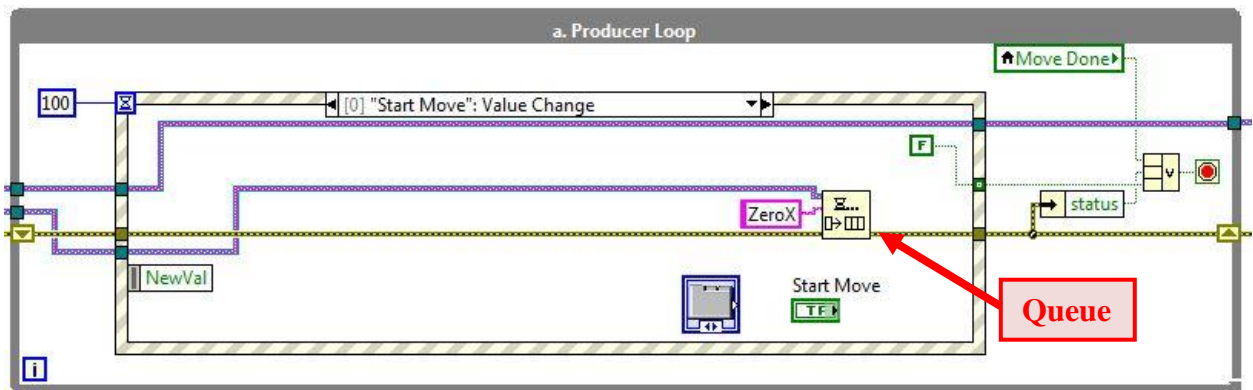


Figure 2.23 Producer loop for the bone scaffold fabrication code. The queue is highlighted by a red arrow.

2.7.2.2 Consumer loop 1

The program entered CL1 (Figure 2.24) when the user clicked “Start Move”. CL1 was a while loop which contains a queue handler and a case structure. A queue handler pulls elements off the queue from the producer loop, and a case structure contains one or more subdiagrams, or cases, and executes one of these cases at a time. Case structures contain three elements for operation: (1) selector terminal, (2) case selector label, and (3) subdiagrams (cases). The data wired to the selector terminal determines the current state of the case structure, which is displayed in the case selector label. In this application, the first element in the queue, which was removed by the queue handler, was attached to the selector terminal of the case structure

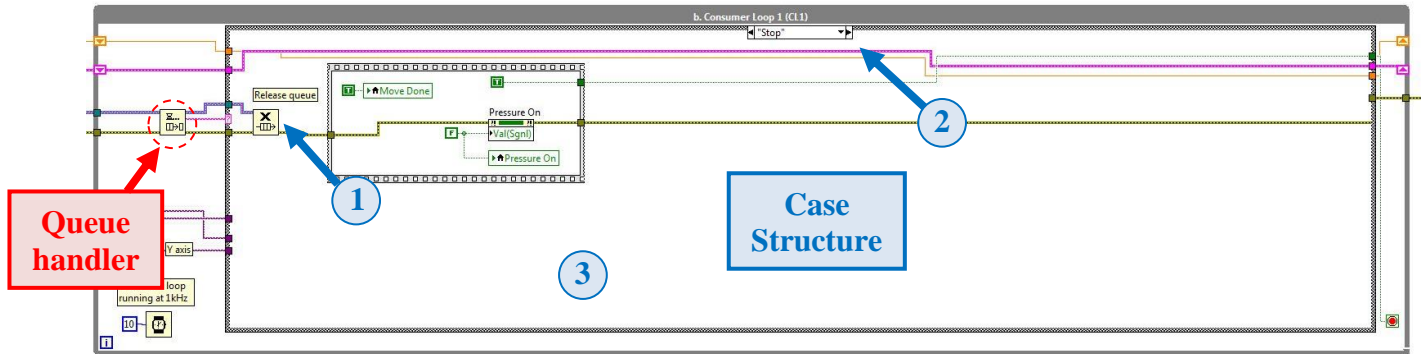


Figure 2.24 Consumer loop 1 for the bone scaffold fabrication code. The outer structure was a while loop running at 1 kHz, with a queue handler and case structure inside. The three elements of a case structure include: (1) selector terminal, (2) case selector label, and (3) subdiagram (case).

The case defined the current state of the DW printer which had the following sequence for scaffold fabrication:

1. Start
2. Zero X
3. Zero Y
4. Zero Z
5. Lead in Lines
6. Layer 1
7. Move Z
8. Layer 2
9. Move Z
10. Stop

There was a subdiagram (case) created for each of these eight steps within the case structure. Similar to a state machine, the DW printer could only be in one of the states at a given time. After completion of the processes within a given case, the next state was added to

the queue. States 1-5 were executed once, followed in order, and had the next state hard-coded into the structure. For states 6-9, these states were repeated and logic was incorporated into the structure to determine the next state. The external input to determine the next state for states 6 and 8 was a local variable defined as “Layer Number”, which was incremented by one after a scaffold layer was complete. The code monitored this value and included the following logic:

If Layer Number = user defined layer, enqueue Stop case.

If Layer Number \neq user defined layer, enqueue Move Z case, and move on to next layer.

Additional details about each of the states within the case structure can be found in Appendix D.

2.7.2.3 Consumer loop 2

The outer structure of CL2 (Figure 2.25) was a while loop containing a notifier, which is a structure that communicates between and synchronizes two independent processes. The structure is similar to a mailbox, where one process sends data to the mailbox, and the other process receives data from the mailbox. The main benefit of notifiers is that the process that receives the data only runs when new data is sent, and stops running while waiting in order to reduce computer processing time. In this application, the producer loop sent data to the CL2 using the notifier only when the user changed the pressure value on the GUI.

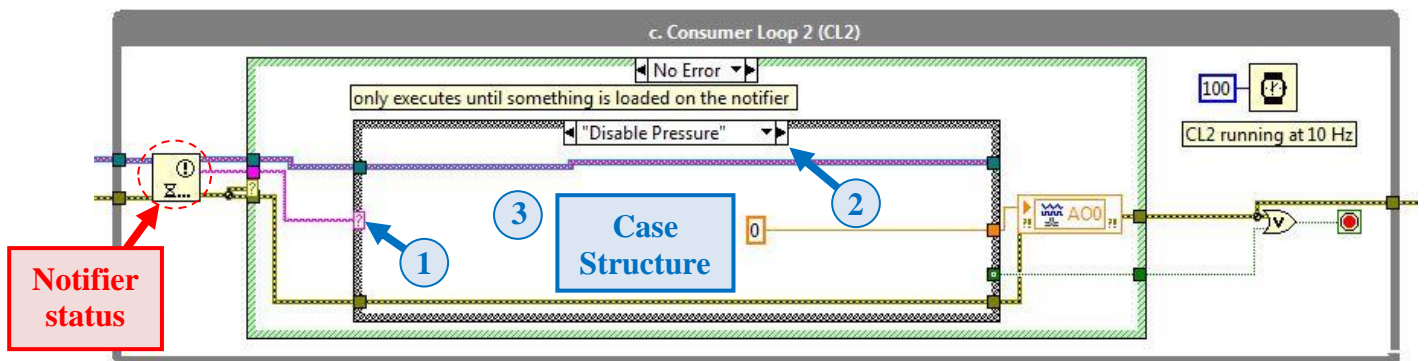


Figure 2.25 Consumer loop 2 for the bone scaffold fabrication code. The outer structure was a while loop running at 10 Hz, with a notifier and case structure inside, which contained the same 3 elements as Figure 2.24.

2.7.2.4 Printing loop

The printing loop (Figure 2.26) was a simple while loop which ran at a slower rate than CL1 and CL2. This loop used a Read Express VI (Figure 2.14) to receive position information for each axis. The Read Express VI processed the encoder pulses of each axis and outputted the position in mm. The position data was bundled and displayed on the “Move Position” graph on the GUI..

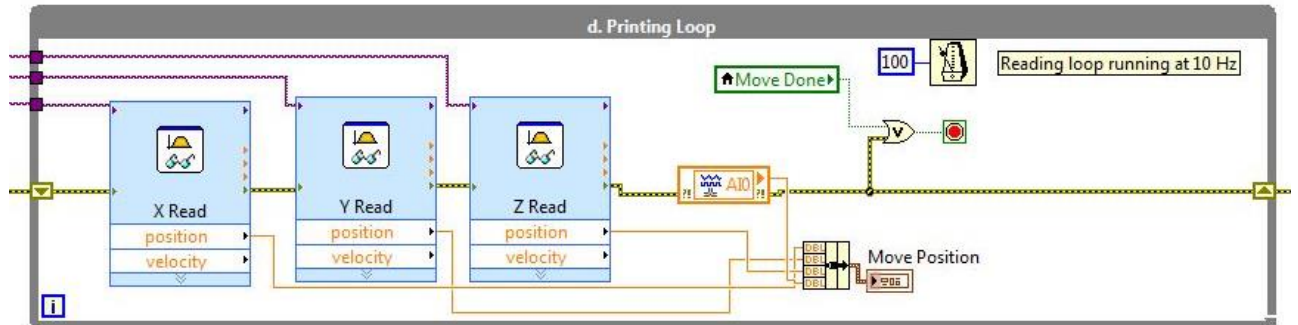


Figure 2.26 Printing loop for the fabrication of a lattice structure, which was a while loop containing three Read Express VIs to read the position of each axis and output this to the graph on the GUI.

2.7.3 Shutdown

The program entered the shutdown step when the “stop” button was pressed, or when the DW printer finished printing a bone scaffold. Shutdown included a flat sequence structure (Figure 2.27) in which (a) all axes were disabled, (b) the pressure output was set to 0 psi, (c) Boolean variables were set to default values to make the program ready for the next run, (d) position data on the plot was exported to excel, and (e) error from each loop was bundled and displayed on the GUI. All of these steps were performed before the program stopped running.

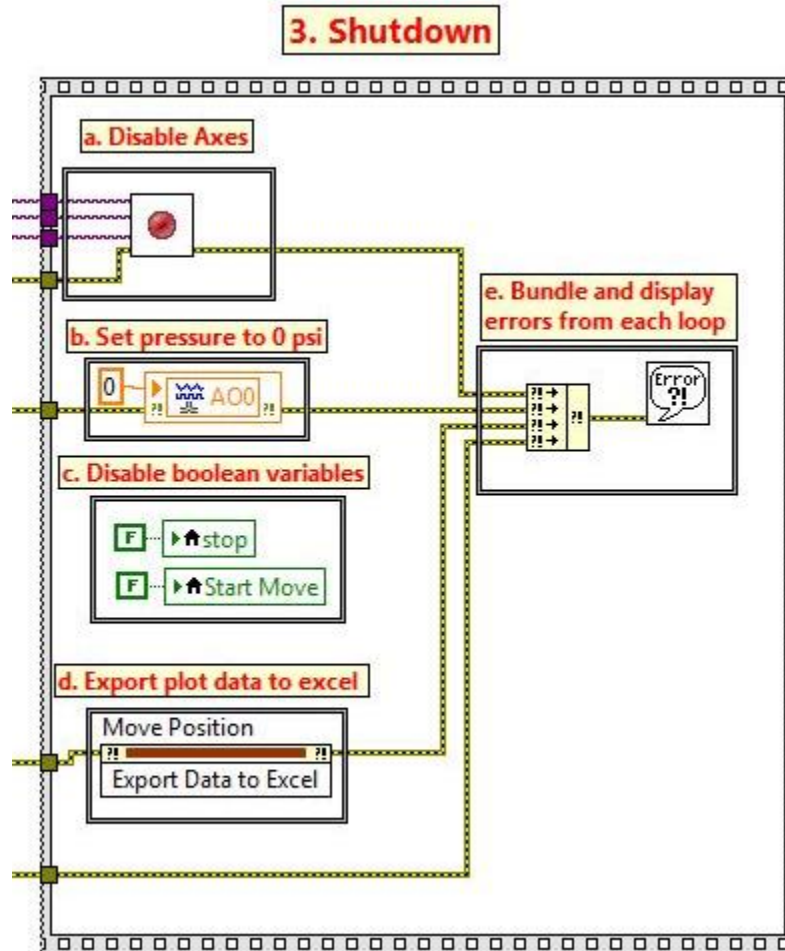


Figure 2.27 Shutdown code in a flat sequence structure, which included 6 steps (a-f). Each step occurred before exiting the bone scaffold fabrication code.

2.8 Conclusion

In summary, this chapter discussed the four main components of the easy-to-use DW printer developed for bone scaffold fabrication. The dispensing material was a colloidal ink, the substrate was an aluminum plate, the extrusion system utilized a pressure regulator and a syringe for pneumatic extrusion, and the positioning system was a three-stage motion platform. In addition, this chapter discussed the hardware and data acquisition components used to control the extrusion system and positioning platform. Finally, the main code structure implemented in LabVIEW was presented. Additional information on the electrical wiring and code structure can be found in the Appendix.

Chapter 3

Material Preparation

3.1 Introduction

A unique feature of direct-write printing is the process by which the ink transforms into a semisolid immediately after exiting the nozzle. In contrast to other freeform fabrication techniques, such as gel casting or fused deposition modeling, the suspension does not require polymerization reactions or solidification of a polymeric melt for the solid transformation [77]. Instead, the structural integrity of the manufactured part is achieved with fine control of the solids loading of the powder, viscosity, and rheology of the ink, which will be discussed later in this chapter. These characteristics are especially important for parts that contain self-supporting features, such as lattice structures typically used for bone scaffolds. The scaffolds in Figure 3.1 were printed with unsuitable ink and illustrate that ink rheology is crucial in determining the quality of the scaffold. In both scaffolds, the ink was not sufficiently stiff to span gaps in underlying layers without significant deformation. Further, it is evident that the viscosity of the ink decreased mid-print, demonstrating a phenomenon termed “filter-pressing” in which the liquid and solid phases separate due to the applied pressure. The “filter-pressing” behavior is evident from the big clumps of ink, which blocked pores resulting in large globs instead of a smooth, lattice structure. This type of behavior is a clear sign of improperly tuned ink.

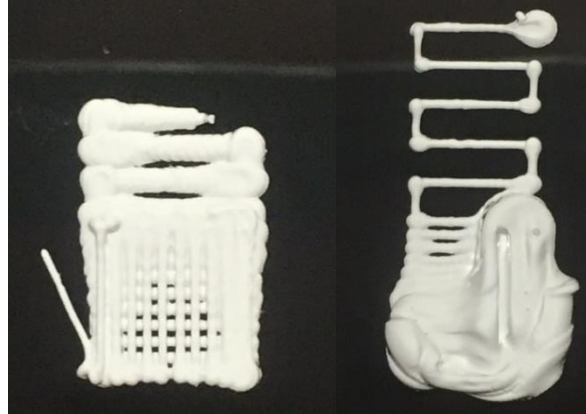


Figure 3.1 Scaffolds printed with poorly-tuned ink in which the ink viscosity decreased mid print due to phase separation, or “filter-pressing”.

The remainder of this chapter briefly reviews the colloidal science principles utilized to make concentrated inks for scaffold fabrication (Section 3.2). An extensive review of this material can be found in [78], [79]. The chapter will conclude with an application of these colloidal science principles to make colloidal ink used for bone scaffold fabrication in this study (Section 3.3).

3.2 Colloidal Science

Direct-write printing involves the extrusion of colloidal suspensions. A colloid is a mixture in which small particles in the $10^{-3} - 10 \mu\text{m}$ size range are suspended in another substance [80]. For particles with high surface to volume ratio, the contact area between the particles and the dispersing medium is large, and therefore interparticle forces strongly influence suspension behavior [80]. Colloids are also known as colloidal dispersions since the substances remain dispersed and do not settle to the bottom of the container [81].

The rheologic properties of the ink must be carefully tuned for the ink to obtain sufficient stiffness to span gaps, permitting fabrication of porous structures. There are two main requirements for the colloidal ink used to make scaffolds. The first is that during deposition, the ink should flow smoothly through the nozzle and then set immediately to facilitate shape retention. This behavior is called shear thinning behavior [82]. To achieve this behavior, the ink should have a well-controlled viscoelastic response and a high elastic shear modulus ($\sim 10^5$ Pa) [83]. The second requirement is that after assembly, there should be

minimal drying-induced shrinkage, which can be achieved by using an ink with high solids loading [83]. Solids loading is the ratio of suspended solids volume to total suspension volume.

Four steps are necessary to achieve these characteristics:

1. Ensure smooth, monosized particles for the solid phase (Section 3.2.1).
2. Create a stable colloid (Section 3.2.2).
3. Adjust the viscosity of this suspension (Section 3.2.3).
4. Induce a system change to promote a fluid-to-gel transition (Section 3.2.4).

3.2.1 Powder Preparation

The base powder of a colloidal ink must comply to strict requirements. These requirements fall into two categories: 1) physical and 2) chemical constitution. First, powder surface morphology influences the stabilization of the colloidal ink. Second, the phase composition is critical for bone scaffold performance *in vivo*. The chemical constitution will vary depending on the application. In this work, we are interested in bone regeneration so we will use calcium phosphate (CaP) materials. CaP materials with a molar Ca:P ratio between 1 and 2 are biocompatible and thus can be used to make synthetic bone scaffolds. The two phases of interest in this Ca:P range are β -tricalcium phosphate (β -TCP, β -Ca₃(PO₄)₂), and hydroxyapatite (HA, Ca₅(PO₄)₃OH).

3.2.1.5 Surface Morphology

To make ink, the particles are ideally small, monosized, spherical particles with a large specific surface area (SSA). Manufacturing processes commonly used to make raw ceramic powder, however, often produce powder batches with rough surfaces, which form large agglomerates [84]. Large particles are unfavorable for fabrication since they can clog the nozzle during deposition and result in irregular grain growth during sintering [84]. Irregular grain growth can lead to stress concentrations, which reduce the mechanical strength of the final product. Further, as-received powder is typically porous, which increases the solids loading; each individual porous particle acts as a sponge and absorbs the liquid [83]. The morphology of the raw powder must be optimized to obtain a high solids loading through two powder processing steps: calcining and ball milling.

Calcining is a high-temperature heat treatment process that results in smoother and more dense powder particles. Through calcination, the morphology of powder changes from faceted grains to round particles [85]. Smoother particles lead to a lower ink viscosity and deposition pressures, and consequently a reduction in the number of manufacturing defects [24], [85]. Calcination also densifies the as-received particles, which results in a reduction of the SSA. The SSA reduction facilitates adsorption of the additives used in the ink making process, which increases the suspension stability and allows particles to pack tightly to form a strong gel network [85]. In [24], the most significant SSA reduction occurred only after a half hour of calcination, while several calcination hours were required to achieve the optimal powder morphology.

Calcination also encourages agglomeration and increases the average particle size, therefore, it is accompanied by cycles of a grinding process to break down these agglomerated particles and decrease particle size (PS). Ball milling is a specific type of grinding process, where a solution of powder and solvent in a large Nalgene container is continuously agitated with alumina milling media. The powder particles are mainly ground by mechanical forces such as impact from the milling media. In general, ball milling and calcination have opposite effects on PS and SSA [24]. Ball milling decreases PS and increases SSA, while calcination encourages agglomeration, resulting in an increase in PS and a reduction in SSA. Thus, the amount of calcination and ball milling must be empirically determined to achieve the necessary physical properties of the powder.

Determining the optimal ball milling conditions is challenging since there are many milling parameters that have a strong influence on the final powder properties, including grinding atmosphere, solvent, milling time, rotation speed, vessel radius, and milling media amount and surface area [86]. Thus, research findings from other labs cannot be generally applied since parameters vary significantly between machines, labs, and contexts.

There are some consistent trends on the effect of ball milling parameters in the literature. First, media loading in the ball milling process is one of the most important parameters and should be optimized for each process [87]. Ideally, the powder is impacted between the milling media. If the media to powder ratio is too high, the media will strike itself leading to media wear and insufficient milling. Second, a reduction in median PS is achieved

with an increase in milling time [88] and a faster milling speed [89], [90]. Faster milling speeds, however, result in an increase in particle shape irregularity [89]. [91] showed that a narrower size distribution is achieved at slower speeds. Finally, the critical ball milling speed should be used, which is defined as the speed at which the milling media tumble along the side of the container as opposed to falling from the top during rotation (Figure 3.2). The tumbling motion can be achieved through optimizing the media charge, which is the vol% of milling media in the container, and the critical ball milling speed.

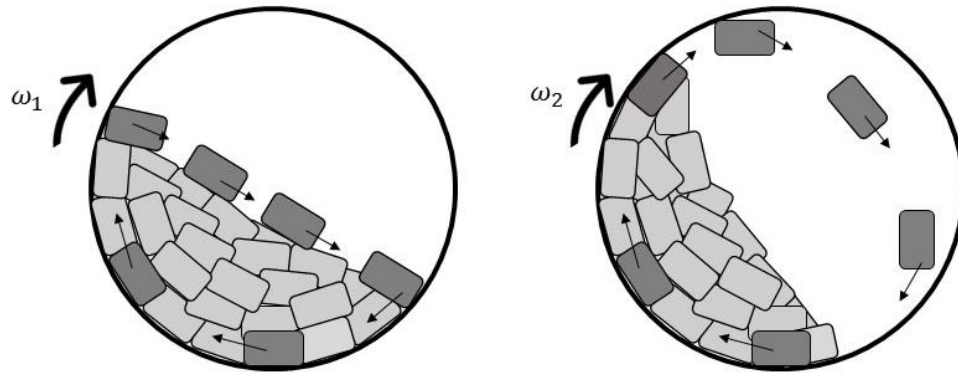


Figure 3.2 Illustration of speed dependent milling media motion in a ball mill. Tumbling (left) and falling (right). Typically, $\omega_1 < \omega_2$.

3.2.1.6 Phase Composition

The phase composition of the base powder is determined by the chemical composition of the powder after processing, which is measured by X-ray diffraction (XRD) analysis (Appendix A.1 and A.2). If the starting powder does not have the required phase composition (which is lab dependent), the same two processing steps are required to induce a chemical reaction: calcining and ball milling. Calcining induces phase transformations in the powder, and ball milling is required between heat treatments to ensure complete mixing and homogeneity.

The equilibrium state of a chemical reaction can be represented on a phase diagram. Each state has a stability field, defined as the composition where the free energy is lower than all other possible states of the system within a temperature range. If a multi-component powder blend is used, the state with the lowest free energy could be either a single phase or a mixture

of phases [92]. As the solid-state reaction progresses, the phase composition converges towards one of the stability fields depending on the temperature and starting powder blend.

3.2.2 Colloid Stability

A colloidal ink for direct-write printing must be stable, meaning particles won't agglomerate into larger particles. Brownian motion of colloidal particles in suspension results in frequent collisions, and the stability of the suspension is determined by the particle interactions. If attraction dominates, the particles agglomerate. If repulsion dominates, the particles remain dispersed and the suspension is stable. Stability is governed by the total interparticle potential energy, V_{tot} :

$$V_{tot} = V_{vdW} + V_{elect} + V_{ster} + V_{struc}, \quad (3.1)$$

where each potential energy term V_i refers to the contribution from van der Waals forces (vdW), electrostatic interactions (elect), steric interactions (ster), and structural interactions (struc), respectively.

3.2.2.1 Van der Waals Forces

Van der Waals forces are relatively weak electric forces that attract all like materials. When powder is added to a solution, van der Waals forces pull particles together [24], and V_{vdW} is the attractive potential energy due to long range van der Waals interactions between particles [80]. To achieve colloidal stability, the long-range attractive van der Waals forces must be counteracted with long-range repulsive forces. Dispersing agents are commonly added to a solution that utilize one or more of the stabilization interactions to prevent agglomeration. Examples of dispersing methods include surrounding colloidal particles with an electrical double layer (electrostatic), adsorption of polymeric molecules (steric), or the addition of free polymers in the dispersion medium (structural). The chemical and electrical interactions between the dispersing agent and colloid must be tailored to ensure proper stabilization.

3.2.2.2 Stabilization Methods

V_{elect} is the repulsive energy resulting from electrostatic interactions between like-charged particle surfaces [80]. With this stabilization technique, ionic groups from the dispersing agent adsorb to the particle surface and form a charge-neutral double layer (Figure 3.3A). Mutual repulsion of these double layers provides stability. The degree of stabilization, however, is sensitive to the ionic strength of the dispersing medium and particle solubility may limit the working pH range [79]. As a result, the suspension may only be stable in a limited pH range.

Steric stabilization provides an alternate route for controlling colloidal stability. V_{ster} is the repulsive energy resulting from steric interactions between particle surfaces coated with adsorbed polymeric species (Figure 3.3B). With steric stabilization, dispersing agents include macromolecules which attach to particle surfaces and the tails extend radially outward for suspension stabilization. The macromolecules should be strongly anchored to the particle surface to avoid desorption during particle collisions. Many types of polymers with different architectures can be used for steric stabilization, including homopolymers, diblock copolymers, comblike copolymers, and short-chain polymers [80].

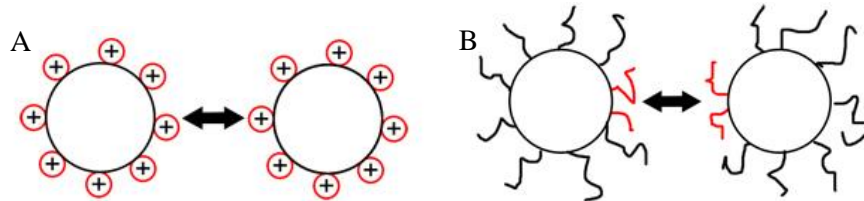


Figure 3.3 Diagram illustrating (A) electrostatic and (B) steric stabilization. Image from [93].

Structural stabilization is a method in which the macromolecules are free in solution, and do not attach to the particle surface. V_{struc} is the potential energy resulting from the presence of nonadsorbed species in solution, which can either increase or decrease suspension stability.

In practice, it is common to use a combination of stabilization methods. Electrosteric stabilization inhibits particle aggregation by the combined effects of electrostatic and steric stabilization. Polyelectrolyte species are additives that can impart electrostatic and steric

stabilization to a colloidal suspension. A polyelectrolyte is a polymer with dissociating groups in their repeat units that dissociate in aqueous solutions and holds a charge along the length of the polymer chain [79]. Polar groups in the polymer bind to the acidic or basic sites on the particle surface (electrostatic stabilization), and the functional groups serve to stabilize the suspension (steric stabilization).

The solvent conditions must be altered to ensure proper adsorption behavior of the polyelectrolytes. Stabilization increases with higher adsorbed amounts, and adsorption levels increase when the particle surface and the polyelectrolyte carry opposite charges. In addition, an increase in pH increases the steric interaction length, δ (Figure 3.4), which is attributed to an increase in interparticle repulsion as the charge on the polymer increases [94]. As δ increases, the functional groups of the polyelectrolyte extend out radially from the particle. Since a charge is carried along the length of the chain, this discourages agglomeration of the particles and increases the colloidal stability.

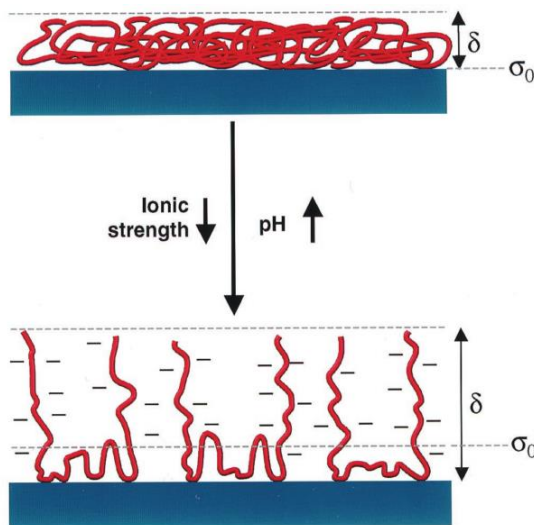


Figure 3.4 Adsorbed polyelectrolyte species on a ceramic surface (blue) as a function of pH and ionic strength. δ is the steric interaction length. Image from [80].

Copolymers are effective at stabilizing since there are two different monomers incorporated into the same polymer chain: one polymer serves as the anchor group to attach to the particle surface, and the other polymer as soluble group that provides the steric barrier [79]. Ideally, the charge along the polymers is opposite of the charge on the particle surface to ensure proper adhesion.

Homopolymers, however, are less expensive and are sufficient for ceramic colloidal suspensions used in this work. Polyacrylates are a specific type of homopolymers that provide both electrostatic and steric stabilization. Polyacrylates have a linear backbone with an ionizable carboxylic acid group that adsorb to the particle surface, increasing the strength of anionic charges on the particle surface and causing them to repel one another and remain dispersed. Polymers containing carboxyl groups are the most effective steric stabilizers since the carboxyl groups hold negative charges and interact strongly with positively charged ions often present on the ceramic particle surface [79]. Since the strength of this ionization increases with pH, the pH must be adjusted to ensure stability in a colloidal solution.

3.2.3 Suspension Rheology

The viscosity of the colloidal ink must be adjusted to achieve the optimal rheological behavior for direct-write printing. Rheology is the science of the flow and deformation of fluids under an applied force. The simplest case is Newtonian fluids, where there is a linear relationship between shear stress and shear rate (Figure 3.5A, a) and the viscosity, η , is independent of shear rate (Figure 3.5B, a). In reality, most fluids are non-Newtonian, meaning the viscosity is dependent on the shear rate. Three possible characteristics of non-Newtonian fluids include a non-linear relationship between shear stress and shear rate (Figure 3.5A, b, c, and e), a non-zero yield stress (Figure 3.5A, d-e), or a time dependent viscosity (Figure 3.5B, b-e). A type of non-Newtonian fluid is a “yield stress” fluid, which does not flow until the shear stress exceeds the yield stress [82].

Colloidal inks should be a yield-pseudoplastic fluid (Figure 3.5e), which is a specific class of yield stress fluids [24]. Yield-pseudoplastic fluids are semisolid and do not deform under stresses below the yield stress, τ_y (Figure 3.5A, e). Above τ_y , the fluid is pseudoplastic, or shear-thinning, which means the viscosity decreases with shear rate. As a result, yield-pseudoplastic fluids are initially resistant to flow at low shear rates, but flow more freely at higher shear rates as the viscosity decreases (Figure 3.5B, e).

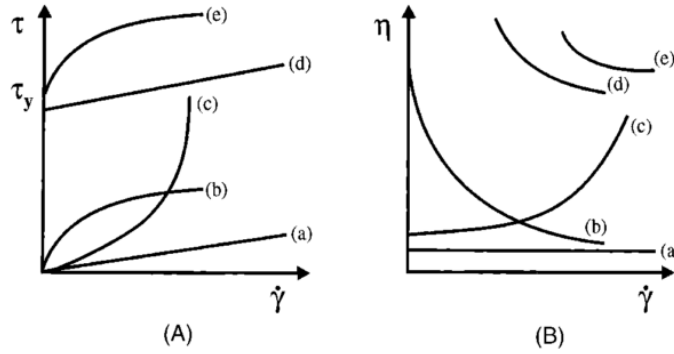


Figure 3.5 Types of rheological behavior for shear rate vs. yield stress (A) and shear rate vs. viscosity (B). (a) Newtonian flow; (b) shear thinning; (c) shear thickening; (d) Bingham plastic; and (e) pseudoplastic with a yield stress. Image from [80].

The viscosity provides a measurement to assess the effects of particle stability and morphology on flow behavior. To compute viscosity, analysis of the flow properties of the hard sphere model system is used, and serves as a benchmark for assessing more complicated systems. In hard sphere systems, the structure is solely dictated by hydrodynamic interactions and Brownian motion. Further, interparticle interactions do not occur until the point of contact, where interaction is infinitely repulsive (Figure 3.6). The Krieger-Dougherty relationship calculates the relative viscosity, η_{rel} , as a function of solids loading, ϕ , of the suspension:

$$\eta_{rel} = \left(1 - \frac{\phi}{\phi_{max}}\right)^{-K\phi_{max}}, \quad (3.2)$$

where ϕ_{max} is the max solids loading (60-65% for monomodal distribution of particles [80]) and K is the hydrodynamic shape factor (2.5 for monodisperse spheres). Deviations in K are expected given the non-spherical nature of the particles.

Hard sphere analysis is the ideal case and does not apply to particles suspended in a colloid. Instead, most ceramic suspensions with adsorbed dispersants are considered soft sphere systems. Additives added to the suspension adsorb to the particle surface, creating a soft layer around each particle. In soft sphere systems, repulsive interactions occur some characteristic distance away from the particle surface (Figure 3.6). The flow behavior between hard and soft sphere systems is similar if the adsorbed layer on the particle surface is accounted

for in the effective solids loading [80]. Equation (3.2) can be modified to be more representative of the system by substituting ϕ with ϕ_{eff} , which is calculated in Equation (3.3).

$$\phi_{eff} = \phi \left(1 + \frac{\rho_s \delta A_s}{a} \right)^3. \quad (3.3)$$

The hard sphere model is adjusted for irregular shaped particles using powder density (ρ_s), SSA (A_s), adsorbed layer thickness (δ), and particle radius (a). The ρ_s and δ are assumed constant, and ϕ_{eff} is solely dependent on the particle morphology. As a result, a larger specific surface area and smaller particle radius leads to a higher effective solids loading and higher ink viscosity, which was confirmed empirically in [24].

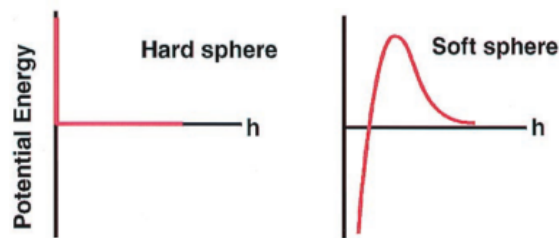


Figure 3.6 Potential energy as a function of h , the separation distance between particles for hard sphere and soft sphere systems. Image adapted from [80].

Ceramic powder suspensions with small particles ($<10 \mu\text{m}$), and a monosized distribution that are dried from a suspension, typically pack into a consolidated structure that is 65% of the theoretical suspension density [77]. A solids loading just below this consolidated density is critical for proper flow behavior. Figure 3.7 depicts the viscosity of typical ceramic powder suspensions as a function of solids loading. At low solids loading, suspensions have low viscosities and essentially behave as Newtonian fluids. As the solids loading approaches 60 vol%, inter-particle collisions and interactions become dominant. As a result, the viscosity drastically increases and the rheological behavior transitions to shear thinning. Beyond 65 vol% solids loading, particle mobility becomes restricted and the rheological behavior transitions to shear thickening. Thus, a solids loading of 50-65 vol% ceramic powder is optimal

for direct write printing (green region in Figure 3.7) [24], [77], [80]. At high solids loading levels, the ink viscosity is very sensitive to slight changes in solids loading (Figure 3.7) since small changes in solids loading results in large changes in ink viscosity.

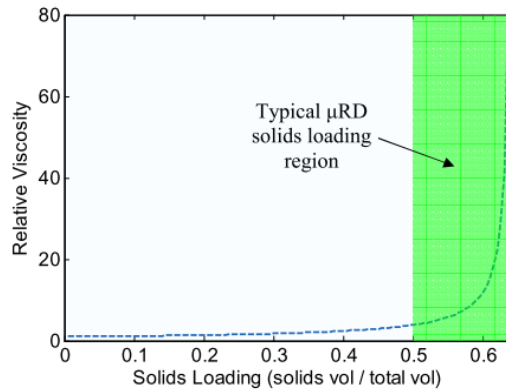


Figure 3.7 Krieger-Dougherty relationship, with the region of typical solids loading values for colloidal ink shaded in green. Image from [24].

Binders are commonly added to colloidal ink to adjust the viscosity. A binder is a polymer chain that adsorbs to the particle surfaces and links the particles together. The binder provides the ink with the necessary shear thinning flow and yield stress characteristics. Figure 3.8 is an illustration of how binder fibers in a colloidal ink respond to shear stress. Under no shear, the fibers are randomly oriented, forming a rigid network. Under shear stress, the fibers align with the shear forces and the viscosity decreases.

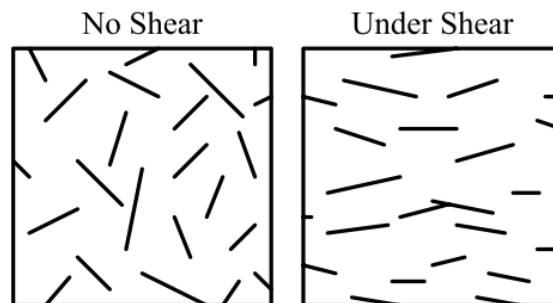


Figure 3.8 Behavior of cellulose binder fibers under shear. Image from [24].

3.2.4 Fluid to Gel Transition

The final step to make colloidal ink is to initiate a fluid to gel transition (Figure 3.9) since a well-dispersed high-solids-loading suspension is not stiff enough to span gaps without significant deformation. A small amount of flocculation is necessary to increase the elastic modulus, and is achieved through the addition of a gelling agent. The fluid to gel transition occurs as the pH is adjusted to the point of zero charge [78]. Ideally, dispersion and flocculation are balanced to achieve a stable solution with a high yield stress to prevent shape changes.

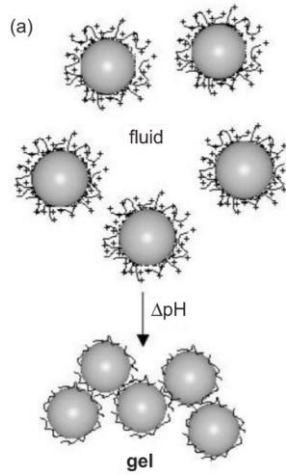


Figure 3.9 Fluid to gel transition for colloidal inks. Image from [78].

3.2.5 Ink Behavior during Printing

Gel-based inks flow with a three-zone velocity profile within the nozzle [78]. The core is an unyielded mass of gel moving at a constant velocity. Surrounding this core is a yielded fluid shell experiencing laminar flow. Finally, there is a thin layer without colloidal particles along the nozzle wall. As the gel exits the nozzle, it is extruded as a continuous rod-like filament with a rigid gel core and fluid shell. After deposition, the fluid shell, now devoid of a shear stress, quickly transforms to a gelled state as the particle bonds reform [78]. The rods maintain their cylindrical shape during extrusion and drying due to the high yield stress of the colloidal ink.

A properly tuned colloidal ink will behave as a pseudoplastic fluid (Figure 3.5). Below the yield stress, the suspension is in the linear viscoelastic region, where the Elastic modulus is independent of applied stress. Above the yield stress, the interparticle bonds begin to rupture,

leading to decrease in the Elastic Modulus. Shear thinning behavior results when these networks are disrupted under high shear stresses.

3.3 CaP Based Ink Preparation

This study focuses on CaP-based materials for bone regenerative applications. In previous work, HA powder was used as the solid phase of the ink. After processing, we ended with a biphasic composition of HA and β -TCP. Despite having the proper phase composition, the powder produced inconsistent results since it contained impurities, and each new batch had a different phase composition and particle geometry. As a result, a lot of time was spent characterizing each batch before making ink.

An alternative method to using off-the-shelf HA powder is to blend pure precursor powders. This process theoretically gives full control of the final powder biphasic composition, expressed as wt-% of HA and β -TCP. A repeatable process from colleagues at the RMS Foundation (Bettlach, Switzerland), who make a pure CaP blend, was adopted to make a pure raw powder with the desired phase composition.

3.3.1 Powder Preparation

The standard procedure at RMS to make the base powder used as the solid phase of the colloidal ink is based on a solid-state reaction between two precursor powders: di-calcium phosphate (CaHPO_4 , GFS Chemicals, CAS No: 77757-93-9) and calcium carbonate (CaCO_3 , Merck, CAS No: 471-34-1). The two precursor powders do not have the desired properties (both physical and chemical characteristics), and the powder blend must be adjusted through processing steps: calcining and ball milling. A major goal of this work was to try to modify their protocol to suit our needs. This adjustment involved determining the proper powder processing protocols that would yield the target ranges for powder composition and particle morphology (Table 3.1).

Table 3.1 Physical and chemical characteristics of the starting powders and the ideal final blend.

	Physical Characteristics	Chemical Characteristics
--	--------------------------	--------------------------

	Particle Size (μm)	Specific surface area (m^2/g)	HA wt-%	b-TCP wt-%
Final Blend	1.5	2.5	80-95	5-15

3.3.1.1 Surface Morphology

The two precursor powders used in this work had large ($>10 \mu\text{m}$) particles and a blocky particle morphology (Figure 3.10). A calcination temperature of 1050°C was used with extensive dwell times to allow the particles to adopt a smooth, pore-free morphology. Further, wet ball milling was used as the grinding process to decrease PS.

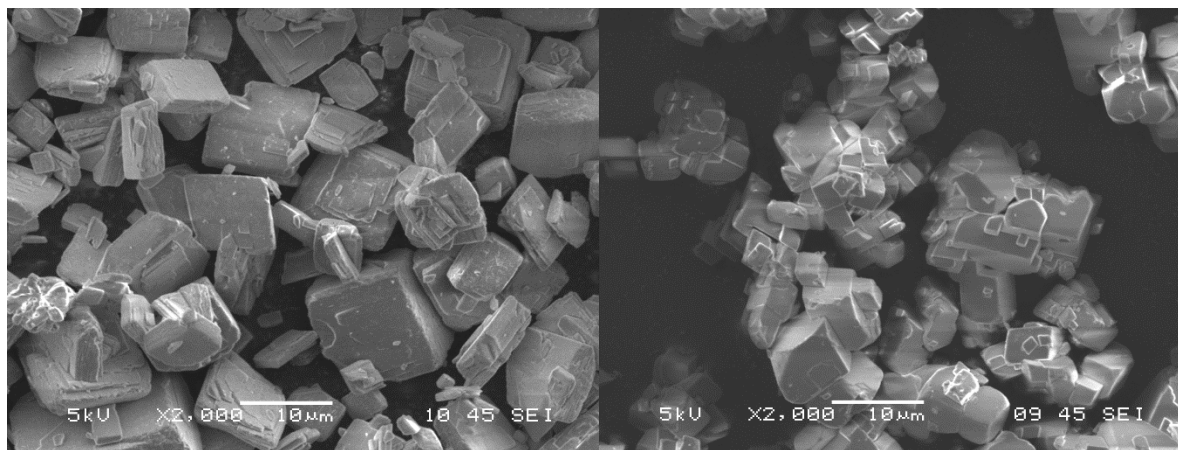


Figure 3.10 SEM images of the raw precursor powders: a) CaHPO_4 and b) CaCO_3 .

The powder was ball milled with ethanol as the solvent using a tumbling ball mill (ACM Labmill 8000 Jar Mill Machine). Monosize, cylindrical alumina media were used as the grinding media. The slurry (powder and ethanol) and media were added to the milling container (a cylindrical Nalgene container), and subsequently placed on the mill.

To find the optimal ball milling conditions, general trends from the literature (discussed in Section 3.2.1) were first applied, and then the optimal ball milling parameters for the system of interest were determined empirically. The critical ball milling speed was determined by attaching a light to the back of the Nalgene container and observing when the milling media transitioned from falling to tumbling. At this critical speed, two parameters were varied: volume percentage of media and slurry, and the ratio of media to slurry. Increasing the volume

of alumina media relative to the slurry led to an improvement of the final PS distribution of the powders. The empirically determined optimal ball milling conditions are listed in Table 3.2. The weight of the media was 273 g, corresponding to a 40 vol-% in ball filling of the Nalgene container (media charge).

Table 3.2 Optimal ball mill conditions determined empirically.

Milling Speed	Ethanol to powder ratio	Milling Media Charge
Dial 2.4 = 77.5 RPM	5:1	40%

3.3.1.2 Phase Transformation

Colleagues at RMS compiled information from several sources and developed a CaP phase diagram relevant to the chemical reaction between di-calcium phosphate (CaHPO_4) and calcium carbonate (CaCO_3) (Figure 3.11). Most published CaP phase diagrams consider a dry atmosphere, which is not useful in many applications since HA cannot form under this condition [95]. Alternatively, H_2O partial pressure in ambient humidity is sufficient to obtain HA. The information in RMS's phase diagram is relevant for a H_2O partial pressure of 550 mm Hg. Figure 3.11 illustrates that there is no stability field with three or more phases: it is either a single-phase composition on the vertical lines, or a biphasic composition with variable phase ratio depending on the bulk Ca and P content, or in this case the amount of di-calcium carbonate and calcium carbonate. The phase composition converges to a single or biphasic composition, which is the thermodynamically most stable form for the bulk composition. Thus, if three or more phases are present in the powder, the reaction has not yet reached equilibrium.

Generally, it is assumed that the only volatile components are H_2O from dehydration and CO_2 from the reaction of carbonates and organic additives. Since it is assumed that the bulk calcium and phosphate content remain unaffected by calcination, the initial Ca:P of the blend of raw powders should theoretically remain constant throughout heat treatment.

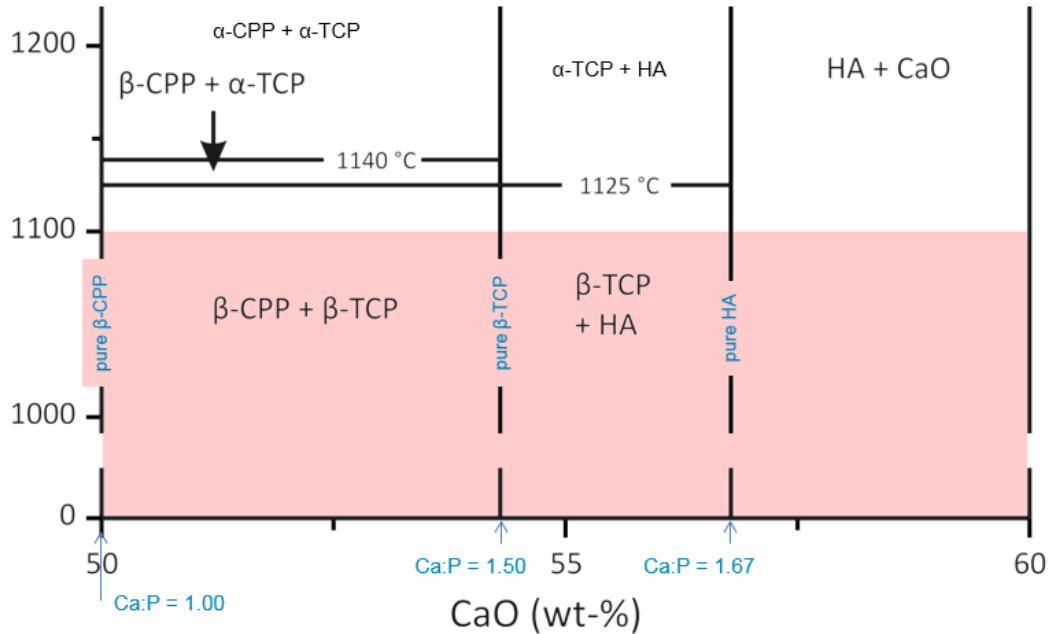


Figure 3.11 Unpublished CaP phase diagram at $P_{H_2O} = 550$ mm Hg developed by colleagues at RMS. The data for 1700-1200 °C was obtained from [96], 1200-1000 °C data was obtained from [97], and the 0-1000 °C data was obtained from data at RMS. CaO (wt-%) = $\text{CaO}/(\text{CaO} + \text{P}_2\text{O}_5)$. The biphasic region of interest in this work is outlined in red dashed lines.

There are a few important takeaways from the phase diagram. First, the Ca:P ratio must be greater than 1.5 for HA to form. Secondly, for the application of interest here, the Ca:P ratio should stay between 1.5 and 1.67 to ensure a biphasic composition of HA and β -TCP. Finally, 1100 °C is the maximum calcination temperature to avoid the formation of α -TCP.

Theoretically, the final phase composition after a complete reaction (meaning there is no longer a change in phase composition after continued calcinations) can be predicted using the Ca:P ratio of the starting powder blend. The main idea behind this calculation is that Ca and P are non-volatile, so the amount contained in the precursor powders should not change during the reaction. XRD analysis reports the weight percentage (wt-%) of all phases present in the material, which are multiplied by the total sample weight to calculate the weight of each phase. The weight is converted to moles by dividing it by the molar mass. Finally, the moles

of Ca and P ions are computed for each phase, summed, and the Ca:P ratio is computed. To predict the final phase composition of the powder, this calculation is reversed.

An example Ca:P calculation for a 100 g sample with a phase composition of 90 wt-% HA and 10 wt-% β -TCP is shown below in Table 3.3. The molar mass of β -TCP is 310.1767 g/mol, and the molar mass of HA is 502.3114 g/mol. The chemical formula for β -TCP is β -Ca₃(PO₄)₂, so each mole contains 3 moles of Ca ions and 2 moles of P ions. The chemical formula for HA is Ca₅(PO₄)₃OH, so each mole contains 5 moles of Ca ions and 3 moles of P ions. The total moles of Ca for this sample is 0.0967 + 0.896 = 0.9927 mol Ca, and the total moles of P is 0.0645 + 0.5376 = 0.6021 mol P. Thus, the Ca:P ratio is 0.9927/0.6021 = 1.65.

Table 3.3 Example calculation of the number of moles of Ca and P in a 100 g sample which is 90 wt-% HA and 10 wt-% β -TCP.

β-TCP Calculation	HA Calculation
$100\text{ g} * 0.1 = 10\text{ g}$	$100\text{ g} * 0.9 = 90\text{ g}$
$\frac{10\text{ g}}{310.1768\text{ g/mol}} = 0.0322\text{ mol}$	$\frac{90\text{ g}}{502.3114\text{ g/mol}} = 0.1792\text{ mol}$
$3 * 0.0322\text{ mol} = 0.0967\text{ mol Ca}$	$5 * 0.1792\text{ mol} = 0.896\text{ mol Ca}$
$2 * 0.0322\text{ mol} = 0.0645\text{ mol P}$	$3 * 0.1792\text{ mol} = 0.5376\text{ mol P}$

The calculation does not accurately predict the final phase composition of the material; there is a drift in the final Ca:P ratio (and thus, the final phase composition) from what is predicted. The assumption that Ca and P are non-volatile is not entirely true, which is why an offset (determined empirically) is needed to account for the change in Ca:P ratio which occurs at some point in the reaction. For the purpose of this discussion, this phase diagram will be used as the reference. So an offset refers to a shift on this phase diagram. The environment and processing steps at RMS result in a rightward shift on the phase diagram. The processing steps in our work, however, result in a leftward shift on the phase diagram. The source of this drift is currently under investigation in the literature, and should be determined empirically for specific raw powders and lab environments. Colleagues at RMS currently hypothesize that the drift is a result of PO₄ evaporation. Several factors are suspected to influence the amount of

drift including initial phase composition, type and duration of milling, atmosphere exposure, and furnace position.

To obtain specific biphasic CaP composition through thermal treatment, the bulk Ca:P ratio of the final powder must be tightly controlled. The final phase composition is sensitive to the Ca:P ratio; small changes in the ratio of starting powders will lead to several percentage changes in the final phase composition. An example is outlined in Table 3.4, where a 0.5 g increase in the amount of di-calcium carbonate powder shifts the final phase composition by about 5%.

Table 3.4 Example of the theoretical calculation of the final phase composition. For a 0.5 g increase in CaHPO₄ in the starting powder, the final phase composition shifts by ~ 5%.

	Starting Powder	Mass (g)	Ca:P Ratio	Predicted Phase Composition
Blend #1	CaCO ₃	15.6	1.695	63.4 wt-% HA, 35.57 wt-% β-TCP
	CaHPO ₄	35		
Blend #2	CaCO ₃	15.6	1.597	58.3 wt-% HA, 41.7 wt-% β-TCP
	CaHPO ₄	35.5		

In this work, four main parameters affected the final phase composition of the powder: 1) ratio of the precursor powders, 2) calcination temperature, 3) calcination time, and 4) ball milling parameters. Ball milling is also critical to ensure the proper phase composition. In fact, powder with different CaP phases react differently to ball milling [86]. Adzila et al. found that an increased milling speed resulted in a decrease in the fraction of HA in the final powder blend [89]. Further, if the two powders are not well mixed, the reaction between di-calcium phosphate and calcium carbonate to form HA and β-TCP cannot take place. In fact, small traces of intermediate phases such as CaO (lime) and β-Ca₂P₂O₇ (β-CPP) can form. A CaO phase in the final powder will increase the pH beyond acceptable levels when implanted *in vivo*. Improving the blending process and increasing calcination time will ensure a complete reaction.

The procedure defined by collaborators at RMS was first employed, and then adjusted empirically to achieve a final phase composition in the range of 80-95 wt-% HA and 5-20 wt-% β -TCP which has been used in previous studies with these scaffolds [12], [22], [45], [98]–[102]. Theoretically, a blend of the starting powders with a Ca:P ratio in the range of 1.642-1.658 would result in a final powder with a phase composition in this range. However, a powder blend with a Ca:P ratio of 1.69 resulted in a suitable biphasic composition. A negative offset of -0.04 was required in this application to predict the final phase composition of the powders after thermal treatment.

The specific steps to create a batch of powder are outlined in Appendix A. Briefly, di-calcium carbonate and calcium carbonate are blended and calcined in three cycles. Ball milling was performed between each calcination. Since the SSA needs to remain high, a lower calcination temperature (1050 °C) was used with long calcination times (60 total hours) relative to colleagues at RMS. The diffusion mechanisms are different at lower temperatures, and a lower temperature will induce less grain growth. 60 total hours of calcination at 1050 °C were divided into three segments: 10, 20 and 30 hours. An 8 hour ball mill was performed between each calcination.

The thermal treatment outlined above and the ball milling parameters listed in Table 3.2 produced a ceramic powder that satisfies all requirements in Table 3.1. The powder batch has small (<2 μm), monosized particles with few agglomerates (Figure 3.3), and has a phase composition in the desired range (Table 3.1). Powder satisfying these requirements is now suitable for the formation of a colloidal ink for extrusion.

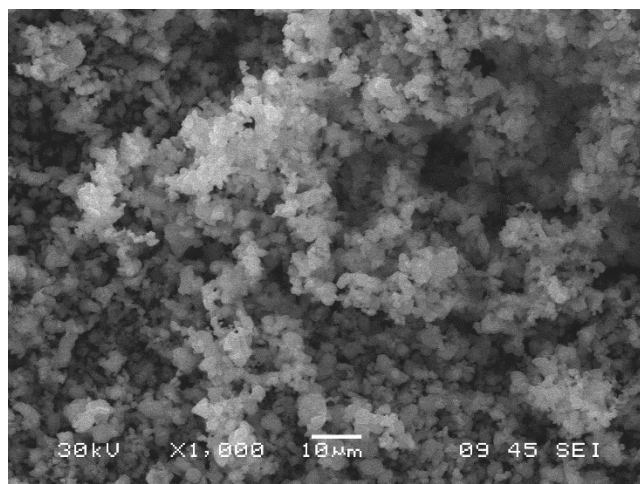


Figure 3.12 SEM image of the final powder blend after heat treatment and ball milling. The particles are sufficiently small (~1-2 μm) and have a tight PS distribution.

3.3.2 Stabilization of Colloidal HA Ink

A stable suspension was prepared by mixing deionized water and a dispersant (Darvan 821A, a 40 wt-% ammonium polyacrylate solution). Polyacrylates are homopolymers which employ electrosteric stabilization to ensure stability of the colloidal ink. 5M Ammonium Hydroxide (HN_4O_4), a basic solution used to increase pH, is added to the suspension to maintain a pH of 10. At this pH, the polymer species are fully ionized. The processed HA powder is added to the solution in three aliquots and the solution is sonicated between each addition to ensure sufficient mixing.

The suspension must have a powder solids loading in the 50-65 vol% range (Section 3.2.3). To achieve this, the fluid must be removed after suspension stabilization. The suspension was placed in a centrifuge for one hour at 2000 rpm to separate the fluids and colloid, and concentrate the ink to the optimal solids loading.

3.3.3 Rheological Adjustments

In this work, hydroxypropoyl methylcellulose (Methocel F4m) was the binder used as the viscosifying agent. Methocel is a carbohydrate polymer which dissolves in water by swelling and subsequent hydration. There is a time delay with hydration and subsequent viscosity increase, which is a function of surface level treatment, temperature, and pH [103].

The addition of a base to raise the pH reduces this time delay and results in a faster hydration. Further, after the addition of Methocel, agitation was continued until full viscosity was reached.

3.3.4 Fluid to Gel Transition of HA Colloidal Ink

Here, polyethylenimine (PEI) was used as the gelling agent since the positively charged amine groups along the PEI backbone interact with the negatively charged carboxylic acid groups of the polyacrylic dispersant. As a result, the attractive forces between particles strengthened, and the pH decreased. In this work, the maximum elasticity occurred when the ratio of gelling agent to dispersing agent was 1:2, with little further increase in elasticity at higher PEI additions [83].

In summary, a stable suspension of powder, water, and Darvan C dispersant was first created. Then, Methocel F4M was added to increase viscosity. Finally, ink was gelled by adding PEI as a flocculant. The specific steps to create HA powder and ink are outlined in Appendix A.3 and A.4.

3.4 Post Processing Scaffolds

After deposition, the scaffolds dry in air and are removed from the substrate. In order to tailor the microstructure and achieve a high density, the ceramic green bodies are then sintered at high temperatures (1100 °C – 1300 °C). This temperature range promotes HA densification without decomposition, and avoids formation of α -TCP [104].

In summary, this chapter reviewed colloidal science principles to illustrate how concentrated colloidal inks are made for scaffold fabrication. The processing steps required to modify the precursor powders to have the desired physical and chemical compositions were outlined.

Chapter 4

System model and control strategies

The major challenge addressed in this chapter is providing relatively high-performance motion control with a “low” performance system, while maintaining the constraint of ease of use. Motion control involves system modeling, disturbance rejection, and control design. In this work, each of these topics were addressed and implemented in a way that someone outside of the controls field would understand. Chapter 4 is organized as follows. First, the development of linear models for each axis is presented. The physical phenomena that acted as disturbances to these linear models and methods incorporated to reject these disturbances are discussed. Further, motion control strategies implemented on each axis using the system models are outlined. Two additional motion control techniques are presented: a simplified iterative learning controller to improve tracking performance for repeated trajectories, and a pressure regulation algorithm to reduce the amount of ink buildup during axis transitions. The performance of these controllers for bone scaffold fabrication is tested and discussed in Chapter 6.

4.1 System Identification

System identification is a methodology to develop mathematical models of dynamical systems based on observed data from physical systems. A general definition of a system is an object in which variables interact and produce observable signals [105], which are typically called system outputs. External stimuli including inputs (signals that can be manipulated by the user) and disturbances, affect system behavior. When interacting with a system, it is useful to know how these signals are related to maintain sufficient control of the system output [105]. An assumed relationship between the inputs and outputs is called the system model. A common route to develop system models is system identification: a methodology to develop mathematical models of dynamical systems using the system’s input and output signals. There

are numerous system identification techniques, but each technique has three basic entities [105]:

1. *The data.* Input and output signals are measured from the system in the frequency or time domain.
2. *Model selection.* Based on the type of system, a mathematical model is chosen. The measured data is used to estimate parameters in a given model structure.
3. *Model validation.* Model quality is typically validated by comparing the model response to the measured system output.

System identification requires that the measured data and model structure capture the important dynamics of the system since system identification cannot fully capture the dynamics of physical systems [105]. Instead, the model is an idealization of system behavior, and the complexity of such a model depends on the application.

In application, most physical systems behave nonlinearly to some degree. Nonlinear models, however, are complex and add significant complexity to motion control. Instead, linear models are commonly employed since it is often assumed that the system dynamics are approximately linear within the working region.

4.1.1 Plant Dynamics

Each axis of the three-axis cartesian robot was assumed to be completely decoupled from the others. Further, each axis was modeled as a second-order sliding mass system:

$$m\ddot{x} + b\dot{x} = F_u + F_{dist}, \quad (4.1)$$

where x is the axis position, m is the axis mass, b is viscous damping, F_u is the thrust force generated from the motors, and F_{dist} is the lumped disturbance force. Here, b was assumed to equal 1 to simplify system identification. This assumption will be addressed later in this chapter. The force output of the motor (F_u) was modeled as:

$$F_u = K_m u, \quad (4.2)$$

where K_m is the gain of the mechanical system and u is the control input.

4.1.2 System Disturbances

The axes suffer from several unknown position-dependent disturbances (F_{dist}). For control design, removing disturbances before performing system identification is critical to ensure that the model captures the system dynamics. The disturbances on each axis of the DW printer were likely to come from three main sources: coulombic and viscous frictional forces, force ripple, and cog forces. This work only considered friction since the others are beyond the scope of a user-friendly motion control platform. In addition, the effect of gravity was identified for Z-axis compensation.

4.1.2.1 Friction compensation

Friction is defined as the tangential reaction force between two surfaces in contact, and can arise from many mechanisms, which depend on factors such as contact geometry, topology, surface properties, and lubrication [106]. Feedforward friction compensation methods supplement the control effort to make each axis behave more like an ideal linear plant, speed up the response during velocity reversals, and reduce tracking error [107]. These methods can be divided into model based and non-model based friction compensation. Since it is very difficult to construct general friction models from physical first principles [106], this work utilized a non-model based friction method, which aimed at identifying the essential phenomena relevant to improve axis performance.

A simple and non-model based technique to eliminate some effects of friction is the use of a dither signal, which is a high frequency mechanical signal added to the control signal to modify system behavior by smoothing velocity reversal [108]. Dither signals can be applied in the normal or tangential directions of motion; tangential dither modifies frictional influences by averaging their effect, while normal dither changes the friction coefficient [108].

In this work, a method similar to dither was employed: feedforward friction terms were added to the control input to smooth the discontinuous effects of friction at low velocities. The effect of this friction compensation method was that it introduced additional forces such that the total applied force to the system was larger than the static friction at velocity reversals.

The simple algorithm, based on the sign of the commanded velocity, v , employed in this work was characterized by:

$$u_{ff} = c_{pos} + b_{pos} * v, \quad v > 0 \quad (4.3)$$

$$u_{ff} = c_{neg} + b_{neg} * v, \quad v < 0 \quad (4.4)$$

where u_{ff} is the feedforward control effort, c_{pos} and c_{neg} are the coulombic friction constants, and b_{pos} and b_{neg} are the viscous friction constants. The coulombic and viscous friction parameters were identified by commanding a range of control inputs and recording the corresponding average axis velocities, generating a figure similar to Figure 4.1. In a plot of the control effort vs. average velocity (Figure 4.1), the y-intercepts were the coulombic friction constants and the slopes were the viscous friction coefficients.

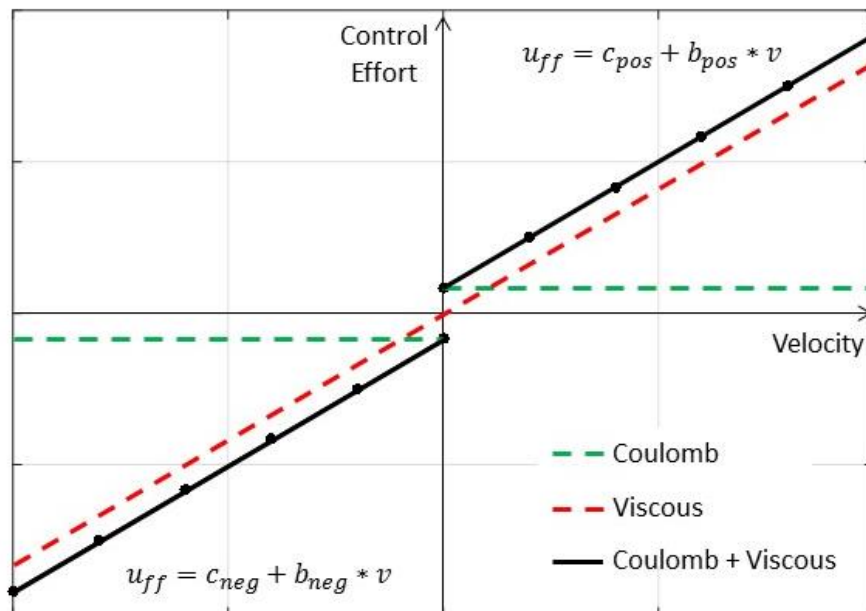


Figure 4.1 Control effort plotted as a function of velocity for sliding friction compensation. The black dots represent an example of data points collected by commanding a range of control inputs and recording the corresponding axis velocity.

4.1.2.2 Identification of Feedforward friction gains

In SoftMotion, the user cannot choose or modify control inputs since SoftMotion operates in closed-loop and the control output is embedded within the module itself. Thus, to perform this friction identification method in SoftMotion, each axis was commanded to move

at a certain velocity using a Straight Line Move Express VI, and a Read Express VI was used to record the Drive Command sent to the axis. This method was implemented on each axis, and the results are shown in Figures 4.2 and 4.3. In Figures 4.2 and 4.3, the slopes were zero, indicating that coulombic friction was the main friction component and that viscous friction was negligible. Thus, the feedforward friction compensation was simply a constant that depended on the sign of the commanded axis velocity. As a note, the data presented in Figure 4.3 were collected with the Z-axis motor and ball screw positioned horizontally to remove the effect of gravity (Figure 4.4).

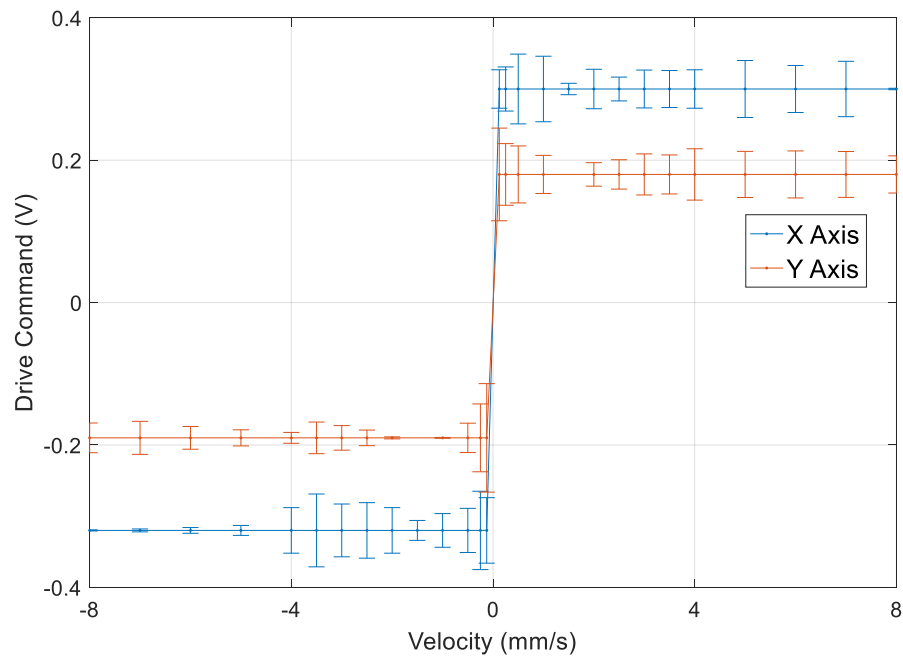


Figure 4.2 Friction compensation results for the X and Y-axes.

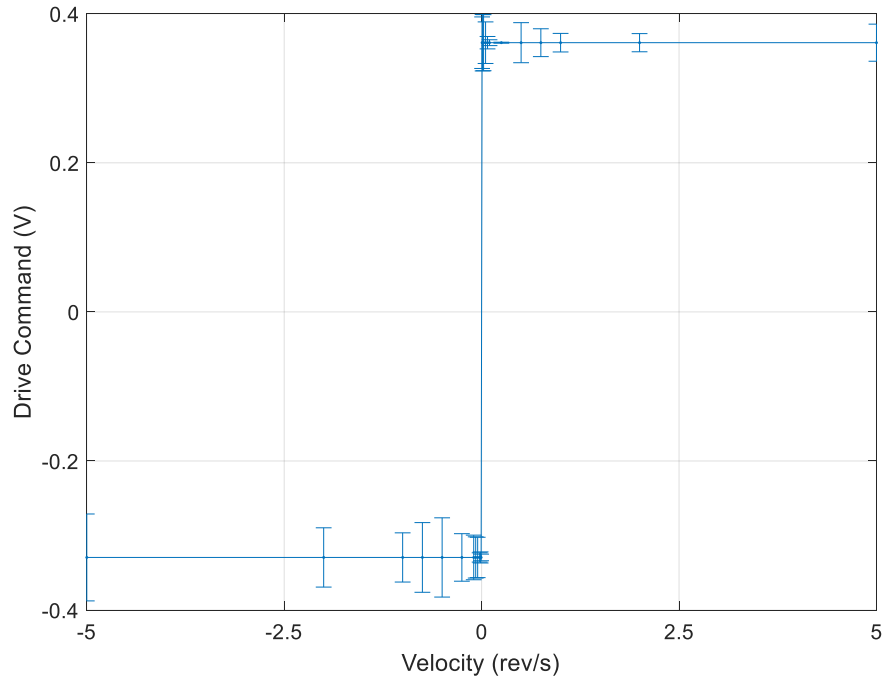


Figure 4.3 Friction compensation results for the Z-axis.

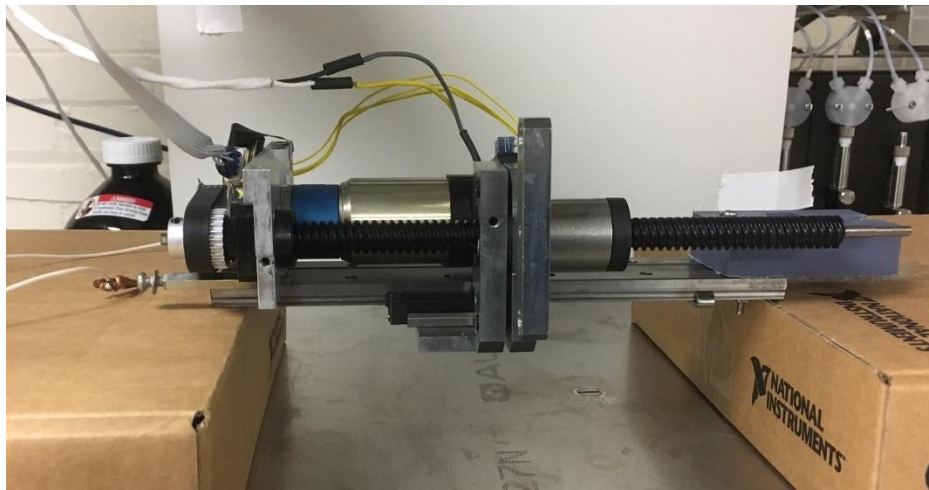


Figure 4.4 The Z-Axis positioned horizontally to remove the effects of gravity during friction compensation.

4.1.2.3 Friction Compensation Implementation

To implement the feedforward friction compensation in the restricted SoftMotion control environment (Figure 4.5), the outer loop involving Commanded Velocity (CV) was

used, which is highlighted by a dashed red line. Using the SoftMotion nomenclature, Equations (4.3) and (4.4) and were written as:

$$u_{ff} = V_{ff} * Sgn(CV), \quad (4.5)$$

where $V_{ff} = V_{ffp}$ if CV was positive and $V_{ff} = V_{ffn}$ if CV was negative. Thus, the product of the axis velocity (CV) and the feedforward gain (V_{ff}) was the feedforward term. The magnitude of V_{ffp} and V_{ffn} were chosen based on the axis CV to ensure that u_{ff} was slightly larger than the identified coulombic friction components c_{pos} or c_{neg} to exceed the static friction level. Table 4.1 lists the friction compensation results for each axis. The feedforward gains were set as axis parameters, and switch between V_{ffp} and V_{ffn} based on the direction of movement.

It was evident that other types of friction exist, such as pre-sliding friction. A Dahl friction model [109], [110] could be used to analyze these data, but this was beyond the scope of an easy-to-implement friction compensation model. Due to the restrictions on the feedforward terms in SoftMotion, the only type of friction compensated for here was coulombic, which was sufficient for the target application.

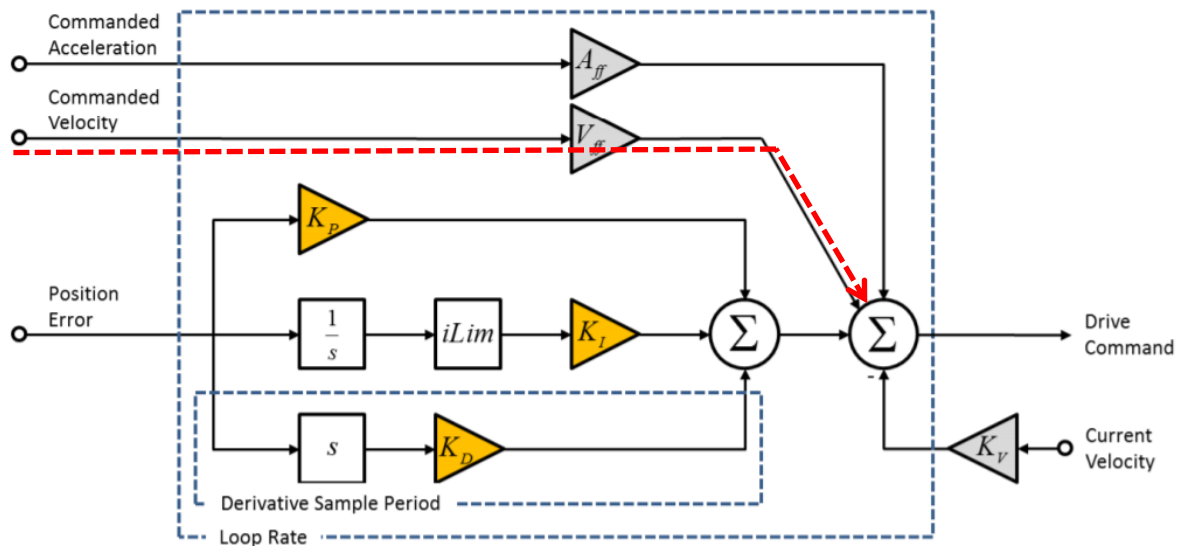


Figure 4.5 PID plus Feedforward control loop embedded in the NI 9514 modules.

Table 4.1 Identified coulombic friction parameters for each axis.

Axis	c_{pos}	c_{neg}	u_{ffp}	u_{ffn}
X	0.30	-0.32	0.31	-0.33
Y	0.18	-0.19	0.19	-0.20
Z	0.36	-0.33	0.37	-0.34

4.1.2.4 Gravity Compensation

Gravity affected the performance of the Z-axis; the same control effort resulted in different behavior for the positive and negative directions. For gravity compensation, a one revolution, square wave signal was sent to the Z-axis ball-screw drive system oriented horizontally (Figure 4.4). Next, the same square wave signal was sent to the Z-axis oriented vertically, and the V_{ff} gain was increased until the behavior was deemed similar. Results are shown in Figure 4.6, where the experimental protocol was as follows: move down, up, down, up. The blue line is the Z-axis position data when the carriage was oriented horizontally; the positive and negative direction movements were similar since gravity was eliminated. The red curve is the Z-axis position data when the axis is positioned vertically without a gravity compensation offset. At roughly 12 seconds the Z-axis oriented vertically moves only a quarter of the amount of the horizontally oriented axis (highlighted by a red dashed oval). Ideally, the vertical Z-axis behavior with a gravity compensation offset matched the horizontal behavior. A value of 0.04 Vs/mm was determined to be sufficient for the gravity offset, since increasing beyond this value did not result in an improvement of the position control. This value was added to the Z-axis friction compensation value V_{ffp} to increase the feedforward input.

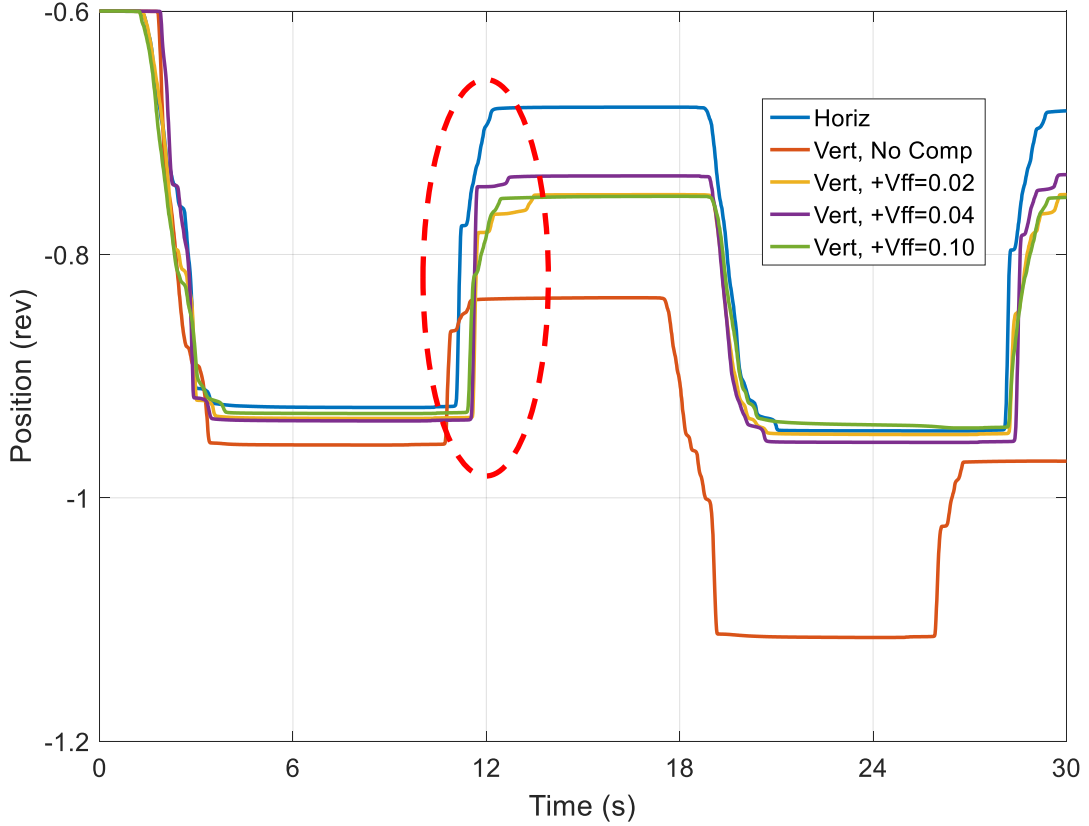


Figure 4.6 Gravity offset determination.

4.1.3 Plant Models

The true behavior of cartesian axes are more accurately represented with complicated nonlinear models. In this application, however, each axis was assumed to have dominantly linear dynamics. After the main disturbances (F_{dist}) were removed via friction compensation, the dynamics of the linear model were identified. Plugging Equation (4.2) into Equation (4.1) with F_{dist} removed, and taking the Laplace transform, the system model for each axis was:

$$G(s) = \frac{P(s)}{U(s)} = \frac{K_m}{\tau_m s^2 + s}. \quad (4.6)$$

With this assumed model structure, each axis was characterized by the steady-state gain (K_m), and the mechanical time constant (τ_m). Equation (4.6) represents the transfer function that relates the axis position to control input. For simplicity, it was assumed that the motor

driver and its internal current control loop were a part of each axis model. Thus, the identified model represents the relationship between axis position and the drive command from the controller.

4.1.4 System Identification Techniques

The SoftMotion environment limited the choice of system identification techniques since the Drive Command must be implemented in closed-loop, eliminating the use of any commonly used open-loop system identification methods. Thus, to operate in closed-loop, the gains in the inner feedback loop (K_P , K_I , and K_D) must be set during system identification. To simplify the closed-loop method, only K_P was used and K_I and K_D were set to 0.

4.1.4.1 Logarithmic decrement method

The model parameters of each axis were identified through the logarithmic decrement system identification technique, in which the time-domain response to a step input of an underdamped system was analyzed to determine model parameters [111], [112]. In this work, the only experimental data required was the axis position. The identified V_{ff} gains were included to remove friction and isolate the plant model. Further, the viscous damping term (b) was set to 1 to simplify the system model and system identification technique.

While the ultimate goal was to identify K_m and τ_m , the standard second-order system parameters (damping ratio and damped natural frequency) were first computed using well-established formulae. The model parameters were then computed by matching coefficients between the expected system model and the standard form of a second-order underdamped system. The logarithmic decrement δ of an oscillatory response was used to find the damping ratio, which defines how a system response decays over time [113]. To enable a highly oscillatory response to a step input, the proportional gain of the closed-loop architecture (K_P) was set to a value that caused the axis to oscillate before reaching a steady state value. The logarithmic decrement, δ , is defined as the natural log of the ratio of the amplitudes of any two successive peaks as in Equation 4.7:

$$\delta = \frac{1}{n} \ln \left(\frac{x(t)}{x(t+nT)} \right), \quad (4.7)$$

where $x(t)$ was the amplitude at time t , and $x(t+nT)$ was the amplitude n peaks away. A larger n value was desirable since it provided more information, resulting in a more accurate system model. Thus, K_p was increased to give at least three to four oscillations. The damping ratio was then defined as:

$$\delta = \frac{1}{\sqrt{1 + \left(\frac{2\pi}{T}\right)^2}}, \quad (4.8)$$

where T is the average time in seconds between successive peaks. δ was used to find ω_d and ω_n :

$$\omega_d = \frac{2\pi}{T} \quad (4.9)$$

$$\omega_n = \frac{\omega_d}{\sqrt{1 - \zeta^2}} \quad (4.10)$$

The system gain and time constant were then computed (Equations 4.11 and 4.12).

$$\tau_m = \frac{1}{2\zeta\omega_n} \quad (4.11)$$

$$K = \omega_n^2 \tau_m \quad (4.12)$$

To calculate the motor gain K_m , the system gain K was divided by the closed-loop gain K_p . For implementation in the SoftMotion environment, a step input was commanded to each axis using a Straight Line Move Express VI. The corresponding position was recorded via the Read Express VI. An example of this method is shown in Figure 4.7 for the X-axis. This experiment was repeated multiple times for each axis, and the system parameters for each trial and the average values are reported in Tables 4.2 - 4.4.

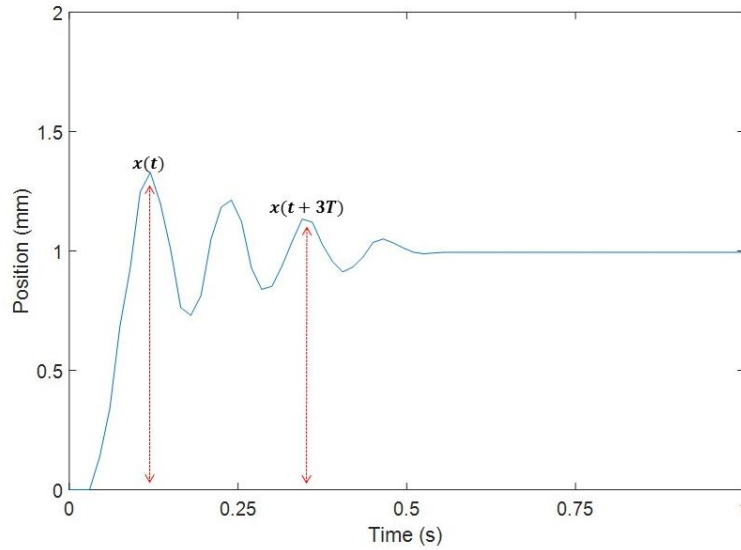


Figure 4.7 Logarithmic decrement system identification method implemented on the X-Axis.

Table 4.2 Model parameters from system identification tests for the X axis.

System Model	Trial	K_m	τ_m
$\frac{K}{\tau s^2 + s}$	1	12.01	0.083
	2	12.09	0.083
	3	10.79	0.080
	4	10.76	0.070
Average		11.50	0.080

Table 4.3 Model parameters from system identification tests for the Y axis.

System Model	Trial	K_m	τ_m
$\frac{K}{\tau s^2 + s}$	1	15.41	0.030
	2	19.14	0.032
	3	17.57	0.036
	4	16.09	0.044
Average		20.80	0.034

Table 4.4 Model parameters from system identification tests for the Z axis.

System Model	Trial	K_m	τ_m
$\frac{K}{\tau s^2 + s}$	1	38.90	0.049
	2	50.13	0.048
	3	38.93	0.047
	4	36.26	0.048
Average		41.05	0.048

4.1.4.2 Model Validation

The average K_m and τ_m for each axis were used in the assumed linear model structure and implemented in a Simulink block diagram. For model validation, a step response in simulation was compared to experimental data. For the X and Y axes, a 5 *mm* step input was used for the X and Y axes and a 0.5 *rev* step input was used for the Z axis. Despite friction compensation, the simulated linear system model did not fully capture the dynamics of the experimental system. Further, the experimental results showed that each axis had a pure time delay, which was either a plant delay or an actuator delay. An actuator delay results from a delay in transmitting the controller output to the plant. Despite the source, the delay was included in the system model since the motor drivers were included in the system model for simplicity.

The logarithmic decrement system identification technique was employed to try and fit experimental data to a linear model. Each of the axes, however, were nonlinear and some of the model discrepancy may have been due to nonlinear damping. To compensate for some of the nonlinear damping and improve the system model, Equation (4.6) was modified to include the damping term, b (Equation (4.13)) instead of assuming $b = 1$ (an assumption discussed in Section 4.1.1) and a time delay, τ_d .

$$G(s) = \frac{P(s)}{U(s)} = \frac{K_m e^{-\tau_d s}}{\tau_m s^2 + bs}, \quad (4.13)$$

For model improvement, the same K_m and τ_m values were used, but the damping term and time delay were incrementally increased until the simulated model sufficiently matched the experimental data. A small damping term and a time delay resulted in valid system models (Figures 4.8 - 4.10), and the numerical values identified for each axis are listed in Table 4.5.

While the linear viscous term cannot account for all of the nonlinear damping, feedback and feedforward control (Section 4.2) can account for any remaining uncertainty. The slight software delay was accounted for by trajectory planning since in this application only one axis moved at a time.

Table 4.5 System identification results, which match between experiment and simulation, for each axis.

System Model	Axis	K_m	τ_m	b	τ_d
$\frac{K_m e^{-\tau_d s}}{\tau_m s^2 + bs}$	X	11.50	0.080	2.440	0.050
	Y	20.80	0.034	2.900	0.035
	Z	41.05	0.048	5.2	0.043

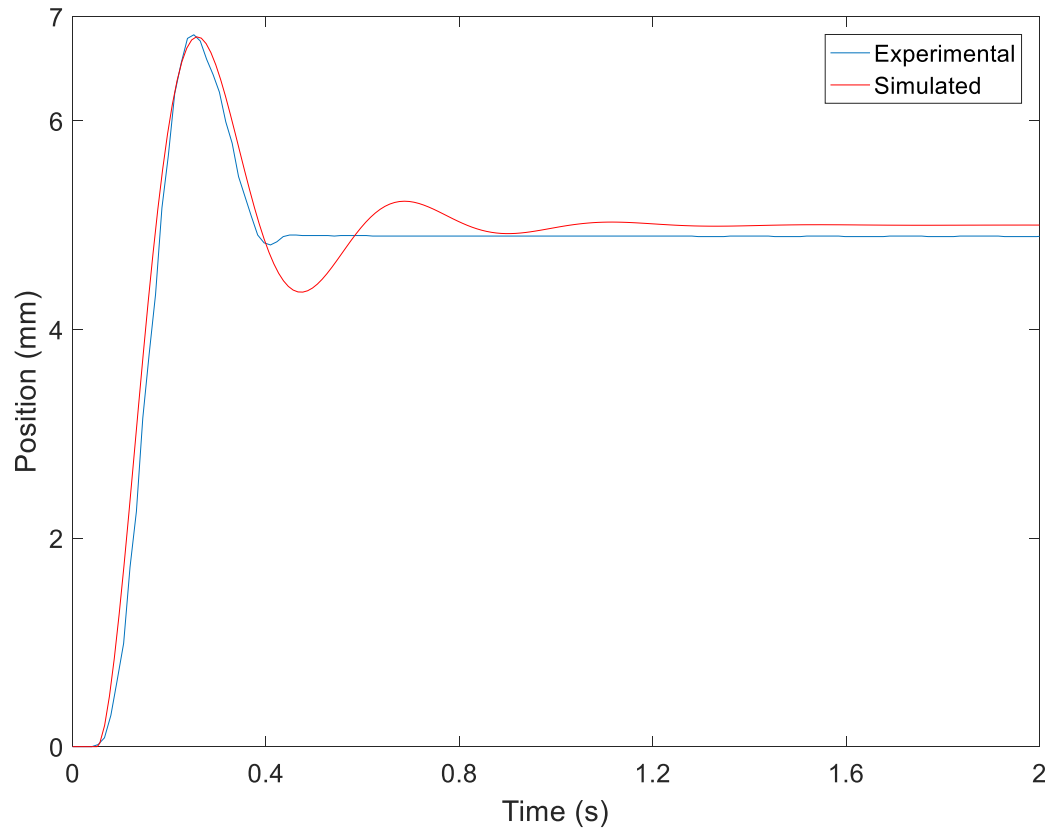


Figure 4.8 Step response for X-axis model validation.

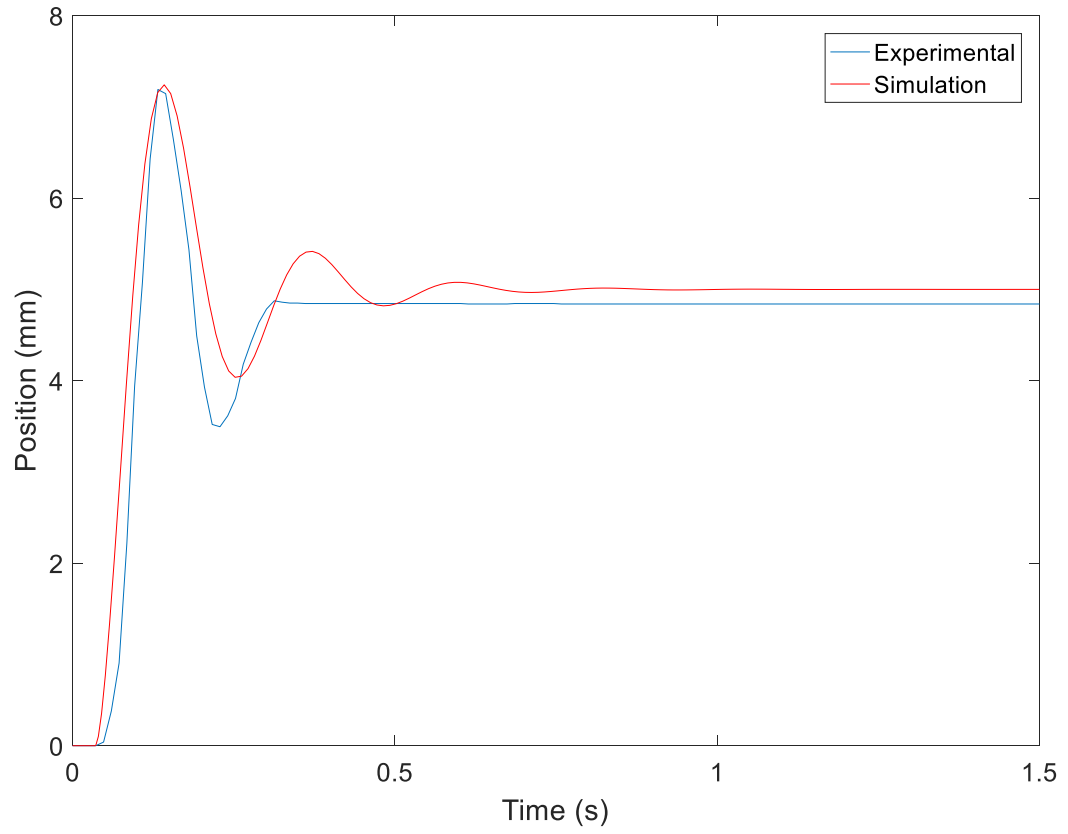


Figure 4.9 Step response for Y-axis model validation.

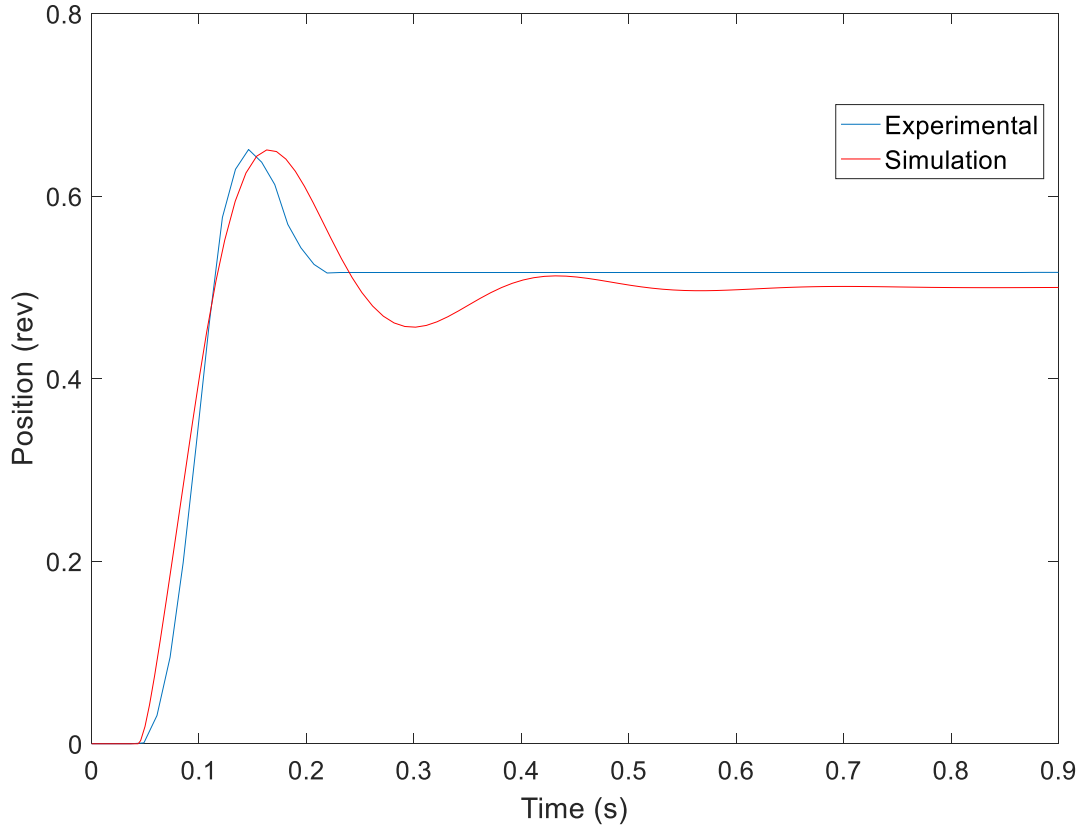


Figure 4.10 Step response for Z-axis model validation.

4.2 Control Architecture

In addition to the quality of the colloidal ink, a properly tuned control algorithm was necessary to fabricate bone scaffolds with the desired precision. The control architecture implemented in this work includes three parts: 1) a feedback controller tuned by pole placement; 2) a feedforward friction compensation (discussed in Section 4.1.2); and 3) an Iterative Learning feedforward controller. A constraint on the control architecture was to minimize the number of tuning parameters. Based on anecdotal evidence from collaborators in other fields, it was determined that a maximum of 5 parameters should be available to the end-user.

As with model development, control design assumed the axes were dynamically decoupled. The same control strategy was developed and implemented on all three axes.

4.2.1 Feedback Controllers

The SoftMotion control environment dictated the controller design employed in this work since the PID + Feedforward control loop (Figure 4.5) was embedded within the NI 9514 modules. The feedforward compensation was employed in Section 4.1.2. This section will discuss the PID feedback loop, which used the real-time encoder readings to ensure axis stability and increase disturbance rejection.

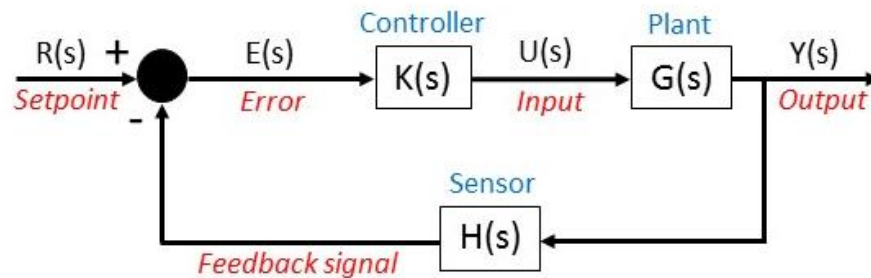


Figure 4.11 Illustration of a feedback diagram used for reference tracking.

A classical tracking configuration diagram is illustrated in Figure 4.11. In positioning system applications, reference tracking involves steering the axes to a location specified by the end user. Thus, in this work, the goal was to design a controller that followed an external reference as well as possible. The feedback diagram components for the XYZ positioning platform in this work are listed below:

System Components

- $K(s)$ = controller. The controller structure was embedded in the NI 9514 modules and is illustrated in Figure 4.5.
- $G(s)$ = plant. The plant refers to an axis. A separate feedback diagram was designed for each axis.
- $H(s)$ = sensor. In this application, the sensor was an encoder to measure the axis position.

Signals

- $R(s)$ = setpoint. The target axis position in mm.
- $Y(s)$ = system output. Refers to the actual axis position in mm.

- $E(s)$ = error. This signal was computed as $R(s)-Y(s)$ and was used as the controller input.
- $U(s)$ = plant input. The manipulated variable, calculated using $U(S) = E(S)*K(s)$ and which depended on the controller structure, $K(s)$.

The error between the set point and feedback signal was fed into the PID control structure. The three terms of a PID controller include proportional, integral, and derivative terms. In general, the P term is proportional to the error via the gain K_p , and the I term continually sums the error over time and is proportional to the integral of the error via K_I . The D term adds control input based on the derivative of the error signal times the derivative gain, K_D . Derivative action, however, amplifies noise in the sensor output, resulting in chatter and potential instability in the controller output. The consequence of a sensor output that repeatedly changes from a rapidly increasing slope to a rapidly decreasing slope is a series of derivative terms with large and alternating values. For this application, instead of applying a filter to the sensor outputs, a PI controller was employed ($K_d = 0$), which was adequate for this application. As a result, the PID loop only had two tuning parameters to adjust.

The sum of the P and I terms was the control input to the plant, a voltage command. The transfer function of a PI controller is

$$C_{PI}(s) = K_P + \frac{1}{s} K_I = \frac{K_P s + K_I}{s}. \quad (4.14)$$

The closed-loop transfer function can be computed using Equations (4.13) and (4.14), giving Equation (4.15)

$$H(s) = \frac{C_{PI}(s)G(s)}{1 + C_{PI}(s)G(s)} = \frac{K_m(K_P s + K_I)}{(\tau_m s^3 + b s^2) e^{\tau_d s} + K_m(K_P s + K_I)}. \quad (4.15)$$

Equation (4.15) demonstrates that the closed-loop system's gain and pole locations can be modified through tuning of the PI gains. Tuning a control loop involves the adjustment of the control parameters to the optimal values to achieve the desired system response. The pole location corresponds directly to the eigenvalues of the system, which dictate the system

response. The pole locations were placed in the left half plane to ensure stability, and the PI gains were further modified to achieve desired performance specifications.

Root locus design was used to determine the controller parameters for each axis. The root locus diagram plots the closed-loop pole trajectories in the complex plane as the system gain varies. Sisotool in MATLAB was used to move the controller zero and gain to achieve the desired closed-loop response, given some design criteria. Stability was a basic requirement, but beyond that specific design requirements imposed include a maximum overshoot of 10% and a settling time less than 1 second.

Before testing the controllers on the experimental system, the closed-loop response was analyzed in simulation using MATLAB Simulink. The resulting controllers are reported in Table 4.6. In addition, the controller performance was validated by implementing the K_p and K_i gains on each axis (Figures 4.12 - 4.14). The step input is shown as a dashed red line and the settling time is indicated by a dashed green line. All three plots have an overshoot less than 10%, and a settling time less than one second.

Table 4.6 PI controllers designed in simulation using the system models for each axis.

Controller form	Axis	K_p	K_I
$C(s) = \frac{K_p s + K_I}{s}$	X	1.462	0.166
	Y	1.550	0.280
	Z	1.400	0.200

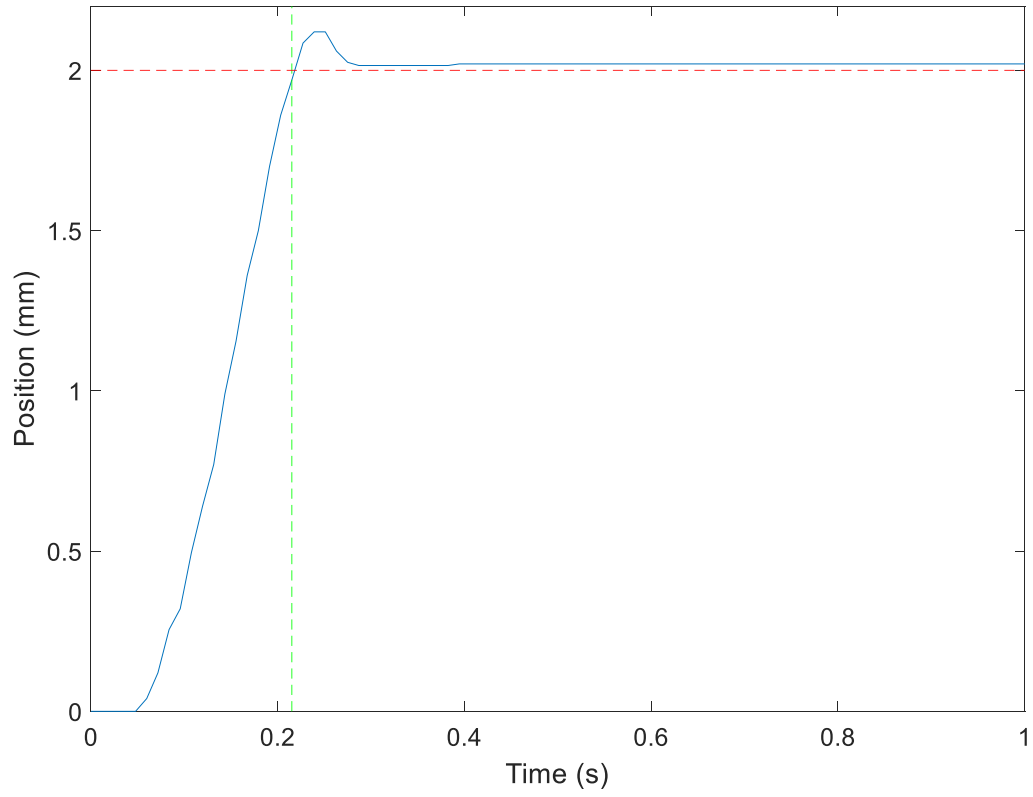


Figure 4.12 Performance of the X axis to a 2 mm step input with the designed PI controller implemented.

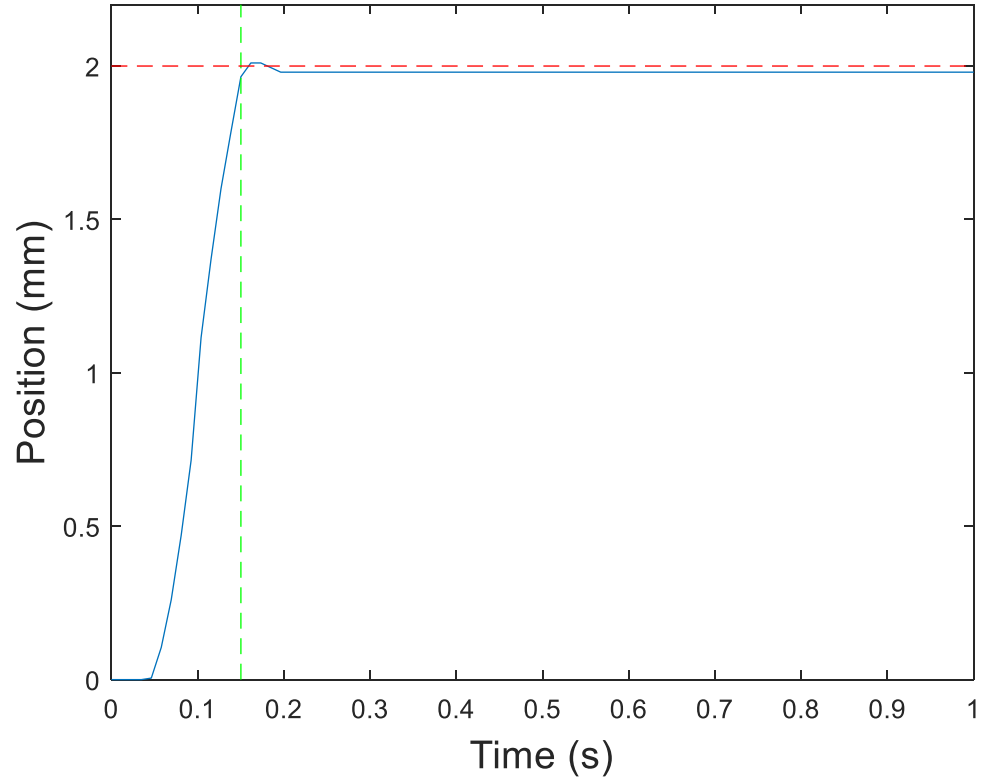


Figure 4.13 Performance of the Y axis to a 2 mm step input with the designed PI controller implemented.

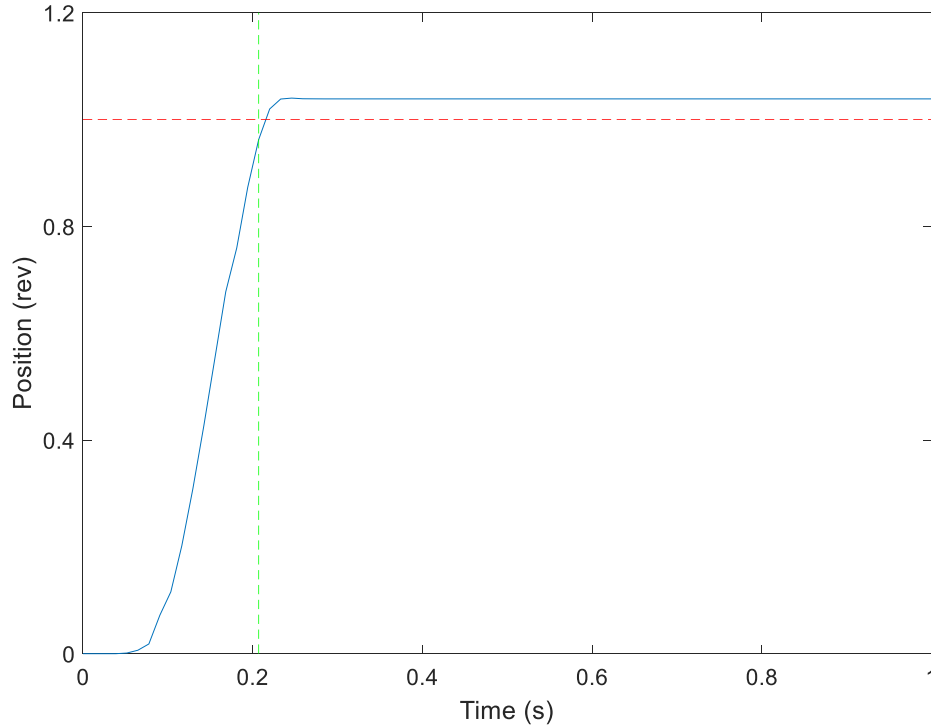


Figure 4.14 Performance of the Z axis to a 1 rev step input with the designed PI controller implemented.

As illustrated in the above figures, the tuned PI gains were adequate for small step inputs. During bone scaffold fabrication, however, the axes moved at much slower speeds and tracked larger references. Thus, a higher controller gain was required to achieve a faster response and better disturbance rejection during the slower moves. With a higher gain, the integral gain was reduced to avoid vibrations and instability. The simulated PI gains were hand tuned on the experimental system to ensure each axis was sufficiently tracking the reference during bone scaffold fabrication. The resulting PI gains for printing operation are listed in Table 4.7.

To simplify future modifications by the end-user, Figures 4.15 - 4.17 include a region of acceptable PI gains for each axis. The PI gains chosen for operation are indicated by an asterisk. Remaining inside the region highlighted in red, yellow or blue will ensure a stable response. In general, axis chatter was more sensitive to changes in the integral term than the proportional term. These maps serve to limit the gains entered by the end-user.

Table 4.7 PI controllers designed for printing operation for each axis.

Controller form	Axis	K_P	K_I
$C(s) = \frac{K_P s + K_I}{s}$	X	16.0	0.14
	Y	6.00	0.20
	Z	18.0	0.16

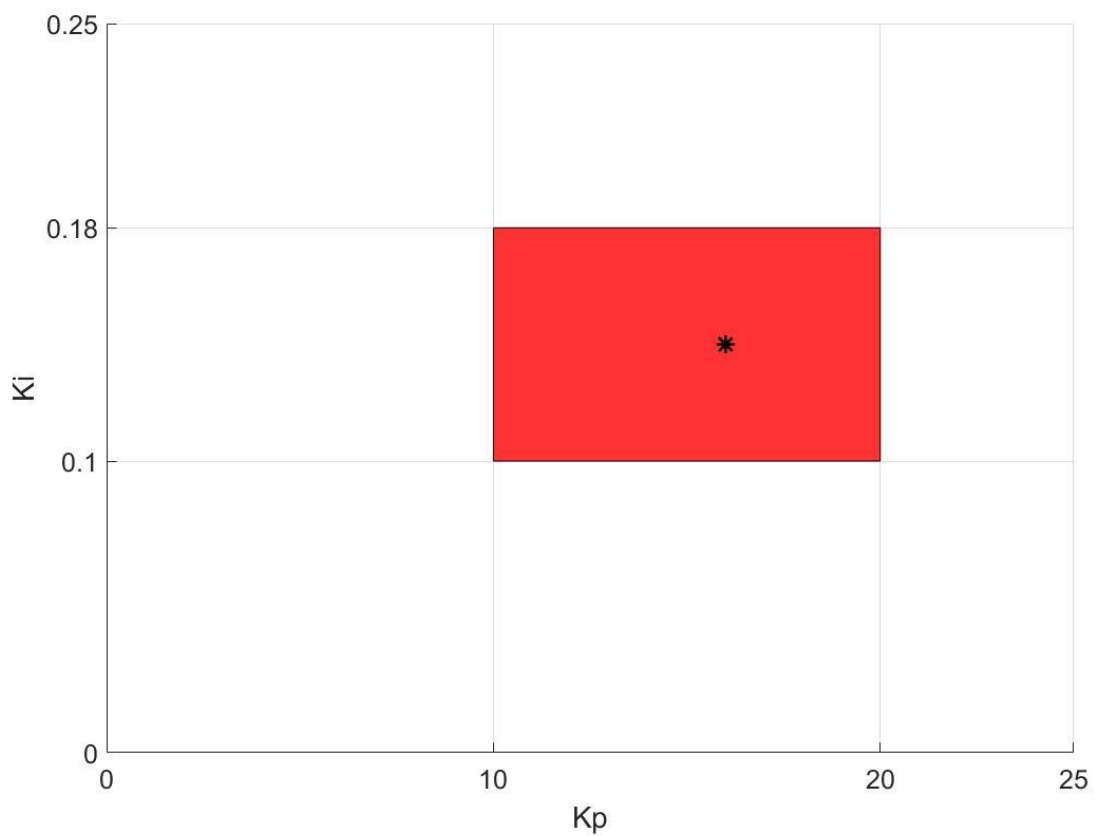


Figure 4.15 Region for stable operating PI gains for the X axis. The PI gains chosen for operation are indicated by an asterisk.

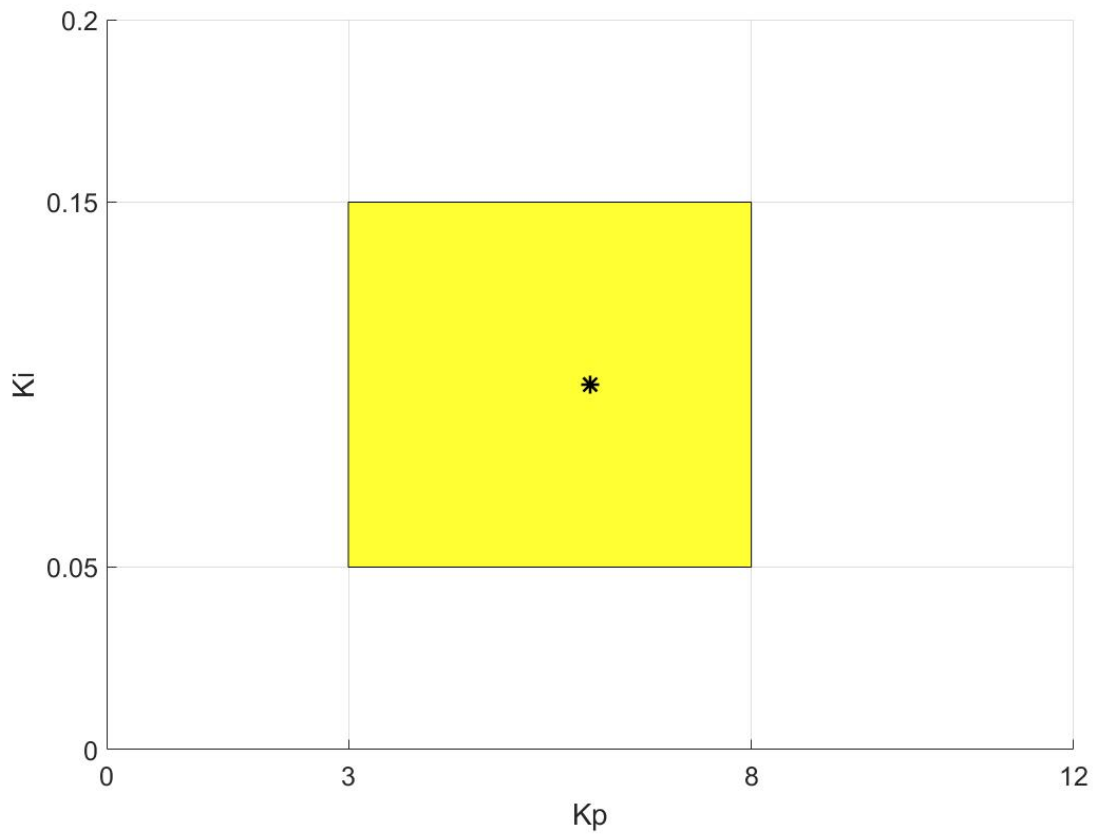


Figure 4.16 Region for stable operating PI gains for the Y axis. The PI gains chosen for operation are indicated by an asterisk.

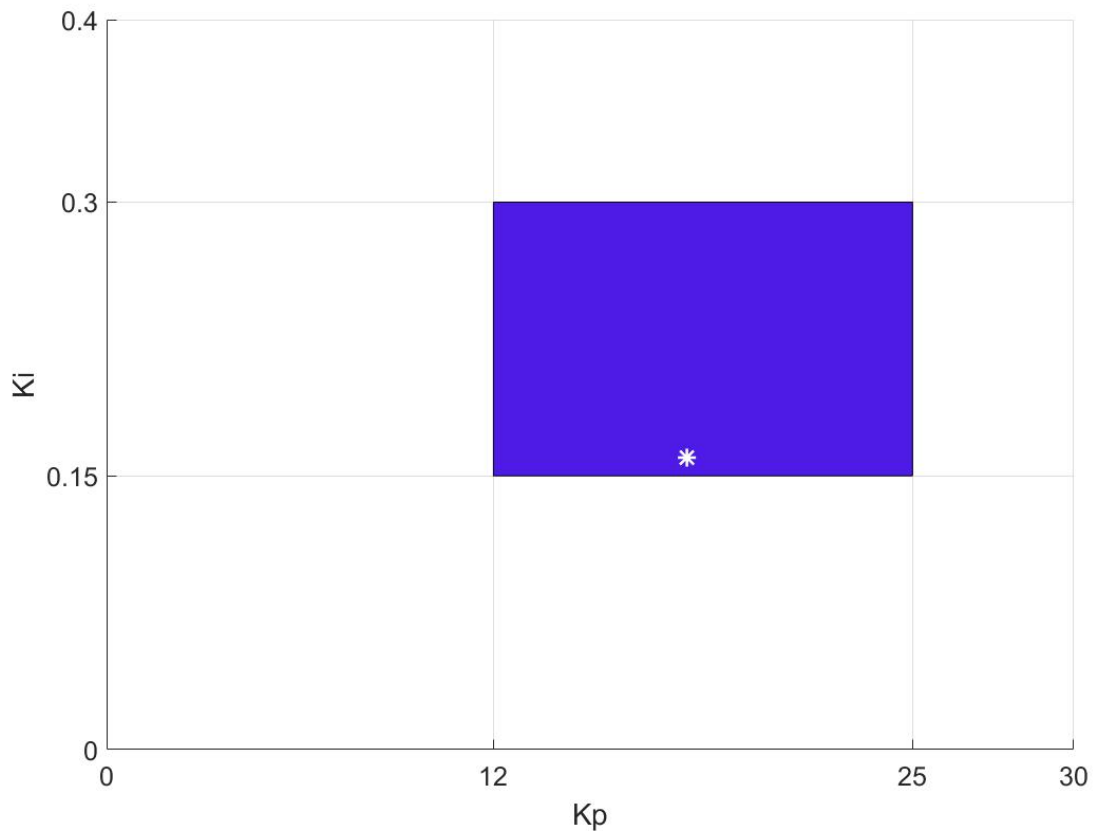


Figure 4.17 Region for stable operating PI gains for the Z axis. The PI gains chosen for operation are indicated by an asterisk.

4.2.2 User friendly iterative learning control

Even with the feedforward friction and feedback compensation, however, there were variations in these values that were both iteration and position dependent. Moreover, model uncertainties and nonlinearities in the system model played a role in decrementing tracking performance at low velocities (DW printer operating conditions). In addition, PID approaches are reactionary, resulting in a lag in transient tracking: the controller waits to respond until an error shows up, resulting in irreversible defects, and consistent defects from layer-to-layer. As a result, errors are propagated from layer-to-layer since the PID control structure was not adaptive, and errors may exceed tolerance requirements before the feedback controller has an opportunity to react. These reasons demonstrate the need for implementation of a more

sophisticated controller. In repetitive manufacturing processes, iterative learning control (ILC) is a common choice. An ILC algorithm examines error from previous iterations and maps it to the input signals of the current trial, effectively learning the proper control input through repeated iterations and decreasing tracking error. Through this training protocol, ILC can compensate for some of the un-modeled nonlinearities in the system model. A more detailed background on ILC and its applications can be found in [114].

An ILC approach was useful in the fabrication of bone scaffolds because of the layered and repetitive architecture. However, given the underlying goal of an easy-to-use (bio) 3D printer, one of the challenges of this work was to develop an ILC implementation in a limited control architecture (SoftMotion) that was easy for the end-user to follow. Ideally, ILC was incorporated in a way that a non-controls person could easily understand.

A framework for a user-friendly ILC code is presented, involving offline calibration for the reference command. Essentially, the code was an offline training routine where the axis error was used to update the position reference. A test run, where the X and Y-axes moved through Layers 1 and 2 defined by the left image in Figure 4.18, was executed without ink extrusion. The errors at each “end point” were added to the position arrays to give the axis an augmented input in order to reach the desired position. The numbers in the arrays were modified at each iteration based on the performance of the previous iteration. In this work, the ILC implementation was proportional to the error with a proportionality constant equal to one. The position arrays before and after the implementation of the simple ILC code are shown in Figure 4.18.

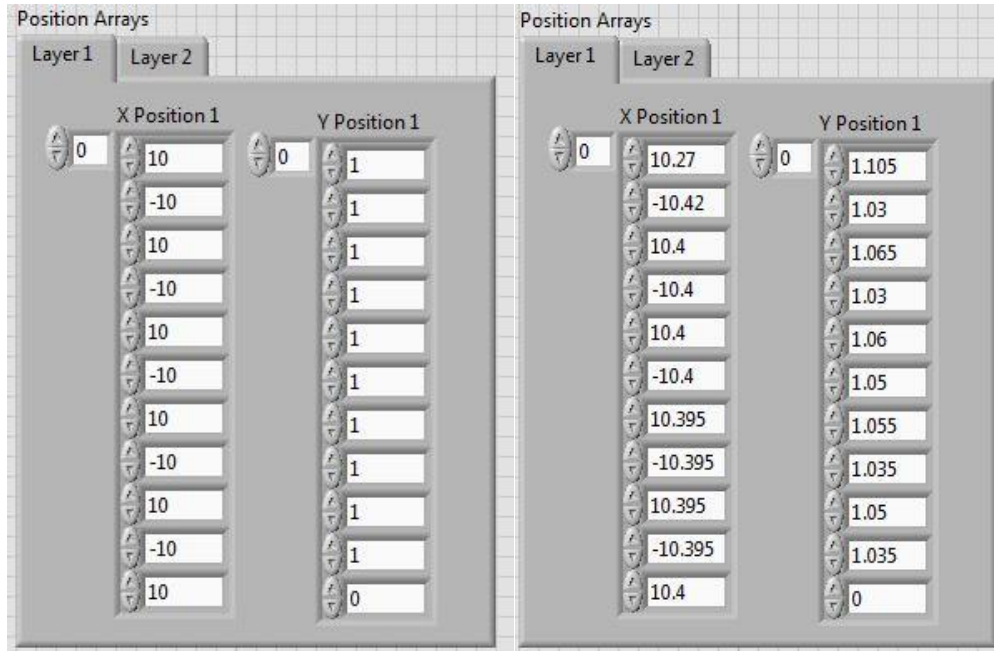


Figure 4.18 Position arrays before (left) and after (right) the ILC test run.

4.2.3 Pressure regulation

During velocity reversals within a scaffold layer at the points circled in red in Figure 4.19, excess ink “drooled” out of the nozzle. This process caused ink to build up at the edges of the scaffold, making the rod cross-section nonuniform in those regions, and changing the scaffold structure compared to the original design. An active pressure control was implemented to eliminate this behavior, and the protocol was outlined as follows. As an axis moved, a constant pressure set-point was used to ensure a uniform rod cross-section. During axis transitions, however, the pressure set point was reduced to avoid ink buildup at the scaffold edges from “drooling”. In the limited control environment, the pressure reduction was implemented as a series of steps. The analog output (AO) value sent to the pressure regulator was gradually decreased in a matter of milliseconds to ensure a smooth pressure reduction. The subsequent pressure increase was implemented as another series of steps. Both the pressure reduction and pressure increase were implemented as subVIs and placed within the main code structure (Figure 4.20). In LabVIEW, subVIs are short code sequences that are referenced by the main code. The pressure reduction subVI was placed between the X position reference and the Y position reference at the velocity reversal. The pressure increase subVI was placed after

the short Y axis movement at the scaffold edge to raise the pressure back to the constant pressure set-point. Each subVI contained a *for loop* where the AO signal was reduced or increased by a user defined amount (parameter #1). The number of times the *for loop* executed was also defined by the user (parameter #2). This method successfully reduced the amount of ink buildup during velocity reversals, which are circled in red in Figure 4.19.

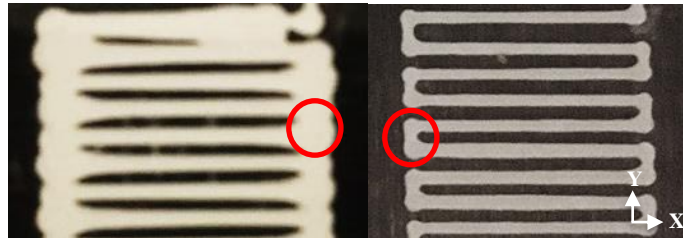


Figure 4.19 Single layer scaffolds printed before (left) and after (right) active pressure control.

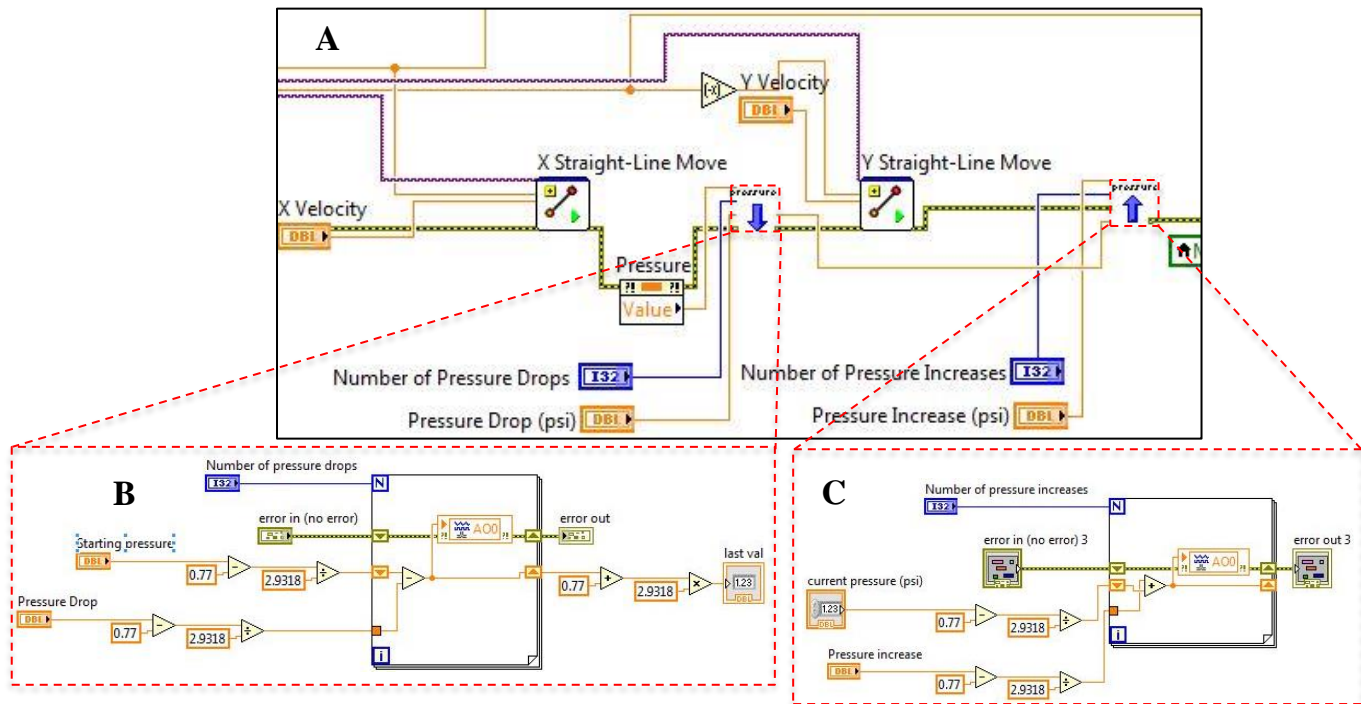


Figure 4.20 Pressure reduction and subsequent increase subVIs implemented in the main code structure (A). Code layout of the pressure reduction (B) and pressure increase (C) subVIs.

Colloidal inks, however, are very compressible and vary significantly from material to material and batch to batch [24]. Because of the irregularities in ink batch rheology, the active pressure control parameters (1. pressure increase/decrease per step, and 2. number of steps) must be adjusted for each ink batch. Each of these parameters are selected by the user in the main GUI (Figure 4.21).

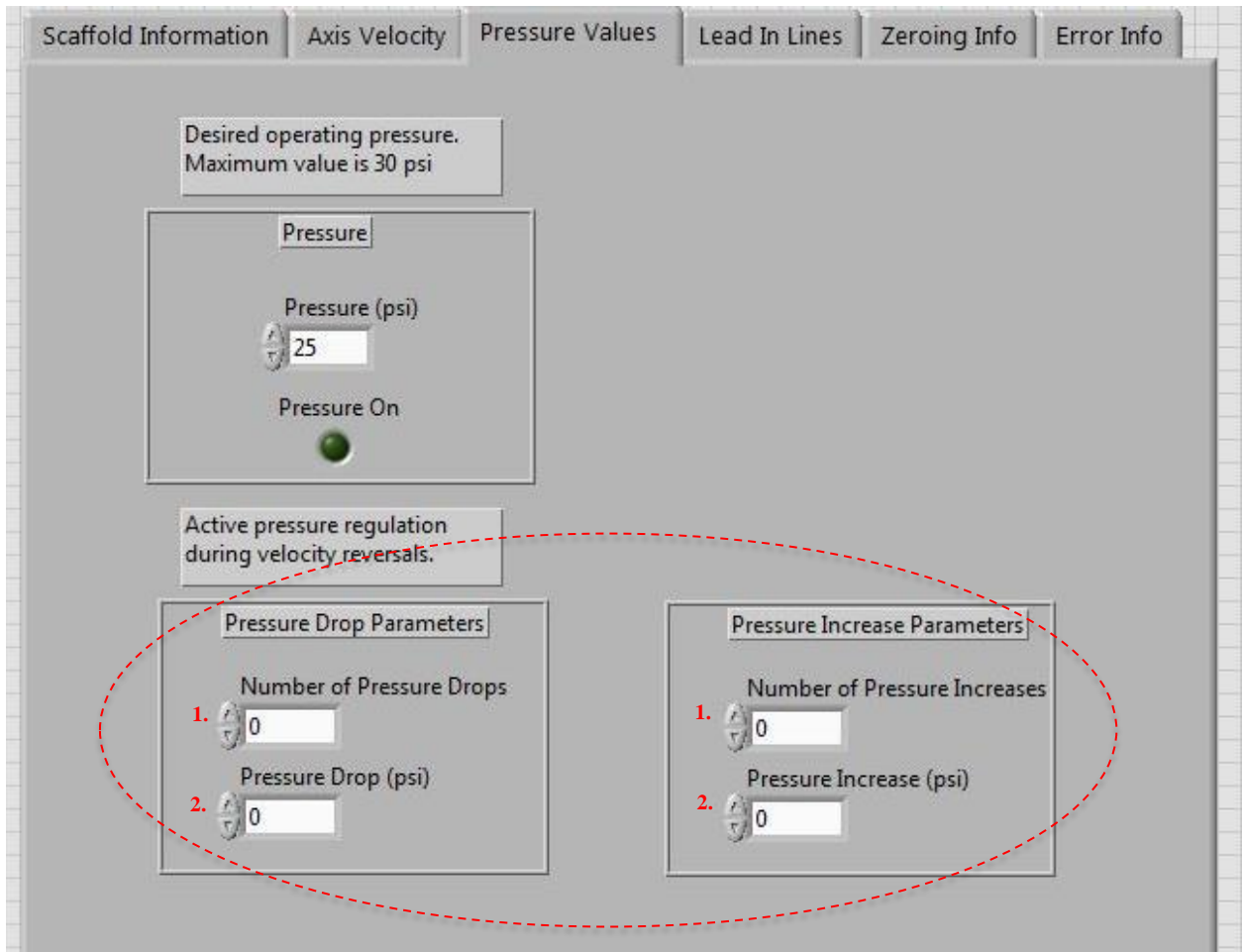


Figure 4.21 Main program GUI where the user was able to modify the two parameters for both pressure reduction and pressure increase.

In summary, this chapter presented the development of a user-friendly motion control platform. Common, non-trivial motion control problems were addressed and implemented in a way that researchers outside of the controls field could understand. A dynamic model of the 3-stage positioning system for bone scaffold fabrication was presented. In addition, control design for a feedforward plus feedback controller and a user-friendly ILC feedforward

compensator was outlined. Finally, this chapter reviewed an active pressure control protocol, that was implemented to reduce ink build up at the scaffold edges and improve part quality.

Chapter 5

Bone Tissue Engineering

While the work presented in this thesis is not directly in the field of tissue engineering, the parts printed using the developed DW printer are bone scaffolds. This chapter serves to review tissue engineering, bone anatomy, and bone scaffold principles to ensure the end user understands the application of this DW printer. Since there are many subfields within bone scaffold research, this chapter concludes with a discussion on the specific type of bone scaffolds that are relative to this work.

5.1 Tissue Engineering

Tissue engineering (TE) employs biology and engineering principles and involves the use of cells, engineering materials, and/or biochemical factors for the repair of damaged tissues and organs. The science community, however, does not yet fully understand the biological principles. To date, small three-dimensional microtissues have been engineered, but scaling up to enable functional, human-sized tissues remains a challenge [115]. Kang et al. developed an integrated tissue-organ printer that is capable of fabricating human-scale tissue constructs such as mandible bone, ear-shaped cartilage, and skeletal muscle [39]. The follow-up implantation studies, however, assessed cell survival and tissue formation, and did not evaluate immune response or *in vivo* functionality. Skeletal muscle, for example, must be able to generate forces, and to be useful for the patient, the regenerated tissue should be functional. Functionality is a remaining challenge in TE.

The fundamental questions of tissue replacement include: 1) how to make the synthetic biological tissue; 2) how to implant the biological tissue; and 3) how to integrate the fabricated tissue with the host tissue? TE relies on the use of porous 3D scaffolds to provide a suitable environment for tissue and organ regeneration, which serve as templates for tissue formation [116]. While scaffolds are occasionally seeded with cells and growth factors, the term scaffold

herein refers to the 3D biomaterial before cells have been added [116]. Further, the specific scaffold requirements depend on the tissue of interest. This work will focus on osseous tissue (bone).

5.2 Review of Bone Anatomy

This section briefly reviews bone anatomy and the bone remodeling process. More thorough reviews can be found in [117]–[119].

5.2.1 Composition of Bone

Bone is a complex composite consisting of mineral (mainly calcium phosphates, hydroxyapatite), organic matrix (collagen and other proteins), and water [34], and has a structural organization at multiple size scales. As a result of its structural hierarchy (Figure 1.1), bone is heterogeneous and anisotropic [118]. At the macroscale, bone tissue is either cortical or trabecular bone. Cortical bone is the dense, outer layer which is highly compact due to the circular nature of its microscopic structural unit, the osteon. Osteons are composed of concentric rings of a calcified matrix called lamella [120]. Osteons house osteocytes and canaliculi, which are small channels to provide nutrients and oxygen to cells. The center of osteons contains a central channel with vessels and nerves.

Trabecular bone is the spongy, inner part of the bone with 50-90% porosity. The microscopic structural unit of trabecular bone is a network of trabecula, which are struts and plates that grow along the principal stress directions. Trabecular bone is more elastic and has a higher turnover rate relative to cortical bone. The relative composition of each type of bone tissue depends on the anatomical location, applied loads, age, and diseases [118].

At the nanoscale, collagen fibers provide a surface for adherence of inorganic salt crystals, which form when calcium phosphate and calcium carbonate combine to create hydroxyapatite [120]. Bone mineral (small crystals in Figure 5.1), provides mechanical rigidity and strength to bone, while the organic matrix (largely collagen molecules) renders the bone elastic and flexible [121].

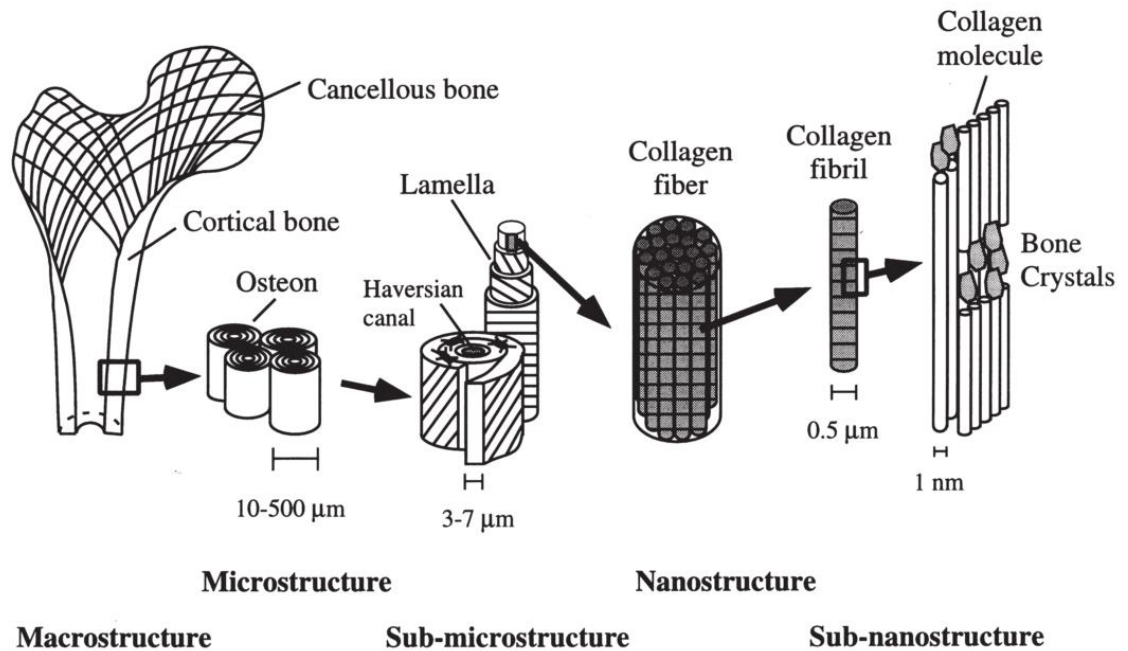


Figure 5.1 Hierarchical organization of bone. Image from [118].

5.2.2 Bone Structure

There are five types of bone in the human skeleton: long, short, flat, irregular and sesamoid. All bone types contain collagen, calcium phosphate, and bone cells (discussed below), yet there are considerable differences in composition between the different bone types. The biggest difference is seen in flat bones (the skull, for example) and long bones in extremities. These bones differ in their susceptibility to bone resorption since the skull is relatively insensitive to changes in hormones or mechanical stimuli, while long bones regularly adapt to mechanical loading. The phenotypic differences between the bone cells in the skull and long bones, however, are not well understood. It has been speculated that the differences in the composition of the matrix surrounding the bone cells helps to explain the varying behavior characteristics [122]. This chapter will briefly review the structure of long and flat bones, since short and irregular bones have similar structures to flat bones.

Long bones support the weight of the body and work with skeletal muscle to facilitate movement. Long bones (Figure 1.3A) contain an epiphysis, the wider section located at end of the bone, and a diaphysis, a tubular shaft which sits between the proximal and distal ends of the bone. The epiphysis is filled with trabecular bone and red marrow, which fills the pores.

The diaphysis contains a ring of cortical bone which surrounds a central cavity, called the medullary cavity, containing yellow marrow. The bone surface surrounding the medullary cavity is called the endosteum, and is where bone growth, repair and remodeling occurs. The outer surface of the bone is lined with a fibrous membrane called the periosteum, which contains blood vessels and nerves for nourishment.

Flat bones, in contrast, provide protection for internal organs such as the brain and heart. Flat bones (Figure 1.3B) contain a layer of trabecular bone, often called a diploe, lined with cortical bone on either side. Similar to long bones, bone marrow fills the pores within the trabecular bone.

Bone marrow is the soft, spongy tissue found in the hollow spaces in the bone interior [123]. There are two types of bone marrow: red marrow (hematopoietic tissue) and yellow marrow (fatty tissue). Red marrow produces red blood cells, white blood cells and platelets, while yellow marrow produces fat, cartilage, and bone. At an early age, most of the body's bone marrow is red, and with age, red bone marrow is gradually replaced by yellow bone marrow [123].

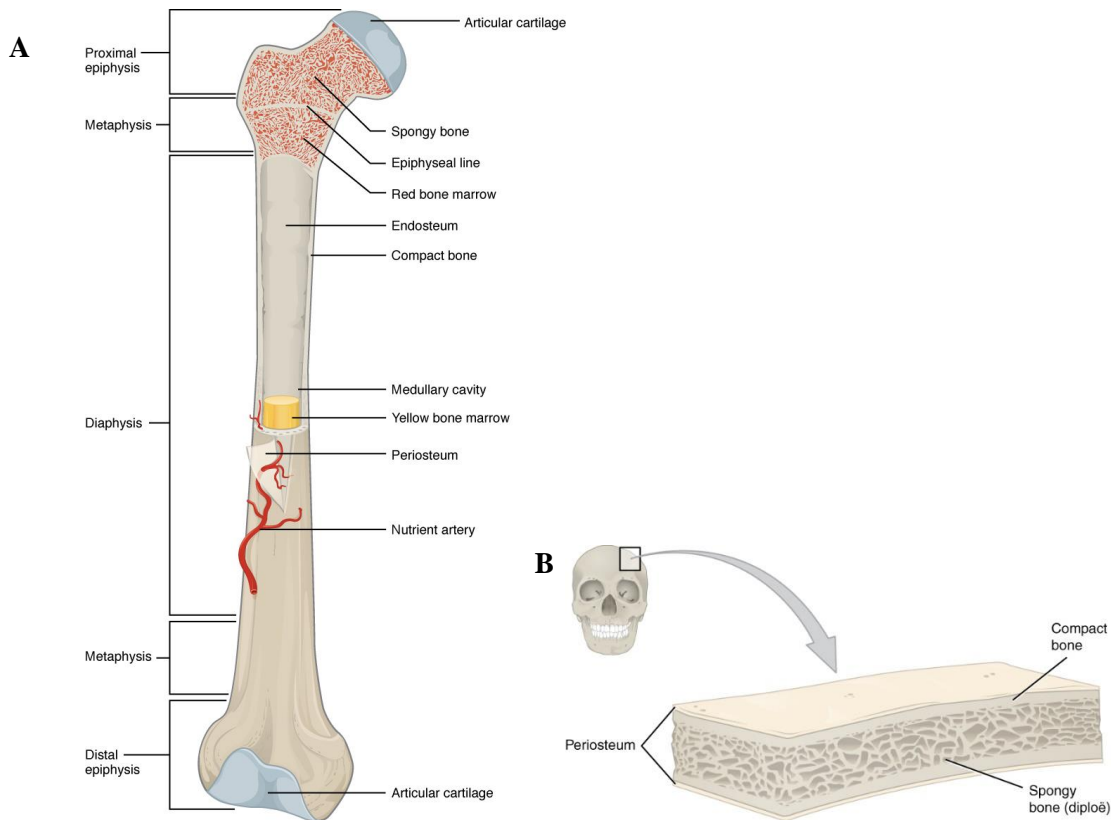


Figure 5.2 Bone anatomy, which is made up of compact bone (cortical bone), spongy bone (trabecular bone), and bone marrow. Cortical bone makes up the outer layer, while trabecular bone, which contains red marrow, is mostly found at the ends of long bones (A), or between plates of compact bone for flat bones (B). Red marrow contains blood stem cells which differentiate into red blood cells, white blood cells, or platelets. Yellow marrow is largely composed of adipocytes and is found in the medullary cavity.

Images from [120].

5.2.3 Bone Cells

Human bones contain four types of cells: osteoblasts, osteocytes, osteoclasts, and osteogenic cells. The osteoblast is responsible for building new bone, and is found on bone surfaces. Osteoblasts synthesize and secrete calcium salts and the collagen matrix [120]. The secreted matrix eventually calcifies, and traps osteoblasts within it. As a result, the osteoblasts change morphology and become osteocytes, which are the mature bone cells.

Osteocytes communicate with other cells, maintain the mineral concentration through enzyme secretion, sense mechanical stimuli, and control the activity of other cells to maintain the desired bone volume fraction [120]. Osteocytes are connected to each other and to bone surface cells through long, slender cytoplasmic processes that radiate in all directions [124]. Each osteocyte is housed in a space called a lacuna and is surrounded by bone tissue. Osteocytes sense mechanical stimuli and respond with an alteration in the production of signaling molecules. As a result, bone tissue can sense and adapt to mechanical loading.

Osteoclasts breakdown the bone matrix by secreting acid and collagenase, an enzyme that breaks the peptide bonds in collagen. Unlike osteoblasts and osteocytes, which are of mesenchymal origin, osteoclasts are of hematopoietic origin [122]. Osteoclasts are large, multinucleated cells that arise from the fusion of macrophages, a type of white blood cell that engulf and digest foreign substances through phagocytosis. Maturation of macrophages into osteoclasts requires two essential molecules: macrophage colony-stimulating factor (M-CSF) and receptor for activation of nuclear factor kappa B (RANK) ligand (RANKL), which are secreted by marrow stromal cells, osteocytes and osteoblasts. RANKL stimulates precursor cells to commit to the osteoclast phenotype [124]. Stromal cells, osteocytes and osteoblasts also express a protein called osteoprotegerin (OPG), which blunts osteoclastogenesis since it is a receptor that competes with RANK for RANKL [124], inhibiting the final differentiation of osteoclasts. Thus, it is a balance between the expression of RANKL (stimulator of osteoclastogenesis) and OPG (inhibitor) that dictates osteoclast activity and the level of bone resorption.

Osteoblasts, osteocytes, and osteoclasts do not undergo cell division, which presents the need for osteogenic cells for replenishment. Osteogenic cells are bone stem cells found in the bone marrow and periosteum that differentiate and develop into osteoblasts in the proper microenvironments. Bone cells are derived from two types of stem cells in the bone marrow: hematopoietic stem cells (HSCs) and mesenchymal stem cells (MSCs). Red marrow contains HSCs, which differentiate into red blood cells, white blood cells, and platelets. The stromal fraction of bone marrow contain MSCs, which are multipotent stem cells that that can differentiate into several cell lineages including cartilage, bone, tendon, ligament, and adipose

tissue [125]. Since osteoclasts arise from the fusion of white blood cells, osteoclasts originate from HSCs. Osteoblasts, on the other hand, are derived from MSCs.

5.2.4 Cell Differentiation

As reviewed previously, the composition of trabecular bone and long bones consists of a ring of bone surrounding a region containing mostly fat, cells, and blood vessels in the interior. MSCs present in bone marrow can differentiate into both bone and fat. Even though bone and fat differ greatly in phenotype, they descend from a common MSC precursor. For bone regeneration purposes, it would be useful to know what factors commit MSCs to the osteogenic lineage versus adipocyte lineage. Lineage commitment of stem cells is a complex, two-step process involving lineage commitment (MSCs to lineage specific progenitors) and maturation (from progenitors to specific cell types). These processes are not yet fully understood, but are known to be regulated by several cues in the local tissue microenvironment, including chemical, physical and biological factors [126].

Due to the mechanical nature of this work, the physical factors of differentiation will be briefly reviewed. *In vivo*, MSCs physically interact with components in the microenvironment since cells sense and respond to their environment through mechanotransduction. While it is widely accepted that cell adhesion and the level of cytoskeletal tension effect stem cell fate, the regulatory mechanisms of mechanics-based differentiation are not yet established [127]. The physical factors involved in stem cell fate decision include cell shape, external mechanical forces, extracellular matrix (ECM) composition, and geometric cues (Figure 5.3) [126].

Cell shape is an important regulator of MSC commitment to different lineages. In fact, changes in cell shape alone are sufficient to mediate the switch in MSC commitment between adipogenic and osteogenic fates [128]. McBeath et al. found that MSCs allowed to adhere, flatten and spread across the matrix underwent osteogenesis, while round, unspread cells became adipocytes [128]. These results indicate that stem cells exposed to an environment that enables spreading have a higher chance of differentiating into osteoblasts. Further, McBeath's conclusions are similar to *in vivo* bone and fat cells: differentiated adipocytes are round and fat-laden, while osteoblasts are elongated and cuboidal [126].

Cell differentiation also depends on substrate stiffness and mechanical forces since cells use focal adhesions to sense the environment. With an increase in substrate stiffness, the size and number of focal adhesions increase, which encourages cell spreading and changes the cell's mechanical properties. As a result, stem cell lineage depends on the stiffness of the substrate it is attached to [129]. Without local stress via focal adhesions, stem cells do not differentiate. Engler et al. investigated lineage commitment of MSCs by placing stem cells on substrates with varying stiffness to simulate mechanical environments *in vivo* [130]. Matrices mimicking the stiffness of the brain (0.1 – 1 KpA) supported neurogenic differentiation, stiffer matrices mimicking striated muscle (8-17 kPa) promoted myogenic differentiation, and even stiffer matrices that mimic the crosslinked collagen in osteoids (25-40 kPa) supported osteogenic differentiation [130]. Numerous studies have demonstrated that as the substrate becomes more stiff, cells have a higher chance of committing to an osteogenic lineage due to an increase in cell spreading [129]–[131].

Components in the ECM also dictate stem cell fate by binding to transmembrane proteins, such as integrins, on cell surfaces and induce signaling pathways for differentiation. Integrins are transmembrane proteins that mediate cell adhesion to matrices and other cells through signal transduction across the plasma membrane [126]. Ligands that bind to integrin lead to its activation, which is followed by activation of a series of signaling proteins. Fibronectin, for example, is an important component of the ECM that interacts with integrin receptors resulting in suppression of adipogenesis transcription factors [126].

Finally, geometric cues, such as micron and submicron scale changes, also play a role in MSC lineage commitment. Localized patterns of cytoskeletal tension induced by geometrical features such as the subcellular curvature, adhesive area, and aspect ratio trigger patterns of differentiation to different lineages [131], [132]. Kilian et al. used microcontact printing to control cell shape, and found that cell shapes promoting increased cell contractility resulted in more osteogenesis, while cell shapes that promoted low contractility preferred an adipocyte lineage [132]. Further, in sinusoidal monolayers *in vitro*, Ruiz et al. found that high levels of tension generated at convex edges increased osteogenesis in MSCs [131].

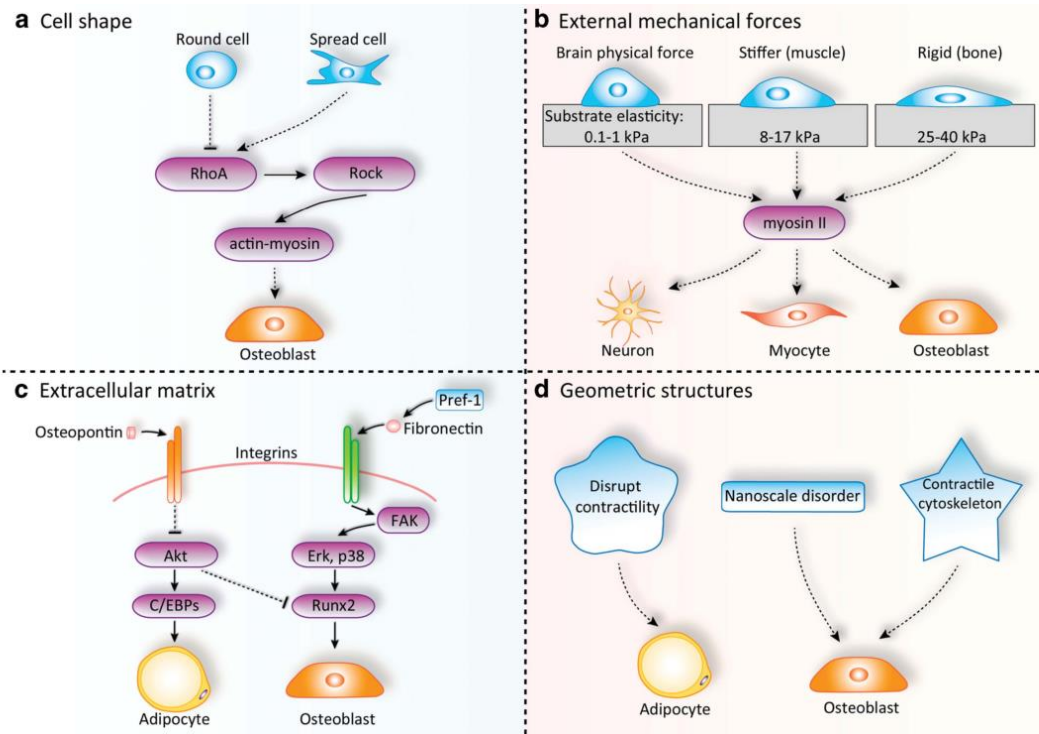


Figure 5.3 Physical factors regulating lineage commitment of MSCs. The physical factors involved in stem cell fate decision include cell shape, external mechanical forces, extracellular matrix, and geometric structures. A) Spread cells tend to differentiate into osteoblasts while round cells tend to become adipocytes. B) Physical forces can direct MSC differentiation by controlling motor proteins such as myosin II. C) ECM components can regulate differentiation by binding to cell adhesion molecules like integrins. D) Geometric changes can also dictate cell differentiation. Image from [126].

In summary, mechanical cues in the scaffold microenvironment are integral to the commitment of stem cell fate. Osteogenesis would be optimal if bone scaffold design considered the following mechanical cues:

- Cell shape – cells are allowed to flatten and spread out;
- External mechanical forces – substrate stiffness should be similar to bone tissue;
- ECM – scaffolds contain factors that bind to integrins on the surface of MSCs and activate osteogenic signaling pathways; and

- Geometric structures – nanoscale geometric cues which promote cell contractility.

5.2.5 Bone Functions

Bone is a rigid organ with mechanical, synthetic, and metabolic functions. The mechanical functions of bone include supporting external loads, protecting vital organs within the body, and interacting with muscles for force generation and movement. The synthetic function involves the generation of both bone and blood cells within the bone marrow [133]. The metabolic function of bone includes the regulation of calcium and phosphate levels in the body due to the reservoir of minerals in the bone matrix [117]. Further, bone includes growth factors and fat deposits.

Recently, human bone has been classified as an endocrine organ since it secretes bone-specific factors which contribute to the regulation of a number of metabolic processes [134]–[139]. One of these functions includes glucose homeostasis, which is regulated by osteocalcin, an osteoblast specific hormone [136]. Osteocalcin has been shown to regulate glucose metabolism in mice [139]. Further, a hormone called fibroblast growth factor 23 (FGF23) produced by osteocytes regulates serum phosphate levels by altering vitamin D and activities in the kidney [138]. Both osteocalcin and FGF23 operate in an endocrine fashion since they are produced exclusively in the bone and act on distant target organs. Further investigating the endocrine role of the human skeleton could improve the ability to diagnose and treat patients with metabolic diseases such as osteoporosis [140].

5.2.6 Bone Remodeling

Bone is an active tissue which undergoes continuous remodeling with little change in shape to facilitate adaptation to changing mechanical environments. In fact, it is estimated that the entire skeleton in the adult human body is renewed every 7 years [126]. When bone experiences loading, mechanical stimuli triggers the production of signaling molecules which attract and activate osteoblasts, but repel osteoclasts [122]. In the absence of mechanical stimuli, osteocytes produce factors which activate osteoclasts, resulting in bone resorption [122]. In homeostatic equilibrium, bone formation by osteoblasts and bone resorption by

osteoclasts are tightly regulated so that old bone is continuously replaced by new tissue to adapt to loading. An imbalance of these two processes results in various diseases such as osteopetrosis and osteoporosis [124].

The remodeling cycle involves all bone cell types, and consists of three consecutive phases: resorption, reversal and formation [117]. During bone resorption, osteoclasts dig a tunnel through cortical bone or a trench along the surface of trabecular bone [122]. Osteoclasts are followed by bone lining cells which clean the resorption pits. Osteoblasts then start the formation of new bone using nutrients and oxygen from nearby blood vessels. The regulation of bone resorption and formation is not fully understood, but a few theories exist. The first is that osteoclasts deposit chemical signals within the resorbed bone, similar to a trail of breadcrumbs, which attract and guide the bone lining cells and osteoblasts [122]. Another theory links the mechanical sensing of osteocytes to the coordinated actions of osteoclasts and osteoblasts. As osteoclasts dig a tunnel within the bone matrix, an area in front of this region experiences relative mechanical unloading [122]. Osteocytes within this region are suspected to experience apoptosis, which stimulate RANKL expression in neighboring osteocytes, increasing osteoclastogenesis and leading to further bone resorption [122].

In resorption, osteoclasts adhere to the bone surface using integrins and dynamic structures called podosomes. Osteoclasts move along the bone surface through the continual assembly and disassembly of the podosomes. Bone is resorbed by acidification and proteolysis of the bone matrix and hydroxyapatite crystals. This process requires a low pH to dissolve calcium phosphate crystals, achieved by the recruitment of a high concentration of protons, and a number of enzymes to cleave the organic matrix components [122]. To contain bone resorption to a specific area, the protons and enzymes are secured in a sealing zone within osteoclasts, which surround the ruffled border where the molecules are released [122]. In the reversal phase, mononuclear cells prepare the bone surface for bone formation and secrete signals for osteoblast differentiation and migration. Finally, the formation phase involves osteoblasts depositing new bone in the resorbed area. Osteoblasts initially deposit collagen, which is followed by collagen mineralization until the osteoid becomes fully mineralized. It is assumed that there is coordination between bone resorption and bone formation, and that osteocytes actively attract osteoblasts. The coordination between bone cells, however, is not

yet fully understood. Osteocytes have receptors for many of the factors produced by osteoclasts and produce RANKL, which makes it plausible that a communication line between these types of cells exists [122].

Small scale remodeling to regulate chemical homeostasis and repair microdamage from small stresses occurs every day. Microdamage is an extreme form of mechanical stimulus which triggers osteocyte apoptosis and bone matrix fracture. High numbers of osteoclasts and apoptotic osteocytes have been found in the direct vicinity of induced microdamage [141]. Further away from this region, the surviving osteocytes express large quantities of RANKL [141], which could serve to attract osteoclasts to remove the damaged bone.

Since bone has high regeneration capabilities, most fractured bones will heal on their own. Large bone defects, however, need an implanted template for orchestrated bone regeneration [142]. Further, stem cells that do not experience local stresses via focal adhesions with their surroundings do not differentiate [130]. Thus, in a defect of considerable size, cells cannot grow in open space and must generate forces through interaction with a scaffold to encourage osteogenesis.

5.3 Artificial Bone Scaffolds

Since cells respond to the chemistry, geometry, and mechanics of the local environment [129], scaffold design considerations include biological, mechanical, and material requirements. A summary of specific features necessary for successful scaffold implantation and integration [15], [16] are listed below, which will be discussed in more detail in the following sub sections.

- Osteoconductivity: allow native bone cells to adhere, proliferate and form ECM.
- Osteoinductivity: induce new bone formation through biomolecular or mechanical stimuli.
- Osteogenicity: act as a reservoir for MSCs and osteoblasts for the formation and mineralization of new osseous tissue.
- Osteointegrity: form strong bonds with surrounding native tissue for material continuity

- Biocompatibility: compatible with living tissue to avoid immunological rejection.
- Biodegradability: degrade gradually, with non-harmful degradation products.

Despite extensive research efforts, clinical progress in bone tissue engineering (BTE) is limited [14]. Most commercially available BTE products currently used in the clinic do not have a defined 3D shape and are used to fill defect sites (i.e. putty) [14]. 3D printed bone scaffolds have yet to overcome major obstacles, such as understanding the external geometry and internal pore architectures needed to promote cell infusion and vascularization. These design parameters must be optimized before 3D printed bone scaffolds of considerable size are transitioned to the clinic [14].

5.3.1 Biological Considerations

From a biological point of view, scaffolds should act as a template for bone regeneration, minimize adverse immune responses, and allow nutrient transport from surrounding tissue and waste disposal from the tissue being formed. Osteogenesis requires cell colonization and extracellular matrix development. Scaffolds should enable osteoprogenitor cells to attach, proliferate, and differentiate into functional osseous tissue [15]. As discussed in Section 5.2.3, differentiation of stem cells into osteoblasts and osteoclasts requires appropriate mechanical stimuli, which should be accommodated by implanted scaffolds.

In addition to osteogenesis, scaffold implantation should minimize inflammation. Implantation of any foreign material into the body elicits an inflammatory reaction, which influences the behavior of the cells involved in regeneration and determines implant success [143]. Inflammation is a complex, multistage process involving multiple cell types and signals. After surgical implantation, chronic inflammation occurs in the immediate area in response to specific antigen recognition. Macrophages are one of the cell types recruited to the site of infection during inflammation. The immune response of macrophages to 3D printed scaffolds is sensitive to both surface chemistry and scaffold geometry, such as porosity and pore size [69].

Since the maximum diffusion distance for cells to survive without vascularity is 100 – 200 μm [144], scaffolds larger than this size require vascularity. This is facilitated by

incorporating porosity into scaffolds at multiple length scales: macro and microporosity. Macroporosity is defined as the spacing between rods ($>100\ \mu\text{m}$), and is necessary, and microporosity includes the porosity within a rod ($<50\ \mu\text{m}$), which is not necessary but enhances regeneration [10], [45]. Both types of porosity are illustrated in Figure 5.4. Total porosity and pore interconnection channels are controlled by choosing the appropriate rod diameter (nozzle size) and nozzle trajectory. Microporosity is induced by the addition of pore forming agents (Section 3).

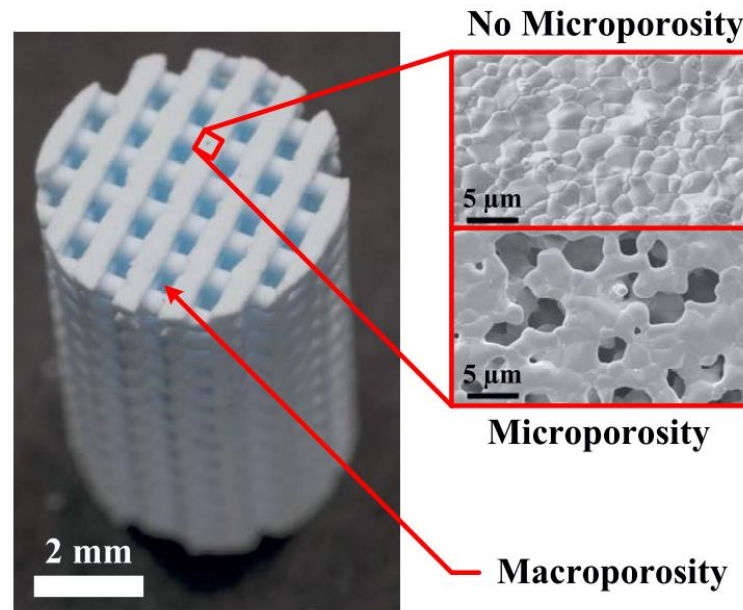


Figure 5.4 Bone scaffold with an inter-rod microporosity and macroporosity between rods. Lattice structures can be prepared with or without microporosity, which is created by pore forming agents during ink fabrication. Image from [24].

Porous structures with interconnected channels incorporated into the scaffold architecture enhance cell adhesion, cell proliferation, blood vessel and nerve ingrowth, and nutrient and metabolic waste exchange [145]. While the optimal porous architecture of bone scaffolds remains unknown, there are a few consistent trends in the literature. Non-stochastic porous structures have higher mechanical properties [146] and improved cell penetration in the center of the scaffold [147] relative to structures with stochastic pore sizes and configurations. Moreover, larger macropores facilitate internal cell colonization and stimulate osteoblast differentiation relative to narrower pores [15]. Increased void space from a higher pore

fraction, however, reduces mechanical strength. Thus, pore size selection is a balance between improved osteointegration and mechanical strength. The critical pore size that maintains mechanical integrity of the scaffold and provides optimal bioactivity must be determined for specific defects [16].

5.3.2 Mechanical Requirements

Mechanical requirements include load bearing capacity, and scaffold stiffness to create a microenvironment that encourages osteogenic differentiation. First, the biomechanical properties should closely match the properties of the healthy surrounding osseous tissue for the scaffold to be functional (i.e. load bearing) immediately after implantation. This requirement is challenging since the mechanical properties of human bone vary depending on anatomical location and function. Thus, the scaffold's mechanical properties must be tailored to match the defect site.

In addition, the scaffold must have the mechanical integrity to function during the duration of the tissue ingrowth and regeneration process. The scaffold should have controlled degradation to create void space where new tissue can grow. The degradation rate should be as close as possible to the bone growth rate to maintain stable mechanical properties in the tissue-scaffold complex during repair [16]. Further, to encourage stem cells to differentiate into osteogenic cells, scaffolds should have similar stiffness to the adjacent bone tissue (Section 5.2.3) since the microenvironment plays a role in stem cell differentiation [129]–[131].

5.3.3 Material Requirements

The scaffolds' mechanical properties also depend on the material composition, as these properties go hand in hand. The design of bone scaffolds presents a biomaterial challenge since it is difficult for any single biomaterial to satisfy all of the requirements listed at the beginning of Section 1.4 [15].

Materials for bone repair can be classified into two groups depending on the degradation performance: bio-inert and biodegradable materials [148]. While bio-inert materials have been used for clinical use with success, there are some downsides [148]. These

materials stay in the human body forever unless they are removed surgically after sufficient tissue regeneration. Biodegradable materials are often sought since they would not require a second surgery for removal. Further, a biodegradable bone scaffold will degrade over time and host tissue will replace the void space, restoring normal biomechanical function. In fact, bone regeneration is often higher when a biodegradable material is used for the base scaffold [148]. The degradation rate, however, must be controlled to free up space for regenerated bone tissue without compromising mechanical properties.

In addition to controlled degradability, the scaffold material is ideally osteoinductive. Biomaterials that demonstrate osteoinductive properties include natural and synthetic ceramics and their composites, such as HA/poly(lactic-co-glycolic acid) (PLGA) [15]. The biological mechanisms that induce bone formation, however, have not yet been fully elucidated [15]. Two theories for osteoinductive materials exist: 1) the biomaterial surface features adsorb and subsequently present osteoinductive factors to surroundings and 2) the biomaterials release ions that encourage differentiation of stem cells to bone cells [15]. Ceramic materials, however, have various downsides (discussed below) and many other materials are used in the investigation of bone scaffolds, including metals, polymers, and ceramics which will be briefly discussed.

Metal implants have high mechanical strength and fracture resistance, but the strength and stiffness of metallic materials are much higher than those of human bone. Thus, the scaffold will bear most of the load after implantation and the stress level of adjacent bone tissue is dramatically decreased, resulting in increased bone resorption and implant loosening [15]. This is known as “stress shielding.” Additionally, most metals used for scaffolds (including titanium and stainless steel) are not biodegradable and do not provide an environment for the growth of new osseous tissue [149]. Further, metal ions are often released into the body after implantation which can cause an immune response. While some biodegradable metals exist (such as magnesium metal), these materials have rapid and uncontrolled degradation [15]. The degradation rate is faster than TCP ceramic scaffolds, and is on the order of one or two weeks [148].

Biodegradable polymers have tunable degradation and similar mechanical properties to trabecular bone. The mechanical properties, however, are not comparable to cortical bone so

the application of these scaffolds is limited to the repair of small, non-load bearing defect locations. Further, this material shows rapid strength degradation *in vivo* which leads to the formation of a local acidic environment and adverse tissue responses [16].

Calcium phosphate (CaP) ceramics are biocompatible, have corrosion resistance, and have been shown to be osteoinductive [148]. Moreover, CaP materials are commonly used due to the chemical and structural similarities to the mineral phase of bone [145], [150]. Two common CaP ceramics include hydroxyapatite (HA, a type of CaP material) and tricalcium phosphate (TCP). While pure HA has good bioactivity and biocompatibility since it is a major inorganic component of bone tissue, its usefulness as a single-material scaffold is limited since HA is too brittle and has too slow of a degradation rate [145]. An HA-based scaffold implanted in a rabbit femoral bone displayed minimal degradation and slow resorption 12 weeks after implantation [151]. TCP, on the other hand, has a higher rate of biodegradation relative to HA after *in vivo* implantation [148]. A TCP-based scaffold implanted in a rat tibia displayed almost complete resorption (95%) after just a month and a half after implantation [148]. This resorption rate is faster than the rate of new bone growth, which would result in a reduction in the mechanical properties of the scaffold *in vivo*. Thus, while TCP has good biodegradability, biocompatibility, and antibacterial properties, it has low mechanical strength and degrades relatively quickly *in vivo* [145].

A mixture of HA and TCP of different ratios is commonly used to create a biphasic CaP (BCP) material. BCP scaffolds enhance osteoblasts' cellular response (measured by viability and proliferation) *in vitro* relative to pure TCP scaffolds [150]. The success of BCPs arises in part to the combination of higher solubility of TCP with the lower solubility of HA. Thus, the release of calcium ions during TCP resorption promotes bone formation, while the remaining HA scaffold material can structurally support the defect site during repair. Tailoring the HA/TCP ratio presents the possibility to tailor degradation kinetics of scaffold, which is useful for the varying anatomical locations of bone defects. While ceramics may not have optimal mechanical properties, rapid osteointegration of the implant will improve mechanical stability due to fast bone tissue ingrowth [150].

High temperature post-processing of ceramic scaffolds (discussed in Chapter 3) enhances the mechanical strength of the scaffold and enables scaffolds to be structurally sound

when implanted. The use of high temperatures, however, limits the ability to incorporate cells or biofactors that are altered or destroyed at high temperatures (termed heat-labile) into the scaffold material [34].

5.4 Scaffold system of interest in this work

Despite substantial prior research, the treatment and repair of large and load-bearing bone defects remains a challenge [22]. This difficulty largely arises from the hierarchical structure of bone and the range of length scales that must be considered in scaffold design [152]. While there are numerous scaffold parameters under investigation, Dr. Wagoner Johnson's lab concentrates on *in vivo* bone growth in BCP scaffolds with different macro- and microporosity. The investigations use constructs made of layers of orthogonal rods separated by macropores ($>300\ \mu\text{m}$). Microporosity is incorporated to induce vascular networks and discourage tissue necrosis at the center of the scaffold, and use a pig mandible model to assess the efficacy of the scaffolds.

The structural hierarchy of the scaffold system of interest is shown in Figure 5.5. The figure starts at the whole bone level (left), and moves down in length scale. The defect envelope can contain domains with different structural characteristics, requiring multiple-domain scaffolds. The scaffold must incorporate large interconnected rod spaces for bone ingrowth, but each domain can have different size spacing [22].

In past studies, this lab has demonstrated that BCP scaffolds with both macro and microporosity enhance bone regeneration and healing *in vivo* relative to scaffolds with just macropores [99]–[101]. In addition, micropore-induced capillarity was shown to enhance bone growth and facilitate uniform regeneration throughout the scaffold [45]. In this lab's research, macro- and microporosity was varied in both single and multiple domain scaffolds. In single domain scaffolds, microporosity improved the average bone volume fraction and bone distribution, and the average trabecular thickness increased in samples with larger macropores that incorporated microporosity [22]. In multidomain scaffolds, the average bone volume fraction was comparable to the single-domain counterparts, suggesting that bone regeneration in domains of multidomain scaffolds can be predicted and are not influenced by neighboring

domains [22]. These results will be useful in addressing defect sites that incorporate multiple domains with different micro and macroproperties.

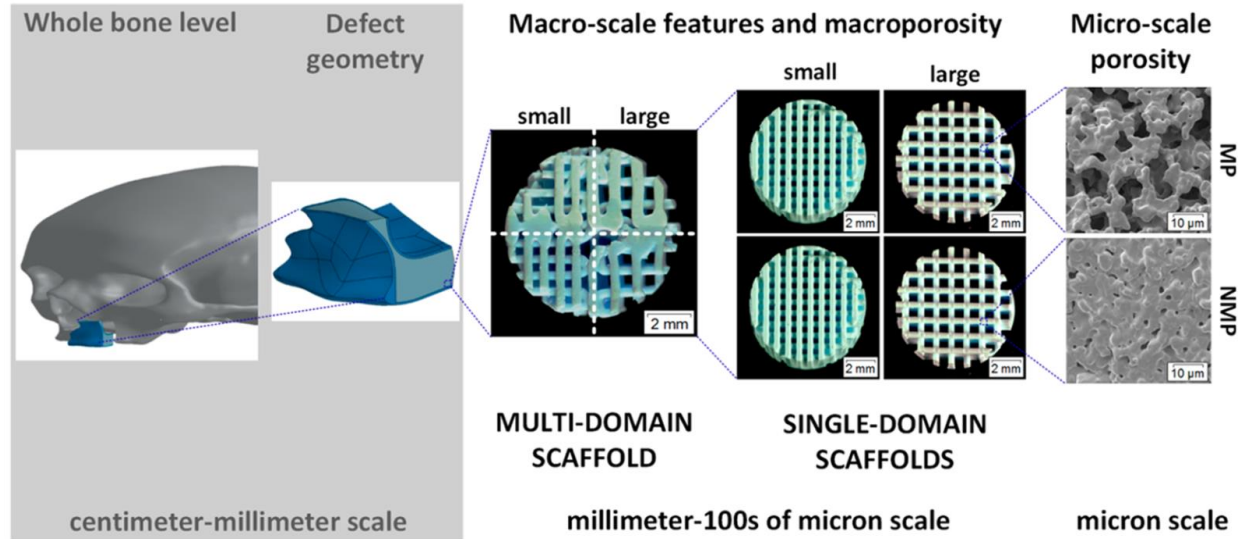


Figure 5.5 Structural length scales considered in the design of bone scaffolds. The defect site is highlighted in blue. Here, the envelope involves multiple domains with different macro and microscale properties. Scaffolds made of orthogonal layers of rods can incorporate single or multiple domains, which have different macropore spacing. Further, rods can either be microporous (MP) or nonmicroporous (NMP). Image from [22].

In summary, this chapter reviewed principles of tissue engineering and bone anatomy. Further, the process of cell differentiation was reviewed to illustrate how stem cells differentiate into bone, and how this knowledge could be incorporated into the design of bone scaffolds. In addition, bone scaffold requirements to enable in vivo functionality were reviewed. This chapter concluded with a discussion on the specific type of bone scaffolds relevant in this work to better understand the application of the DW printer.

Chapter 6

Machine Capabilities and Future Directions

In this chapter, the performance of the DW printer developed for bone scaffold fabrication is assessed. In addition, the capabilities and limitations of this system are highlighted, which illustrate how this DW printer fits within the manufacturing space discussed in Chapter 1. Future work in the fields of bone scaffold fabrication and additive manufacturing are briefly discussed. Finally, the chapter concludes with a thesis summary.

6.1 Goal assessment

The goal of this easy-to-use DW bioprinter was to find a balance between high performance and ease of use for the fabrication of rectilinear bone scaffolds. To assess whether this goal was accomplished, the machine performance and usability were evaluated. Performance of the DW printer was determined by the following characteristics:

- Ability to track a ramp (i.e. a position reference signal with a positive slope, meaning it consistently increases with time)
- Minimal ink build up at velocity reversals (i.e. places where the nozzle turns a corner to change directions)
- Alignment of successive layers
- Repeatable rod spacing (i.e. to generate uniform macropore spacing)

The fabrication of rectilinear bone scaffolds was used to evaluate whether the defined performance characteristics were achieved.

6.1.1 Machine Performance

An 8-layer bone scaffold was printed with 500 μm diameter rods spaced 500 μm from center-to-center and a 500 μm layer height (Figure 6.1). Deposition speed was 4 mm/s for the X and Y-axes, and 0.5 rev/s for the Z-axis. Experimental results show the controller to be

effective in tracking repeated trajectories since successive layers were aligned with the previous layers, and there was minimal ink build up at velocity reversals. The part width, height, and rod spacing were evaluated quantitatively and the error of each feature from what was prescribed by the end user was less than 10 μm . Further, the dimensions refer to an un-sintered scaffold, as sintering results in a 15-20% reduction in overall dimensions.

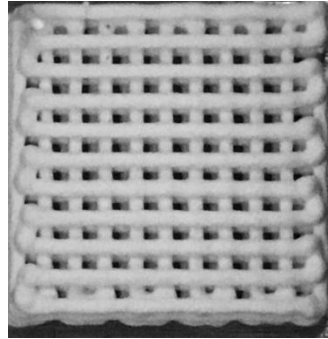


Figure 6.1 Bone scaffold deposition to test controller effectiveness.

6.1.2 Usability

Motion control problems commonly faced in positioning system applications are often barriers in the development of easy-to-use systems. Desired machine capabilities addressing these problems are presented in Table 6.1. The Yes/No column indicates whether a feature was included in the machine developed in this work. The characteristics not included were not needed for the fabrication of single-material, rectilinear bone scaffolds, but can be easily implemented for future projects.

For the end-user to operate and modify the (bio) 3D printer in this work, he or she should understand the following concepts:

- System model
- Input and output to a system
- Error compensation through feedback
- Effect of friction and gravity on motion

Since these characteristics are within the capabilities of most technically proficient people, the (bio) 3D printer design platform presented can be operated by the target end-users.

Table 6.1 Machine characteristics which address common motion control problems.

Desired Machine Capabilities	Yes	No	Comments
Straightforward control loop gain selection	✓		Chapter 4 and Appendix C
System modeling and friction compensation	✓		Chapter 2
Simple user-interface	✓		Chapter 4, Appendix B and D
Minimal tuning parameters to adjust system performance	✓		4 tuning knobs (K_P , K_I , V_{ffp} , V_{ffn})
Manageable hardware selection and implementation	✓		Through SoftMotion and NI controllers (Chapter 2)
Pressure regulation to avoid ink buildup at velocity reversals	✓		4 simple parameters to adjust for pressure increase/decrease at velocity reversals (Chapter 4)
Multi-material		✓	Precise start/stop flow of the ink was demonstrated. For multi-material printing, modify end-effector and add another pressure regulator
STereoLithography (STL) file incorporation, which is a file format that describes the surface geometry of a CAD-designed 3D object		✓	Simple to add. This feature would enable the end user to design a more advanced scaffold design

6.2 Machine Capabilities and Limitations

The DW printer developed in this work was intended to primarily print rectilinear bone scaffolds. This section will highlight additional machine capabilities and discuss the current machine limitations.

6.2.1 Capabilities

Multiple LabVIEW code structures were developed to enable fabrication of a single scaffold (Figure 6.1), multiple scaffolds (Figure 6.2), scaffolds with open pores to illustrate the ability to start/stop ink flow (Figure 6.6), and single layer scaffolds with curvilinear features

(Figure 6.10). The code architectures for fabrication of each of these structures are further discussed in Appendix D.

6.2.1.3 Scaffold fabrication

The main scaffold code structure is programmed to print n scaffolds each with m layers. Both n and m are defined by the end user in the main GUI. Additional user-defined values in the main GUI are discussed in Chapter 2. The scaffolds illustrated in Figure 6.2 were printed in the same printing session. The right scaffold is more precise than the scaffold on the left since the reference signal for the right scaffold included the error compensation from the user-friendly ILC algorithm to demonstrate its effectiveness.

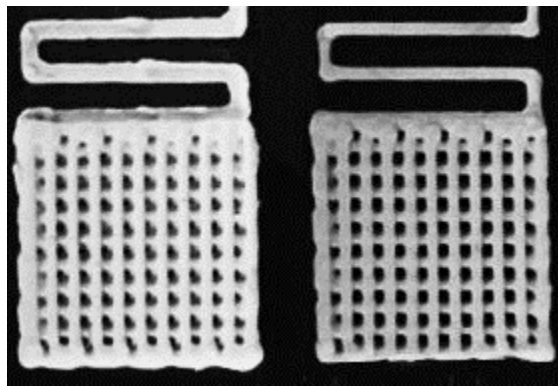


Figure 6.2 Multiple bone scaffolds printed in the same printing session. Here, the user chose $n=2$ and $m=4$.

6.2.1.4 Start/stop flow of the ink

Multi-material printing does not simply entail turning one material off and turning on another since ink dynamics add complications. In fact, there is a long time delay before ink flows out of the nozzle at ink start-up, and another delay before a fully developed flow is achieved [56]. This behavior is illustrated in Figure 6.3, which was generated with mechanical extrusion. Similar behavior was observed in this work with pneumatic extrusion, which complicated ink start-up and material termination. To address the long delay in ink flow for ink start-up, single material scaffolds were fabricated with lead-in-lines, which provided ample

time for the development of a full ink flow before scaffold fabrication begins. Further, lead in lines allowed the user to modify the applied pressure for inks with different rheology.

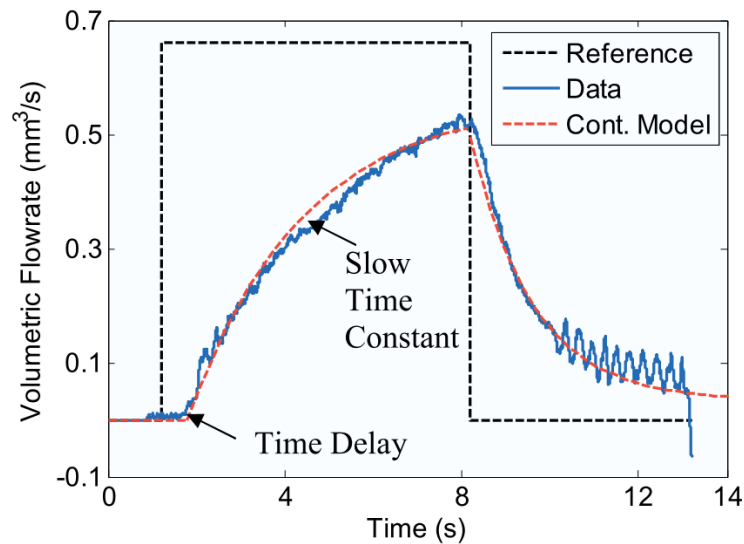


Figure 6.3 Ink dynamics during ink start-up and material termination. The response included a time delay and a slow time constant, which made precise start/stop of the ink flow challenging. Image from [24].

To accomplish a smooth transition between materials, ink flow must be precisely controlled with tuned algorithms to achieve start/stop flow. Towards this end, this work investigated whether precise start/stop of the colloidal ink could be achieved with the given positioning system and control environment. This work used a similar method commonly employed in Stratasys FDM systems for start/stop flow of the material [153]. The filament feed rate is controlled with a series of step inputs. At material start-up, Stratasys over-steps the roller speed, defining the pre-pump phase. At material termination, they under step the roller speed, resulting in material pull-back (Figure 6.4). This technique is run in open loop with the timing and pulse amplitude determined empirically [153].

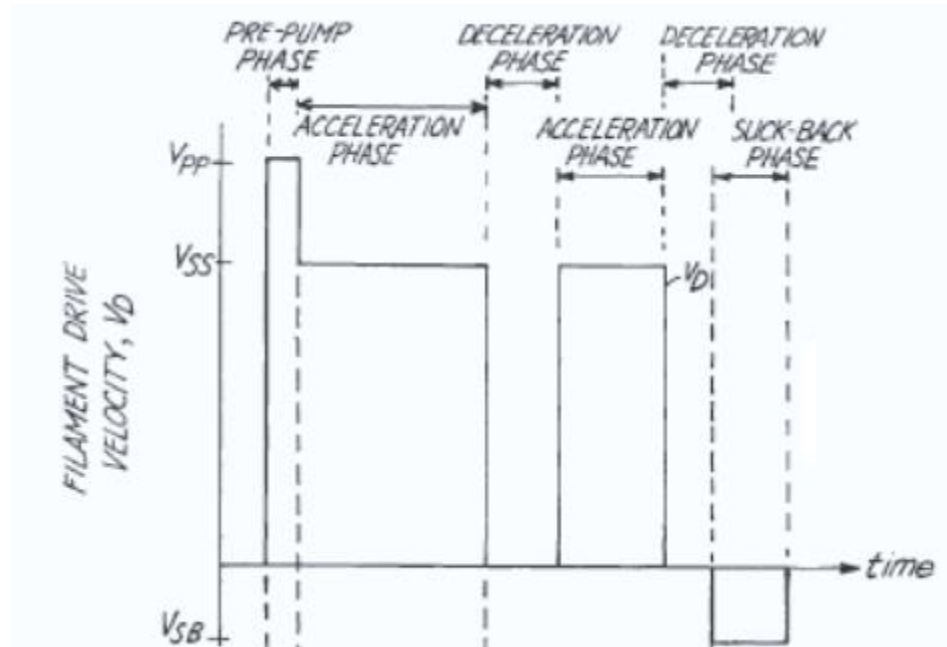


Figure 6.4 Timing diagram for start/stop flow of the polymer material in a Stratasys FDM printer [153].

A simplified version of the Stratasys method was implemented in a single scaffold layer to illustrate the machine capability of start and stop ink flow (Figure 6.6). A single scaffold layer with open pores at the scaffold edge (velocity reversals), illustrates precise start and stop of ink flow to enable multi-material printing.

The pressure reference signal profile developed to enable immediate start and stop of ink flow is shown on the time vs. pressure plot in Figure 6.5, which was included in the main program's GUI to make parameter selection more clear for the end-user. The pressure reference signal began at the operating pressure (OP) during fabrication of a rod in the X direction. At the scaffold edge, the X axis stopped moving and the pressure was cut to the No Flow Pressure (NFP), defined as the maximum pressure that does not result in material extrusion. The pressure reduction to NFP occurred at position A in Figure 6.5. Before the Y axis began the 1 mm movement at the scaffold edge, a wait time (WT) was coded into the sequence to ensure the ink had stopped flowing. The pressure remained at the NFP as the Y axis traversed the smaller, 1 mm movement (position B) where there was no material extrusion. At position C, the pressure reference signal increased as a series of short steps to smoothly

increase the pressure from NFP to OP. This transition ideally resulted in an ink start-up before the next scaffold rod was printed (position D). This sequence was repeated at each velocity reversal and successfully produced a single layer scaffold with start/stop ink flow.

In the GUI, the user chose the OP, NFP, step amplitudes (S1-S4), and timing parameters (WT, dt1, dt2, dt3). Each of these parameters were adjustable since colloidal inks are compressible and have a complex rheology that varies from batch to batch. For each new ink batch, the first step was to determine the NFP. Next, the step amplitudes and timing parameters were tuned to ensure a precise stop and smooth ink start-up after the velocity reversal.

While dropping the pressure to 0 psi resulted in an immediate stop in ink flow, any pressure buildup within the syringe was completely eliminated. Thus, when pressure was again applied during ink start up, ink “splurged” out in response to the large step response. For this particular ink batch, maintaining the maximum amount of pressure that did not result in ink flow (similar to a pre-stress) and smaller pressure modifications resulted in less ink “splurting” and smoother start/stop of ink flow. The pressure reference parameters selected for this ink batch are listed in the GUI control tabs in Figure 6.5.

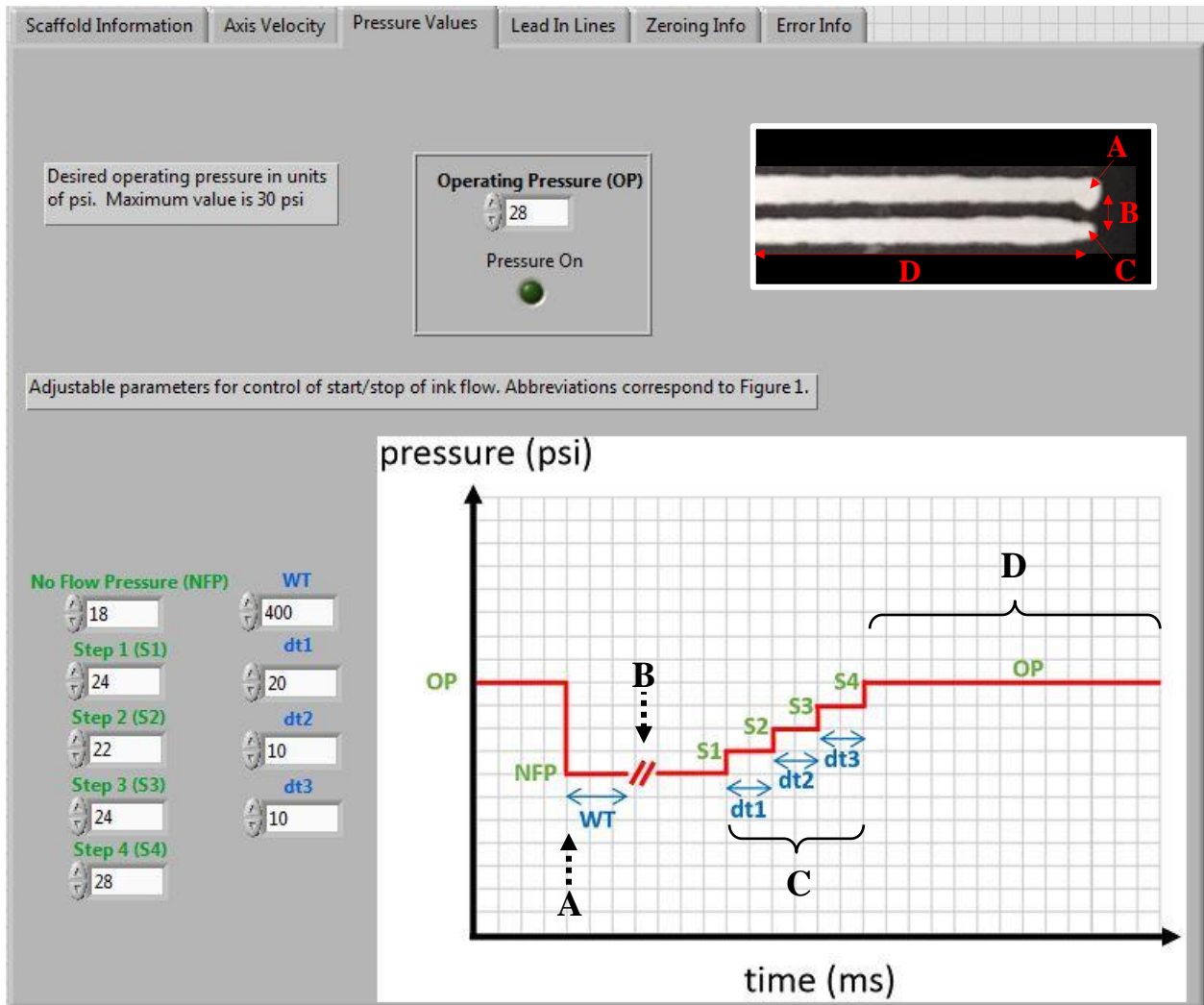


Figure 6.5 GUI in the start/stop ink flow LabVIEW code. The user-adjustable parameters are shown on the left, and the colors correspond to the parameters labeled in the time vs. pressure plot. Points A-D refer to specific locations in a scaffold print, shown in the black and white scaffold image.

Using the pressure reference signal with tuned step amplitudes and timing parameters, precise start/stop flow of the ink was demonstrated to illustrate the capability of multi-material printing in this system (Figure 6.6). Future work to incorporate multi-material printing into this system is discussed in Section 6.3.

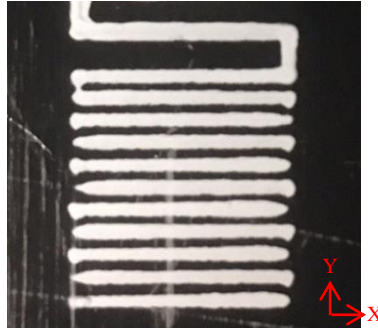


Figure 6.6 Preliminary results of start/stop flow of the ink in a single scaffold layer.

6.2.1.5 Curvilinear features

Despite enhanced bone growth in periodic, rectilinear scaffolds with multiscale porosity [10], [45], the structural units within bone are non-uniform and non-periodic. The discrepancy between the architecture of rectilinear scaffolds and the structural units within host bone present the need for curvilinear AM capabilities. As an example, trabeculae within trabecular bone (Chapter 5), align along the principle stress directions (Figure 6.7). Scaffolds implanted into these regions should incorporate curved rods into the layer architecture.

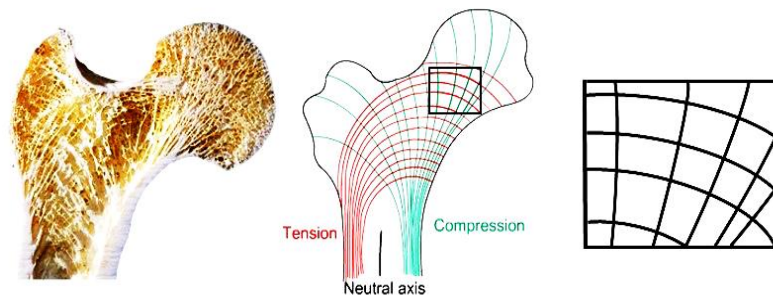


Figure 6.7 Cross section of a femur bone illustrating curved and non-uniform trabeculae (left), and a schematic highlighting how trabeculae follow principle stress-directions (middle). An example of a material deposition pattern for a curvilinear scaffold (right). Left two images adapted from [154], [155].

While the DW printer developed in this work did not print multi-layer scaffolds with curvilinear features, this section presents initial development steps for this capability and preliminary results. The design steps to create a motion profile for a curvilinear, single layer scaffold in the SoftMotion programming environment are listed below.

First, the motion profile was sketched in SolidWorks. The sketch started with a 10 x 10 *mm* reference square, which was the size of the rectilinear bone scaffolds commonly printed on the DW printer. Ideally, all curvilinear rods would fit into this reference square since future *in vivo* studies would potentially compare the amount of bone regeneration in uniform, rectilinear scaffolds to curvilinear scaffolds of similar size. Next, 12 circles with increasing radii were added to the drawing. The radii of each circle was incrementally increased to incorporate a gradient of radii of curvature. Further, each circle was tangent to reference lines drawn co-linear to the top (horizontal reference line) and right (vertical reference line) sides of the 10 x 10 *mm* reference square to simplify the implementation of the motion profile. Next, the circles were reduced to arcs, which were defined as the regions of the circle within the reference square. The angles of each arc were measured using the SolidWorks measurement tool. The motion profile developed for a single layer scaffold layer with 12 curvilinear rods is shown in Figure 6.8. The start point is circled in red, which is followed by arc 1 movement, a Straight Line Move in the + Y direction, arc 2 movement, a straight line move in the +X direction, and so on.

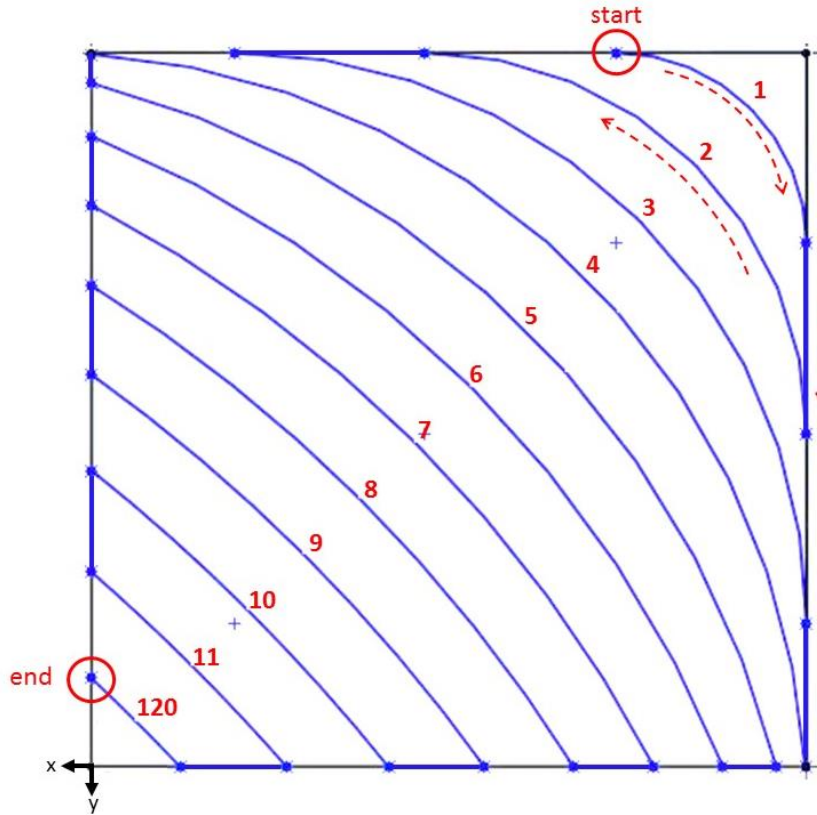


Figure 6.8 Initial Solidworks sketch of a scaffold with curvilinear rods in a single layer. The ideal end-effector path is outlined in blue. Each arc is labeled with a number.

The curvilinear design pattern was implemented as a series of Arc Move Mode Express VI's in SoftMotion, which perform a circular arc move on a motion reference (in this case, the reference was the X and Y axes). The user parameters defined an arc in the x-y plane of a two-dimensional coordinate space. The required user parameters were the motion reference (X and Y axes), velocity, circle radius, starting angle (SA), and travel angle (TA). The GUI which allows the user to change each of these parameters for each arc is shown in Figure 6.9. The number of arcs and each of the arc parameters could easily be changed by the end user.

The GUI also includes a picture of how the arc parameters were defined in SoftMotion. The image was projected onto the printing platform and the direction of each axis is indicated. The radius parameter was the radius of the circle reference, defined in *mm*. The region of this reference circle defining the arc motion profile was described by two parameters: SA and TA. The SA was defined as the angle clockwise from the $\theta = 0^\circ$ point of the circle. The TA was

the angle of the arc segment. The radius, SA, and TA were all measured within Solidworks using the sketch consisting of the reference square and 12 arcs. The X and Y axis straight line move distances, incorporated between each arc segment, were also measured in Solidworks, and were defined as the distance between each intersection point with the reference square.

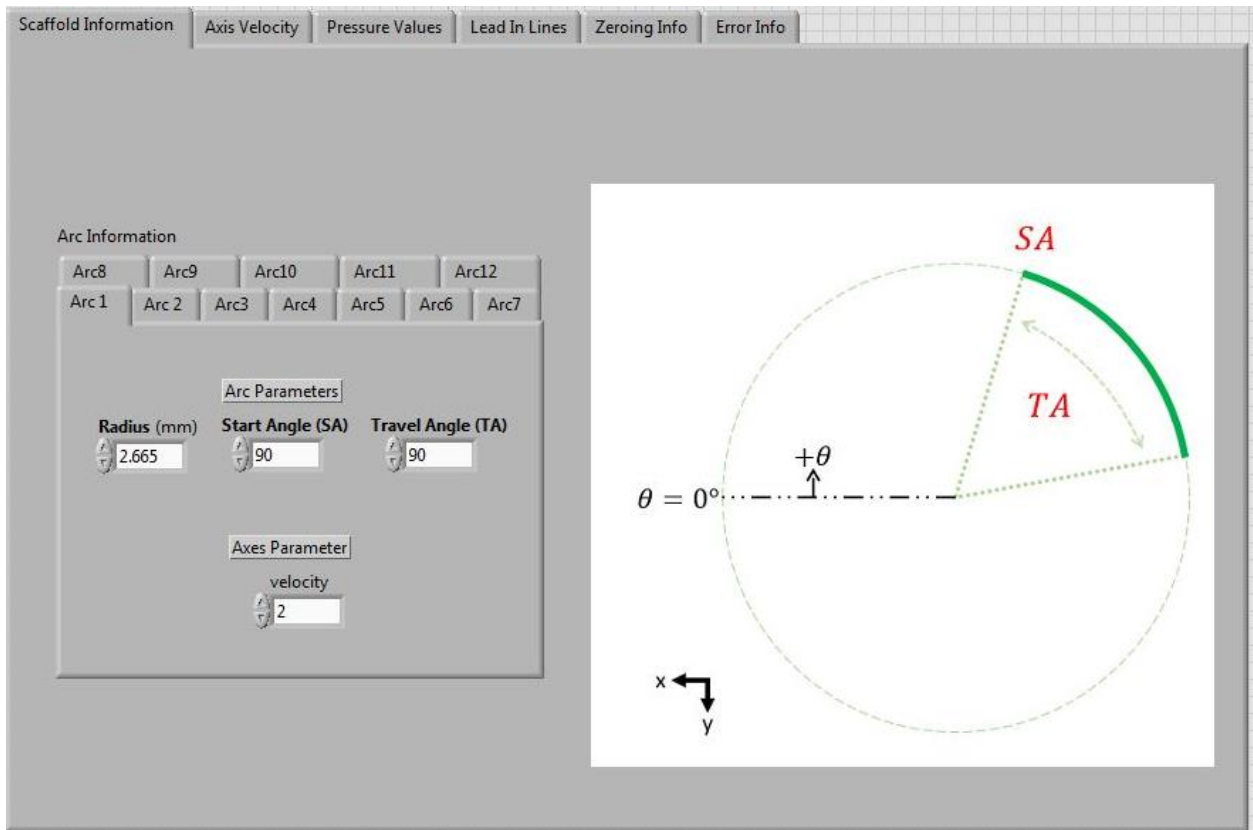


Figure 6.9 GUI of the curvilinear scaffold code implemented in LabVIEW. For each of the arc segments, the user must define the radius, SA, TA, and axis velocity. The parameters for each arc segment are organized as tabs.

This protocol was successfully implemented in SoftMotion, resulting in a single layer bone scaffold with curved rods (Figure 6.10). The parameters defined for each arc segment are listed in Table 6.2 for reference. The ink build up at velocity reversals is currently being addressed for future work.



Figure 6.10 Implementation of the curvilinear architecture on the DW printer with colloidal ink. The vertical rod at the top of the image is part of the lead-in-line, which was incorporated to ensure fully developed ink flow before starting scaffold fabrication.

Table 6.2 Arc segment parameters defined in Figure 6.9 used to fabricate the curvilinear scaffold shown in Figure 6.10.

Arc Segment #	Radius (mm)	Start Angle (SA) (degrees)	Travel Angle (TA) (degrees)
1	2.665	90.000	90.00
2	5.335	180.00	-90.00
3	8.000	80.000	90.00
4	10.665	176.41	-82.83
5	13.335	104.48	61.04
6	16.000	157.97	-45.95
7	18.665	117.66	34.67
8	21.335	147.91	-25.82
9	24.000	125.69	18.63
10	26.665	141.32	-12.64
11	29.335	131.32	7.540
12	32.000	136.56	-3.130

6.2.2 Limitations

As discussed previously, the main application of this printer was the fabrication of rectilinear bone scaffolds. More advanced bone scaffold architectures would require a positioning platform with higher precision, and a more advanced control architecture. The SoftMotion control architecture limited the control scheme to a simple Feedforward + Feedback control structure (Chapter 2). Thus, any advanced control algorithms such as model predictive control (MPC) and ILC could not be implemented. While a user-friendly ILC algorithm was presented, this offline training protocol only accounted for error in the X and Y directions for a single iteration, and any errors in the Z direction were ignored. Further, the SoftMotion feedback loop was a simple PID control structure. When a PID control strategy is implemented on a system with delays (each axis in this work had delays), the controller waits to respond until an error shows up, resulting in irreversible defects. These errors propagate from layer to layer since the PID control architecture is not adaptive.

Another consequence of the SoftMotion was that the programming environment was required to operate in closed-loop, eliminating any open-loop system identification methods. As a result, obtaining accurate system models for each axis was challenging and completely eliminating nonlinear disturbances was not possible. Despite these restrictions, the implementation of a PID feedback loop, friction compensation and user-friendly ILC algorithm enabled fabrication of precise rectilinear bone scaffolds.

6.2.3 Placement in current manufacturing space

The current manufacturing space of DW printing with ceramic colloidal ink discussed in Chapter 1 enables the fabrication of multi-material, net shape bone scaffolds [12]. Despite a few exceptions, the DW printers in this manufacturing space are often confined to a single shape and designated for a single project. Moreover, the controllable printing parameters are often limited to controls such as path speed, path width, nozzle size and deposition rate. Even further, difficulties faced from motion control problems in initial machine set up are rarely discussed and positioning control parameters are often not accessible to the end-user. These considerations limit the machine flexibility and end-user design (EUD). Instead, it would be

ideal if equipment used in multi-material research, such as 3D printing for biological applications, was easy-to-use and easy-to-adjust for all members on a given research team.

While the capabilities of this DW printer do not advance the current technical state of the art for DW printing, one the unique aspects of this work was the consideration of user-centered design (UCD) in the control system design and setup. The design steps presented in this work, which included disturbance rejection, system modeling, control design, active pressure regulation, and simple ILC implementation, were presented in a way that end-users outside of the controls field could follow. This work hopes to encourage EUD in future motion control and algorithm development applications to ensure this technology can be used by a wider audience.

6.3 Future Directions

This section will first discuss future work for this DW printer. In addition, future direction for the fields of bone tissue engineering and AM will be discussed.

6.3.1 Future work for this DW printer

6.3.1.1 ILC Implementation

The training protocol resembling a simple ILC algorithm (Chapter 4) should be further developed to include additional training iterations and weightings on axis movements with large errors. For example, the first X axis movement was typically smaller than the successive X axis movements during fabrication. A higher weighting on the control effort for the first X axis movement would improve reference tracking and minimize errors.

Further, this offline training algorithm, which improved performance in rectilinear bone scaffold fabrication, was not possible with the curvilinear architecture (Figure 6.9) since there was not a method in SoftMotion to calculate curvature errors. This limitation demonstrates the need for a more advanced control structure for error correction in AM parts with curvilinear features.

6.3.1.2 Start/stop of ink flow

While the preliminary results of precisely starting and stopping ink flow were promising, significant improvements could be made to the algorithm and each of the parameters could be further optimized. One of the biggest errors occurred at velocity reversals, where an immediate ink-start was not achieved. The time delay in the development of a full ink flow is evident in Figure 6.6 at the scaffold edges. An example of a modification in the pressure reference signal is shown in Figure 6.11. The operating pressure (OP) was still dropped to the no flow pressure (NFP), but a pressure spike (PS) was incorporated at ink start up to attempt to eliminate the time delay seen in the development of full ink flow. This method is similar to the Stratasys method, which over pumped material during the “pre-pump phase” (Figure 6.4) [153]. Preliminary results using this modified pressure reference signal are shown on the right of Figure 6.11. The PS resulted in large ink blobs, which could have been due to using ink with too low of a viscosity, or improper tuning of the modified pressure reference signal. Future modifications should involve optimizing this reference signal to achieve precise ink start-up at velocity reversals.

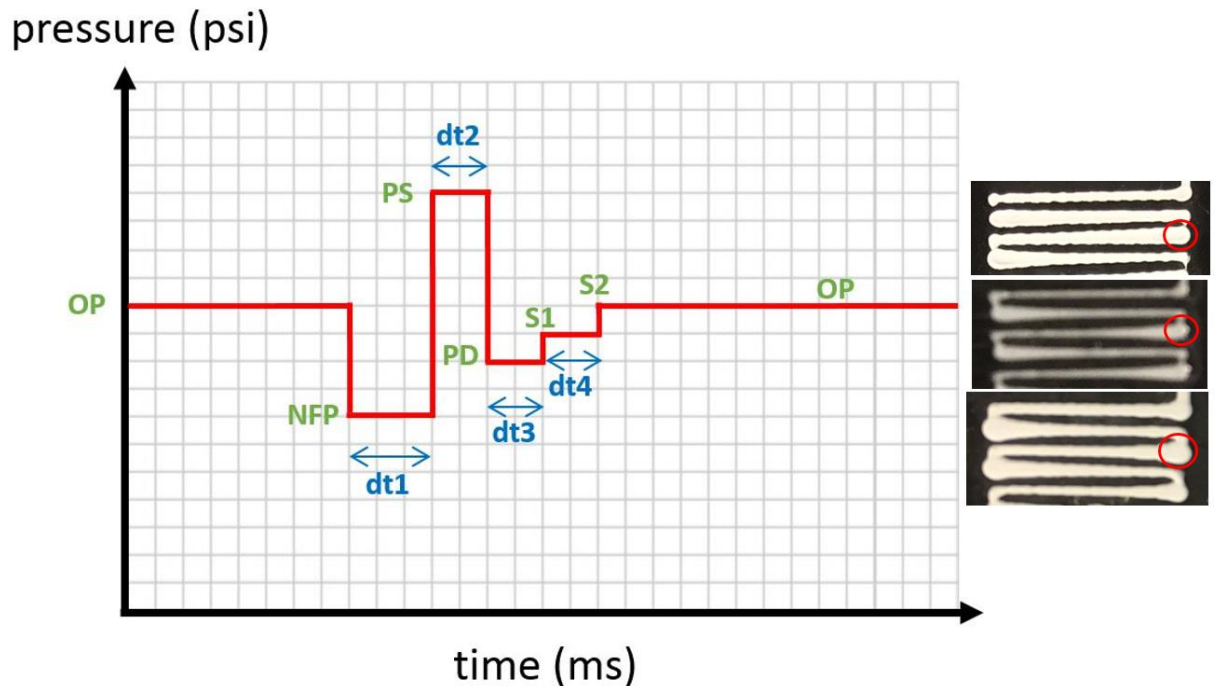


Figure 6.11 Modified pressure reference signal, where a pressure spike (PS) was incorporated to attempt to reduce the time delay in the development of full ink flow.

6.3.1.3 Multi-material printing

In addition to improved pressure regulation discussed above, multi-material printing would require adjustments to the extrusion system. The end-effector would need to be redesigned to hold two syringes. Further, either another pressure regulator would need to be purchased for control of the pressure applied to the additional syringe of material, or a Y valve could be incorporated to enable switching of applied pressure between the two syringes.

In addition, the original machine platform included two extruder heads. Only one of these was modified and controlled for scaffold fabrication. Instead of including two syringes on the same extrusion system, future work could involve modifying the additional head for multi-material printing. Precise movement coordination between the two heads would be required for precise start/stop of multi-material inks within a single build.

6.3.1.4 Curvilinear scaffolds

While this work demonstrated a single layer scaffold with curvilinear features, defining the arc segment parameters was tedious and was performed in an external program (Solidworks). Future work should ideally incorporate a mathematical equation or algorithm to compute the radii of each rod and the arc segment's SA and TA based on a user-inputted figure or design specifications. Further, the code protocol designed in LabVIEW SoftMotion should be extended to additional layers. To more closely follow the non-uniform architecture of the structural units of bone, the radii of curvature gradient should vary from layer to layer.

6.3.2 Bone Tissue Engineering (BTE)

One of the current limiting features in tissue engineering is AM techniques, since AM processes inevitably induce defects, which deteriorate the performance of additively manufactured scaffolds [15]. Additional research on AM process parameter control are in urgent need to advance the field of BTE [15]. In addition, Murphy et al. defined specific areas within BTE where future research is needed [2].

- Increased speed and resolution of the positioning platforms of AM processes
- Scaling up for commercial applications
- Combining bioprinting techniques to overcome technical challenges

Another key area of future research in (bio) 3D printing lies in direct *in situ* bioprinting, where cells and biomaterials are printed directly onto a patient [51]. This technique has the potential to enhance tissue regeneration and reduce recovery time [51]. Similar to the areas defined by Murphy, this technique requires improvements in speed and resolution of the bioprinting technologies.

In the field of bone tissue regeneration (BTE), in particular, there is still a research gap in fabricating net shape bone scaffolds which more closely resemble the non-uniform, non-periodic architectures of bone structural units. As discussed in Chapter 5, *in vitro* experiments have illustrated that surface curvature enhances the amount of bone tissue regeneration [156], [157]. Thus, future bone scaffold designs should incorporate curved features in the scaffold architecture. Towards this end, Naddeo et al. have developed an FEA-based algorithm to fabricate bone scaffolds with curvilinear features that more closely resemble the internal structure of bone. The scaffold rods were mostly oriented along the principal stress directions according to the loads applied at the boundary conditions [158]. The advanced scaffold design, however, was printed on a commercial SLA printer with a polymer-based material. This architecture is not currently possible with DW printing of ceramic colloidal inks.

6.3.3 Additive Manufacturing (AM)

Despite significant recent advancements, a major limitation of DW printing and AM in general is the lack of direct process control. An assumption in this work, and in many AM systems both on the market and in academia, is that precision control in the machine axis frame (joint space) is equivalent to precision control in the material deposition frame (task space) since the position measurements are taken at the axis level through rotary and linear encoders, and not at the deposition tip. Due to imperfect coordination between the joint and task spaces, however, there is no guarantee perfect regulation of the joint space results in the desired task space results. Further, the errors between the two spaces would accumulate due to a lack of direct process monitoring in the task space. In fact, there is currently no 3D printing on the market with closed loop control on the material deposition frame. Layer defects, resulting from fluctuations in process parameters or external disturbances, can't be eliminated in an open loop control system. These defects are compounded layer-by-layer.

One of the most challenging aspects for process control in AM, however, is the limited access to the build chamber and the need for intensive computing power with the sensor data [159]. Further, even if sensing data is accessible, a remaining challenge is relating the sensing data to a process parameter of interest.

Future work in AM should include direct measurement of the deposition tip and closed-loop control in the task space. The development of in situ monitoring and advanced control strategies are needed to avoid defects which impact functional and mechanical outcomes of the printed constructs [159]. There are not, however, many researchers discussing defects in the fabrication process, especially in the field of DW printing of artificial bone scaffolds. While process control is a completely separate and challenging field, the DW printing technology would be further developed if researchers in biology and material scientists work more closely with control engineers to improve process monitoring and control in general.

6.3.3.1 ILC Development

Future development should include the development of easy-to-use advanced control algorithms to further improve system performance. For curvilinear features, a more advanced ILC algorithm could be used to develop a training library for curvilinear features. Instead of continuously updating the control signal from layer to layer, a scaffold with curvilinear features could be broken down into the simple basis tasks. Hoelzle et al. developed an offline training library of control signals for each basis task of rectilinear scaffolds, which were sequenced to develop the control signal for a complete manufacturing cycle [160]. An example basis sequence for a scaffold layer would include: start, steady state, stop, corner, etc. A similar type strategy with a modified ILC algorithm could be developed to extend the method presented in [160] to curvilinear architectures. The library would consist of control signals for different radii of curvatures and Z axis movements to ensure tight control of the geometry in plane and layer height.

In addition, future work should focus on developing tuning guidelines for ILC parameters from the prospective of the finished part. For scaffolds, for example, tuning parameters of the ILC algorithm should be correlated to specific scaffold parameters: the X parameter of an ILC algorithm is specifically affected by viscosity, while the Y parameter in

the algorithm is affected by porosity, for example. This type of development would enable more intuitive tuning which would be easily related to the end result. Further, end-process related tuning parameters would enable end-users outside of the controls field to more easily adjust advanced control structures.

6.4 Thesis Summary

This thesis outlined the design steps for the development of a DW printing system for fabrication of rectilinear bone scaffolds. A description of DW printing and a review of the current manufacturing space was presented in Chapter 1. Chapter 2 described each component of the DW printing system including the positioning system, extrusion system, and hardware components. A review of Colloidal science and the steps required to make CaP-based colloidal ink were presented in Chapter 3. Chapter 4 presents system models and control strategies to improve performance of both the positioning and extrusion systems. Common motion control problems were addressed and implemented in a way that researchers outside of the controls field could easily understand. A review of bone tissue engineering and bone anatomy was presented in Chapter 5. Finally, Chapter 6 presented the current machine capabilities and limitations, and discussed future work for this DW printer and in the fields of AM and bone tissue engineering. While this work focused on DW printing, the design steps and motion control presented could be applied to the development of printers using other AM techniques, such as FDM.

This work presented the development of an easy-to-use DW printing system for two main reasons. First, the end users were typically graduate students in bioengineering or materials science who were assumed to have minimal knowledge of motion control. Thus, both printing properties and control parameters were adjusted with a minimal amount of user programming. Our hope is that this system can be easily operated and adjusted by future users for a wide range of projects. Second, processes involved in the development of a 3D printer, such as motion control, hardware selection, and machine coding, present a technical hurdle for some research groups looking to utilize the technology in other research fields. In addition, there are currently limited resources explaining each step of the machine design process. We hope the design and development steps presented in this work can be extended to other systems

to lower the technical hurdle of motion control for any laboratory or researcher with an interest in using DW printing in his or her field.

References

- [1] M. H. Ibrahim T. Ozbolat, “Current advances and future perspectives in extrusion-based bioprinting,” *Biomaterials*, vol. 76, pp. 321–343, 2016.
- [2] S. V Murphy and A. Atala, “3D bioprinting of tissues and organs,” *Nat. Biotechnol.*, vol. 32, no. 8, pp. 773–785, 2014.
- [3] S. Patra and V. Young, “A Review of 3D Printing Techniques and the Future in Biofabrication of Bioprinted Tissue,” *Cell Biochem. Biophys.*, pp. 93–98, 2016.
- [4] J. Zheng, “A multi-material 3D printing system and model-based layer-to-layer control algorithm for ink-jet printing process,” vol. 2014, no. April, 2014.
- [5] B. K. Gu, D. J. Choi, S. J. Park, M. S. Kim, C. M. Kang, and C.-H. Kim, “3-Dimensional Bioprinting for Tissue Engineering Applications,” *Biomater. Res.*, vol. 20, p. 12, 2016.
- [6] C. Bergmann *et al.*, “3D printing of bone substitute implants using calcium phosphate and bioactive glasses,” *J. Eur. Ceram. Soc.*, vol. 30, no. 12, pp. 2563–2567, 2010.
- [7] D. Hoelzle, S. Svientek, A. Alleyne, and A. W. Johnson, “Manufacturing Controls for the Fabrication of Tissue Scaffolds with Graded Microstructures,” in *Materials Science and Technology (MS&T)*, 2011, pp. 1469–1476.
- [8] D. J. Hoelzle, A. J. W. Johnson, and A. G. Alleyne, “Near-Net shape structures fabricated by micro-robotic deposition using precision extrusion control,” in *ASME/ISCIE International Symposium on Flexible Automation*, 2012, pp. 1–8.
- [9] D. J. Hoelzle, A. G. Alleyne, and A. J. Wagoner Johnson, “Micro-robotic deposition guidelines by a design of experiments approach to maximize fabrication reliability for the bone scaffold application,” *Acta Biomater.*, vol. 4, no. 4, pp. 897–912, 2008.
- [10] L. E. Rustom *et al.*, “Multiscale porosity directs bone regeneration in biphasic calcium phosphate scaffolds,” *ACS Biomater. Sci. Eng.*, p. acsbiomaterials.6b00632.
- [11] D. J. Hoelzle, S. R. Svientek, A. G. Alleyne, and A. J. Wagoner Johnson, “Design and Manufacture of Combinatorial Calcium Phosphate Bone Scaffolds,” *J. Biomech. Eng.*,

- vol. 133, no. 10, p. 101001, 2011.
- [12] Y. Xie *et al.*, “Net shape fabrication of calcium phosphate scaffolds with multiple material domains,” *Biofabrication*, vol. 8, no. 1, p. 15005, 2016.
- [13] C. Le *et al.*, “Advances in Bone Tissue Engineering,” *Regen. Med. Tissue Eng.*, pp. 599–614, 2013.
- [14] R. Mishra, T. Bishop, I. Valerio, J. Fisher, and D. Dean, “The potential impact of bone tissue engineering in the clinic,” *Regen. Med.*, vol. 11, no. 6, pp. 571–87, 2016.
- [15] A. R. Amini, C. T. Laurencin, and S. P. Nukavarapu, “Bone Tissue Engineering: Recent Advances and Challenges,” *Crit. Rev. Biomed. Eng.*, vol. 40, no. 5, pp. 363–408, 2012.
- [16] M. A. Velasco, C. A. Narvaez-Tovar, and D. A. Garzon-Alvarado, “Design, materials, and mechanobiology of biodegradable scaffolds for bone tissue engineering,” *Biomed Res. Int.*, vol. 2015, p. 729076, 2015.
- [17] A. Oryan, S. Alidadi, A. Moshiri, and N. Maffulli, “Bone regenerative medicine: classic options, novel strategies, and future directions,” *J. Orthop. Surg. Res.*, vol. 9, no. 1, p. 18, 2014.
- [18] A. J. Wagoner Johnson and B. A. Herschler, “A review of the mechanical behavior of CaP and CaP/polymer composites for applications in bone replacement and repair,” *Acta Biomater.*, vol. 7, no. 1, pp. 16–30, 2011.
- [19] H. C. Pape, A. Evans, and P. Kobbe, “Autologous Bone Graft: Properties and Techniques,” *J. Orthop. Trauma*, vol. 24, no. 3, pp. S36–S40, 2010.
- [20] L. H. Nguyen *et al.*, “Vascularized Bone Tissue Engineering: Approaches for Potential Improvement,” *Tissue Eng. Part B Rev.*, vol. 18, no. 5, pp. 363–382, 2012.
- [21] S. V. Murphy and A. Atala, “3D bioprinting of tissues and organs,” *Nat. Biotechnol.*, vol. 32, no. 8, pp. 773–785, 2014.
- [22] L. E. Rustom *et al.*, “Multiscale porosity directs bone regeneration in biphasic calcium phosphate scaffolds,” *ACS Biomater. Sci. Eng.*, p. acsbiomaterials.6b00632, 2016.
- [23] D. A. Bristow and A. G. Alleyne, “A high precision motion control system with application to microscale robotic deposition,” *IEEE Trans. Control Syst. Technol.*, vol. 14, no. 6, pp. 1008–1020, 2006.

- [24] D. J. Hoelzle, "Reliability Guidelines and Flowrate Modulation for a Micro Robotic Deposition System," University of Illinois at Urbana-Champaign, 2007.
- [25] H. Lieberman, F. Paternò, and V. Wulf, "End User Development," *End User Dev.*, vol. 9, no. August, p. 492, 2006.
- [26] P. W. Quimby, R. Khire, F. Leonardi, and S. Sarkar, "A Novel Human Machine Interface for Advanced Building Controls and Diagnostics," *3rd Int. High Perform. Build. Conf.*, pp. 1–10, 2014.
- [27] K. R. Guerin, C. Lea, C. Paxton, and G. D. Hager, "A framework for end-user instruction of a robot assistant for manufacturing," *2015 IEEE Int. Conf. Robot. Autom.*, pp. 6167–6174, 2015.
- [28] N. Gowda, W. Ju, D. Sirkin, and M. Baltzer, "Prototyping HMI for Autonomous Vehicles : A Human Centered Design Approach," pp. 229–231, 2016.
- [29] A. Kubler *et al.*, "The user-centered design as novel perspective for evaluating the usability of BCI-controlled applications," *PLoS One*, vol. 9, no. 12, pp. 1–22, 2014.
- [30] M. D. Griffiths and H. M. Pontes, "Handbook of Digital Games and Entertainment Technologies," pp. 1–22, 2015.
- [31] H. Lieberman, F. Paternò, and V. Wulf, *End User Development*, vol. 9, no. August. 2006.
- [32] Z. Yang, S. Ki, and N. Kevin, "User-centered design for additive manufacturing as a customization strategy.," in *International Conference on Progress in Additive Manufacturing*, 2016, pp. 234–239.
- [33] A. Ferreira, K. M. Arif, S. Dirven, and J. Potgieter, "Retrofitment, open-sourcing, and characterisation of a legacy fused deposition modelling system," *Int. J. Adv. Manuf. Technol.*, 2016.
- [34] R. Trombetta, J. A. Inzana, E. M. Schwarz, S. L. Kates, and H. A. Awad, "3D Printing of Calcium Phosphate Ceramics for Bone Tissue Engineering and Drug Delivery," *Ann. Biomed. Eng.*, vol. 45, no. 1, pp. 1–22, 2016.
- [35] L. E. Bertassoni *et al.*, "Direct-write bioprinting of cell-laden methacrylated gelatin hydrogels," *Biofabrication*, vol. 6, no. 2, p. 24105, 2014.
- [36] B. Paquette, "Direct Write Printing on Thin and Flexible Substrates for Space

- Applications Introduction : Direct-Write Printing and Aerosol Jet Printing,” pp. 1–22, 2016.
- [37] M. Dukic *et al.*, “Direct-write nanoscale printing of nanogranular tunnelling strain sensors for sub-micrometre cantilevers,” *Nat. Commun.*, vol. 7, p. 12487, 2016.
- [38] A. M. N. Al-Mobin, R. Shankar, W. Cross, J. Kellar, W. K.W., and D. E. Anagnostou, “Advances in Direct-Write Printing of RF-MEMS using M3D,” *Microw. Symp. (IMS), IEEE MTT-S Int.*, p. 2, 2014.
- [39] H.-W. Kang, S. J. Lee, I. K. Ko, C. Kengla, J. J. Yoo, and A. Atala, “A 3D bioprinting system to produce human-scale tissue constructs with structural integrity,” *Nat. Biotechnol.*, vol. 34, no. 3, pp. 312–319, 2016.
- [40] Y. S. Zhang *et al.*, “3D Bioprinting for Tissue and Organ Fabrication,” *Ann. Biomed. Eng.*, pp. 1–16, 2016.
- [41] W. Chen *et al.*, “Direct metal writing: Controlling the rheology through microstructure,” *Appl. Phys. Lett.*, vol. 110, no. 9, 2017.
- [42] R. D. Farahani, K. Chizari, and D. Therriault, “Three-dimensional printing of freeform helical microstructures: a review,” *Nanoscale*, vol. 6, no. 18, pp. 10470–85, 2014.
- [43] M. Gou *et al.*, “Bio-inspired detoxification using 3D-printed hydrogel nanocomposites,” *Nat. Commun.*, vol. 5, no. May, pp. 1–9, 2014.
- [44] R. Bey-Oueslati, S. J. Palm, D. Therriault, and S. Martel, “High Speed Direct-Write For Rapid Fabrication Of Three- Dimensional Microfluidic Devices,” *Int. J. Heat Technol.*, vol. 26, no. 1, pp. 125–131, 2008.
- [45] L. E. Rustom *et al.*, “Micropore-induced Capillarity Enhances Bone Distribution in vivo in Biphasic Calcium Phosphate Scaffolds,” *Acta Biomater.*, vol. 44, pp. 5–7, 2016.
- [46] B. Bhushan and M. Caspers, “An overview of additive manufacturing (3D printing) for microfabrication,” *Microsyst. Technol.*, vol. 23, no. 4, pp. 1117–1124, 2017.
- [47] R. Bogue, “3D printing: the dawn of a new era in manufacturing?,” *Assem. Autom.*, vol. 33, no. 4, pp. 307–311, 2013.
- [48] T. Wohlers, “Wohlers Report 2014,” Fort Collins, 2014.
- [49] A. Bournias-Varotsis, “Industrial FDM vs. Desktop FDM,” 2017.

- [50] S. T. Inc., “No Title,” 2010. [Online]. Available: <http://www.si2technologies.com/manufacturing/>.
- [51] N. A. Sears, D. R. Seshadri, P. S. Dhavalikar, and E. Cosgriff-hernandez, “A Review of Three-Dimensional Printing in Tissue Engineering,” vol. 22, no. 4, pp. 298–310, 2016.
- [52] Stratasys, “Stratasys Products.” [Online]. Available: <http://www.stratasys.com/3d-printers/design-series>.
- [53] P. Sitthi-amorn, J. Lan, and W. Wang, “MultiFab : A Machine Vision Assisted Platform for Multi-material 3D Printing,” *ACM Trans. Graph.*, no. 34, p. 11, 2015.
- [54] I. Raza, L. Iannucci, and P. T. Curtis, “Introducing a Multimaterial Printer for the Deposition of Low Melting Point Alloys , Elastomer , and Ultraviolet Curable Resin,” *3D Print. Addit. Manuf.*, vol. 4, no. 2, pp. 82–89, 2017.
- [55] J. O. Hardin, T. J. Ober, A. D. Valentine, and J. A. Lewis, “Microfluidic Printheads for Multimaterial 3D Printing of Viscoelastic Inks,” *Adv. Mater.*, pp. 3279–3284, 2015.
- [56] D. J. Hoelzle, A. G. Alleyne, and A. J. Wagoner Johnson, “Iterative Learning Control for robotic deposition using machine vision,” *2008 Am. Control Conf.*, pp. 4541–4547, 2008.
- [57] J. A. Reid, P. A. Mollica, G. D. Johnson, R. C. Ogle, R. D. Bruno, and P. C. Sachs, “Accessible bioprinting: adaptation of a low-cost 3D-printer for precise cell placement and stem cell differentiation,” *Biofabrication*, vol. 8, 2016.
- [58] M. Fasano and S. Dirk, “4-axis, Multi-Material Extruding, Direct Write Additive Manufacturing Tool,” Sandia National Labs, 2017.
- [59] A. Zocca and G. Franchin, “Direct Ink Writing of a Preceramic Polymer and Fillers to Produce Hardystonite ($\text{Ca}_2\text{ZnSi}_2\text{O}_7$) Bioceramic Scaffolds,” no. May, 2016.
- [60] E. Feilden, E. G. T. Blanca, F. Giuliani, E. Saiz, and L. Vandeperre, “Robocasting of structural ceramic parts with hydrogel inks,” *J. Eur. Ceram. Soc.*, vol. 36, no. 10, pp. 2525–2533, 2016.
- [61] C. Wu *et al.*, “3D-printing of highly uniform CaSiO_3 ceramic scaffolds: preparation, characterization and in vivo osteogenesis,” *J. Mater. Chem.*, vol. 22, no. 24, pp.

- 12288–12295, 2012.
- [62] C. F. Marques *et al.*, “Biphasic calcium phosphate scaffolds fabricated by direct write assembly: Mechanical, anti-microbial and osteoblastic properties,” *J. Eur. Ceram. Soc.*, vol. 37, no. 1, pp. 359–368, 2017.
- [63] L. Rueschhoff, W. Costakis, M. Michie, J. Youngblood, and R. Trice, “Additive Manufacturing of Dense Ceramic Parts via Direct Ink Writing of Aqueous Alumina Suspensions,” vol. 830, pp. 821–830, 2016.
- [64] W. J. C. Jr, L. M. Rueschhoff, A. I. Diaz-cano, J. P. Youngblood, and R. W. Trice, “manufacturing of boron carbide via continuous filament direct ink writing of aqueous ceramic suspensions,” *J. Eur. Ceram. Soc.*, vol. 36, no. 14, pp. 3249–3256, 2016.
- [65] J. L. Ricci, E. a. Clark, A. Murriky, and J. E. Smay, “Three-Dimensional Printing of Bone Repair and Replacement Materials,” *J. Craniofac. Surg.*, vol. 23, no. 1, pp. 304–308, 2012.
- [66] J. Franco, P. Hunger, M. E. Launey, a. P. Tomsia, and E. Saiz, “Direct write assembly of calcium phosphate scaffolds using a water-based hydrogel,” *Acta Biomater.*, vol. 6, no. 1, pp. 218–228, 2010.
- [67] P. Ravi, P. Shiakolas, J. C. Oberg, S. Faizee, and A. Batra, “On the development of a modular 3D bioprinter for research in biomedical device fabrication,” in *ASME 2015 International Mechanical Engineering Congress and Exposition*, 2015, pp. 1–9.
- [68] G. Vozzi, a Previti, D. De Rossi, and a Ahluwalia, “Microsyringe-based deposition of two-dimensional and three-dimensional polymer scaffolds with a well-defined geometry for application to tissue engineering.,” *Tissue Eng.*, vol. 8, no. 6, pp. 1089–1098, 2002.
- [69] C. R. Almeida, T. Serra, M. I. Oliveira, J. A. Planell, M. A. Barbosa, and M. Navarro, “Impact of 3-D printed PLA- and chitosan-based scaffolds on human monocyte/macrophage responses: Unraveling the effect of 3-D structures on inflammation,” *Acta Biomater.*, vol. 10, no. 2, pp. 613–622, 2014.
- [70] Z. Wang, J. K. Min, and G. Xiong, “Robotics-driven printing of curved 3D structures for manufacturing cardiac therapeutic devices,” *2015 IEEE Int. Conf. Robot. Biomimetics, IEEE-ROBIO 2015*, pp. 2318–2323, 2016.

- [71] D. B. Kolesky, K. A. Homan, M. A. Skylar-Scott, and J. A. Lewis, “Three-dimensional bioprinting of thick vascularized tissues,” *Proc. Natl. Acad. Sci. U. S. A.*, vol. 113, no. 12, pp. 3179–84, 2016.
- [72] “National Instruments NI-9514.” [Online]. Available: <http://www.ni.com/en-us/support/model.ni-9514.html>.
- [73] “Advanced Motion Controls.” [Online]. Available: <https://www.a-m-c.com/products/?page=product&cid=root&id=AZB12A8>.
- [74] “Faulhaber Product Overview.” [Online]. Available: https://fmcc.faulhaber.com/details/overview/PGR_5826_13838/PGR_13838_13804/en/GLOBAL/.
- [75] “PRO-MIC Roll Measurement Systems Online Store.” [Online]. Available: http://www.pro-mic.com/store/products/product_details.php?pn=PM-PRT302.
- [76] “Gurley Precision Instruments Linear Encoders.” [Online]. Available: http://www.gurley.com/Encoders/08_Linear.htm.
- [77] J. Cesarano, “A Review of Robocasting Technology,” *MRS Proc.*, vol. 542, pp. 133–139, 1999.
- [78] J. A. Lewis, “Direct ink writing of 3D functional materials,” *Adv. Funct. Mater.*, vol. 16, no. 17, pp. 2193–2204, 2006.
- [79] J. Shi, “Steric Stabilization, Literature Review,” 2002.
- [80] J. A. Lewis, “Colloidal Processing of Ceramics,” *J. Am. Ceram. Soc.*, vol. 83, no. 10, pp. 2341–2359, 2000.
- [81] J. Law and A. Brab, “Colloids,” 2017. [Online]. Available: https://chem.libretexts.org/Core/Physical_and_Theoretical_Chemistry/Physical_Properties_of_Matter/Solutions_and_Mixtures/Colloid.
- [82] R. S. Subramanian, “Non-Newtonian Flows.” pp. 1–5.
- [83] S. Michna, W. Wu, and J. a. Lewis, “Concentrated hydroxyapatite inks for direct-write assembly of 3-D periodic scaffolds,” *Biomaterials*, vol. 26, no. 28, pp. 5632–5639, 2005.
- [84] J. S. Reed, *Introduction to the Principles of Ceramic Processing*. United States of America: John Wiley and Sons, 1987.

- [85] P. Miranda, E. Saiz, K. Gryn, and A. P. Tomsia, "Sintering and robocasting of b-tricalcium phosphate scaffolds for orthopaedic applications," vol. 2, pp. 457–466, 2006.
- [86] M. A. Lopez-Heredia, M. Bohner, W. Zhou, A. J. A. Winnubst, J. G. C. Wolke, and J. A. Jansen, "The effect of ball milling grinding pathways on the bulk and reactivity properties of calcium phosphate cements," *J. Biomed. Mater. Res. - Part B Appl. Biomater.*, vol. 98 B, no. 1, pp. 68–79, 2011.
- [87] A. B. Makokha, M. H. Moys, A. M. Muumbo, and R. J. Kiprono, "Optimization of in-mill ball loading and slurry solids concentration in grinding of UG-2 ores: A statistical experimental design approach," *Miner. Eng.*, vol. 39, pp. 149–155, 2012.
- [88] A. Bignon, J. Chevalier, and G. Fantozzi, "Effect of ball milling on the processing of bone substitutes with calcium phosphate powders," *J. Biomed. Mater. Res.*, vol. 63, no. 5, pp. 619–626, 2002.
- [89] S. Adzila *et al.*, "Mechanochemical synthesis of nanohydroxyapatite bioceramics," *Indian J. Chem. - Sect. A Inorganic, Phys. Theor. Anal. Chem.*, vol. 52, no. 12, pp. 1570–1575, 2013.
- [90] J. Zhang, N. Epstein, and J. R. Grace, "Prediction of product size distributions for a stirred ball mill," *Powder Technol.*, vol. 84, pp. 101–106, 1995.
- [91] Y. Chen, X. Lian, Z. Li, S. Zheng, and Z. Wang, "Effects of rotation speed and media density on particle size distribution and structure of ground calcium carbonate in a planetary ball mill," *Adv. Powder Technol.*, vol. 26, no. 2, pp. 505–510, 2015.
- [92] P. Welche, "Phase Diagrams, Practical 19." Interference Lab, pp. 1–8, 2009.
- [93] Ayouril, "Electro-Steric Stabilization.jpg." Wikipedia Commons.
- [94] S. Biggs and T. W. Healy, "Electrosteric Stabilisation of Colloidal Zirconia with Low-molecular-weight Polyacrylic Acid," *J. Chem. Soc.*, vol. 90, no. 22, pp. 3415–3421, 1994.
- [95] N. Dobelin, "Personal Communication via Email (nicola.dobelin@rms-foundation.ch)." 2016.
- [96] P. V. Riboud, "Composition and stability of apatites in the system CaO-P2O5-iron oxide-H2O at high temperature.," *Ann. Chim.*, vol. 8, pp. 381–390, 1973.

- [97] J. H. Welch and W. Gutt, “High-temperature Studies of the System Calcium Oxide-Phosphorous Pentoxide,” *J Chem Soc*, no. 874, pp. 4442–4444, 1961.
- [98] J. R. Woodard *et al.*, “The mechanical properties and osteoconductivity of hydroxyapatite bone scaffolds with multi-scale porosity,” *Biomaterials*, vol. 28, no. 1, pp. 45–54, 2007.
- [99] S. K. Lan Levengood *et al.*, “The effect of BMP-2 on micro- and macroscale osteointegration of biphasic calcium phosphate scaffolds with multiscale porosity,” *Acta Biomater.*, vol. 6, no. 8, pp. 3283–3291, 2010.
- [100] S. K. Lan Levengood *et al.*, “Multiscale osteointegration as a new paradigm for the design of calcium phosphate scaffolds for bone regeneration,” *Biomaterials*, vol. 31, no. 13, pp. 3552–3563, 2010.
- [101] S. J. Polak, S. K. L. Levengood, M. B. Wheeler, A. J. Maki, S. G. Clark, and A. J. W. Johnson, “Analysis of the roles of microporosity and BMP-2 on multiple measures of bone regeneration and healing in calcium phosphate scaffolds,” *Acta Biomater.*, vol. 7, no. 4, pp. 1760–1771, 2011.
- [102] S. J. Polak, L. E. Rustom, G. M. Genin, M. Talcott, and A. J. Wagoner Johnson, “A mechanism for effective cell-seeding in rigid, microporous substrates,” *Acta Biomater.*, vol. 9, no. 8, pp. 7977–7986, 2013.
- [103] Dow, “Chemistry of METHOCEL™ Cellulose Ethers - A Technical Review Chemistry of METHOCEL™ Cellulose Ethers,” 2013.
- [104] A. J. Ruys, M. Wei, C. C. Sorrell, M. R. Dickson, A. Brandwood, and B. K. Milthorpe, “Sintering effects on the strength of hydroxyapatite,” *Biomaterials*, no. 16, pp. 409–415, 1995.
- [105] L. Ljung, *System Identification: Theory for User*. Englewood Cliffs, New Jersey: PTR Prentice Hall, 1987.
- [106] H. Olsson, K. J. Astrom, C. Canudas de Wit, M. Gafvert, and P. Lischinsky, “Friction Models and Friction Compensation,” *Eur. J. Control*, pp. 176–195, 1998.
- [107] V. Van Geffen, “A study of friction models and friction compensation,” *Eindhoven Univ. Technol.*, 2009.
- [108] A. A. Pervozvanski and C. Canudas-de-wit, “Asymptotic analysis of the dither effect

- in systems with friction,” *Automatica*, vol. 38, pp. 105–113, 2002.
- [109] P. A. Bliman and M. Sorine, *Models of hysteresis*. John Wiley and Sons, 1993.
- [110] F. Al-bender, “Fundamentals of friction modeling,” 2010, pp. 117–122.
- [111] P. U. ME 365, “Lab 6: System identification of a second order system.” pp. 1–5, 2008.
- [112] C. . Lamarque, S. Pernot, and A. Cuer, “Damping identification in multi-degree-of-freedom systems via a wavelet-logarithmic decrement-Part 1: theory,” *J. Sound Vib.*, vol. 235, no. 3, pp. 361–374, 2000.
- [113] “Free vibration of a damped, single degree of freedom, linear spring mass system,” *Brown University*. [Online]. Available: https://www.brown.edu/Departments/Engineering/Courses/En4/Notes/vibrations_free_damped/vibrations_free_damped.htm.
- [114] D. D. a. Bristow, M. Tharayil, and A. a. G. Alleyne, “A survey of iterative learning control,” *IEEE Control Syst. Mag.*, vol. 26, no. June, pp. 96–114, 2006.
- [115] Y. Zheng and M. A. Roberts, “Scalable vascularized implants,” *Nat. Mater.*, vol. 15, no. 6, pp. 597–599, 2016.
- [116] F. J. O’Brien, “Biomaterials & scaffolds for tissue engineering,” *Mater. Today*, vol. 14, no. 3, pp. 88–95, 2011.
- [117] D. J. Hadjidakis and I. I. Androulakis, “Bone remodeling,” *Ann. N. Y. Acad. Sci.*, vol. 1092, pp. 385–396, 2006.
- [118] J. Y. Rho, L. Kuhn-Spearing, and P. Zioupos, “Mechanical properties and the hierarchical structure of bone,” *Med. Eng. Phys.*, vol. 20, no. 2, pp. 92–102, 1998.
- [119] P. Schatz, “Anatomy & Physiology.” [Online]. Available: <http://philschatz.com/anatomy-book/contents/m46281.html>.
- [120] P. Schatz, “Anatomy & Physiology.” .
- [121] B. Clarke, “Normal bone anatomy and physiology.,” *Clin. J. Am. Soc. Nephrol.*, vol. 3 Suppl 3, pp. 131–139, 2008.
- [122] A. D. Bakker and V. Everts, “Osteocytes and osteoclasts, a relationship under strain,” *Clin. Rev. Bone Miner. Metab.*, vol. 12, no. 1, pp. 14–26, 2014.
- [123] D. Farhi, *Pathology of Bone Marrow and Blood Cells*, 2nd ed. Lippincott, Williams and Wilkins, 2009.

- [124] S. L. Teitelbaum, “Bone Resorption by Osteoclasts,” *Science* (80-.), vol. 289, no. 5484, pp. 1504–1508, 2000.
- [125] Y. Jiang, B. N. Jahagirdar, and R. L. Reinhardt, “Pluripotency of mesenchymal stem cells derived from adult marrow,” *Nature*, vol. 25, pp. 41–49, 2002.
- [126] Q. Chen *et al.*, “Fate decision of mesenchymal stem cells: adipocytes or osteoblasts?,” *Cell Death Differ.*, vol. 23, no. 7, pp. 1128–1139, 2016.
- [127] K. A. Kilian, B. Bugarija, B. T. Lahn, and M. Mrksich, “Geometric cues for directing the differentiation of mesenchymal stem cells,” *Proc. Natl. Acad. Sci.*, vol. 107, no. 11, pp. 4872–4877, 2010.
- [128] R. McBeath, D. M. Pirone, C. M. Nelson, K. Bhadriraju, and C. S. Chen, “Cell shape, cytoskeletal tension, and RhoA regulate stem cell lineage commitment,” *Dev. Cell*, vol. 6, pp. 483–495, 2004.
- [129] M. Rumpfer, A. Woesz, J. W. . Dunlop, J. T. van Dongen, and P. Fratzl, “The effect of geometry on three-dimensional tissue growth,” *J. R. Soc. Interface*, vol. 5, no. 27, pp. 1173–1180, 2008.
- [130] A. J. Engler, S. Sen, H. L. Sweeney, and D. E. Discher, “Matrix Elasticity Directs Stem Cell Lineage Specification,” *Cell*, vol. 126, no. 4, pp. 677–689, 2006.
- [131] S. A. Ruiz and C. S. Chen, “Emergence of Patterned Stem Cell Differentiation Within Multicellular Structures,” *Stem Cells*, vol. 26, no. 11, pp. 2921–2927, 2008.
- [132] K. A. Kilian, B. Bugarija, B. T. Lahn, and M. Mrksich, “Geometric cues for directing the differentiation of mesenchymal stem cells,” *Proc. Natl. Acad. Sci.*, vol. 107, no. 11, pp. 4872–4877, 2010.
- [133] S. J. Morrison, D. T. Scadden, M. G. Hospital, R. Biology, and F. Darwin, “The bone marrow niche for haematopoietic stem cells,” *Nature*, vol. 505, no. 7483, pp. 327–334, 2014.
- [134] A. Guntur and C. Rosen, “Bone as an Endocrine Organ,” *Endocr Pr.*, vol. 18, no. 5, pp. 758–762, 2012.
- [135] W. P. Cawthorn, E. L. Scheller, B. S. Learman, and E. Al., “Bone marrow adipose tissue is an endocrine organ that contributes to increased circulating adiponectin during caloric restriction,” *Cell Metab.*, vol. 20, no. 2, pp. 368–375, 2014.

- [136] J. Wei and G. Karsenty, “An Overview of the Metabolic Functions of Osteocalcin,” *Curr. Osteoporos. Rep.*, vol. 13, no. 3, pp. 180–185, 2015.
- [137] D. J. DiGirolamo, T. L. Clemens, and S. Kousteni, “The skeleton as an endocrine organ,” *Nat. Rev. Rheumatol.*, vol. 8, no. 11, pp. 674–683, 2012.
- [138] Y. Lu and J. Q. Feng, “FGF23 in skeletal modeling and remodeling,” *Curr. Osteoporos. Rep.*, vol. 9, no. 2, pp. 103–108, 2011.
- [139] T. L. Clemens and G. Karsenty, “The osteoblast: An insulin target cell controlling glucose homeostasis,” *J. Bone Miner. Res.*, vol. 26, no. 4, pp. 677–680, 2011.
- [140] D. J. DiGirolamo, T. L. Clemens, and S. Kousteni, “The skeleton as an endocrine organ,” *Nat. Rev. Rheumatol.*, vol. 8, no. 11, pp. 674–683, 2012.
- [141] O. D. Kennedy, B. C. Herman, D. M. Laudier, R. J. Majeska, H. B. Sun, and M. B. Schaffler, “Activation of resorption in fatigue-loaded bone involves both apoptosis and active pro-osteoclastogenic signaling by distinct osteocyte populations,” *Bone*, vol. 50, no. 5, pp. 1115–1122, 2012.
- [142] X.-Y. Zhang, G. Fang, and J. Zhou, “Additively Manufactured Scaffolds for Bone Tissue Engineering and the Prediction of their Mechanical Behavior: A Review,” *Materials (Basel)*, vol. 10, no. 1, p. 50, 2017.
- [143] J. M. Anderson, A. Rodriguez, and D. T. Chang, “Foreign body reaction to biomaterials,” vol. 20, pp. 86–100, 2008.
- [144] R. K. Jain, P. Au, J. Tam, D. G. Duda, and D. Fukumura, “Engineering vascularized tissue,” *Nat. Biotechnol.*, vol. 23, no. 7, pp. 821–823, 2005.
- [145] Y. Wang *et al.*, “3D fabrication and characterization of phosphoric acid scaffold with a HA / β -TCP weight ratio of 60 : 40 for bone tissue engineering applications,” pp. 1–17, 2017.
- [146] D. T. Queheillalt and H. N. G. Wadley, “Cellular metal lattices with hollow trusses,” *Acta Mater.*, vol. 53, no. 2, pp. 303–313, 2005.
- [147] F. P. W. Melchels, A. M. C. Barradas, C. A. Van Blitterswijk, J. De Boer, J. Feijen, and D. W. Grijpma, “Effects of the architecture of tissue engineering scaffolds on cell seeding and culturing,” *Acta Biomater.*, vol. 6, no. 11, pp. 4208–4217, 2010.
- [148] Z. Sheikh, S. Najeeb, Z. Khurshid, V. Verma, H. Rashid, and M. Glogauer,

- “Biodegradable materials for bone repair and tissue engineering applications,” *Materials (Basel)*, vol. 8, no. 9, pp. 5744–5794, 2015.
- [149] X. Wang *et al.*, “Topological design and additive manufacturing of porous metals for bone scaffolds and orthopaedic implants: A review,” *Biomaterials*, vol. 83, no. March, pp. 127–141, 2016.
- [150] M. Castilho *et al.*, “Direct 3D powder printing of biphasic calcium phosphate scaffolds for substitution of complex bone defects,” *Biofabrication*, vol. 6, 2014.
- [151] J. Brandt, S. Henning, G. Michler, W. Hein, A. Bernstein, and M. Schulz, “Nanocrystalline hydroxyapatite for bone repair: An animal study,” *J. Mater. Sci. Mater. Med.*, vol. 21, no. 1, pp. 283–294, 2010.
- [152] S. Wu, X. Liu, K. W. K. Yeung, C. Liu, and X. Yang, “Biomimetic porous scaffolds for bone tissue engineering,” *Mater. Sci. Eng. R Reports*, vol. 80, no. 1, pp. 1–36, 2014.
- [153] J. W. Comb, P. J. Leavitt, and E. Rapoport, “Velocity Profiling in an Extrusion Apparatus,” 6054077, 2000.
- [154] O. Anatomy, “Anatomy Lesson #39.” [Online]. Available: <http://www.outlanderanatomy.com/anatomy-lesson-39-dem-bones-human-skeleton/>.
- [155] “DoITPoMS,” *TLP Library Structure of bone and implant materials - structure and composition of bone*. [Online]. Available: <https://www.doitpoms.ac.uk/tlplib/bones/structure.php>.
- [156] V. Hosseini *et al.*, “Fiber-Assisted Molding (FAM) of Surfaces with Tunable Curvature to Guide Cell Alignment and Complex Tissue Architecture,” pp. 4851–4857.
- [157] S. J. Lee and S. Yang, “Micro glass ball embedded gels to study cell mechanobiological responses to substrate curvatures,” *Rev. Sci. Instrum.*, vol. 83, no. 9, 2012.
- [158] F. Naddeo, N. Cappetti, and A. Naddeo, “Novel ‘load adaptive algorithm based’ procedure for 3D printing of cancellous bone-inspired structures,” *Compos. Part B Eng.*, pp. 1–9, 2016.
- [159] Y. Huang, M. C. Leu, J. Mazumder, and A. Donmez, “Additive Manufacturing:

Current State, Future Potential, Gaps and Needs, and Recommendations,” *J. Manuf. Sci. Eng.*, vol. 137, no. 1, p. 14001, 2015.

- [160] D. J. Hoelzle, A. G. Alleyne, and A. J. W. Johnson, “Iterative learning control using a basis signal library,” *Proc. Am. Control Conf.*, pp. 925–930, 2009.

Appendix A

Powder Prep and XRD Tips

A.1 Powder Preparation

This section outlines the steps to prepare the two precursor powders (CaCO₃ and CaHPO₄) to make the biphasic base powder of the colloidal ink with a nominal phase composition of 70 wt-% HA and 30 wt-% β -TCP.

Powder Preparation Steps

1. Measure powder
 - a. Measure desired powder amount into a weight boat. (Table A.1).
 - i. Note: the composition is VERY sensitive to these quantities. Please see Section 3.3.1.2 for an example calculation of the shift in final phase composition resulting from a minor change in the amount of precursor powders.

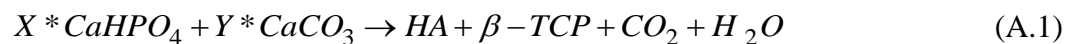
Table A.1 Amount of precursor powder to achieve the desired final phase composition. The amounts listed are for a half batch of ink.

CaCO ₃	CaHPO ₄
23.4 g	51.8 g

2. Ball Mill
 - a. Place both powders in a Nalgene bottle. The powder should weigh ~ 75g, so place 375 g alumina beads (5:1 ratio) inside the Nalgene bottle.
*Warning: the scale doesn't always go above 250g measurements, so you may need to do incremental steps here.
 - b. Measure out 150 mL of ethanol in a beaker and pour this into the Nalgene bottle. The optimal ethanol to powder ratio, determined empirically, is 5:1.

- c. Place on ball mill for 8 hours.
 - i. See Section 3.2.1.5 for a discussion on the optimal ball milling conditions.
- 3. Dry out ethanol
 - a. Pour out as much of the mixture from the Nalgene container as possible into a glass pan. Use the sieve over the sink to separate the powder and ethanol mixture from the alumina beads. You can use additional ethanol to dry to get all powder out of the container. The glass pan should contain the powder and ethanol mixture, and the sieve should contain all of the milling media.
 - b. Place in the Carbolite furnace for 8 hours at 100C.
 - c. Clean the milling media and place on a towel to dry for the next round of ball milling.
- 4. First calcine
 - a. Place the powder onto the flat ceramic trays. Ideally, we don't want a layer thicker than 0.25-0.5 inches, but this may not be possible with the flat trays.
 - i. Note: The flat ceramic plates are made from zirconia and are 6x6x0.375" (L x W x lip height). These were ordered from Zircoa.
 - b. Calcine for **10** hours at 1050C.
 - 1. First set point: 1050C
 - 2. Ramp up: 1000C
 - 3. Dwell time: 10 hours
 - 4. Ramp down: 1000C
 - 5. Second set point: 25C
 - 6. Second dwell time: max amount of hours, 99 hours (this doesn't matter as much, just try to maximize to ensure the glass pan is taken out of the furnace before moving onto the next heating profile).
- 5. Ball mill
 - a. Repeat steps 2 and 3.
- 6. SEM imaging and XRD measurements (if needed)

7. Second calcine
 - a. Place the powder onto the flat ceramic trays.
 - b. Calcine for **20** hours at 1050C. Ramp at 1000C.
8. Ball mill
 - a. Repeat steps 2 and 3
9. SEM imaging and XRD measurements (if needed)
10. Third calcine
 - a. Place the powder onto the flat ceramic trays.
 - b. Calcine for **30** hours at 1050C. Ramp at 1000C.
11. Ball mill
 - a. Repeat steps 2 and 3
12. SEM imaging (to check for homogeneous particle sizes) and XRD measurements (to check phase composition). A separate particle size analysis is recommended from time to time. This could be done commercially by companies (Micromeritics, Particle Techn Labs) for several hundred dollars per sample. It could potentially be done at MRL using the Zetasizer.
13. Measure SSA (needed for ink formulation)
 - a. Send a sample to a collaborator at Notre Dame (see Prof WJ for contact information)
 - b. Or, get a quote from an external company (Mircomeretics, Particle Tech Labs)
14. Measure mass of powder batch (needed for ink formulation)
 - a. Note: during the first calcination we expect to lose a consistent amount of powder (~10 g) due to mass loss of CO₂ and H₂O. The source of the mass loss is due to CO₂ and H₂O from our calculations. X and Y refer to the starting amount of precursor powder to achieve the desired final phase composition. The reaction equation between the two precursor powders is listed in Equation A.1.



A.2 Ink Formulation

For ink formulation, refer to Dr. Hoelzle's thesis (Hoelzle, D.J., 2007. *Reliability Guidelines and Flowrate Modulation for a Micro Robotic Deposition System*. University of Illinois at Urbana-Champaign). More specifically, see Appendix B, page 108. The Day 1 and Day 2 steps in Dr. Hoelzle's instructions are modified in this work to the steps listed above in Section A.1. Follow Dr. Hoelzle's ink making directions starting on Day 3. Use the "HA Ink Generic Formulation NEW" excel document.

If the ink exhibits filter-pressing behavior (Figure 3.1), the liquid and solid phases are being separated due to high extrusion pressures. In this case, try to decrease the viscosity of the ink to enable extrusion at a lower pressure. To decrease viscosity, add base (Ammonium Hydroxide) to the ink that exhibits filter-pressing behavior in 100 μL increments. Place the ink in the Nalgene container on the paint shaker for 30 minutes after each addition. With this viscosity reduction, the ink will need less pressure for extrusion and therefore be less likely to filter-press.

A.3 Furnace Operation and Thermal Processing Tips

Since the zirconia plates are fairly porous, some ions can diffuse in the plate. This should only have an effect if there are drastic changes in the starting Ca:P ratio. Before you use the plates with a new powder blend, place a small layer of the material blend on the plates (sprinkle the powder on the surface to cover the whole base of the plate) and do a short conditioning heat treatment to ensure equilibrium with the material. Heat the plate with a small powder layer for 10 hours at 1050 C. Throw away the powder after the heat treatment.

If there are blue and white patches in the powder after the thermal treatments (Figure A.1), this is a clear sign of inhomogeneity and insufficient blending. Placing the powder on plates ensures better air exposure relative to calcination in tall crucibles. The blue color in the CaP materials is often associated with the HA phase. The spatial distribution of the blue and white regions reflects areas with Ca-excess and Ca-deficiency, respectively.



Figure A.1 Image looking down into tall cylindrical crucibles to illustrate the blue and white patches present in a powder mixture. The top of the powder mixture (left) and the mixture with the first layer pierced into (right) to highlight the blue and white regions.

A.4 XRD SOP

The user will learn how to load powder into the sample holder and operate the Siemens-Bruker D5000 XRD machine through MRL training. However, this section serves to supplement this training, and includes tips in both preparing and loading the HA powder into the sample holder.

A.4.1 Sample preparation in the lab

Around 1 g of powder is needed for XRD analysis. After the last calcination step, the powder batch will likely have hard chunks. Thoroughly crush the particle agglomerates using the mortar in MEB 113 before loading the sample into the XRD machine. The powder should look like flour – monosized particles devoid of hard agglomerates. This will make it easier to load the powder into the sample holder in the XRD machine and reduce the amount of time required proper sample loading.

A.4.1 Sample loading in XRD machine

Use the glass sample holder with the larger diameter hole. The x-rays diffract off the top powder layer, so the evenness of the powder relative to the sample holder is important; we want to evenly load the powder into the sample holder to ensure a flat and level surface. If the sample layer is too high or low, the diffraction peaks obtained from the measurements will be slightly shifted. Small voids should be avoided, however excess powder sitting outside of the

center circle is not a big deal since the x-ray beam is optimized to interact with the sample and not the area outside of the sample.

First, load less powder than what will fill the container to ensure a smooth bottom layer. If any chunks remain in the powder, crush them using the glass slide on the outer diameter of the sample holder. Do not simply flatten the powder into the holder since this will place the powder in a preferential orientation, resulting in the loss of some phases in the diffraction data. Instead, tap and move the powder across the holder using the edge of the glass slide in small increments. Before loading the sample holder into the machine, visually inspect that the top layer of the powder is level with the sample holder.

A.5 XRD Software

There are two software options to analyze the raw diffraction data. The first is the Jade software in MRL. The second is a program called Profex, which was developed by a colleague at the RMS foundation. Both Jade and Profex can search the diffraction data for phases manually, however we commonly insert the phases in manually, which informs the software what to match the raw data with.

When analyzing the diffraction data, make sure to first align the diffraction data to the strong β -TCP peaks. You will likely have a small negative phase shift, since the diffraction data will be shifted if the powder was improperly loaded into the sample holder. The XRD machine is very sensitive to the way you load the sample: if the sample sits slightly above the circular insert, this can cause a significant shift in the diffraction data (-0.2 to -0.3 2θ). In the Jade software, you must now save this shifted data as a new data file. Re-open, then run the refinement to match the peaks and get the phase composition. In Profex, however, the file format does not need to be changed. In fact, during refinement, the software optimizes the shift to make the diffraction data match the inputted phases.

If the powder reached a complete reaction, there should only be one or two phases present in the diffraction data. In this work, the two main phases should be HA and β -TCP. However, always check diffraction data for intermediate phases that would form if the two starting powders have not reached a complete reaction. If any of the peaks in the raw data are unaccounted for in the refinement analysis, there are likely additional phases. Possible

additional phases include CaO (lime) and β -Ca₂P₂O₇ (β -CPP). If you find β -Ca₂P₂O₇, this is a clear sign of an incomplete reaction since this phase cannot coexist with HA in a powder batch that has reached equilibrium. Improving the blending process and/or increasing the calcination time should result in a complete reaction. If you find CaO, this could mean two things. If there are three phases (HA, CaO and β -TCP) in the diffraction data, this means the reaction was not complete. If there are two phases (HA and CaO), this means the reaction shifted too far to the right in the phase diagram (see Figure 3.4). Try decreasing the starting Ca:P ratio of the starting powders to shift back into the HA and β -TCP region of the phase diagram.

A.5.1 Jade Software

The Jade Software will be covered during MRL training. Notes for this specific powder is listed below. As a note, the software in MRL is very sensitive to:

- Where you set the background (i.e. the height and distance from the bottom of the diffraction data)
- Shifts in the data
- Which PDF card you choose for each phase

Use the following PDF cards for phase identification:

- HA: 01:089-4405
- Calcium Phosphate (β -TCP): 04-006-9376
- Calcium Phosphate (β -CPP): 04-009-3876
- Calcium oxide (CaO): 01-080-7710
- CaHPO₄ (Monetite): 04-009-3755

A.5.2 Profex Software

The software developed at RMS is called Profex. Instructional manuals and tutorials are available on the profex website: <http://profex.doebelin.org/>

First download the software from the website: <http://www.doebelin.org/nic/tools/profex/>. Choose the “Profex and BGMN Bundle”, since it contains the information for the XRD machine at MRL and the crystal structure files for HA and β -TCP. Thus, the phases relevant for this powder is already preloaded into the software.

Appendix B

Roberta Operating Instructions

B.1 Instructions for Scaffold Fabrication

1. Prep substrate
 - a. Thoroughly clean substrate with ethanol
 - b. Spray black side of substrate with an even coat of hairspray, which helps ensure the ink sticks to the substrate for the first layer
 - c. Let substrate dry (~ 5-10 min)
2. Load ink into syringe
 - a. Place end cap on syringe.
 - b. Pour lamp oil in the syringe to lubricate the syringe walls. Discard extra.
 - c. Load ink in the syringe using a spatula, and put the snap cap on. As you add the ink, tap the syringe down to remove large spaces.
 - d. Place in centrifuge for 5 min at 3000 rpm to spin out the low-density air bubbles. Place capped syringe in a clear centrifuge tube.
 - i. Screw the syringe into the cap of the centrifuge tube.
 - ii. Make sure to counterbalance the centrifuge by filling another centrifuge tube with a small amount of water. The two centrifuge tubes (one with the syringe + ink and the other with water) should weight about the same.
 - e. Place the syringe in the fridge until ready to be used.
3. Prep machine
 - a. Ensure the substrate holder is in the square highlighted by blue tape (Figure B.1)

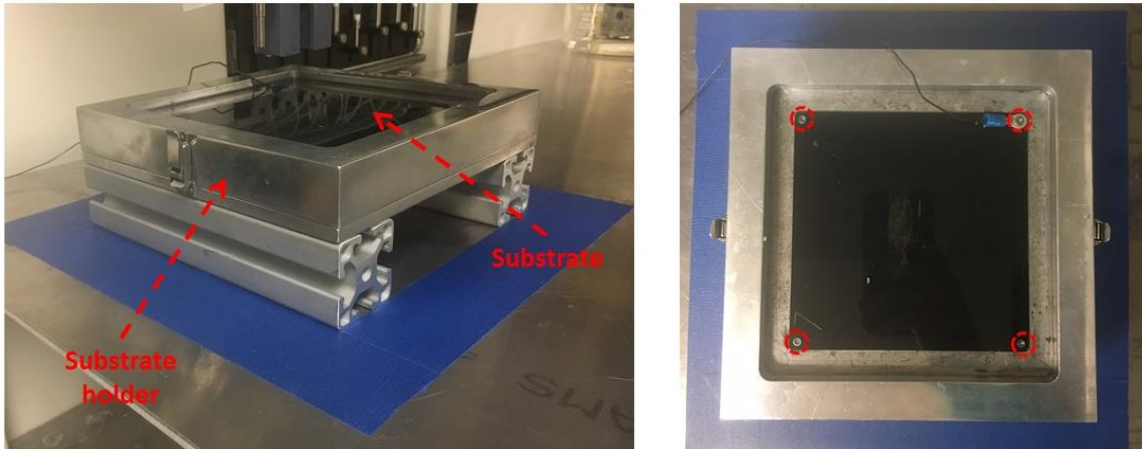


Figure B.1 Substrate holder placed in the region outlined by the blue tape, and a substrate with the location of the four screws to secure the substrate into the substrate holder.

- b. Secure substrate in substrate-holder (4 screws at the 4 corners). Use the small Allen wrench in the small white tub under the deposition table.
 - c. Fill well with oil. Use the small ruler to ensure we have a sufficient depth for the desired scaffold height.
4. Turn on hardware
 - a. Flip the switch on the power strip located on the ground.
 - b. Turn on each of the three desktop variable power supplies manually. These **MUST** be turned on for encoder power.
5. Prep computer
 - a. Log into the computer. Open the “Roberta” LabVIEW Project located in the “Roberta” Desktop folder.
 - b. Select the desired Fabrication code from the Project window (The name and descriptions of each option are discussed in Appendix D.
 - c. Connect to the cRIO
 - i. Right click “mRDcRIO (130.126.178.19)” and select Connect.
6. Get ink ready

- a. Take snap cap off and put a clear plunger in the syringe. Use an Allen wrench to push the plunger down until it is flush with the ink layer.
- b. Take off the end cap and screw on a nozzle with the correct diameter
 - i. Purple = 0.51 mm
 - ii. Pink = 0.25 mm
- c. Secure the Adapter Assembly (blue top) onto the stop of the syringe to connect to the pressure line.
- d. Snap the syringe into the syringe holder on the Z axis.

7. Start Code

- a. Input desired scaffold parameters (Figure B.2)
 - i. Scaffold width: change both the X axis values in the Layer 1 tab and the Y axis values in the Layer 2 tab to the desired scaffold width (in mm)
 - ii. Distance between rods: change both the Y axis values in the Layer 1 tab and the X axis values in the Layer 2 tab to the desired scaffold width (in mm)
 1. Make sure the values maintain the correct sign
 - iii. Choose the applied pressure



Figure B.2 Layer 1 and Layer 2 tabs in the front panel GUI of the main scaffold code. The values outlined in a red dashed box correspond to the desired scaffold width, and the values outlined in a blue dashed box correspond to the desired distance between rods.

- b. Click the arrow in the upper left corner of the LabVIEW front panel to start the code.
 - c. To begin axis movement, click “Start Move”.
 - d. During lead in lines, feel free to adjust the applied pressure value on the front panel GUI. Change the value in the “Operating Pressure (psi)” box and click enter to execute.
 - i. It is very important that the 1st layer appears slightly flattened to ensure the 1st layer fully sticks to the substrate. Restart code and move axes to a new spot if the 1st layer is not flattened.
 - e. During scaffold fabrication, do NOT touch the axes.
8. Ending lattice
- a. After the user-defined number of scaffolds are printed, the axes will be disabled and the code will stop.

- i. The arrow in the upper left corner of the front panel will look like this



- b. If the code must be stopped during printing, click the “Stop Move” button on the main GUI.
- c. In an emergency, flip the switch of the power strip to shut off all power to the machine.

Appendix C

Adjustment Instructions for Future Work

C.1 Modify Axis Properties

In the Project Window, click the + window next to the “mRDcRIO...” portion of the Project Window. Right click the axis and select Properties. The image shown in Figure C.1 will appear. Parameters that need to be set for each axis within the Axis Configuration window include the position loop gains, encoder units and encoder counts, and limit switch information.

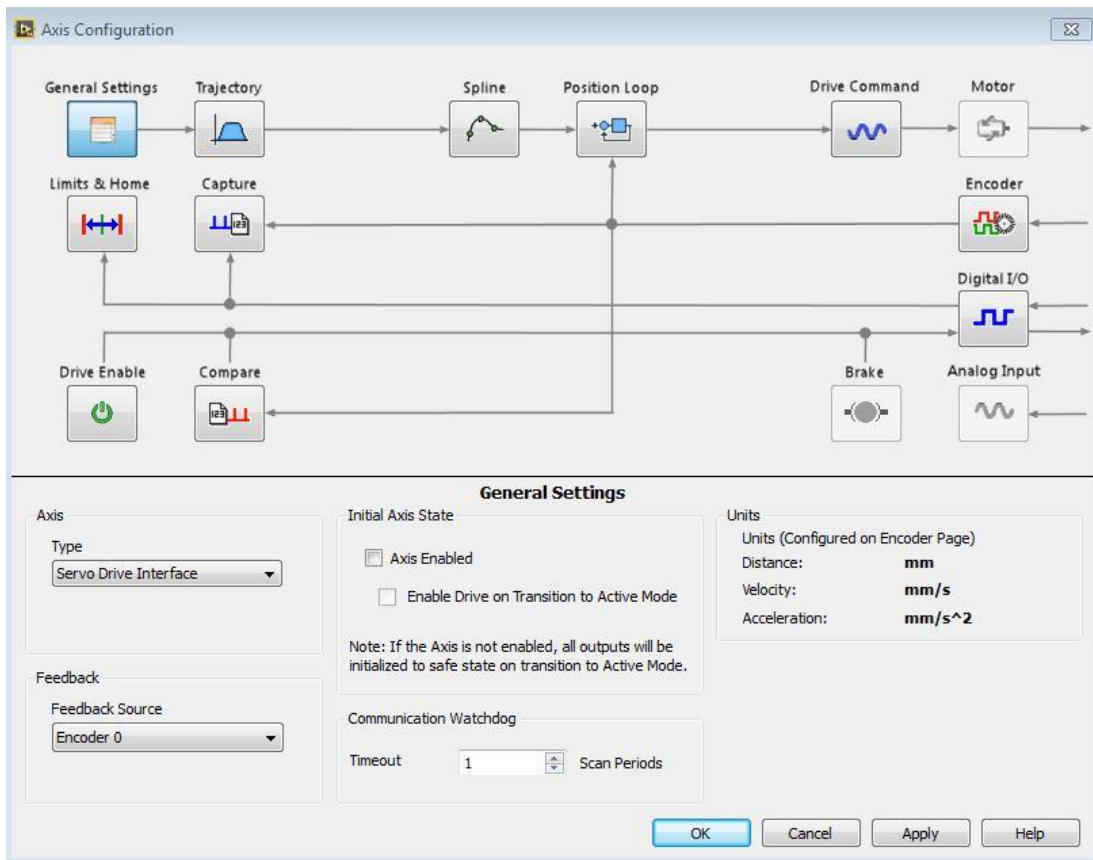


Figure C.1 Axis Configuration window in SoftMotion.

C.1.1 Modify Control gains

Click the Position Loop button in Figure C.1 to adjust Kp, Ki, Kd, Vff, or Aff.

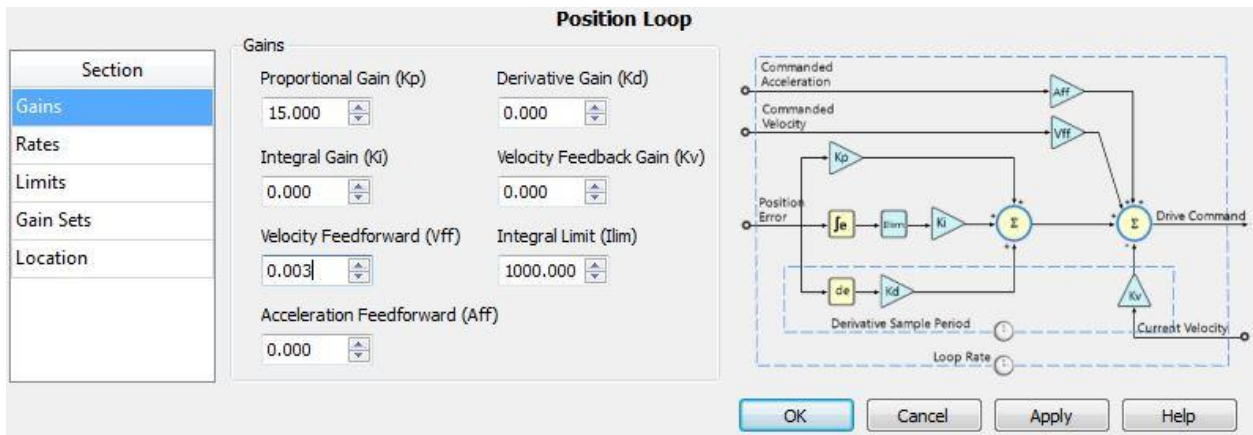


Figure C.2 Position Loop information in the Axis Configuration Window.

C.1.2 Encoder Units

Click the Encoder button in Figure C.1 to adjust the encoder unit, and pulses per unit values.

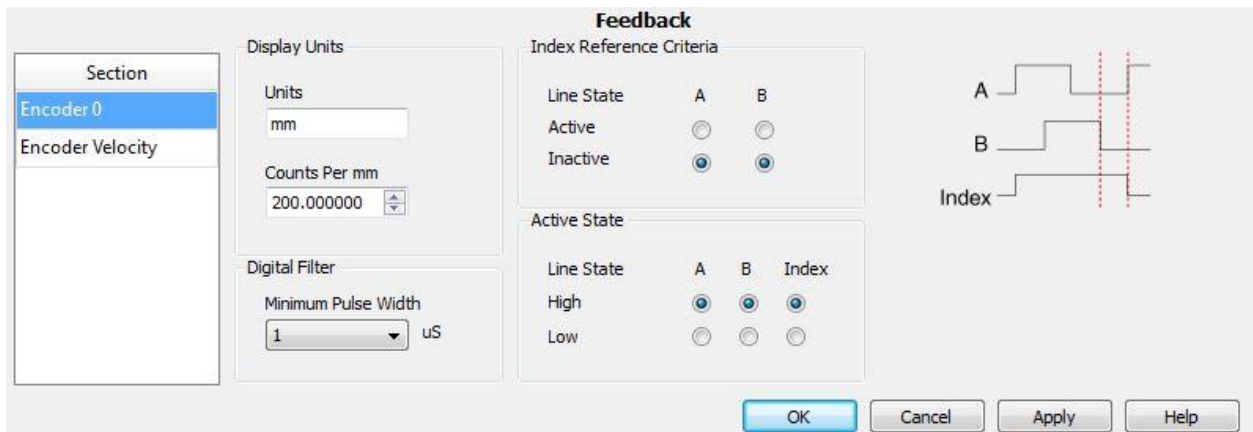


Figure C.3 Encoder units and counts per unit configuration window.

C.1.3 Limit Switch Information

Click the Limits & Home button in Figure C.1 to adjust the limit switch information. For each axis, the forward and reverse limit switches have the following properties:

- Enable ✓

- Stop Mode: Disable Drive
- Input Type: Sourcing
- Active State: On
- Digital Filter: 50 us

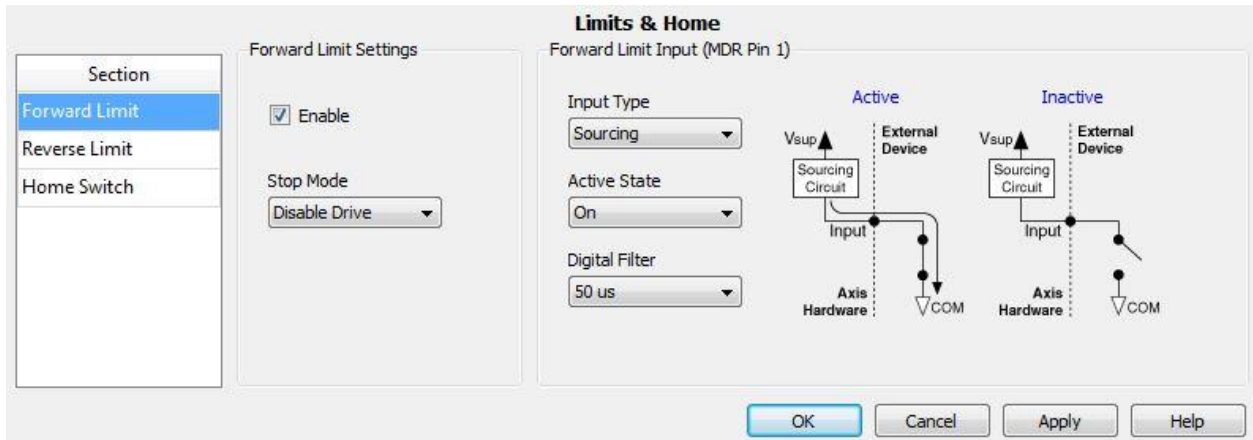


Figure C.4 Limit switch information in the Axis Configuration Window.

Appendix D

Program Descriptions

This section serves to supplement the program descriptions outlined in Chapter 2. First, each of the items listed in the “Roberta” project window (Figure D.1) are briefly discussed. Further, the code structure of each case in the second consumer loop will be briefly discussed. As a reminder, the code is executed as a series of states, which are controlled by the queue.

A LabVIEW project is essentially a large folder that contains the main program files (VIs) and any sub files necessary for those VIs to run properly. The project window for Roberta contains the main VIs and subVIs, which are called by the main VIs during operation. Both the main VIs and subVIs contained in the project window are listed in Table D.1.

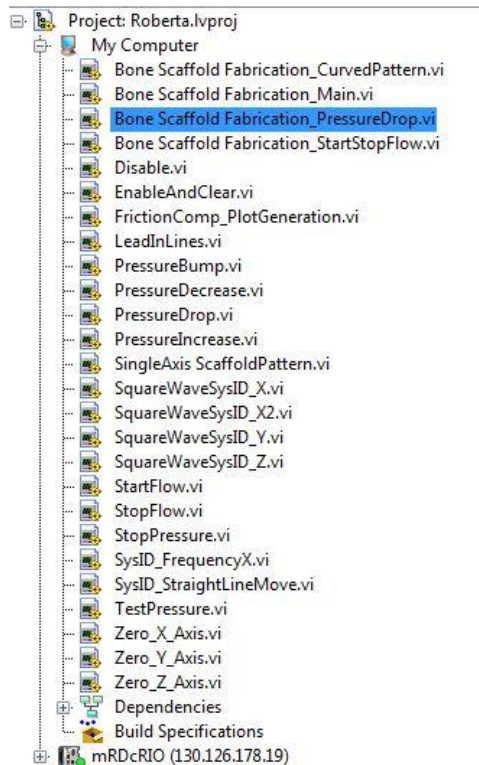


Figure D.1 Project window for the Roberta LabVIEW project. The code that will be used most often is highlighted.

Table D.1 Names and uses of each program listed in the Roberta project window.

Program Name	Type	Use
Bone Scaffold Fabrication_CurvedPattern	Main VI	Print single layer scaffolds with curved rods
Bone Scaffold Fabrication_Main	Main VI	Print multiple, rectilinear scaffolds. No pressure regulation at velocity reversals
Bone Scaffold Fabrication_PressureDrop	Main VI	Print multiple, rectilinear scaffolds WITH pressure regulation at velocity reversals
Bone Scaffold Fabrication_StartStopFlow	Main VI	Print rectilinear scaffolds with open pores (incorporates start/stop flow of the ink)
Disable	Sub VI	Disable axes at code shutdown
EnableAndClear	Sub VI	Enable axes at code startup
FrictionComp_PlotGeneration	Main VI	Code used to test to record drive command for friction compensation
LeadInLines	Sub VI	Move both the X and Y axis in a scaffold-like pattern to test operating pressure and to ensure a fully developed ink flow before scaffold fabrication
PressureBump	Sub VI	Gradually increase pressure set point. Not currently called by a main VI.
PressureDecrease	Sub VI	Gradually decrease pressure set point. Not currently called by a main VI.
PressureDrop	Sub VI	Active pressure control at velocity reversal to reduce ink buildup. Called by “Bone Scaffold Fabrication_PressureDrop”
PressureIncrease	Sub VI	Active pressure control at velocity reversal to reduce ink buildup. Called by “Bone Scaffold Fabrication_PressureDrop”
SingleAxis ScaffoldPattern	Main VI	Code to tests tuned control gains on the axis when commanded to move in a scaffold pattern
SquareWaveSysID_X	Main VI	Command a varying square wave reference signal to the X axis for system identification.
SquareWaveSysID_X2	Main VI	Command a non-varying square wave reference signal to the X axis for system identification.
SquareWaveSysID_Y	Main VI	Command a varying square wave reference signal to the Y axis for system identification.

Table D.1 (cont.)

Program Name	Type	Use
SquareWaveSysID_Z	Main VI	Command a varying square wave reference signal to the Z axis for system identification.
StartFlow	Sub VI	Ink start up at velocity reversal. Called by “Bone Scaffold Fabrication_StopFlow”
StopFlow	Sub VI	Material termination at velocity reversal. Called by “Bone Scaffold Fabrication_StopFlow”
StopPressure	Main VI	Send an immediate AO command to pressure regulator to stop flow. Send 0 if want to stop flow.
SysID_FrequencyX	Main VI	Command a sinusoidal reference signal to the X axis for system identification.
SysID_StraightLineMove	Main VI	Command a step reference signal to the user-defined axis for system identification. Code used in the logarithmic decrement method.
TestPressure	Main VI	Code to tune the pressure for each ink batch. Use to determine the proper operating pressure (OP) and no flow pressure (NFP)
Zero_X, Y or Z	Sub VI	Simple to add. This feature would enable the end user to design a more advanced scaffold design

D.1 Zero Axes

There is a case structure to perform zeroing for each axis. The code structure within the X Axis Zero case is shown in Figure D.2 . The code structures to zero the Y and Z axes follow a similar format.

A “Zero” subVI was created that initiates an axis to move towards one of the limit switches. For the X axis, the X axis moves in the positive direction toward the forward limit switch. When the limit switch is found, the X axis then moves a user-defined distance (“Dist from zero X”) in the negative direction to move to the home position for fabrication. Before exiting this case, the next case (“ZeroY”) is enqueued.

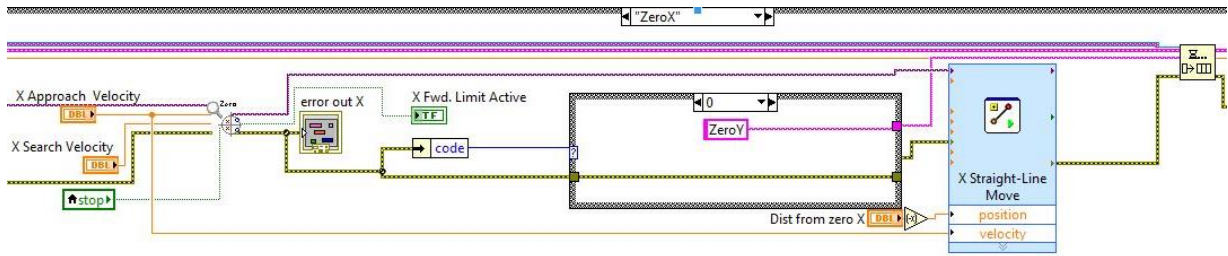


Figure D.2 Code structure of the Zero X case structure implemented in LabVIEW. A similar format was followed for the Y and Z axes.

D.2 Lead in Lines

The code structure for the LeadInLines case is similar to the scaffold layers. First, however, the pressure is turned on to start ink flow. The LeadInLines subVI is then called, which uses Straight Line Move Express VIs to move the X and Y axes. Before exiting the case, Layer 1 is enqueued.

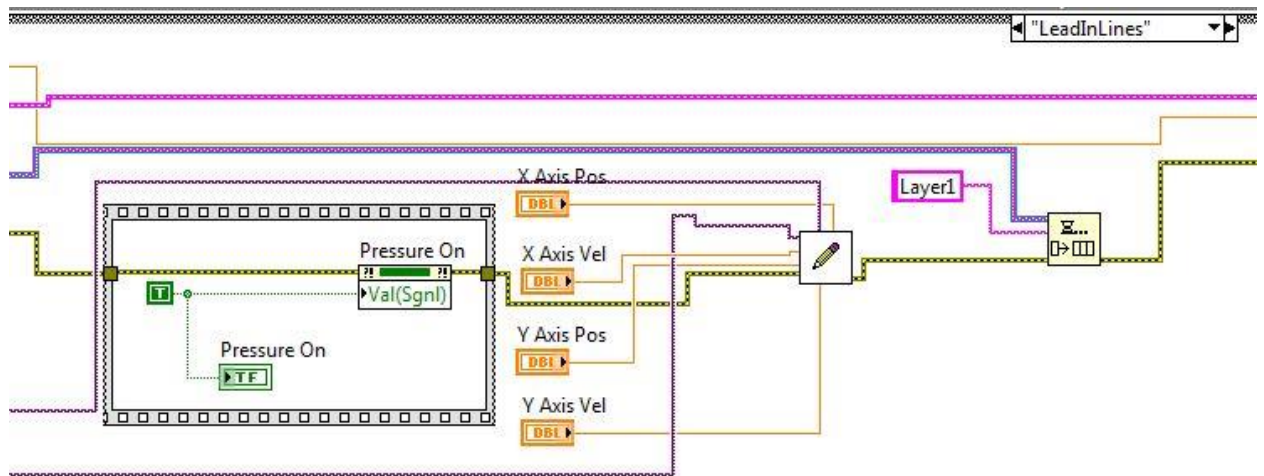


Figure D.3 Code structure for the Lead in Lines case.

D.3 Calibration Layers and Updating Reference Command

The user-friendly ILC structure is implemented in three cases: Calibration Layer 1, Calibration Layer 2, and Update. Calibration Layer 1 and Calibration Layer 2 are implemented as For Loops (Figure D.4). The Layer 1 and Layer 2 arrays on the front panel GUI are wired

to the For Loop input terminal. Auto-indexing is enabled so LabVIEW sets the count terminal to the array size (the amount of times the For Loop is executed is equal to the number of elements in the array). Within the For Loop, a scaffold layer is implemented as a series of Straight Line Move Express VIs. In between each Express VI, however, is a Read Express VI to measure how far each axis moved. The error is computed between the position reference and the actual distance measured by the Read Express VI. The error is then added to the reference command and placed back into the array. Calibration Layer 2 is then enqueued, which follows a similar structure to Calibration Layer 1. After Calibration Layer 2, the Update case (Figure D.5) takes the reference signal augmented with the position error and displays the updated signal on the GUI. In addition, the position references are adjusted to the augmented values. Further, the Y axis is moved to leave room for the lead in lines.

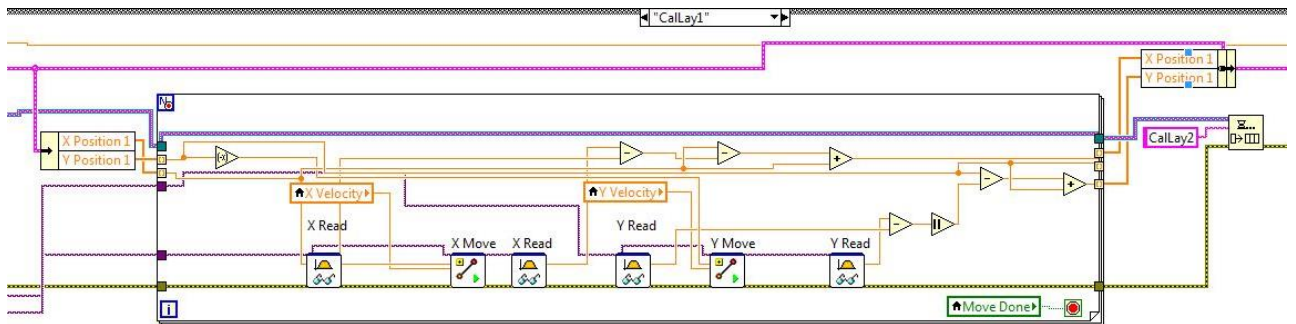


Figure D.4 Code structure for Calibration Layer 1. Calibration Layer 2 follows a similar structure.

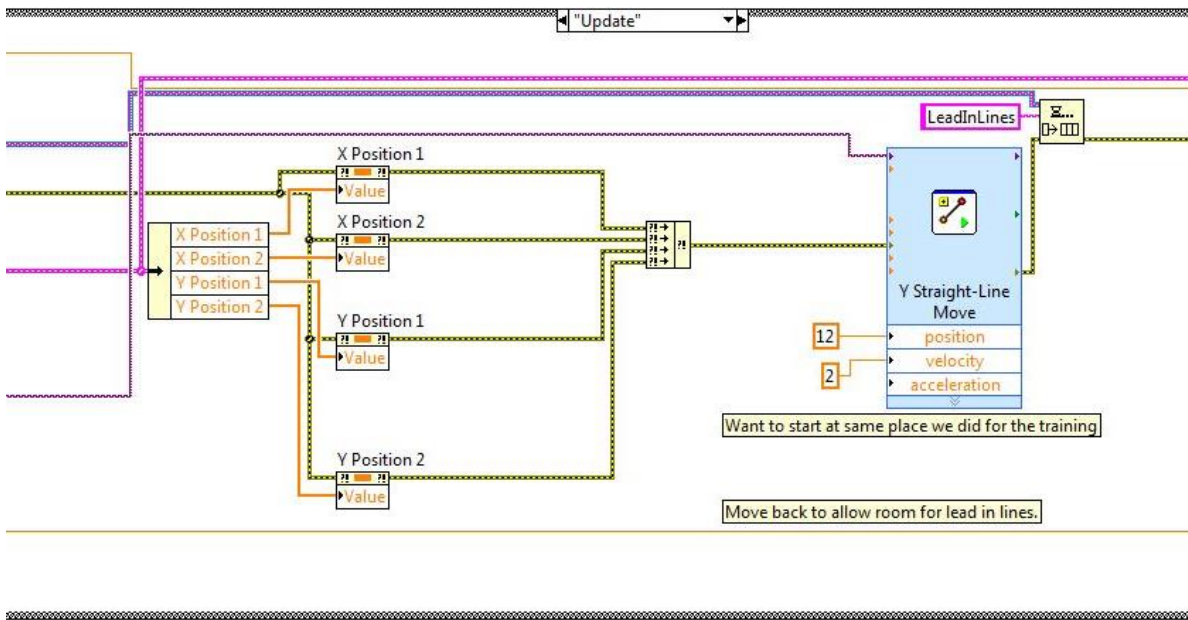


Figure D.5 Code structure for the Update Case.

D.4 Layers 1 and 2

Layers 1 and 2, which are repeated to form a scaffold, are implemented in a for loop (D.6). Similar to the calibration layers, the position arrays on the GUI are wired into the For Loop terminal. With autoindexing, the number of For Loop executions is equal to the number of elements in the array. The position reference signals are fed into StraightLineMove express VIs. In between each axis movement, the pressure is reduced and subsequently through subVIs for active pressure control. After the For Loop execution, the number of layers is increased and the MoveZ case is executed, which is simply a StraightLineMove for the Z axis.

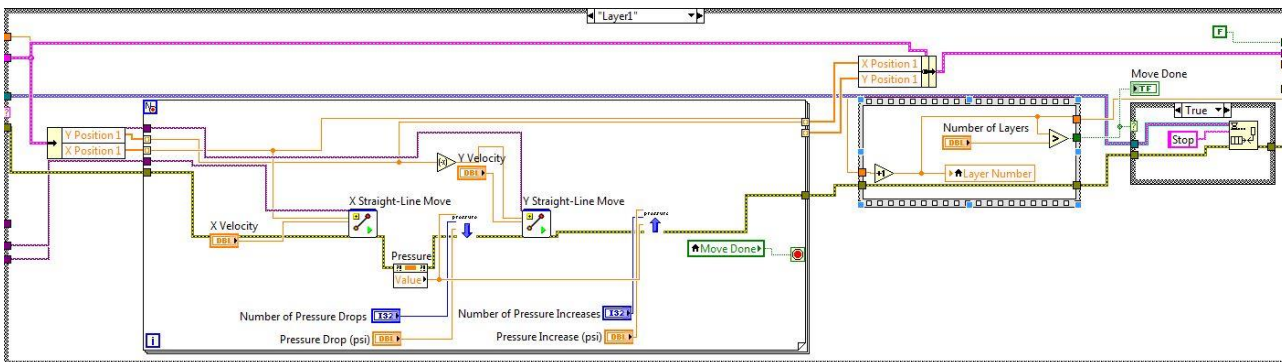


Figure D.6 Code structure for Layers 1 and 2.

Appendix E

Electrical Wiring

The electrical components for the DW printer were organized as shown in Figures E.1 and E.2. To enable flexibility for future projects, all electrical signals between each system component were connected through three breadboards. Solderable breadboards were used to ensure secure connections. Further, DSUB pins and corresponding DSUB ports soldered into the breadboard were used to transmit signals. For signal transmission from Breadboard 3 atop the X axis to Breadboard 1, a cable bundle with a 25 pin DSUB connector on each end was used. This cable was placed in the IGUS cable chain for protection during machine movement.

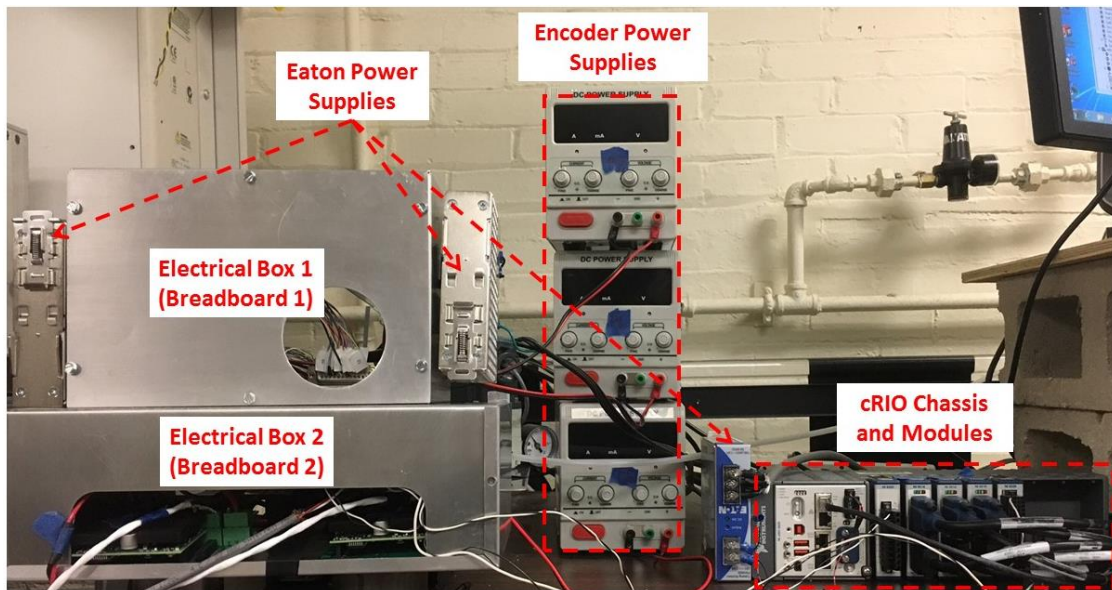


Figure E.1 Organization of all electrical components used for the DW printer.

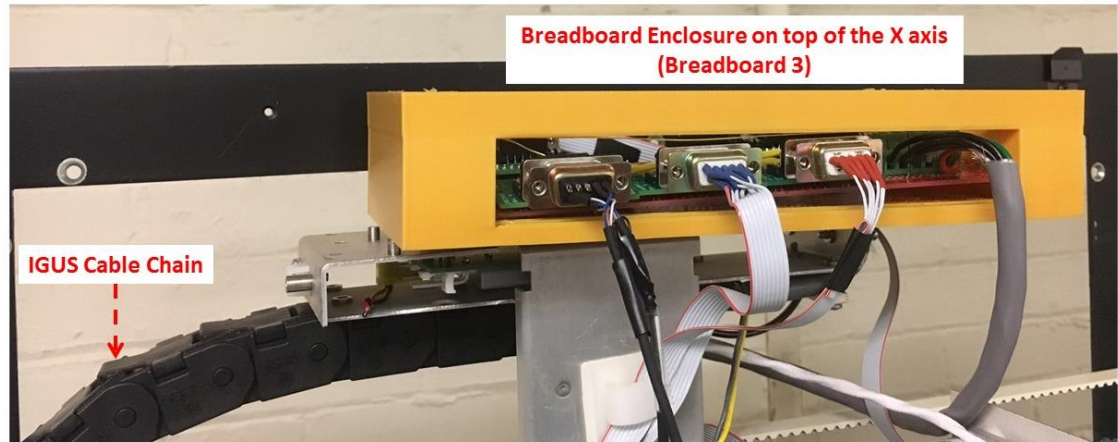


Figure E.2 Breadboard 1 enclosure on top of the X axis.

E.1 Breadboards

The three breadboards are shown in Figure E.3, and the electrical connections on each breadboard are listed in Table E.1. Breadboard 1 is placed within Electrical Box 1, Breadboard 2 is placed within Electrical Box 2, and Breadboard 3 is secured a top the X axis. The Electrical Connections column reference the tables listed in Section E.2. The Breadboard Location column refers to the placement on the breadboard and reference the numbers listed in Figure E.3.

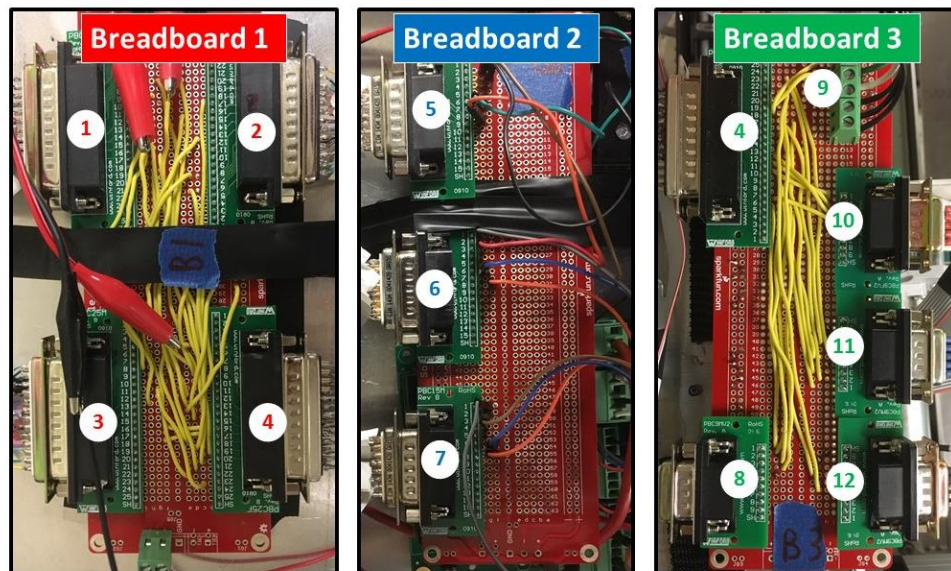


Figure E.3 The three breadboards used for electrical wiring.

Table E.1 Electrical connection information for each breadboard.

Breadboard	Breadboard Location	Electrical Connection(s)	Notes
1	1	A.7 and A.8	25 pin DSUB to access each pin in the MDR Connector from the NI 9514 module connected to the Y axis
	2	A.9 and A.10	25 pin DSUB to access each pin in the MDR Connector from the NI 9514 module connected to the X axis
	3	A.11 and A.12	25 pin DSUB to access each pin in the MDR Connector from the NI 9514 module connected to the Z axis
	4	A.17	Male end of 25 pin DSUB which connects breadboard 1 to breadboard 3
2	5	A.14	9 pin DSUB to access each pin in the DSUB Connector from the NI 9514 module connected to the X axis
	6	A.15	9 pin DSUB to access each pin in the DSUB Connector from the NI 9514 module connected to the Y axis
	7	A.16	9 pin DSUB to access each pin in the DSUB Connector from the NI 9514 module connected to the Z axis
3	4	A.17	Female end of 25 pin DSUB which transmits signals from breadboard 1 to breadboard 3 to send to controller
	8	A.18	9 pin DSUB to provide power to and collect information from the X axis encoder
	9	A.19	6 slot screw terminal to provide power to and collect information from X axis limit switches, and contains zeroing signal for the Z axis (reverse limit switch)
	10	A.20	9 pin DSUB to provide power to and collect information from the Y axis encoder
	11	A.21	9 pin DSUB to provide power to and collect information from the Z axis encoder and Z axis forward limit switch power and signal
	12	A.22	9 pin DSUB to provide power to and collect information from Y axis limit switches

E.2 Electrical and Power Connections

This section outlines the electrical wiring connections outlined in Chapter 2. The electrical connection diagram contained in Chapter 2 is shown as the top part of Figure E.4 for convenience. The tables following Figure E.4 list the individual electrical connections between components illustrated in the figures. Further, the tables are color coded to match the color of the connections indicated in the figures.

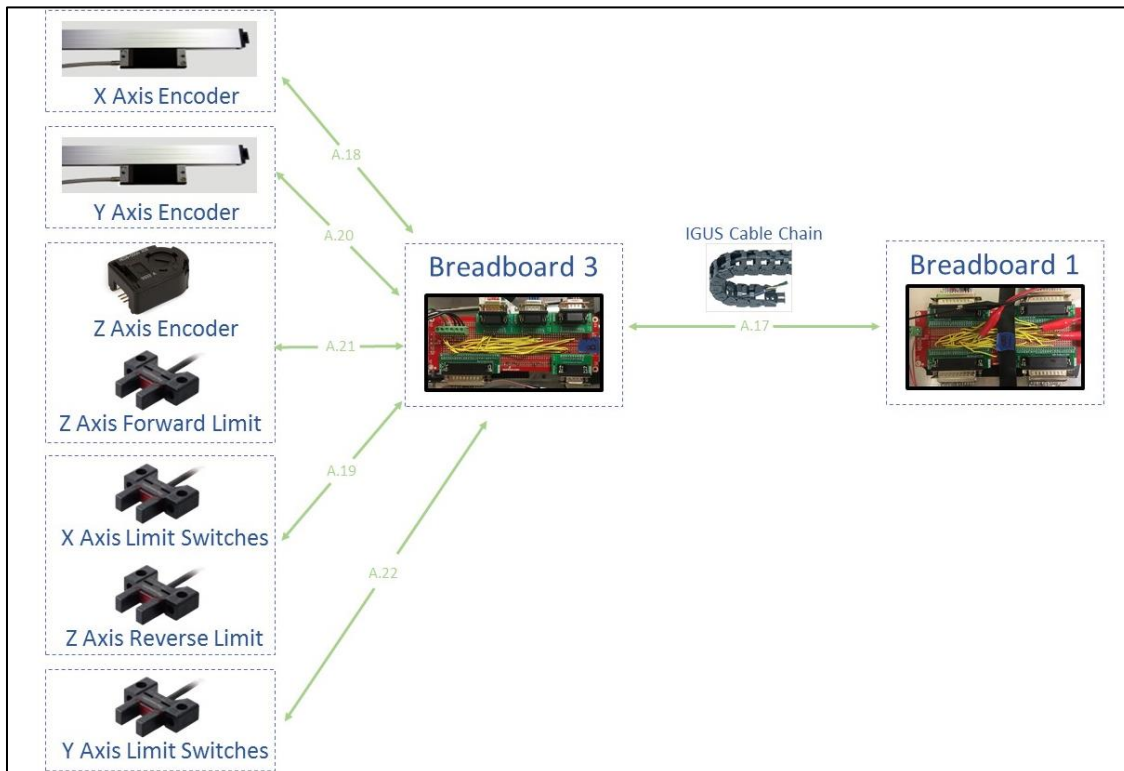
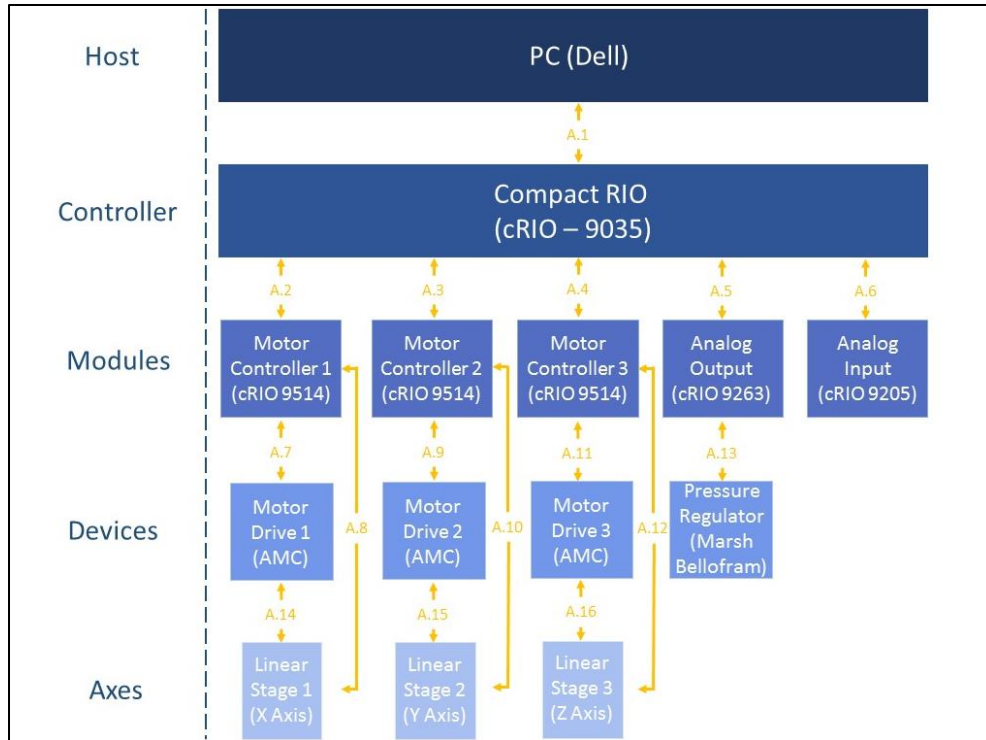


Figure E.4 Electrical connection diagrams for the DW printer. Details of each individual connection (A.1, A.2, etc.) are listed in the tables below.

Table E.2 Details of electrical connection A.1 in Figure 3.4.

A.1			
No.	Host PC	Direction	cRIO
1	Network	↔	Network

Table E.3 Details of electrical connection A.2 in Figure 3.4.

A.2			
No.	cRIO	Direction	Motor Controller 1 (NI 9514, X Axis)
1	cRIO Chassis Slot 2	↔	cRIO Chassis Slot 2

Table E.4 Details of electrical connection A.3 in Figure 3.4.

A.3			
No.	cRIO	Direction	Motor Controller 2 (NI 9514, Y Axis)
1	cRIO Chassis Slot 3	↔	cRIO Chassis Slot 3

Table E.5 Details of electrical connection A.4 in Figure 3.4.

A.4			
No.	cRIO	Direction	Motor Controller 3 (NI 9514, Z Axis)
1	cRIO Chassis Slot 4	↔	cRIO Chassis Slot 4

Table E.6 Details of electrical connection A.5 in Figure 3.4.

A.5			
No.	cRIO	Direction	Analog Output (NI 9263)
1	cRIO Chassis Slot 1	↔	cRIO Chassis Slot 1

Table E.7 Details of electrical connection A.6 in Figure 3.4.

A.6			
No.	cRIO	Direction	Analog Input (NI 9205)
1	cRIO Chassis Slot 5	↔	cRIO Chassis Slot 5

Table E.8 Details of electrical connection A.7 in Figure 3.4.

A.7					
No.	Motor Controller 1 (NI 9514, X Axis)		Direction	AMC Motor Drive 1 (X Axis)	
	15-pin DSUB Connector			AMC Mounting Card	
	Device 1 Pin #	Signal		Device 2 Pin #	Signal
1	1	Drive Command COM	↔	2	SIGNAL GND
2	2	Drive Enable	←	5	INHIBIT IN
3	6	Drive Command	→	1	+REF IN
4	8	Digital Input 1	←	7	FAULT OUT

Table E.9 Details of electrical connection A.8.1 in Figure 3.4.

A.8.1					
No.	Motor Controller 1 (NI 9514, X Axis)		Direction	Linear Stage 1 (X Axis)	
	20-pin MDR Connector			Limit Switches (Panasonic, PM-24)	
	Device 1 Pin #	Signal		Device 2 Pin #	Signal
1	11	Reverse Limit	←	White wire	Sensor Output 2
2	8	COM	↔	Blue wire	0 V

Table E.10 Details of electrical connection A.8.2 in Figure 3.4.

A.8.2					
No.	Motor Controller 1 (NI 9514, X Axis)		Direction	Linear Stage 1 (X Axis)	
	20-pin MDR Connector			Limit Switches (Panasonic, PM-24)	
	Device 1 Pin #	Signal		Device 2 Pin #	Signal
1	1	Forward Limit	←	White wire	Sensor Output 2
2	8	COM	↔	Blue wire	0 V

Table E.11 Details of electrical connection A.9 in Figure 3.4.

A.9					
No.	Motor Controller 2 (NI 9514, Y Axis)		Direction	AMC Motor Drive 2 (Y Axis)	
	15-pin DSUB Connector			AMC Mounting Card	
	Device 1 Pin #	Signal		Device 2 Pin #	Signal
1	1	Drive Command COM	↔	2	SIGNAL GND
2	2	Drive Enable	←	5	INHIBIT IN
3	6	Drive Command	→	1	+REF IN
4	8	Digital Input 1	←	7	FAULT OUT

Table E.12 Details of electrical connection A.10.1 in Figure 3.4.

A.10.1					
No.	Motor Controller 2 (NI 9514, Y Axis)		Direction	Linear Stage 2 (Y Axis)	
	20-pin MDR Connector			Limit Switches (Panasonic, PM-24)	
	Device 1 Pin #	Signal		Device 2 Pin #	Signal
1	11	Reverse Limit	←	White wire	Sensor Output 2
2	8	COM	↔	Blue wire	0 V

Table E.13 Details of electrical connection A.10.2 in Figure 3.4.

A.10.2					
No.	Motor Controller 2 (NI 9514, Y Axis)		Direction	Linear Stage 2 (Y Axis)	
	20-pin MDR Connector			Limit Switches (Panasonic, PM-24)	
	Device 1 Pin #	Signal		Device 2 Pin #	Signal
1	1	Forward Limit	←	White wire	Sensor Output 2
2	8	COM	↔	Blue wire	0 V

Table E.14 Details of electrical connection A.11 in Figure 3.4.

A.11					
No.	Motor Controller 3 (NI 9514, Z Axis)		Direction	AMC Motor Drive 3 (Z Axis)	
	15-pin DSUB Connector			AMC Mounting Card	
	Device 1 Pin #	Signal		Device 2 Pin #	Signal
1	1	Drive Command COM	↔	2	SIGNAL GND
2	2	Drive Enable	←	5	INHIBIT IN
3	6	Drive Command	→	1	+REF IN
4	8	Digital Input 1	←	7	FAULT OUT

Table E.15 Details of electrical connection A.12.1 in Figure 3.4.

A.12.1					
No.	Motor Controller 3 (NI 9514, Z Axis)		Direction	Linear Stage 3 (Z Axis)	
	20-pin MDR Connector			Limit Switches (Panasonic, PM-24)	
	Device 1 Pin #	Signal		Device 2 Pin #	Signal
1	11	Reverse Limit	←	White wire	Sensor Output 2
2	8	COM	↔	Blue wire	0 V

Table E.16 Details of electrical connection A.12.2 in Figure 3.4.

A.12.2					
No.	Motor Controller 3 (NI 9514, Z Axis)		Direction	Linear Stage 3 (Z Axis)	
	20-pin MDR Connector			Zeroing Circuit (self made)	
	Device 1 Pin #	Signal		Device 2 Pin #	Signal
1	1	Forward Limit	←	White wire	Sensor Output 2
2	8	COM	↔	Black wire	GND

Note: in the self-made circuit, the white wire is attached to the nozzle and the black wire is attached to the substrate. When the nozzle touches the substrate, the circuit is closed and the reverse limit switch is turned ON.

Table E.17 Details of electrical connection A.13 in Figure 3.4.

A.13					
No.	Analog Output (NI 9263)		Direction	Pressure Regulator	
	Device 1 Pin #	Signal		Device 2 Pin #	Signal
1	AO1	Analog Output	→	S	SIGNAL
2	AO GND	Ground	→	(-)	GROUND

Table E.18 Details of electrical connection A.14 in Figure 3.4.

A.14					
No.	AMC Motor Drive 1 (X Axis)		Direction	Linear Stage 1 (X Axis)	
	AMC Mounting Card			DC Brushed Motor	
	Device 1 Pin #	Signal		Device 2 Pin #	Signal
1	MOTOR A	Phase A	→	+	Phase A
2	MOTOR B	Phase B	→	-	Phase B

Table E.19 Details of electrical connection A.15 in Figure 3.4.

A.15					
No.	AMC Motor Drive 2 (Y Axis)		Direction	Linear Stage 2 (Y Axis)	
	AMC Mounting Card			DC Brushed Motor	
	Device 1 Pin #	Signal		Device 2 Pin #	Signal
1	MOTOR A	Phase A	→	+	Phase A
2	MOTOR B	Phase B	→	-	Phase B

Table E.20 Details of electrical connection A.16 in Figure 3.4.

A.16					
No.	AMC Motor Drive 3 (Z Axis)		Direction	Linear Stage 3 (Z Axis)	
	AMC Mounting Card			DC Brushed Motor	
	Device 1 Pin #	Signal		Device 2 Pin #	Signal
1	MOTOR A	Phase A	→	+	Phase A
2	MOTOR B	Phase B	→	-	Phase B

Table E.21 Details of electrical connection A.17 in Figure 3.4.

A.17				
No.	25 Pin DSUB			Notes
	Pin #	Signal	Wire Color	
1	5	Z Encoder V+	Green/White	Goes through the IGUS cable chain to transmit signals from breadboard 3 to breadboard 1
2	6	X Encoder V+	Red	
3	7	Y Encoder V+	Red/White	
4	8	X Encoder A	Green/Black	
5	9	X Encoder B	White	
6	10	X Encoder Index	Red/Black	
7	11	Y Encoder A	Blue	
8	12	Y Encoder B	White/Black	
9	13	Y Encoder Index	Orange	
10	14	COM	Black	
11	15	+V	Red	
12	16	Z Encoder A	Red/White	
13	17	Z Encoder B	Green/White	
14	18	Z Encoder Index	Blue/White	
15	19	X Axis Forward Limit	Blue/Black	
16	20	X Axis Home	Green	
17	21	Y Axis Forward Limit	Black/White	
18	22	Y Axis Reverse Limit	Orange/Black	
19	23	Z Axis Forward Limit	Blue/Black	
20	24	Z Axis Reverse Limit	Orange/Black	
21	25	Not Used	Green/Black	

Table E.22 Details of electrical connection A.18 in Figure 3.4.

A.18							
No.	9 Pin DSUB Connector			Direction	25 Pin DSUB Female End On top of X Axis		
	Pin #	Signal	Wire Color		Pin #	Signal	Wire Color
1	1	Encoder A	Yellow	→	8	Encoder 0 Phase A+	Green/Black
2	2	Encoder B	Green	→	9	Encoder 0 Phase B+	White
3	3	Encoder Index	Blue	→	10	Encoder 0 Index+	Red/Black
4	4	+V	Red	←	15	Vsup	Red
5	5	COM	Black	↔	14	COM	Black

Table E.23 Details of electrical connection A.19 in Figure 3.4.

A.19							
No	10 Slot Screw Terminal			Direction	25 Pin DSUB Female End On top of X Axis		
	Pin #	Signal	Wire Color		Pin #	Signal	Wire Color
1	1	COM	Black	↔	21	COM	Black
2	2	COM	Black	↔	15	COM	Black
3	3	COM	Black	↔	14	COM	Black
4	4	+V	White	←	15	Vsup	Red
5	5	X Axis Home	Green	→	20	X Axis Home	Green
6	6	X Axis Forward Limit	Red	→	19	X Axis Forward Limit	Blue/Black

Table E.24 Details of electrical connection A.20 in Figure 3.4.

A.20							
No.	9 Pin DSUB Connector			Direction	25 Pin DSUB Female End On top of X Axis		
	Pin #	Signal	Wire Color		Pin #	Signal	Wire Color
1	1	Encoder A	Yellow Tape	→	11	Encoder 0 Phase A+	Blue
2	2	Encoder B	No Tape	→	12	Encoder 0 Phase B+	White/Black
3	3	Encoder Index	Green Tape	→	13	Encoder 0 Index+	Orange
4	4	+V	Red Tape	←	15	Vsup	Red
5	5	COM	Black Tape	↔	14	COM	Black

Table E.25 Details of electrical connection A.21 in Figure 3.4.

A.21							
No.	9 Pin DSUB Connector			Direction	25 Pin DSUB Female End On top of X Axis		
	Pin #	Signal	Wire Color		Pin #	Signal	Wire Color
1	1	Encoder Index	Yellow Tape	→	18	Encoder 0 Index+	Blue/White
2	2	Encoder B	No Tape	→	17	Encoder 0 Phase B+	Green/White
3	3	Encoder A	Green Tape	→	16	Encoder 0 Phase A+	Red/White
4	4	COM	Black	↔	14	COM	Black
5	5	+V Encoder	Red	←	5	Z Axis Encoder V+	Green/White
6	6	Forward Limit	White	→	23	Z Axis Forward Limit	Blue/Black
7	7	Reverse Limit	White	→	24	Z Axis Reverse Limit	Orange/Black
8	8	+V Limit Switch	Orange	←	15	Vsup	Red
9	9	GND	Blue	↔	14	COM	Black

Table E.26 Details of electrical connection A.22 in Figure 3.4.

A.22							
No.	9 Pin DSUB Connector			Direction	25 Pin DSUB Female End On top of X Axis		
	Pin #	Signal	Wire Color		Pin #	Signal	Wire Color
1-3	1-3	Open					
4	4	Reverse Limit	White	→	22	Y Axis Reverse Limit	Orange/Black
5	5	COM	Blue	↔	14	COM	Black
6	6	Forward Limit	White	→	21	Y Axis Forward Limit	Black/White
7	7	COM	Blue	↔	14	COM	Black
8	8	+ V	Orange	←	15	Vsup	Red
9	9	+ V	Orange	←	15	Vsup	Red